



**HAL**  
open science

# Quasiperiodic arrays of weakly coupled nonlinear oscillators for vibration energy harvesting by electromagnetic or electromagnetic-piezoelectric transductions

Kaouthar Aouali

► **To cite this version:**

Kaouthar Aouali. Quasiperiodic arrays of weakly coupled nonlinear oscillators for vibration energy harvesting by electromagnetic or electromagnetic-piezoelectric transductions. *Vibrations [physics.class-ph]*. Université Bourgogne Franche-Comté; Université de Sfax (Tunisie), 2021. English. NNT : 2021UBFCD065 . tel-03616012

**HAL Id: tel-03616012**

**<https://theses.hal.science/tel-03616012v1>**

Submitted on 22 Mar 2022

**HAL** is a multi-disciplinary open access archive for the deposit and dissemination of scientific research documents, whether they are published or not. The documents may come from teaching and research institutions in France or abroad, or from public or private research centers.

L'archive ouverte pluridisciplinaire **HAL**, est destinée au dépôt et à la diffusion de documents scientifiques de niveau recherche, publiés ou non, émanant des établissements d'enseignement et de recherche français ou étrangers, des laboratoires publics ou privés.



**UNIVERSITÉ DE  
FRANCHE-COMTÉ**



THESE DE DOCTORAT DE L'ETABLISSEMENT UNIVERSITE BOURGOGNE FRANCHE-COMTE

en co-tutelle avec l'Université de Sfax

PREPAREE A L'UNIVERSITE DE FRANCHE-COMTE

Ecole doctorale n°37

Sciences Pour l'Ingénieur et Microtechniques

Doctorat de Sciences pour l'Ingénieur - Spécialité Mécanique

Par

Kaouthar AOUALI

Réseaux quasi-périodiques d'oscillateurs non-linéaires faiblement couplés pour la récupération d'énergie vibratoire par voies électromagnétique ou bien électromagnétique-piézoélectrique

Quasiperiodic arrays of weakly coupled nonlinear oscillators for vibration energy harvesting by electromagnetic or electromagnetic-piezoelectric transductions

Thèse présentée et soutenue à Besançon, le 10/12/2021

Composition du Jury :

Skandar BASROUR	Professeur des Universités, Grenoble-Alpes, Grenoble	Président
M. Najib ICHCHOU	Professeur des Universités, ECL, Lyon	Rapporteur
Mnaouar CHOUCANE	Professeur des Universités, ENIM, Monastir	Rapporteur
Fakhreddine DAMMAK	Professeur des Universités, ENIS, Sfax	Examineur
Noureddine BOUHADDI	Professeur des Universités, UBFC, Besançon	Directeur de thèse
Mohamed HADDAR	Professeur des Universités, ENIS, Sfax	Directeur de thèse
Najib KACEM	Maître de Conférences HDR, UBFC, Besançon	Co-encadrant de thèse



# Acknowledgement

To my family, colleagues and friends ...

*Thank you ...*





# Contents

<b>General introduction</b>	<b>vii</b>
<b>1 State of the art</b>	<b>1</b>
1.1 Introduction	3
1.2 Energy harvesting as a potential solution to the global energy challenge	3
1.3 Ambient energy sources	4
1.4 Classification approach of Vibration Energy Harvesters (VEH)	5
1.4.1 Excitation direction	5
1.4.2 Excitation form	6
1.5 Generic model of a typical VEH	6
1.5.1 Typical structure of a VEH	6
1.5.2 Generic model of a VEH	7
1.6 Electromechanical transduction techniques	8
1.6.1 Electromagnetic transduction (EM)	10
1.6.2 Piezoelectric transduction (PE)	11
1.6.3 Electrostatic transduction	13
1.6.4 Triboelectric transduction	14
1.6.5 Qualitative comparison of the different transduction techniques	15
1.7 PE, EM and commercialized harvesters	16
1.7.1 Piezoelectric energy harvesters	16
1.7.2 Electromagnetic energy harvesters	18
1.7.3 Commercialized energy harvesters	20
1.8 Improvement techniques for Resonant Systems	24
1.8.1 Enlargement of the bandwidth	24
1.8.2 Enhancement of the harvested power	31
1.9 Improvement techniques for Non-Resonant Systems	34
1.9.1 Non-Resonant Electromagnetic Energy Harvesters	34
1.9.2 Non-Resonant Piezoelectric Energy Harvesters	36
1.10 Improvement techniques for multi-directional systems	37

1.10.1	Bi-dimensional harvesting . . . . .	37
1.10.2	Tri-dimensional harvesting . . . . .	39
1.11	Summary . . . . .	40
<b>2</b>	<b>Theoretical analysis and experimental study for electromagnetic energy harvester by fonctionnalization of energy localization and nonlinear dynamics</b>	<b>43</b>
2.1	Introduction . . . . .	45
2.2	Modeling of the dynamic system . . . . .	45
2.2.1	Device of the proposed vibration energy harvester . . . . .	45
2.2.2	Mechanical model . . . . .	46
2.3	Experimental protocol and model confrontation . . . . .	52
2.3.1	Device manufacture . . . . .	52
2.3.2	Experimental test bench . . . . .	52
2.3.3	Energy harvester characterization . . . . .	54
2.4	Illustration of mode localization phenomenon . . . . .	55
2.5	Preliminary study of the linear harvester . . . . .	58
2.5.1	Linear one-beam harvester . . . . .	58
2.5.2	Linear harvester in the case of two beams . . . . .	61
2.6	Preliminary study of the nonlinear harvester . . . . .	65
2.6.1	Nonlinear one beam harvester . . . . .	66
2.6.2	Nonlinear harvester in the case of two beams: Resolution procedure . . . . .	68
2.7	Robustness of energy localization phenomenon and combination of nonlinear dynamics with mode localized phenomenon . . . . .	70
2.7.1	Robustness of energy localization . . . . .	70
2.7.2	Performance comparison of different configurations . . . . .	71
2.7.3	Experimental validation of the retained configuration . . . . .	73
2.8	Experimental investigation of energy localization and nonlinear dynamics combination	74
2.8.1	Energy localization and harvested power in linear and nonlinear cases . . . . .	74
2.8.2	Experimental optimization of the harvester performance by combining energy localization and nonlinear dynamics . . . . .	75
2.9	Summary . . . . .	77
<b>3</b>	<b>Multiobjective optimization of a multimodal electromagnetic VEH by fonctionnalization of mode localization and nonlinear dynamics</b>	<b>79</b>
3.1	Introduction . . . . .	80
3.2	Multiobjective optimization . . . . .	80
3.2.1	General formulation of a multiobjective optimization problem . . . . .	80
3.2.2	Pareto dominance and optimality concepts . . . . .	81
3.2.3	NSGA-II algorithm . . . . .	82

---

3.3	Mechanical Model . . . . .	85
3.3.1	Proposed Design . . . . .	85
3.3.2	Equation of Motion . . . . .	85
3.4	Multiobjective optimization of the validated two-coupled-beams harvester . . . . .	86
3.4.1	Numerical-Experimental confrontation of the 2-DOFs harvester . . . . .	86
3.4.2	Optimization of the validated 2-DOFs model . . . . .	88
3.5	Multiobjective optimization of the five-coupled-beams model . . . . .	90
3.5.1	Determination of the introduced mistuning optimal positions . . . . .	91
3.5.2	Multiobjective optimization of the five-coupled-beams harvester . . . . .	92
3.5.3	Figure of merit for comparison to the state of art . . . . .	96
3.6	Summary . . . . .	97
<b>4</b>	<b>2:1 Internal resonance for a hybrid electromagnetic-piezoelectric vibration energy harvester</b> . . . . .	<b>99</b>
4.1	Introduction . . . . .	100
4.2	Hybrid electromagnetic-piezoelectric vibration energy harvester . . . . .	100
4.2.1	Design of the proposed device . . . . .	100
4.2.2	Modeling of the piezoelectric harvester . . . . .	101
4.2.3	Amplitude and power expressions . . . . .	106
4.2.4	Theoretical results and experimental validation . . . . .	106
4.3	2:1 Internal resonance . . . . .	108
4.3.1	Proposed device . . . . .	108
4.3.2	Mechanical model to obtain commensurate natural frequencies . . . . .	109
4.3.3	Results . . . . .	110
4.4	Energy storage . . . . .	113
4.4.1	Literature review on storage circuits and devices . . . . .	113
4.4.2	Energy storage test . . . . .	116
4.5	Summary . . . . .	119
	<b>Conclusion</b> . . . . .	<b>121</b>
	<b>Conferences and publications</b> . . . . .	<b>125</b>
	<b>Bibliography</b> . . . . .	<b>127</b>



# General introduction

## Context and problem statement

OVER the last years, different applications include excessively embedded and wearable sensors. Most of these devices are based on batteries as the main energy source. However, the batteries have limited life-span and are not environmentally friendly. Moreover, replacing or recharging batteries is costly and can be difficult in critical applications. The fact that can reduce the robustness of these wireless sensor systems. For these reasons, having an unlimited energy source can be an alternative to overcome these limitations. Based on this, the concept of harvesting energy from ambient sources is challenging.

Energy harvesting refers to the techniques that allow converting a form of ambient energy source to electricity in order to power small systems. The concept of locally converting energy by a system in order to operate autonomously is captivating. For that, harvesting energy from different ambient sources has received increased attention. Among the multiple energy sources, harvesting energy from vibrations has garnered considerable attention. To convert vibrations into electricity, four main types of transduction techniques are used namely piezoelectric, electromagnetic, electrostatic and triboelectric. Regarding the application, each technique has benefits and disadvantages.

Despite significant advancements in the field of vibration energy harvesting (VEH), several limitations remain. The most common limitations are namely the narrow bandwidth and the small amount of the harvested energy. Most devices operate near to their resonance frequency the fact that limits their application where energy prevails over a larger frequency bandwidth. In order to overcome these VEH limitations, several approaches have been considered. We can mention the introduction of non-linearity, the fonctionnalization of the energy localization phenomenon, the multimodal configuration, the hybrid transduction techniques, etc.

The introduction of nonlinear dynamics as well as multimodal approach permits considerably enhancing the frequency bandwidth or the output harvested power. Multiple researchers adopted the multimodal configuration in order to cover a larger frequency range. However, others investigated the benefits of multimodal approaches by fonctionnalization of the mode localization phenomenon in order

to increase the harvested power. The phenomenon of energy localization occurs when a symmetry-breaking perturbation is introduced to a periodic structure and is manifested by the vibration energy trapping in regions close to the perturbed regions.

In this thesis, we will study the dynamic behavior of an electromagnetic vibration energy harvester in the beginning. Then, the transduction technique will be transformed to electromagnetic-piezoelectric one and the dynamic behavior of the hybrid system will be also studied. We will investigate the benefits of the nonlinear dynamics and energy localization phenomenon in order to enhance the output performance in terms of frequency bandwidth and total harvested power.

## Manuscript organization

In order to overcome the limitations of the harvesters mentioned above, we propose some concepts that will be theoretically demonstrated and experimentally validated. For that, the manuscript will be divided into four chapters as following:

- In [chapter 1](#), we provide a literature review on vibration energy harvesters. We review the different classification approaches of vibration energy harvesters and present the generic model of a typical VEH. Then, the different transduction techniques are mentioned with detailed examples. A qualitative comparison between these techniques is done. After that, we review in details the different improvement techniques for the different types of VEH.
- In [chapter 2](#), we study an energy harvester with two degrees of freedom (DOFs) based on electromagnetic transduction. The manufacture of the device and the experimental test bench are established. In order to enhance the frequency bandwidth and the harvested power, a first concept of combining the nonlinear dynamics and the energy localization phenomenon is investigated. The Galerkin method is used in order to discretize the continuous equations of motion. The resolution of the equations is done through the method of multiple scales and the analytical model is experimentally validated.
- In [chapter 3](#), we generalize the 2-DOFs system to a 5-DOFs one. Two mass mistuning are introduced in the system. In order to obtain the best locations of the mistuning, a multiobjective optimization is carried out. To simultaneously enhance the harvested power and the frequency bandwidth, a multiobjective optimization is performed while functionalizing the energy localization phenomenon and the nonlinear dynamics.
- In [chapter 4](#), we transformed the electromagnetic energy harvester to a hybrid one by adding piezoelectric layers to the ends of the elastic beams. The hybrid systems is studied. A comparative study between it and the electromagnetic one is established. Then, the phenomenon of internal resonance is investigated in order to further enhance the harvested power and the frequency bandwidth.

# Chapter 1

## State of the art

### Contents

---

<b>1.1</b>	<b>Introduction</b>	<b>3</b>
<b>1.2</b>	<b>Energy harvesting as a potential solution to the global energy challenge</b>	<b>3</b>
<b>1.3</b>	<b>Ambient energy sources</b>	<b>4</b>
<b>1.4</b>	<b>Classification approach of Vibration Energy Harvesters (VEH)</b>	<b>5</b>
1.4.1	Excitation direction	5
1.4.2	Excitation form	6
<b>1.5</b>	<b>Generic model of a typical VEH</b>	<b>6</b>
1.5.1	Typical structure of a VEH	6
1.5.2	Generic model of a VEH	7
<b>1.6</b>	<b>Electromechanical transduction techniques</b>	<b>8</b>
1.6.1	Electromagnetic transduction (EM)	10
1.6.2	Piezoelectric transduction (PE)	11
1.6.3	Electrostatic transduction	13
1.6.4	Triboelectric transduction	14
1.6.5	Qualitative comparison of the different transduction techniques	15
<b>1.7</b>	<b>PE, EM and commercialized harvesters</b>	<b>16</b>
1.7.1	Piezoelectric energy harvesters	16
1.7.2	Electromagnetic energy harvesters	18
1.7.3	Commercialized energy harvesters	20
<b>1.8</b>	<b>Improvement techniques for Resonant Systems</b>	<b>24</b>
1.8.1	Enlargement of the bandwidth	24
1.8.2	Enhancement of the harvested power	31
<b>1.9</b>	<b>Improvement techniques for Non-Resonant Systems</b>	<b>34</b>
1.9.1	Non-Resonant Electromagnetic Energy Harvesters	34
1.9.2	Non-Resonant Piezoelectric Energy Harvesters	36



<b>1.10 Improvement techniques for multi-directional systems</b> . . . . .	<b>37</b>
1.10.1 Bi-dimensional harvesting . . . . .	37
1.10.2 Tri-dimensional harvesting . . . . .	39
<b>1.11 Summary</b> . . . . .	<b>40</b>

---

## 1.1 Introduction

THE idea of having a system able to convert energy locally to run autonomously is intriguing. For that, the concept of harvesting energy from unlimited ambient sources has received considerable attention. In this context, a brief review on the energy harvesting field as a potential solution to the global energy challenge is presented in this chapter. Then, an exhaustive classification of the vibration energy harvesters, their typical structure and the existing transduction techniques are depicted. Next, a qualitative comparison between these techniques is established. After that, a summary of piezoelectric, electromagnetic and commercialized harvesters is presented. Following the literature, we highlight the improvement techniques of the vibration energy harvesters performances.

## 1.2 Energy harvesting as a potential solution to the global energy challenge

Over the last years, wireless sensor systems are receiving an important interest thanks to their flexibility, their ability to retrofit systems and their potential to avoid problems of cost and wiring. They depend on the use of batteries as the main source of energy. Due to the limited lifespan of the battery, the robustness of these devices, which is the most important key in the design of modern wireless technologies, can be degraded. In this case, replacing or recharging batteries is often costly due to the large number of wireless devices in use, and is almost impossible in very critical applications. To overcome these problems, harvesting energy from the environment can be an alternative. This can be achieved based on ambient sources which have been increasingly investigated and received much attention. The concept that a system can locally convert different forms of energy to operate on its own is captivating. In the field of electronic systems, energy harvesting refers to techniques that convert a form of energy present in the ambient environment to power small devices. Based on this attractive principle, the theme of energy recovery (harvesting or scavenging) emerged in the early 1990s. The number of related research works has been growing at a rapid pace since the 2000s as shown in Figure 1.1. This promising technique is considered to be among the green energy solutions that can reduce greenhouse gas emission and thus helps solve global energy challenge without natural resources exhaustion. Energy harvesting technology has various benefits [2, 3]:

- Sustainable energy sources : The operation of the systems is based on the existing renewable ambient energy in the environment that has an unlimited lifespan.
- Environmental friendliness: Energy recovery helps to limit the excessive use of non-rechargeable batteries that have an impact on the environment and once discharged, they are the source of a large amount of non-recyclable waste. Consequently, the use of non rechargeable batteries becomes an important source of pollution.
- Low-cost maintenance: There is no need to run any wires or make any changes to the smart

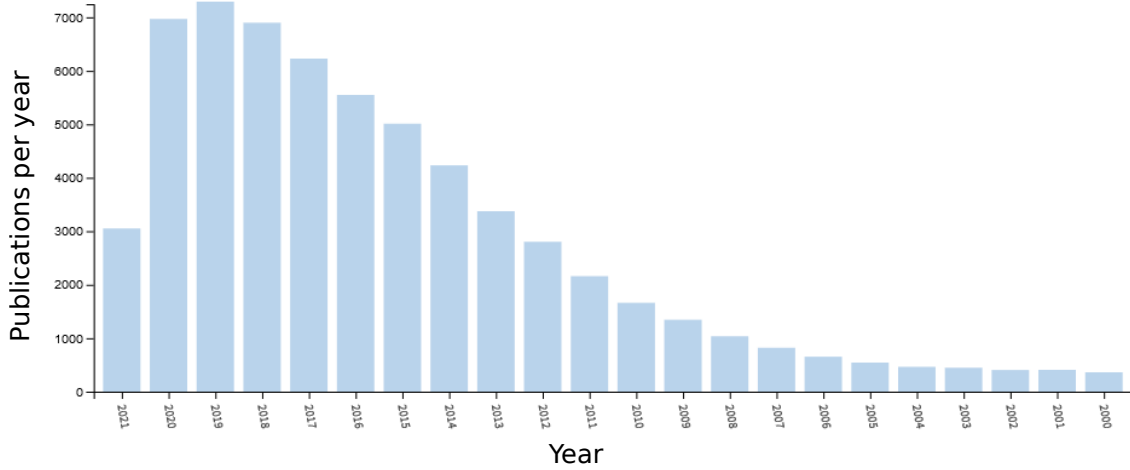


Figure 1.1: Publications number in Scopus in the field of energy harvesting [1]

space’s current energy infrastructure. When compared to battery-powered devices, maintenance costs are significantly cheaper.

- **Autonomy:** if the system’s expected autonomy is larger than the battery’s probable working duration, an energy harvester may be necessary
- **Pervasiveness:** Micro-scale energy harvesting systems may be readily installed as plug-and-play gadgets in smart environments. They may easily and non-intrusively propagate and integrate into daily living activities.

### 1.3 Ambient energy sources

Different ambient sources exist in the environment and can be explored to produce electricity and power systems such as nuclear, heat, solar, radio wave, etc. Energy, also, can be scavenged from animal and human activity. Figure 1.2 gathers mostly used energy sources. Comparing these many sources is difficult because it depends on a variety of elements as well as the application in question. Comparison studies, on the other hand, have been done to examine the power densities of a variety of typical sources. Table 1.1 shows some results. After solar power, it appears that capturing energy from ambient vibrations has the potential to attain the second highest energy density. This source of energy has many advantages, namely the availability in different application fields such as transport, autonomous sensors, industry, etc. Regarding its availability, the vibration energy can exist in typical applications, in buildings, outside, factories and even at home and can be generated for accelerations going from  $0.1 m.s^{-2}$  to  $10 m.s^{-2}$  in different frequency ranges [5]. In the following and throughout the thesis, we are interested in harnessing energy from vibrations.

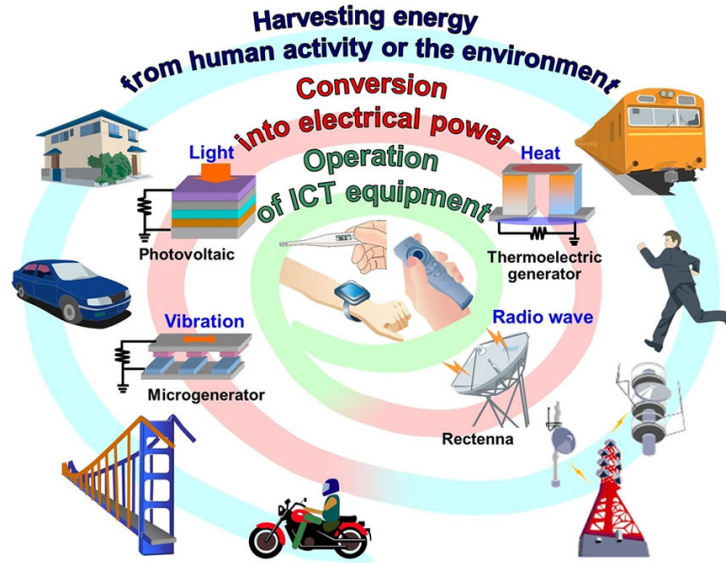


Figure 1.2: Different energy sources [4]

Table 1.1: Power density of different energy scavenging technologies [6]

Technology	Power density
Indoor photovoltaic (yield cell 6%, incident irradiance of $100 \text{ mW}/\text{cm}^2$ )	$100 \mu\text{W}/\text{cm}^2$
Outdoor photovoltaic (yield cell 15%, incident irradiance of $100 \text{ mW}/\text{cm}^2$ )	$15000 \mu\text{W}/\text{cm}^2$
Outdoor wind turbine	$3 - 5 \text{ mW}/\text{cm}^2$
Acoustic noise (100 dB)	$0.9 \mu\text{W}/\text{cm}^3$
Airflow	$0.4 - 1 \text{ mW}/\text{cm}^3$
Thermoelectric for $10^\circ\text{C}$ gradient	$30 - 60 \mu\text{W}/\text{cm}^3$
Small microwaves oven vibrations	$116 \mu\text{W}/\text{cm}^3$
Shoe inserts using piezoelectric materials	$330 \mu\text{W}/\text{cm}^3$

## 1.4 Classification approach of Vibration Energy Harvesters (VEH)

In literature, different classifications of harvesting systems are proposed. Generally, mechanical energy harvesting systems (MEH) are categorized according to the direction and the form of the excitation [7, 8]. This exhaustive categorization approach is displayed in Figure 1.3.

### 1.4.1 Excitation direction

Generally, harvesters can be excited from different directions namely from one-dimensional, two-dimensional or three-dimensional directions. The majority of harvesters are made to scavenge energy from a unique direction. However, ambient excitations are multi-directional. For this reason, other harvesters types are designed to harvest from two or three directions. This approach is considered in several research works in order to improve the harvesters output performances. Detailed examples are discussed in Section 1.10.

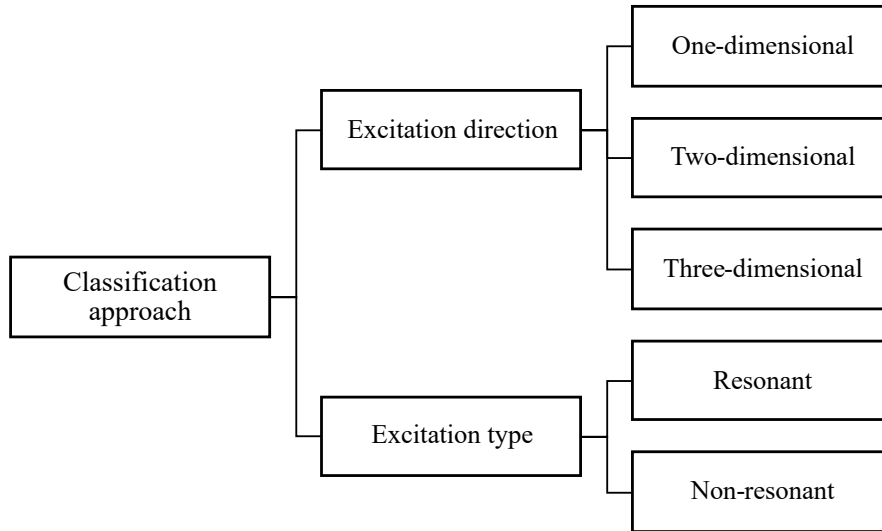


Figure 1.3: Classification approach of MEH systems.

### 1.4.2 Excitation form

According to the form of the excitation, the harvesters can be classified into resonant (RS) or non-resonant systems (NRS). The resonant systems, known also as kinetic energy ones (KES), provide the maximum of harvested power when the system is excited at its resonance frequency. For that, different techniques have been developed to tune the system response to the excitation frequency.

Since the resonant energy harvesters are able to produce the maximum power only when the frequency of excitation matches the resonant frequency of the energy harvester, therefore they operate in a narrow frequency bandwidth. However, non-resonant systems, called also non-kinetic systems (NKES) have the advantage of operating and generating better performance at all operating frequencies. Because they can operate efficiently over a frequencies wide range without any active adjustment, these harvesters have a much better chance of being deployed in a real vibration environment.

Techniques used in RS and NRS are discussed in [Section 1.9](#).

## 1.5 Generic model of a typical VEH

### 1.5.1 Typical structure of a VEH

A typical vibration-based energy harvesting system consists of four components: a mechanical device to optimize mechanical vibrations, an electromechanical device to convert mechanical energy into electrical energy, an extractor circuit to convert electric recovered energy into usable electricity and finally an energy management and storage system as depicted in Figure 1.4.

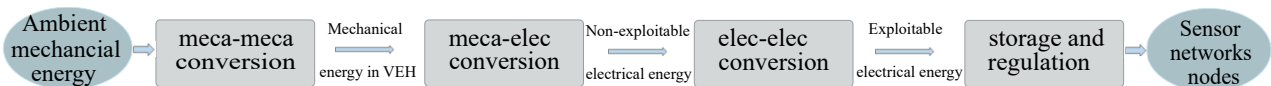


Figure 1.4: Structure of a typical vibration energy harvester: from vibration sources to applications

In order to successfully absorb mechanical energy and then transform it into electrical one, the vibration energy harvester (VEH) must be matched to the source to be used. The extraction circuit's role is done to transform the energy extracted from the harvester into usable energy. It typically consists of two subsystems: an Alternative Current/Direct Current (AC/DC) converter for rectifying and smoothing the electric current, and a Direct Current/Direct Current (DC/DC) converter to adjust the voltage of electrical energy for storage. The storage mechanism generally through a battery or a supercapacitor permits the collection of the energy to be released.

In general, most of the energy harvesters produced to date are equivalent to a mechanical mass-spring resonance system [9, 10]. The electromechanical conversion system has aroused the interest of many researchers, and many distinct transduction techniques have been developed, the characteristics and differences of each one will be discussed in the next paragraph.

### 1.5.2 Generic model of a VEH

The theory of vibration energy harvesting is based on the relative displacement of a mass subjected to a basis excitation as illustrated in Figure 1.5.

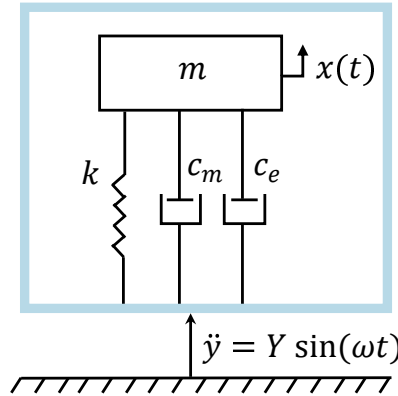


Figure 1.5: 1-DOF energy harvester with base excitation

The governing equation of motion of the system can be written as follows:

$$m \ddot{z} + c \dot{z} + k z = -m \ddot{y} \quad (1.1)$$

where  $m$  is the structure mass,  $z = x - y$  is the relative displacement of the mass,  $c = c_m + c_e$  is the total equivalent damping,  $c_m$  is the mechanical damping,  $c_e$  is the electrical damping and  $k$  is the structure stiffness.

Dividing Equation 1.2 by  $m$ , the following equation is obtained:

$$\ddot{z} + 2(\xi_e + \xi_m)\omega_n \dot{z} + \omega_n^2 z = -\ddot{y} \quad (1.2)$$

where  $\xi_m = \frac{c_m}{2\sqrt{km}}$  and  $\xi_e = \frac{c_e}{2\sqrt{km}}$  are respectively the mechanical and electrical damping factors and  $\omega_n = \sqrt{\frac{k}{m}}$  is the natural frequency of the system.

The device is submitted to a basis harmonic imposed acceleration  $\ddot{y} = Y \sin(\omega t)$  where  $Y$  is the imposed acceleration amplitude and  $\omega$  is the vibration frequency. Let  $z = Z \sin(\omega t)$ . Consequently, the amplitude of vibration  $Z$  is defined by:

$$Z = \frac{Y}{\sqrt{(\omega_n^2 - \omega^2)^2 + (2\xi\omega_n\omega)^2}} \quad (1.3)$$

where  $\xi = \xi_m + \xi_e$  is the total damping factor.

The instantaneous power absorbed by the harvester is defined as follows:

$$P_{inst} = c_e \dot{z}^2 \quad (1.4)$$

which is equivalent to:

$$P_{inst} = c\omega^2 Z^2 \cos(\omega t)^2 \quad (1.5)$$

The harvested power per cycle can be defined as:

$$P_{cycle} = c\omega^2 Z^2 \int_0^T \cos(\omega t)^2 dt = \pi c\omega Z^2 \quad (1.6)$$

where  $T = \frac{2\pi}{\omega}$ . The average power is, consequently, gives:

$$P_{av} = \frac{P_{cycle}}{T} = \frac{c\omega^2 Z^2}{2} \quad (1.7)$$

Substituting Equation 1.3 in Equation 1.7 and dividing by  $\omega_n^2$ , one can obtain:

$$P_{av} = \frac{c \left(\frac{\omega}{\omega_n}\right)^2 Z^2}{2[(1 - (\frac{\omega}{\omega_n})^2)^2 + (2\xi(\frac{\omega}{\omega_n}))^2]} \quad (1.8)$$

The dimensionless form of Equation 1.8 can be obtained by dividing it by  $\frac{Z^2}{m\omega_n}$ :

$$P_{av} = \frac{\xi \left(\frac{\omega}{\omega_n}\right)^2}{(1 - (\frac{\omega}{\omega_n})^2)^2 + (2\xi(\frac{\omega}{\omega_n}))^2} \quad (1.9)$$

Based on Equation 1.9, the dimensionless power with normalized frequency is plotted for  $\xi = 0.1$ . Therefore the maximum of power  $P_{max}$  is marked and the frequency bandwidth  $BW$  based on the half power bandwidth method is shown in Figure 1.6.

## 1.6 Electromechanical transduction techniques

Traditionally, vibrational energy has been absorbed in the form of heat by the damping mechanisms of systems. Instead of wasting vibrational energy in the form of heat, researches have been carried out to transform vibration energy into electrical energy using transducers in energy harvesting devices. Among these techniques, we can mention the most used ones namely: electromagnetic (EM), piezoelectric (PE),

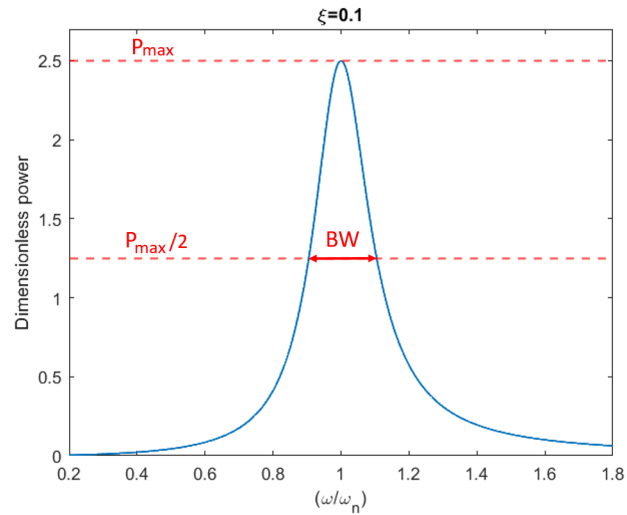


Figure 1.6: Dimensionless power with normalized frequency based on Equation 1.9 for  $\xi = 0.1$

electrostatic (EL) and triboelectric (TR) transductions depicted in Figure 1.7.

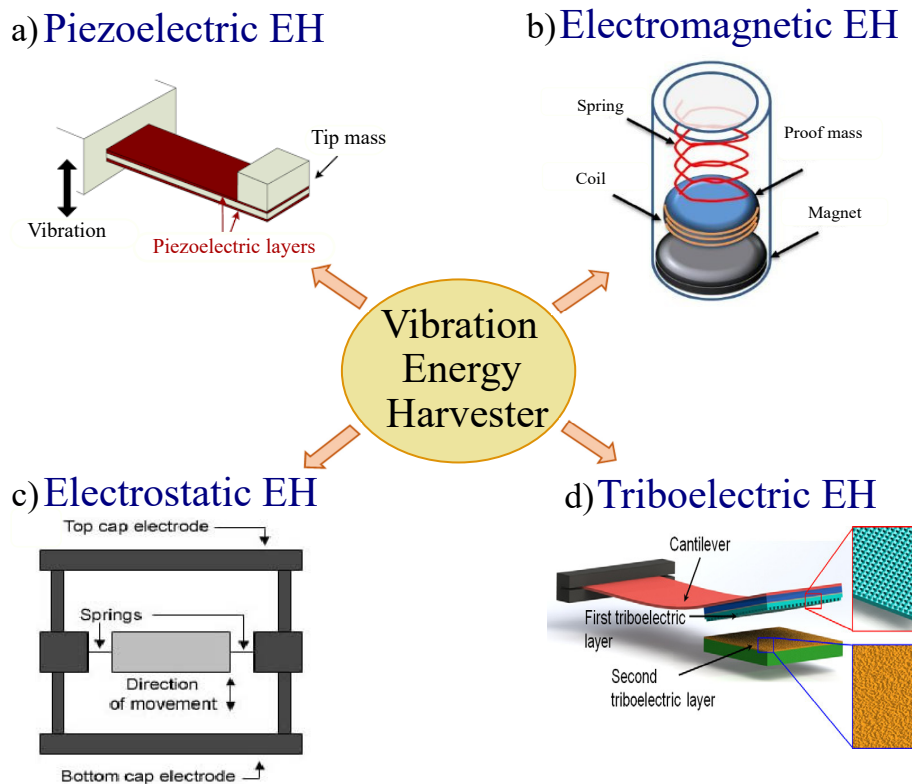


Figure 1.7: Mechanisms for vibration energy harvesters including: a) piezoelectric energy harvesters including a configurations of cantilever with tip mass and top and bottom piezoelectric layers [11], b) electromagnetic energy harvester based on mass-spring resonance [12], c) electrostatic transduction [13], which is represented by parallel top and bottom cap electrodes and internal springs and d) triboelectric transduction represented by a cantilever with two triboelectric layers [14].



### 1.6.1 Electromagnetic transduction (EM)

The generation of electric current in a conductor reigning in a magnetic field is known as electromagnetic induction. This phenomenon has been first discovered by Faraday in 1831. The generator consists typically of a coil and the current can be generated by moving the magnet or the coil or by having variation in the magnetic field. Stand on this concept, electromagnetic energy harvesters are designed based on the relative motion of an electrical conductor in a magnetic field. The motion of a magnetic field relative to a conductive coil causes induction of current through the coil according to Faraday's law of electromagnetic induction. A wire coil linked to a mass connected to a spring is the design of typical electromagnetic energy harvester. When the magnet mass vibrates around its equilibrium position, it emerges in the coil and because of the presence of the magnetic field a current is induced. In earlier years, Williams and Yates [15] were among the first to develop an electromagnetic harvester which consists of a flexible membrane topped with a magnet and a planar coil. They demonstrated the feasibility of energy harvesting from ambient vibrations in 1996 and through this device they showed that they can generate  $3 pW$ . Beeby et al. [16] created an electromagnetic harvester with four magnets placed on an etched cantilever where a wrapped coil is positioned around the magnet as depicted in Figure 1.8. The authors succeed to convert around 30% of the power which is supplied by an air compressor into exploitable electrical power for a frequency range going from 43 to 109  $Hz$  and with accelerations of  $0.19 - 3.7 m.s^{-2}$ .

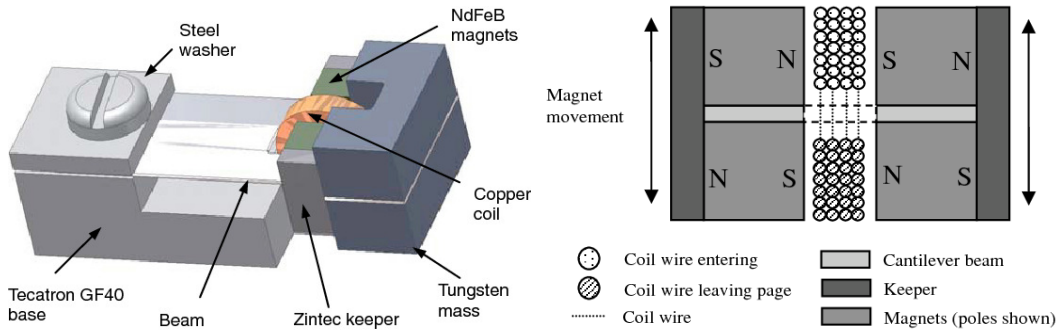


Figure 1.8: Mechanisms for vibration energy harvesters including [16]

A basic electromagnetic transducer consists of one or more magnets creating a magnetic field where a coil is submerged. When a conventional resonant mechanical system as an example a clamped beam is subjected to a vibration, a spring can be used to create a relative displacement  $u(t)$  between the magnet and the coil. According to Faraday's law expressed in Equation 1.10, the change of the magnetic flux  $\phi_m$  over the surface enclosed by the coil produces a proportional voltage  $V$  at the rate of change of the magnetic flux and the number of coil turns  $N$ .

$$V = -N \frac{d\phi_m}{dt} \quad (1.10)$$

To illustrate the induction phenomenon and define the magnetic flow, the simplistic model depicted in Figure 1.9 is considered. When the coil of length  $L$  and including a surface  $S$  is traversed by a magnetic

flux density  $B$  constant over the height of a magnet and nowhere else; the relative displacement between the coil and the magnet is denoted  $z(t)$ . The magnetic flow is then given by:

$$\phi_m = \iint_S B dS \quad (1.11)$$

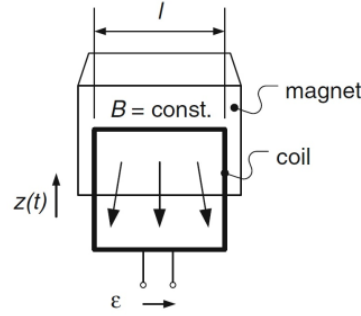


Figure 1.9: Simplistic model of an electromagnetic transducer [17]

The electromagnetic generator can be considered as an actuator and an energy harvester as well. When the magnet moves, the current generates an electromotive force proportional to the current. This flow is represented by the following electromotive damping force  $F_{ce}$ :

$$F_{ce} = \alpha_e i \quad (1.12)$$

Where  $i$  is the induced current.  $\alpha_e = B L$  is the electromotive voltage coefficient.  $B$  is the induced magnetic flow and  $L$  is the total length of the coil.

When the coil inductance is neglected and the electrodes of the electromagnetic energy harvester are connected to a resistance, this force can be expressed as follows:

$$F_{ce} = \frac{\alpha_e^2}{R_{load} + r_{int}} \dot{v} \quad (1.13)$$

Where  $R_{load}$  is the load resistance,  $r_{int}$  is the coil internal resonance and  $\dot{v}$  is the relative velocity between the stator and rotor inducing an electromotive voltage  $e_m$  in the coils defined as:  $e_m = \alpha_e \dot{v}$ . Electromagnetic transducers produce low voltages for high currents.

### 1.6.2 Piezoelectric transduction (PE)

Piezoelectric materials include an electric dipole. This latter is a result of their molecular structure which causes a local charge separation when strained [18]. Piezoelectric transducers are based on the property that certain non-conductive materials can be electrically polarized under the action of a mechanical stress (direct effect), and conversely of being mechanically deformed under the application of an electric field (inverse effect). The direct piezoelectric effect has been demonstrated by Pierre

and Jacques Curie in 1880 [19]. They predicted and verified the existence of piezoelectricity on quartz crystals, silicate salts (tourmaline and topaz), sugar and Rochelle salt. As an application, the direct effect can be observed in the lighter. In fact, when we apply a mechanical force to press the hammer assembly, the crystal generates voltage which is carried by the electrodes at the ignition head to generate a spark as shown in Figure 1.10. This first piezoelectricity characteristic permits the use of the material as a sensor.

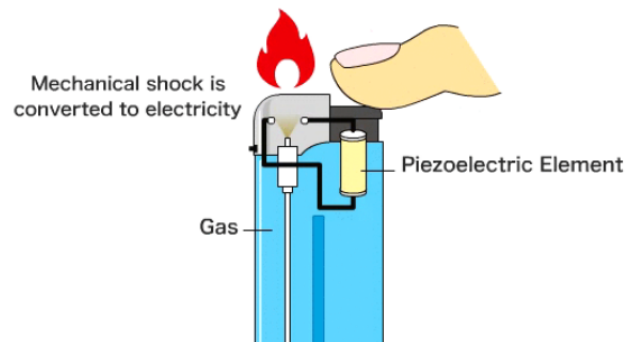


Figure 1.10: Illustration of the direct piezoelectric effect in a lighter [20]

Concerning the inverse effect, its existence was predicted in 1881 by Gabriel Lippmann [21] on the basis of thermodynamic calculations, and immediately verified by the Curies [21]. This effect can be seen in the quartz watches. This second piezoelectricity characteristic permits the use of the material as an actuator. This principle is explained in the following based on the 6 steps [22] shown in Figure 1.11. In a matter of fact, the battery included supplies current to the microchip circuit (step 1) which makes the quartz crystal vibrating (step 2). These oscillations are detected by the microchip circuit. This latter converts regularly the oscillations in such a way that an electric pulse is obtained each second (step 3). A small electric stepping motor is directed by the generated electric pulses. In this way, electrical energy is converted into mechanical power (step 4). Consequently, the gears set in motion and start turning (step 5). Finally, the gears maintain turning and the hands are then also moving around the clockface to keep time (step 6).

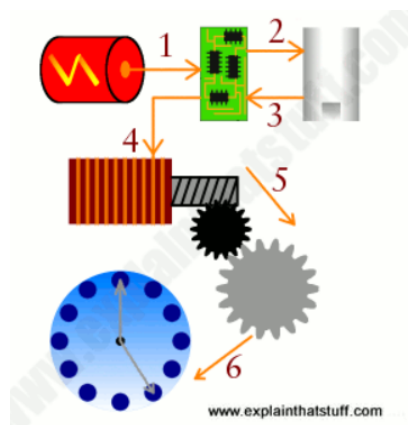


Figure 1.11: Illustration of the inverse piezoelectric effect in a quartz watch (steps from 1 to 6) [22]

In the field of energy harvesting, the direct piezoelectric effect is generally explored by coupling a ceramic PZT patch to the resonant structure as an example the case of a cantilever geometry. With a given imposed force, the cantilever beam is deformed, hence the piezoelectric material is deformed creating a polarization. Based on this typical definition of this device type, a PE energy harvester consisting of two PE layers linked to a cantilever beam and a tip mass is shown in Figure 1.12. Piezoelectric systems, contrarily to electromagnetic ones, provide high levels of voltage for low current.

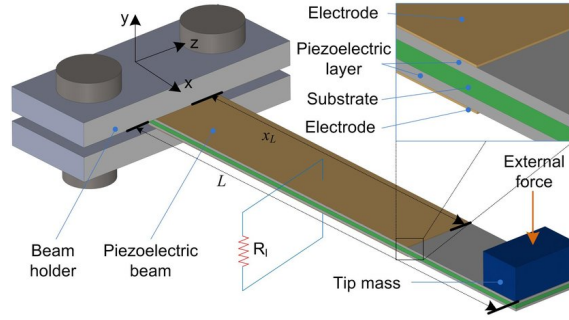


Figure 1.12: Piezoelectric transducer example [23]

The piezoelectric effect is mathematically described by the following constitutive equations [24]:

$$\underline{S} = \underline{s}^E \cdot \underline{T} + \underline{d}^t \cdot \underline{E} \quad (1.14)$$

$$\underline{D} = \underline{d} \cdot \underline{T} + \underline{\epsilon}^T \cdot \underline{E} \quad (1.15)$$

Where  $\underline{S}$  and  $\underline{T}$  are the strain and mechanical stress,  $\underline{D}$  is the electric charges density,  $\underline{E}$  is the electric field,  $\underline{s}^E$  is the mechanical flexibility (inverse of the stiffness matrix) with constant electric field and  $\underline{\epsilon}^T$  is the electric permittivity under constant constraint.  $\underline{d}$  and  $\underline{d}^t$  are the matrix responsible of the direct and inverse piezoelectric effects respectively,  $t$  symbolizes the matrix transpose.

Consequently, the piezoelectric material can be explored in several ways for energy harvesting. Modes of use are evoked, a mode is named after a two-digit number, the first digit corresponds to the axis along which the external action is applied to the material while the second corresponds to the axis along which the potential difference (voltage) appears. The most used modes are mode 33 and mode 31. In Table 1.2, we present the piezoelectric constants for the most used materials for the modes 31 and 33, namely soft and hard lead zirconate titanate piezoceramics (PZT-5H and PZT-5A) and polyvinylidene fluoride (PVDF) [25, 26]. We define  $g$  and  $k$  by the electric field generated per unit of mechanical stress and the electro-mechanical coupling coefficient respectively.  $\epsilon$  is the permittivity of the piezoelectric material and  $\epsilon_0$  is the permittivity of air.

### 1.6.3 Electrostatic transduction

The work principle of the electrostatic transducer is based on Coulomb's Law. Electrostatic harvesters are composed of two electric plates isolated by air or an insulator from each other and pre-charged [27].

Table 1.2: Piezoelectric constants for common materials for 31 and 33 modes [25, 26]

Piezoelectric constant	PZT-5H	PZT-5A	PVDF
$d_{33}$ ( $10^{-12} C N^{-1}$ )	593	374	-33
$d_{31}$ ( $10^{-12} C N^{-1}$ )	-274	-171	23
$g_{33}$ ( $10^{-3} V m N^{-1}$ )	19.7	24.8	330
$g_{31}$ ( $10^{-3} V m N^{-1}$ )	-9.1	-11.4	216
$k_{33}$	0.75	0.71	0.15
$k_{31}$	0.39	0.31	0.12
Relative permittivity ( $\epsilon/\epsilon_0$ )	3400	1700	12

Under the effect of external vibrations, the plates move relatively to each others. If the generator is operated at constant load, the decrease in capacity caused by the change in distance between the two plates will result in an increase in the generator's voltage, hence increasing the potential energy stored in the capacitor. Similarly, by fixing the voltage, the movement of the plates produces a current due to the movement of the charges. A more detailed description of this approach is given by Meninger et al. [28]. These harvesters are particularly adapted to microscopic realizations. Electrostatic generators can be classified into three types: In-plane overlap varying, In-plane gap closing and Out-of-plane gap closing [27, 29]. These types are shown in Figure 1.13.

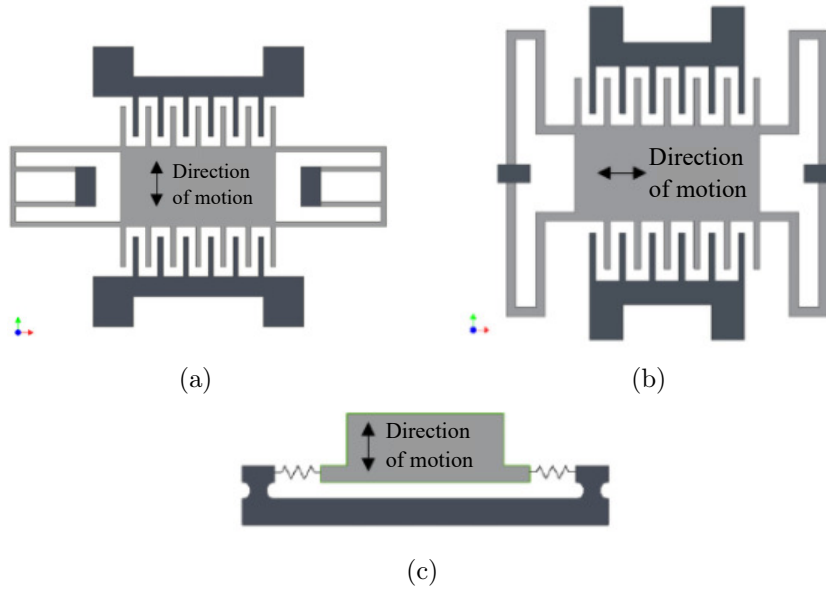


Figure 1.13: Electrostatic generators types: a) In-plane overlap varying, b) In-plane gap closing and c) Out-of-plane gap closing configurations

In 2002, Roundy et al. [29] studied and compared three classical structures of electrostatic harvesters. They showed that the structure of the type "in plane gap closing" allows the highest power density.

#### 1.6.4 Triboelectric transduction

The triboelectric transducers are based on the movement of electrical charges between two materials [30]. The triboelectric effect occurs when two contacting objects develop and collect opposing charges

on their surfaces. In order to obtain a balanced electrochemical potential, charge transfer is done between the objects in contact. In 2012, Wang et al. [31] was the first to design and fabricate a triboelectric transducer depicted in 1.14.

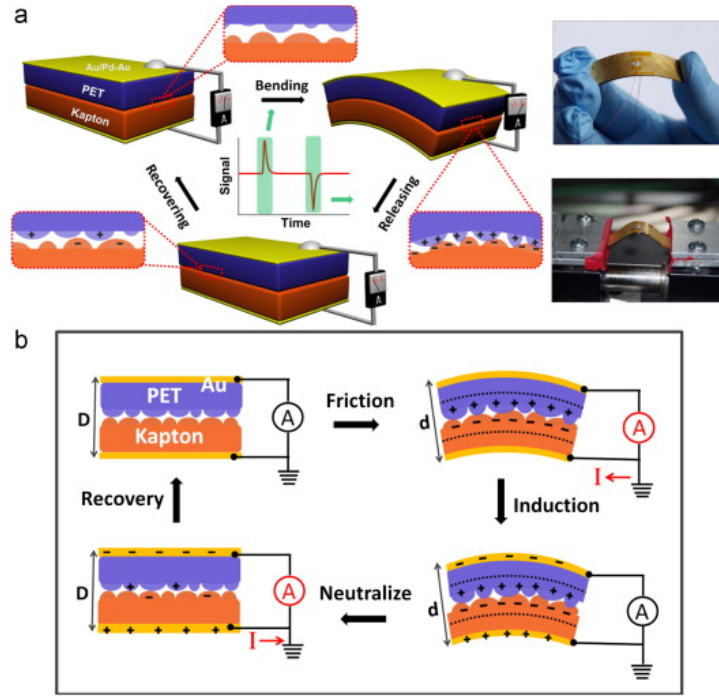


Figure 1.14: Illustration of the structure and working principle of the triboelectric generator [31] a) The first designed triboelectric transducer with its working principle b) Proposed mechanism of the triboelectric generator (charges generation, triboelectric potential creation, flow of current in the external load).

During the separation of materials, some atoms send electrons and others keep them. Consequently, between the two materials an electrical potential difference is created. Also, in order to obtain the same electrical potential, electrons current is formed potential difference by the triboelectric charges. The current  $I$  can be expressed as follows:

$$I = C \frac{\partial V}{\partial t} + V \frac{\partial C}{\partial t} \quad (1.16)$$

Where  $V$  is the electrode voltage,  $C$  is the system capacitance and  $t$  is the time. The first term in the equation consists of the electrodes potential change because of the charges electrostatically induced. Concerning the second term, it describes the capacitance variation.

### 1.6.5 Qualitative comparison of the different transduction techniques

Various studies have been able to recapitulate the advantages and disadvantages of the main transduction techniques used for energy harvesting. Different criteria have been taken into consideration to make the comparison, we can cite the ease of integration of electrostatic systems, output voltage, output impedance, complexity of structure, cost, efficiency, coupling, etc [32,33].

The qualitative comparison in terms of advantages and disadvantages of each transduction technique is summarized in Table 1.3. In Round thesis [34], it has been shown that piezoelectric and electromagnetic energy harvesters produce similar theoretical output power, while the electrostatic energy transducer and the triboelectric ones have much smaller density power.

In particular, it should be noted that PE transduction is attractive due to its ease of implementation and the voltage levels that it offers. However, some factors can be a brake on a long service life and decrease its performance such as the weak electromechanical coupling and the risk of depolarization of the material (due to fatigue, mechanical stresses or too high temperature). The EM transduction technique, which has been extensively tested in industry, exhibits good performance on a macroscopic scale due to a high electromechanical coupling; however, it exhibits significant resistive losses, which degrade its performance, and low output voltages which make exploration of electrical energy more difficult. Electrostatic transduction is more suited to the MEMS field, with outstanding performance at the microscopic scale and high output voltages. However, the need for an external high voltage source is its principal limitation. As for the triboelectric transduction, it is easy to fabricate the corresponding harvester and this latter is able to prove high efficiency. However, the output current is very low and another major disadvantage is the low stability.

Table 1.3: Comparison of the transduction mechanisms in the field of energy harvesting [32, 33]

Transduction mechanism	Advantages	Disadvantages
Piezoelectric	<ul style="list-style-type: none"> <li>- Simple structure</li> <li>- Highest energy density</li> <li>- No separate voltage source</li> <li>- High voltage output</li> <li>- No needs for mechanical stops</li> <li>- Compatible with MEMS</li> </ul>	<ul style="list-style-type: none"> <li>- Low current output</li> <li>- Weak coupling</li> <li>- High impedance output</li> <li>- Charge leakage</li> <li>- Depolarization</li> <li>- Fragility of piezoelectric layers</li> </ul>
Electromagnetic	<ul style="list-style-type: none"> <li>- Strong coupling</li> <li>- High current output</li> <li>- No need for smart materials</li> <li>- Reliable structure</li> </ul>	<ul style="list-style-type: none"> <li>- Low voltage output</li> <li>- Difficult integration with microsystems</li> </ul>
Electrostatic	<ul style="list-style-type: none"> <li>- High voltage output</li> <li>- Easy to fabricate</li> <li>- Integration with MEMS</li> </ul>	<ul style="list-style-type: none"> <li>- Voltage source or external load required</li> <li>- Mechanical stresses required</li> </ul>
Triboelectric	<ul style="list-style-type: none"> <li>- Low cost</li> <li>- Ease of fabrication</li> <li>- High efficiency</li> </ul>	<ul style="list-style-type: none"> <li>- Low current output</li> <li>- Low stability</li> <li>- Low durability</li> </ul>

## 1.7 PE, EM and commercialized harvesters

### 1.7.1 Piezoelectric energy harvesters

Typical piezoelectric generators consist of a beam with piezoelectric ceramic layers. The use of a beam improves the structure's mechanical coupling by adding mechanical stress on the piezoelectric



material when the beam is operating in a bending mode [35–38]. Different models have been developed to simplify the design and take into consideration the nonlinearity in the piezoelectric patches for high displacements [39]. Devices have been designed to experimentally validate the analytical models [36–38, 40, 41]. Roundy and Wright [42] developed a composite piezoelectric cantilever beam shown in Figure 1.15. The prototype consists of piezoelectric layers attached to the sides of the steel beam. A tip mass was attached to the end of the beam and the whole structure resonates at  $120\text{ Hz}$ . The maximum harvested power is of  $80\ \mu\text{W}$  for an optimal load resistance equal to  $250\ \text{k}\Omega$  and a basis excitation of  $2.5\ \text{m}\cdot\text{s}^{-2}$ . It has been concluded through this work that the output power of the optimized structure is proportional to the tip mass.

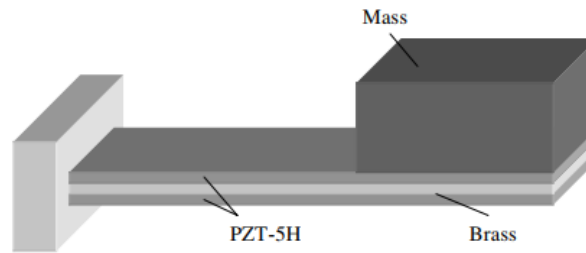


Figure 1.15: Piezoelectric energy harvester developed by Roundy et al. [42]

However, among the limitations of cantilever-based designs, we can cite the fact that they operate in a single direction. Multiple works focused on structures that can vibrate in multiple directions. To have an operation in multiple directions, the pendulum motions in a 3D space are investigated. Xu and Tang [43] proposed a cantilever-pendulum shown in Figure 1.16. This harvester was able to produce the same outputs of a typical cantilever–mass structure.

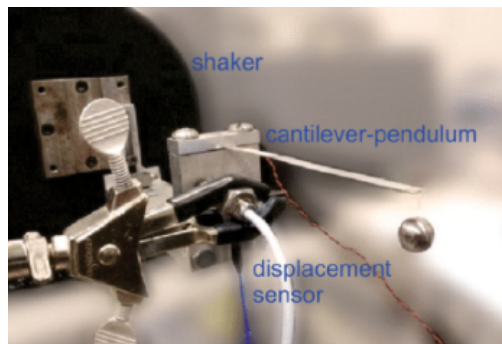


Figure 1.16: Design of the piezoelectric energy harvester based cantilever-pendulum [43]

Add to that, Li et al. [44] suggested coupled two PVDF cantilevers with different resonance frequencies to obtain a bi-resonant structure. This device produces more energy comparing to each cantilever alone because of the interactions created between them at different resonance frequencies. In addition, other designs not based on the cantilever beam system have been studied. Recently, Fan et al. [45] proposed a device that consists of four different piezoelectric cantilever beams and contains a ferromagnetic ball and a cylindrical track. The system, depicted in Figure 1.17, is able to scavenge energy from multiple



directions and from rotational and sway motions. In Table 1.4, we summarize different characteristics of piezoelectric harvesters.

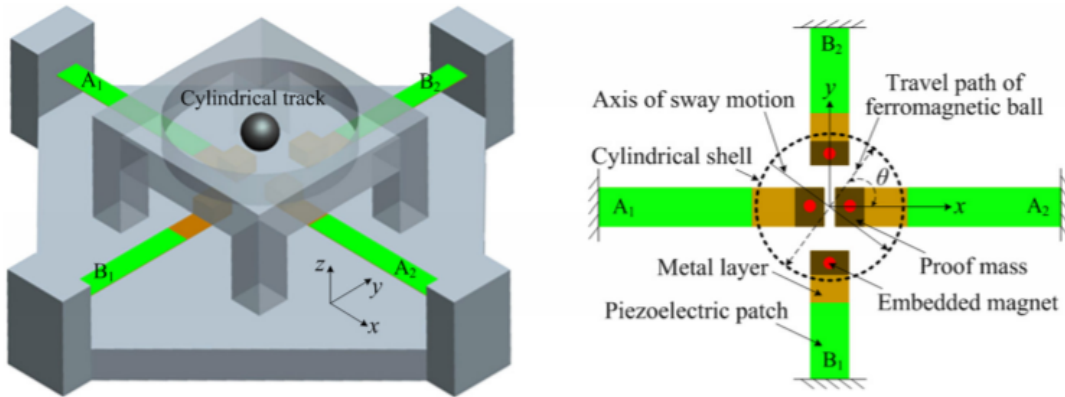


Figure 1.17: Configuration and vertical view of the piezoelectric harvester based on multiple mechanical motions [45]

## 1.7.2 Electromagnetic energy harvesters

Williams et al. [53] proposed an electromagnetic energy harvester that consists of a seismic mass on a spring as shown in Figure 1.18. When subjected to vibrations, the relative displacement between the mass and the housing leads the transducer to induce an electrical current. The harvested power from this device when subjected to excitation frequencies of  $70\text{ Hz}$  and  $330\text{ Hz}$  is of  $1\ \mu\text{W}$  and  $100\ \mu\text{W}$  respectively.

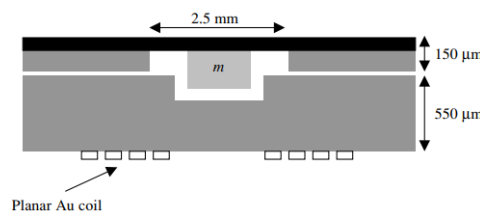
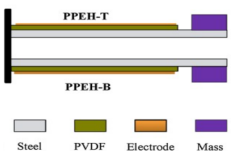
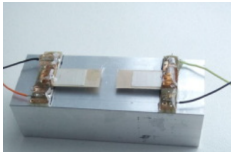
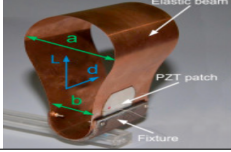
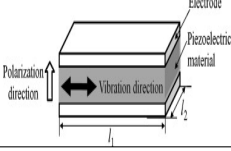
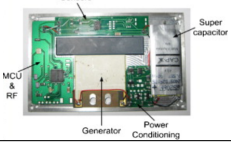
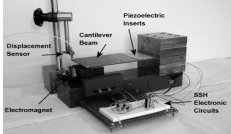


Figure 1.18: Electromagnetic energy harvester developed by [53]

In 2011, Zhu et al. [54] developed a planar structure with a thickness of  $4\text{ mm}$ , based on an arrangement of magnets allowing a strong gradient of magnetic flux and a reduced size, as shown in Figure 1.19. The harvester was subjected to an excitation of  $0.3\text{ g}$  and the harvested power was of  $120\ \mu\text{W}$  when the frequency is  $44.9\text{ Hz}$ .

El-Hami et al developed a vibration-based electromagnetic harvester [55]. The device, depicted in Figure 1.20a, consists of a cantilever beam, clamped at one end and supporting two neodymium (NdFeB) mass magnets having the shape of a core at the beam free end and the copper wire coil is positioned between the two magnets. This harvester has a volume equal to  $240\text{ mm}^3$  and provides  $1\text{ mW}$  when the vibration frequency is of  $320\text{ Hz}$ . Based on El-Hami et al. work, Glynne-Jones et al. [56] fabricated prototypes cantilever-based with different magnets configurations and performed

Table 1.4: Characteristics and performance of different piezoelectric energy harvesters: design, frequency (Freq), acceleration (Acc) or force (F), volume (Vol) and power density (PD)

Piezoelectric harvester	Ref	Freq [Hz]	Acc [ $m.s^{-2}$ ] /F [N]	Vol [ $mm^{-3}$ ]	PD [ $\mu W mm^{-3}$ ]
	[44]	16	9.8	347	0.001
	[46]	1.2	9.8	1680	0.04
	[47]	1204	22.15 N	1750	198.3
	[48]	wind	wind	2758	0.627
	[49]	69.8	9.8	229	0.037
	[50]	35	0.13	$15.9 \cdot 10^3$	0.28
	[38]	63	10	$0.21 \cdot 10^3$	19.04
	[51]	67	3.9	$0.55 \cdot 10^3$	0.44
	[52]	56	0.79	$34 \cdot 10^3$	0.089

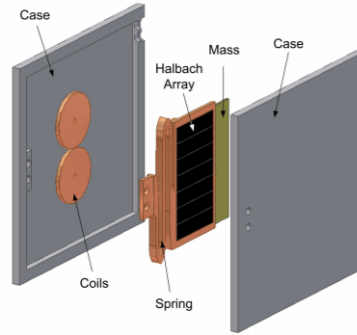


Figure 1.19: Design of the planar electromagnetic transducer developed by [54]

experimental tests. The first prototype had a volume of  $0.84\text{ cm}^3$  and consisted of a moving coil positioned between two fixed magnets. This device produced power of the order of  $180\ \mu\text{W}$  when the beam free-end is subjected to a displacement of  $0.85\text{ mm}$ . Furthermore, a second prototype, shown in Figure 1.20b, based on the contrary principle of the first one was developed in order to improve the level of the harvested power while enhancing the magnetic coupling between the magnets and the coil. In fact, the coil was fixed and four magnets are moving giving a total volume of  $3.15\text{ cm}^3$  and providing more than twice the output voltage of the first harvester. Li et al. [57] proposed a magnet and coil assembly consisting of a laser-micromachined spiral copper spring, a NdFeB magnet, and a coil that is positioned in place on the structure's housing. The volume of the device is of  $1\text{ cm}^3$  and is able to produce  $64\text{ Hz}$  when subjected to an excitation amplitude of  $100\ \mu\text{m}$ . Later in 2007, Wang et al. [58] have developed the similar structure based on a planar spring but with miniaturized size of  $0.32\text{ cm}^3$  as shown in Figure 1.20c. This EM MEMS harvester produced an output power of  $21.2\ \mu\text{W}$  at a resonance frequency of  $280\text{ Hz}$  when subjected to an excitation of  $8\text{ ms}^{-2}$ .

In Table 1.5, we summarize the characteristics and performances of different electromagnetic energy harvesters.

### 1.7.3 Commercialized energy harvesters

Over the recent years, several companies are being specialized in the fabrication of energy harvesters. Focusing on the commercialized electromagnetic harvesters, we can cite PMG Perpetuum Ltd company [68] that provides electromagnetic harvesters used in industrial process monitoring and industrial maintenance. The 'PMGFSSH' harvester provides a power level of  $1\text{ mW}$  for an excitation of  $0.25\text{ ms}^{-2}$  and has a volume of  $130\text{ cm}^3$ . Also, Ferro Solutions [69] develop an electromagnetic energy harvester VEH460 which has a volume of  $170\text{ cm}^3$  and is able to provide  $0.3\text{ mW}$  when the acceleration is of  $25\text{ mg}$  and the resonance vibration frequency is of  $60\text{ Hz}$ . These electromagnetic harvesters are based, approximately, on the same working principle which consists of a magnetic structure guided by springs in translation with respect to a coiled conductor.

The company Mide technology [70] manufactures a range of piezoelectric harvesters aimed at supplying autonomous sensors on vehicles, networks of sensors or implemented gas extraction works. The

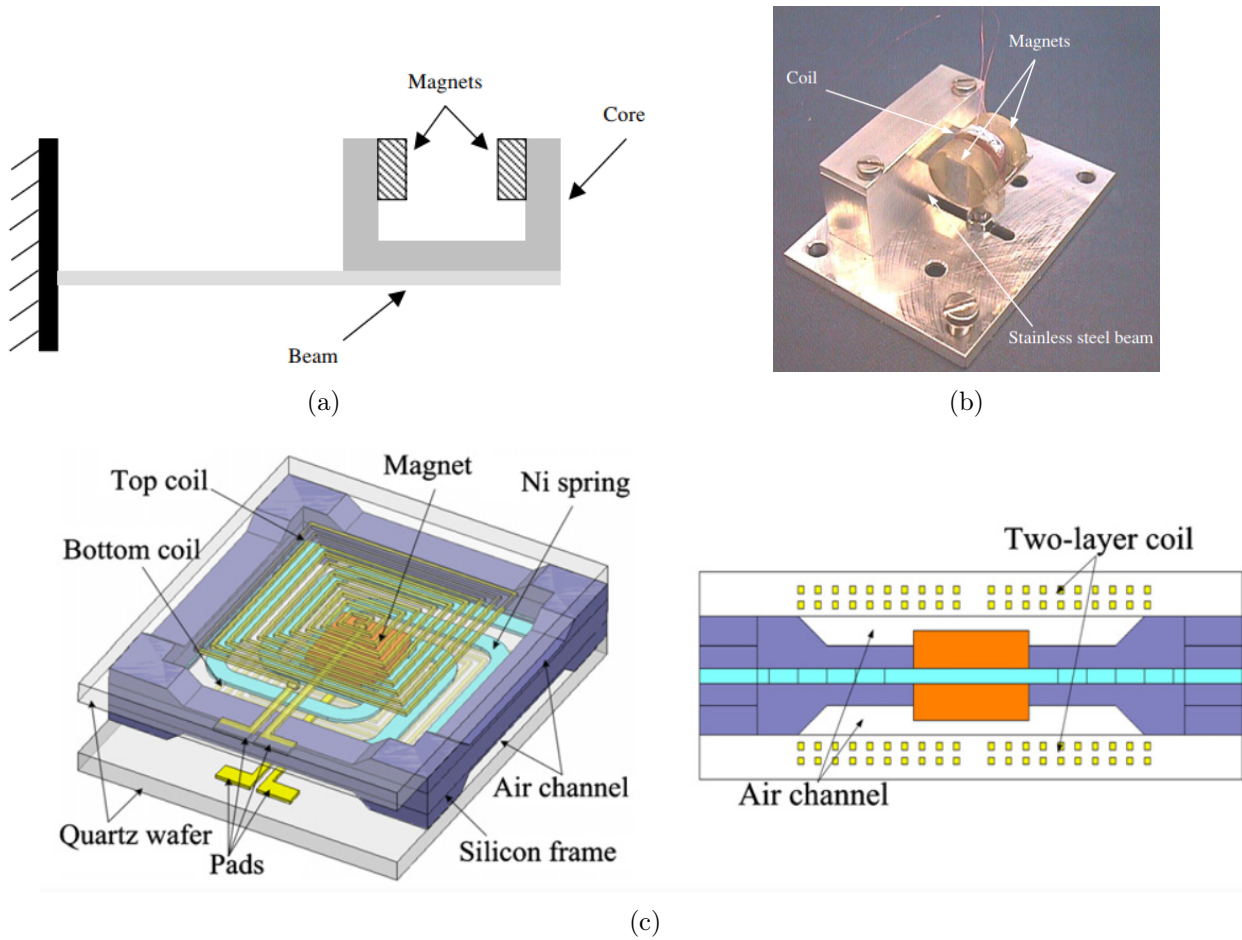
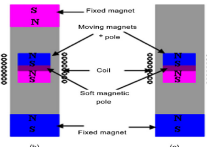
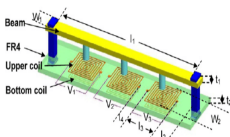
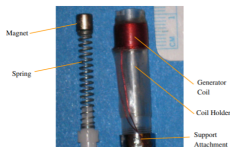
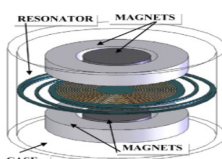
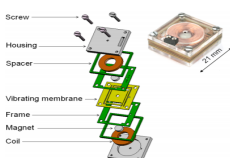
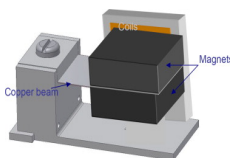
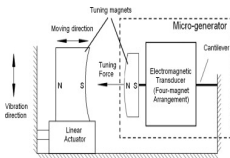
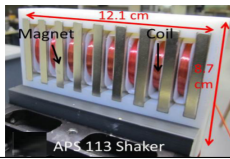
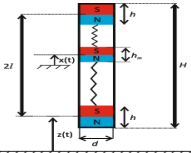


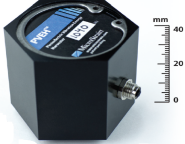



Figure 1.20: a) Design of the electromagnetic harvester based cantilever-beam with two magnet masses fixed at its end [55] b) Prototype of electromagnetic harvester with a fixed coil and moving magnets [56] c) MEMS electromagnetic generator based on a planar spring and a center magnet [58]

Table 1.5: Characteristics and performance of different electromagnetic energy harvesters: design, frequency (Freq), acceleration (Acc) or force (F), volume (Vol) and power density (PD)

Electromagnetic harvester	Ref	Freq [Hz]	Acc [ $m.s^{-2}$ ]/F [N]	Vol [ $mm^{-3}$ ]	PD [ $\mu W mm^{-3}$ ]
	[59]	8	0.38	$12.4 \cdot 10^3$	0.0012
	[60]	948	7.45	$5 \cdot 10^3$	0.0064
	[61]	112	1	$2.3 \cdot 10^3$	0.0035
	[62]	102	1	$8.6 \cdot 10^3$	0.034
	[63]	100	9.8	$1.45 \cdot 10^3$	0.25
	[64]	60	8.83	$0.1 \cdot 10^3$	0.0059
	[65]	67.6-98	0.59	$1.46 \cdot 10^3$	0.107
	[66]	50	1.96	1179000	0.0216
	[67]	26.6	98.1	17000	5.59

harvester 'Vulture PEH25w', as an example, has a volume of  $40.5 \text{ cm}^3$  and is able to provide  $4.5 \text{ mW}$  at  $40 \text{ Hz}$  when subjected to a vibration excitation of  $1 \text{ g}$ . AdaptiveEnergy [71], as well, develops 'Joule Thief' product which has a volume of  $35 \text{ cm}^3$  and is able to provide  $250 \text{ mW}$  when subjected to an acceleration of  $2 \text{ m.s}^{-2}$  at a resonance frequency of  $60 \text{ Hz}$ . The PE commercialized harvesters are all based on the principle of a bending beam except the harvester which uses a piezoelectric element in tension-compression thanks to a transfer structure of the mechanical motion based on an actuator provided by Cedrat Technologies company [72]. We illustrate, in Table 1.6, some commercialized piezoelectric and electromagnetic energy harvesters, their characteristics and their output performances. Over the

Table 1.6: Characteristics and performance of some commercialized electromagnetic and piezoelectric energy harvesters: design, frequency (Freq), acceleration (Acc) or force (F), volume (Vol) and power density (PD)

Commercialized harvester	Ref	Type	Freq [Hz]	Acc [ $\text{m.s}^{-2}$ ]	Vol [ $\text{mm}^{-3}$ ]	PD [ $\mu\text{Wmm}^{-3}$ ]
	[73]	PEH	1000	14.7	$4 \cdot 10^3$	7.5
	[74]	PEH	60	29.4	$140 \cdot 10^3$	0.012
	[73]	EMH	20	1.96	$166 \cdot 10^3$	0.024
	[69]	EMH	60	0.25	$170 \cdot 10^3$	0.0018

last years, several works have been done to improve vibration energy harvesters performance in terms of frequency bandwidth and output harvested power. Improvement techniques can be classified into three categories. Two categories are related to the excitation form namely resonant and non-resonant frequency systems. The last category is based on harvesting energies from multiple directions and is known as multi-directional-harvesting. Improvement techniques for these different harvesters categories are discussed in the next sections.

## 1.8 Improvement techniques for Resonant Systems

Techniques to improve the performances of RS focus on the enlargement of the frequency bandwidth and the increase of the harvested power. Adopted techniques reported from literature are discussed in the following sections.

### 1.8.1 Enlargement of the bandwidth

#### Resonance frequency tuning

Resonance frequency tuning approach consists of adjusting the natural frequency of the harvester. To do that, complex designs are required and manual or automatic adjustments are needed. This can be done through different techniques. We can cite:

- Preload application: We can start by the adjustment of the resonance frequency by varying its mass or stiffness. In this context, Hu et al. [75] and Eichhorn et al. [76] proposed to apply an axial preload in order to modify the device stiffness and hence its resonance frequency. The harvester consists of a piezoelectric beam and includes two additional arms that provides a connection between the tip of cantilever and the base as shown in Figure 1.21. It has been shown that the resonant frequency can be adjusted through the tensile stress or through the compressive load cantilever beam done by the attached wings. In the same way, Leland and Wright [77] suggested to apply a manually adjusted axial compression load to the harvester which consists of a simply supported bimorph beam as shown in Figure 1.22.

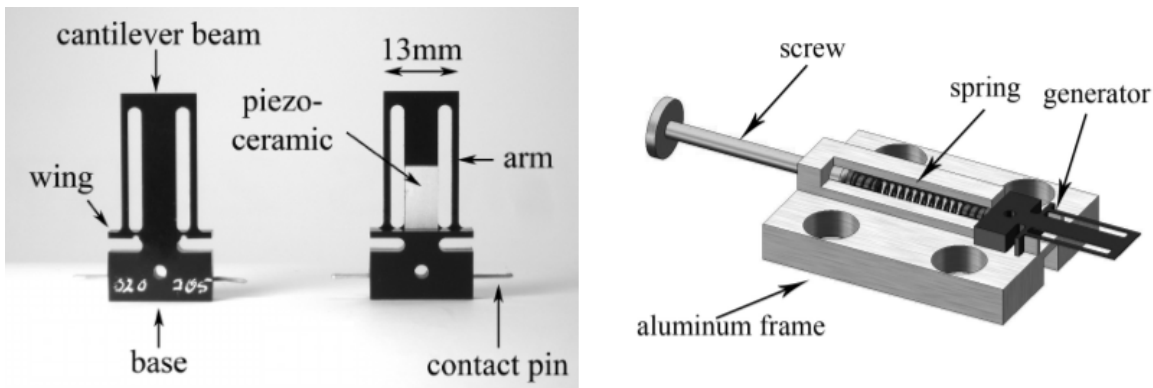


Figure 1.21: Illustration of the harvester consisting of a piezoelectric beam including two additional arms [76]

- Extensional mode resonator: Instead of using the flexion mode, some works developing an adjustable energy harvesting device that operates in the extension mode, called an extensional mode resonator have been done. An adjustable resonator was presented by Morris [78] formed by suspending a seismic mass on the two piezoelectric membranes and a rigid link maintaining them at the center as shown in Figure 1.23. In the same way, Loverich et al. [79] have developed a circular plate where its resonant frequency can be adjusted by a preload.



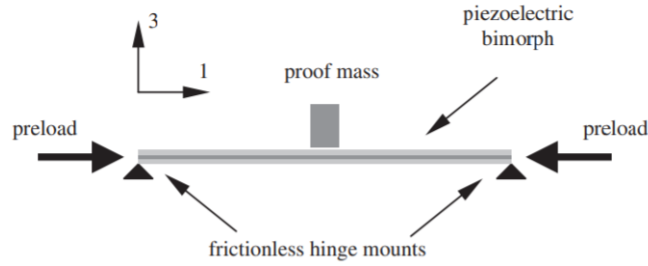


Figure 1.22: Illustration of a resonance frequency tuning for a vibration energy harvester consisting of a simply supported piezoelectric bimorph [77]

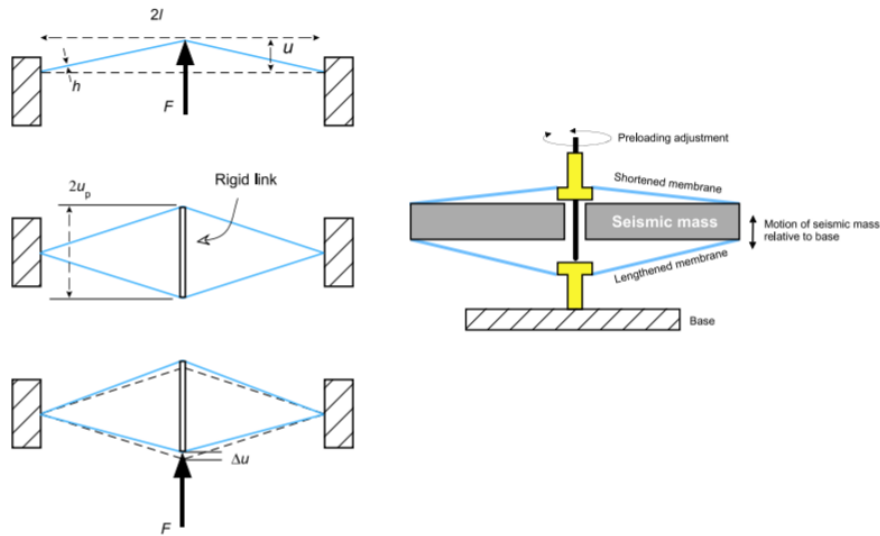


Figure 1.23: Illustration of an extensional mode resonator [78]

- Adjustment of the geometry: The resonance frequency can be also tuned by varying some geometric parameters without changing the system important characteristics like the damping for example. In this context, Karadag et al. [80] proposed two coupled piezoelectric cantilever beams. To one of the cantilever beams which is the tunable one, is fixed an actuator. To the other one, a nail is attached to the actuator's shaft as a tip mass. The schematic of the structure is shown in Figure 1.24. The structure is able to automatically tune its natural frequency. This harvester has self-locking system so that fixing the movable part by the piezometer doesn't need energy and this results in improving the demand of the total energy. A tuning algorithm is implemented in order to determine the tip mass direction which gives the resonance frequency. The results of the algorithm allow increasing the bandwidth by 150 %.

### Multimodal systems

On the other hand, several authors have developed harvesters with multiple degrees of freedom. In this case, the power can be scavenged in a wider bandwidth. This technique is called the multimodal



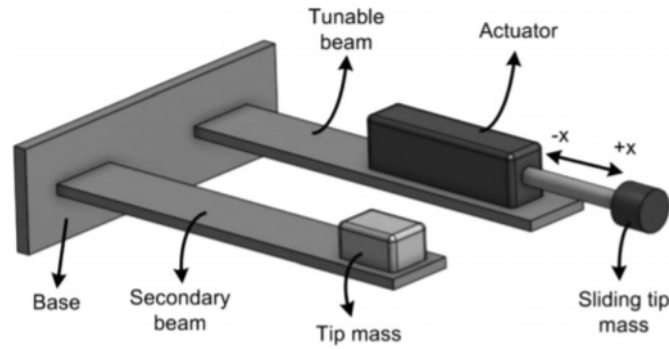


Figure 1.24: Illustration of two coupled piezoelectric cantilevers to tune the natural frequency [80]

configuration. Generally, this configuration is implemented through the exploration of several modes of a continuous bending beam or by an array of free embedded beams. Shahruz [81] designed an energy harvester composed of free-clamped piezoelectric beams having different lengths and seismic masses attached to each beam end shown in Figure 1.25a. This system vibrates at different frequencies forming what is called a "mechanical band-pass filter" where its Bode magnitude is shown in Figure 1.25b illustrating clearly a larger bandwidth. The main disadvantage of this technique is that it requires a large area to constitute the large array. In the same field, Sari et al. [82] developed an

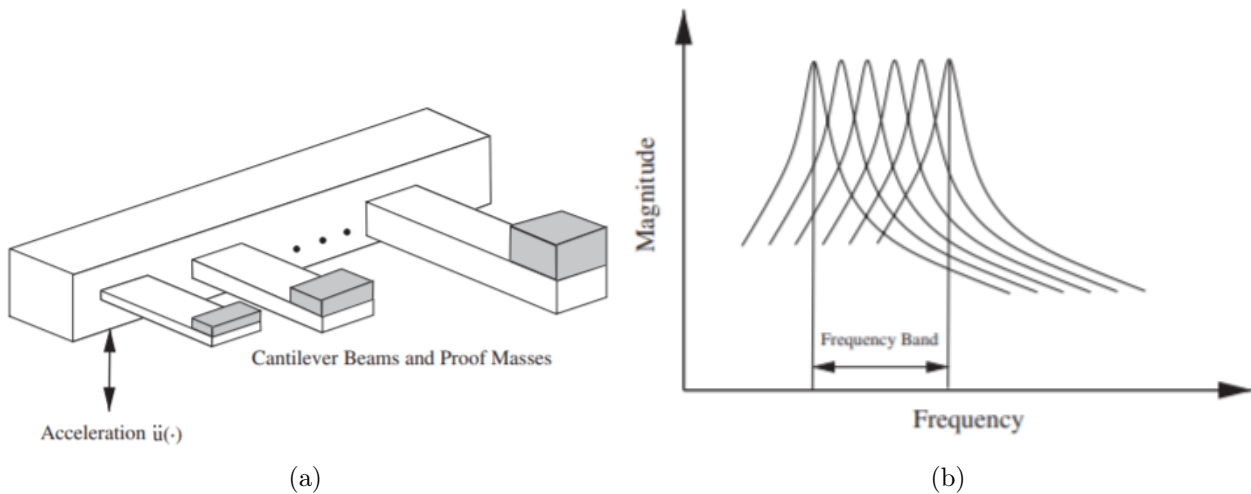


Figure 1.25: a) Illustration of mechanical band-pass filter, b) The plots of the Bode magnitude and the filter frequency band [81]

electromagnetic energy harvester which is composed of 35 clamped-free beams having different lengths moving in the field of a permanent magnet as illustrated in Figure 1.26a. The obtained frequency bandwidth of this proposed harvester is depicted in Figure 1.26b. Toyabur et al. [83] develop a different harvester having more than one seismic mass so that the system has different vibration modes with corresponding different natural frequencies. This system is composed of a bi-clamped beam and four secondary piezoelectric patches linked to secondary beams where tip magnet masses are attached at their ends as shown in Figure 1.27. Below each moving magnet mass is fixed a coil. The frequency response

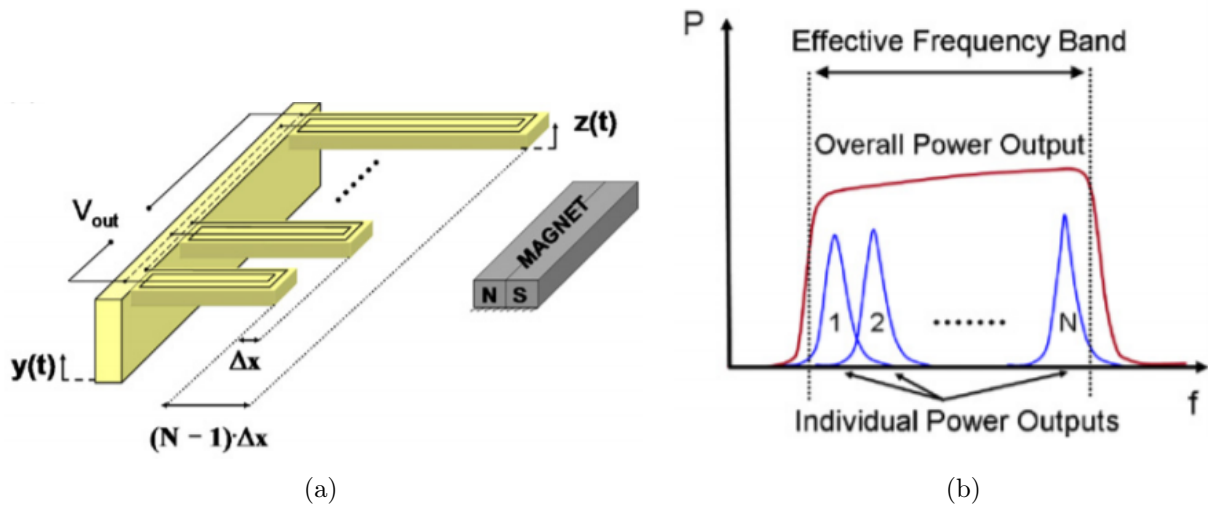


Figure 1.26: a) Illustration of the proposed multimodal electromagnetic harvester , b) The wide frequency bandwidth of the proposed harvester [82]

of the system gives 4 different peaks the fact that enlarges the bandwidth where we can harvest energy.

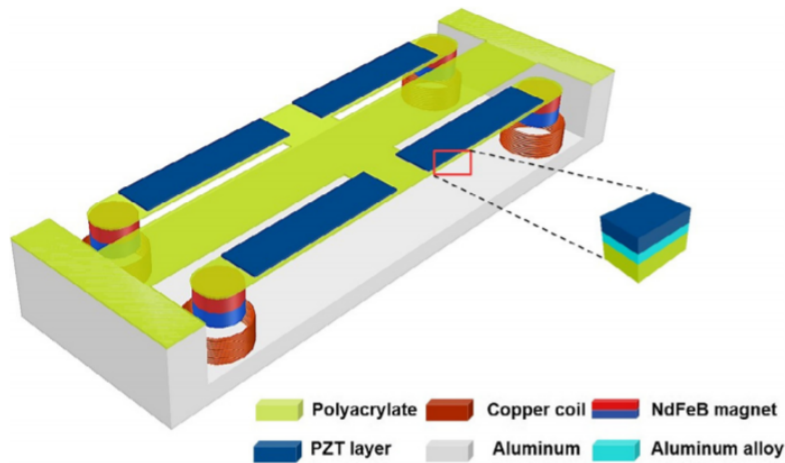


Figure 1.27: Illustration of the harvester composed of a primary beam, four piezoelectric patches attached to the four secondary beams and magnet masses below coils [83]

### Nonlinear systems

In order to extend the frequency bandwidth of the structure, several researchers have attempted to design nonlinear harvesters. We can differentiate between nonlinear internal and external resonances.

- **Nonlinear external resonance:** Although multimodal techniques guarantee the widening of the harvesters frequency bandwidth, they need technological constraints and high costs to implement the structure and its corresponding harvesting electric circuits. Consequently, over the last years, the introduction of nonlinear dynamics in vibration energy harvesters has received considerable

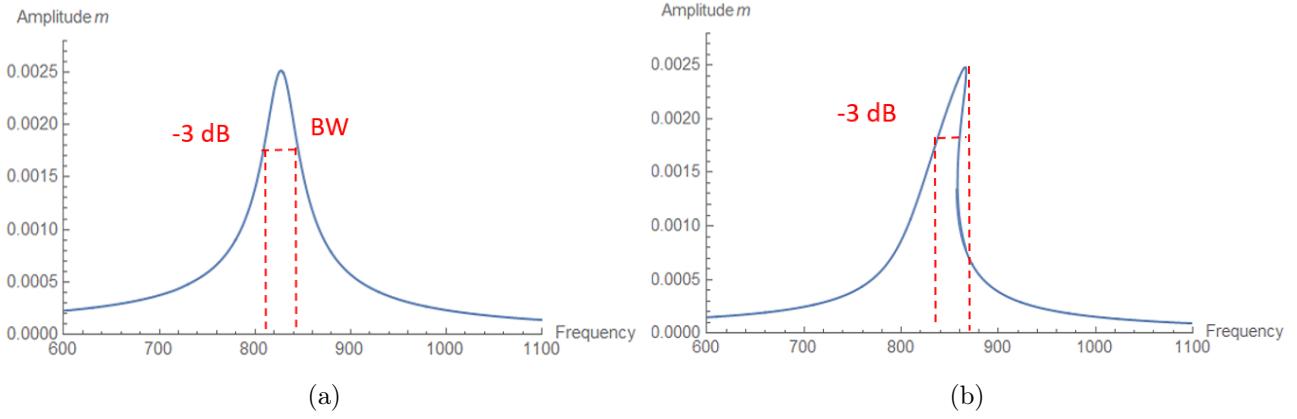


Figure 1.28: a) Linear behavior , b) Nonlinear hardening behavior

attention as being an alternative approach to overcome these limitations. Nonlinearities are generally present in dynamic systems because of geometric or material properties. When a nonlinearity is introduced in the system, we can notice that the frequency response tends to shift to the right (hardening behavior) or to the left (softening behavior) depending on the excitation type. The bandwidth (BW) is defined by the half power bandwidth method (-3 dB) as shown in the following Figures representing a linear and a nonlinear system behaviors depicted in 1.28a and 1.28b. It is introduced in the systems through different methods. It can be introduced with the change of the characteristics of the system [84]. Moreover, it can be explored by imposing high displacements as discussed in Mahmoudi et al. [85] work where the structure consists of a bi-clamped beam with a center magnet mass emerged in a fixed coil and two piezoelectric patches as shown in Figure 1.29a. It has been shown that the frequency bandwidth is enhanced by 30 % comparing to the linear system as depicted in Figure 1.29b.

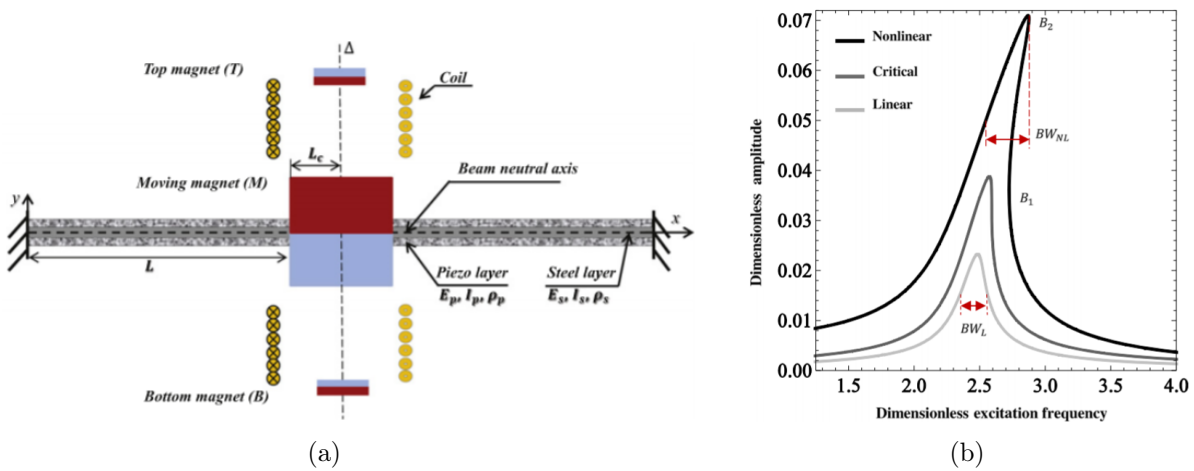


Figure 1.29: a) Illustration of the proposed nonlinear harvester , b) Illustration of the frequency bandwidth in linear, critical and nonlinear configurations [85]

Furthermore, the nonlinearity can occur when the resonator interacts with a magnetic field as

developed in Mann and Sims [86] work. They have proposed an energy harvester with nonlinear oscillations due to magnetic levitation. For low excitation at the base, they showed that the frequency response is similar to the response of a linear system. Nevertheless, in the case of a high excitation, the nonlinear behavior has a strongly softening behavior resulting in larger bandwidth. Abed et al. [87] developed a multi-modal VEH based on arrays of coupled levitated magnets as shown in Figure 1.30a. They showed that it is possible to enhance the frequency bandwidth by 190 %. The frequency response of the single dof is presented in Figure 1.30b where the bandwidth is illustrated for the linear, critical and nonlinear configurations. It is remarkable that the bandwidth of the nonlinear harvester is the wider comparing to the other cases.

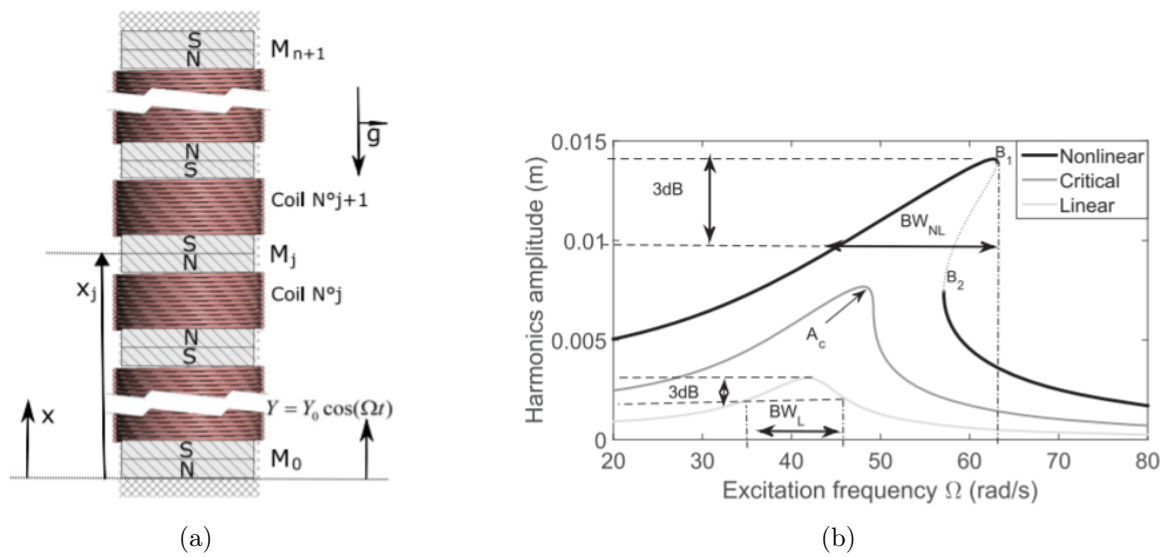


Figure 1.30: a) Illustration of the proposed nonlinear harvester, b) Illustration of the frequency bandwidth in linear, critical and nonlinear configurations [87]

In other recent works [88], the concept of High Static Low Dynamic (HSLD) stiffness is proposed to overcome the limitations resulting from the combined effect of gravity, mechanical damping and the necessity to tune the VEH to very low frequencies.

As a conclusion of the nonlinear dynamics, the frequency response tends to bend to the left or to the right the fact that widens the frequency bandwidth. The magnitude of output power can be conserved or enhanced for low frequencies when the natural frequency is near to a higher frequency.

- **Nonlinear internal resonance:** In addition to nonlinear external resonance which results in only softening or hardening nonlinearity behavior, internal resonance is a phenomenon that occurs in multiple degrees of freedom systems which results in the phenomenon of double jumping in the frequency response as shown in Figure 1.31. In other words, the frequency response bends in two frequency directions namely to the right and to the left simultaneously from the central frequency. This can increase significantly the frequency bandwidth.

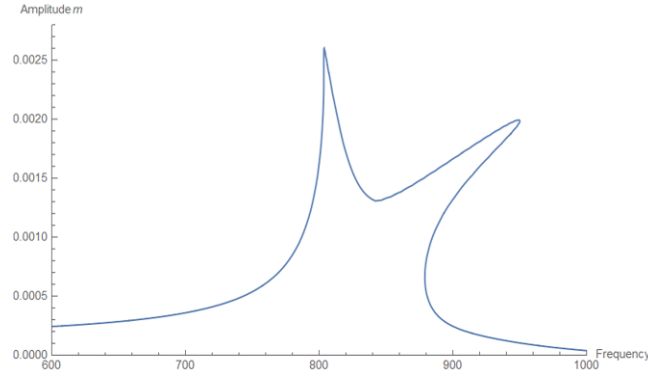


Figure 1.31: Illustration of the nonlinear internal resonance

This phenomenon occurs when the natural frequencies are tuned so that they are commensurable. Xiong et al. [89] developed a piezoelectric energy harvesting and the natural frequencies of the system are tuned by introducing an auxiliary oscillator as shown in Figure 1.32a. 2:1 Internal resonance (the second natural frequency is equal 2 x the first natural frequency) occurred resulting in larger bandwidth by 130% compared to the typical nonlinear system as depicted in Figure 1.32b.

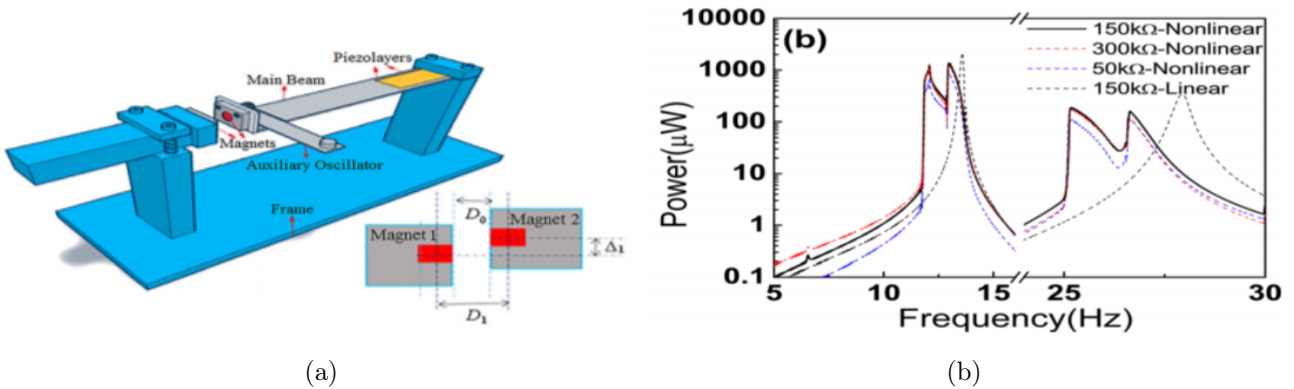


Figure 1.32: a) Illustration of the proposed nonlinear harvester, b) Illustration of the frequency bandwidth in linear, critical and nonlinear configurations [89]

Chen et al. [90] proposed an L-shaped piezoelectric beam clamped at one end supporting a magnet as illustrated in Figure 1.33a. Another fixed magnet is placed at a certain distance from the moving magnet attached to the beams. This distance is tuned so that the second natural frequency is twice the first natural frequency. A comparison of the performances of the nonlinear harvester in the case of internal resonance and away from internal resonance is plotted in Figure 1.33b. It has been proven that the frequency bandwidth and the output power as well are significantly enhanced in the case of internal resonance.

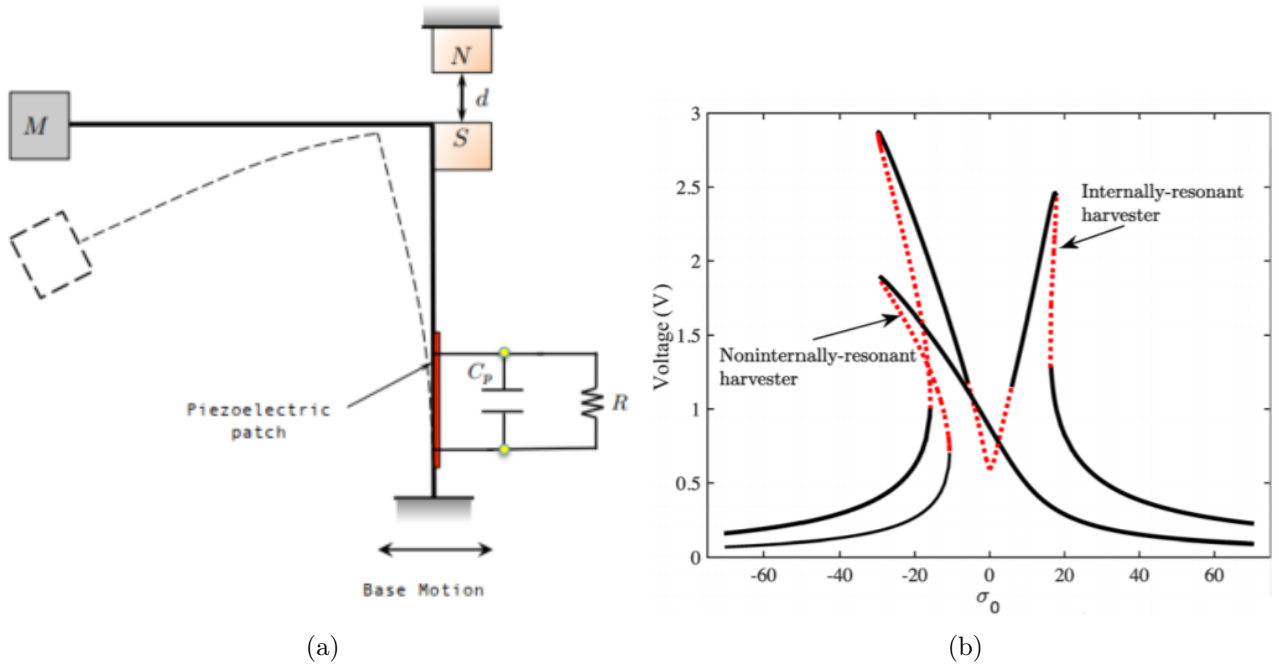


Figure 1.33: a) Illustration of the proposed T-shaped piezoelectric beam, b) Comparison of the non-linear behavior away from internal resonance and the case of internal resonance [90]

## 1.8.2 Enhancement of the harvested power

### Energy localization phenomenon

The energy localization phenomenon known as Anderson localization was, first, discovered by Anderson [91] in quasi-periodic weakly-coupled structures. It is based on the fact that under certain conditions, the energy is not propagated in an equal manner to the work space but it is confined in some specific regions. Therefore, this property attracts the researchers to explore it deeply and to conclude about its effects, consequences, advantages and disadvantages. It has been demonstrated that for a linear periodic system, the phenomenon of mode localization occurs under two conditions:

- A weak substructures coupling
- A broken periodicity of the structure by the existence of a very small structural mistuning.

Hodges et al. [92] were the first in the field of structural dynamics to investigate the mode localization phenomenon by structural irregularity in a system of coupled pendula as shown in Figure 1.34. He proved that an introduced symmetry-breaking in a periodic structure could cause significant change in the structure dynamics. Later, Hodges et al. investigate this phenomenon in stretched string with masses attached to it and controlled the mode shapes and the energy transmission [93]. They proved that once an irregularity is introduced, the individual modes were not anymore extended in the same way in all the structure regions as they were for the case of a periodic system but they were being localized in specific zones.

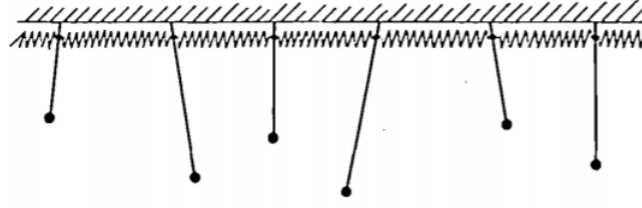


Figure 1.34: Coupled pendula arranged on a chain [92]

As shown in Figure 1.35a, we illustrate a cyclic periodic structure in the form of a fan with 16 blades modeled under Ansys software. It is shown in this figure that the deformation of all the blades is distributed equally and hence the energy is the same in all the system regions. Once some blades mass are changing by adding small mass irregularities, the perturbed blades have the highest displacements, hence, the energy is localized where the perturbation is introduced as depicted in Figure 1.35b.

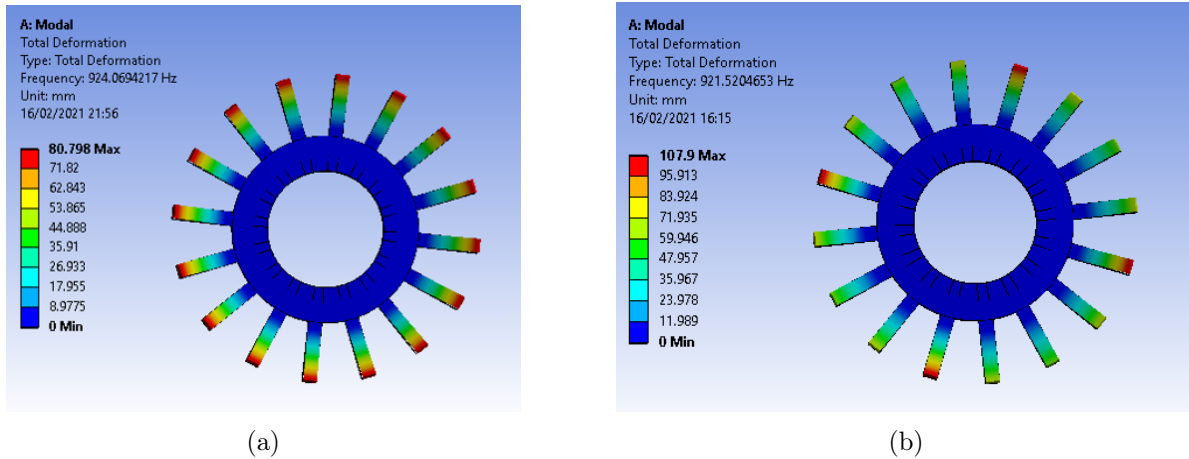


Figure 1.35: Illustration of energy localization phenomenon in a cyclic structure consisting of a fan with 16 blades: a) periodic structure b) quasiperiodic structure

Different works have investigated the benefits of the multimodal configuration cited above with the functionalization of the phenomenon of energy localization. Zergoune et al. [94] explore this phenomenon in an array of beams based on electromagnetic transduction and showed that it permits enhancing the output harvested power while reducing the number of harvesting circuits which could be implemented only in the perturbed zones instead of all regions. This property reduces the technological constraint of the structure and minimizes the cost of the electronics used while maintaining the same output performance of the structure. Also, Malaji et al. [95] investigated the mode localization in a near periodic system which consists of two pendulums weakly coupled through a linear spring. They proved that the amplitude magnitude can be enhanced while harvesting from only the perturbed pendulum [96, 97].



## Hybrid systems

In order to take advantage of different single harvesting mechanisms simultaneously, researchers proposed hybrid systems. Challa et al. [98] presented a coupling hybrid PE-EM harvester based on a piezoelectric cantilever beam with a permanent magnet placed as a tip mass on the vibrating beam. A coil is placed in the magnet motion axis in a way that when the mass vibrates it passes through the coil as shown in Figure 1.36, designed to increase the harvested power through damping match. The experimental tests showed that the harvester's output power was  $332\text{ W}$ , compared to  $275\text{ W}$  and  $244\text{ W}$  for single PE and EM harvesting devices, respectively.

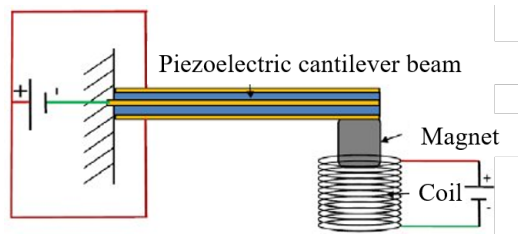


Figure 1.36: Structure of the hybrid piezoelectric-electromagnetic vibration energy harvester proposed by [98]

Mahmoudi et al. [85] proposed, also, a hybrid piezoelectric-electromagnetic vibration energy harvester based on nonlinear dynamics. It has been shown that the hybrid transduction allowed an increase of the harvested power by 84%. Furthermore, Chen et al. [99] developed a hybrid energy harvester that consists of combining piezoelectric and electromagnetic mechanisms in order to power wireless sensors in smart grid. It has been proved that the total output harvested power which is of  $341.9\ \mu\text{W}$  is much higher than the power harvested from stand-alone mechanisms. Li et al. [100] proposed a hybrid piezoelectric-electromagnetic harvester consisting of a bi-clamped beam with two central top and bottom magnet masses, piezoelectric layers attached to its ends and a coil fixed under the magnets as shown in Figure 1.37. They studied the influence of electromechanical coupling effect on the harvester performances. It has been shown that the higher coupling coefficient, the more output harvested power observed.

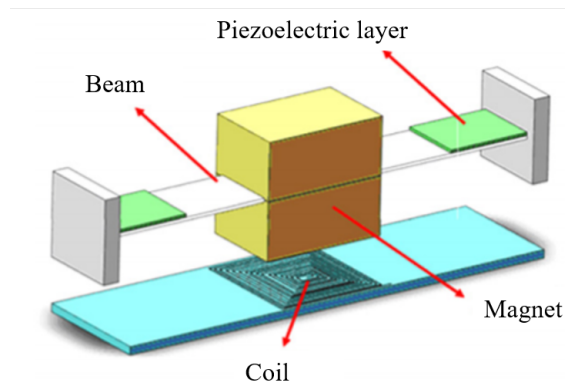


Figure 1.37: Structure of the hybrid piezoelectric-electromagnetic vibration energy harvester based on the vibration of two magnets guided by elastic bi-clamped beam proposed by [100].



## Combine improvement techniques

Some authors tend to combine two or more techniques to enhance forward simultaneously the output harvested power and the frequency bandwidth. In this context, Li et al. [101] designed a hybrid piezoelectric-electromagnetic harvester depicted in Figure 1.38a. The techniques used to enhance the output performances consist of combining the benefits of nonlinear dynamics and hybrid systems. It has been shown that increasing the level of acceleration leads to a nonlinear behavior of the structure and results in an increase output power and an enlargement of the frequency bandwidth simultaneously while showing a decrease in the resonant frequency as shown in Figure 1.38b.

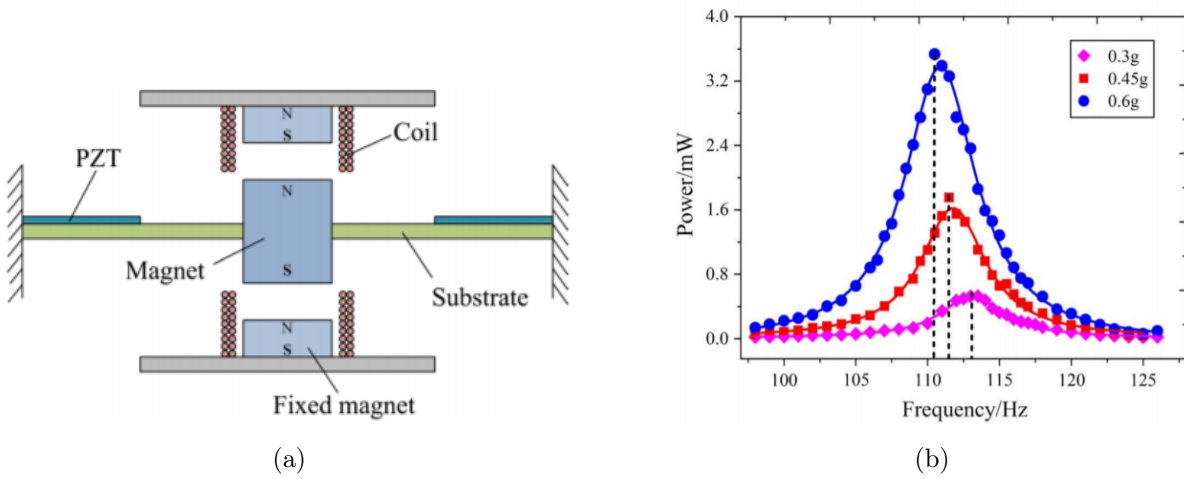


Figure 1.38: (a) Design of the hybrid VEH proposed by [101] (b) Output power with different acceleration levels

## 1.9 Improvement techniques for Non-Resonant Systems

Various techniques are used in non-resonant systems in order to obtain significant displacements at all operating frequencies. Among these methods, one can cite frequency-up conversion, rotary motion, pure rolling mechanisms, and free moving ball based frequency-up conversion, etc [7].

In the next sections, examples of non-resonant electromagnetic and piezoelectric vibration energy harvesters are reported.

### 1.9.1 Non-Resonant Electromagnetic Energy Harvesters

A frequency up-converted non-resonant electromagnetic energy harvester [102] is proposed in order to generate power from human-body motion as from hand motion and shaking. The proposed non-resonant harvester, shown in Figure 1.39, has an overall size of  $6.75 \text{ cm}^3$  and is composed of an acrylic

hollow cylinder, two end caps, two steel springs, a non metallic ball, two neodymium permanent magnets and two wound coils. The end caps are connected to one of each springs ends. The springs other ends are connected to magnets. When the free mobile ball strikes the two magnets repeatedly, each magnet-spring structure begins to oscillate and voltage is produced in the coils at the relatively high resonance frequencies. For an operation frequency from 14 to 22  $Hz$  and when subjected to an acceleration of  $15 m/s^2$ , the structure produces a constant output voltage of  $33.7 V$ . However, for frequencies from 23 to 39  $Hz$ , the output voltages are random and decrease comparing to the ones in the previous mentioned frequencies range. Add to that, when the frequency is higher than 40  $Hz$ , a non-significant movement of the ball supposed to hit the magnets occurs and results in generating small voltages.

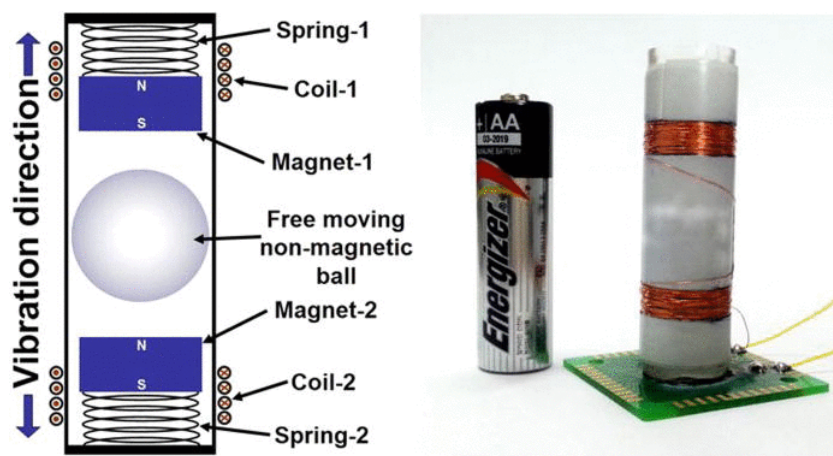


Figure 1.39: Structure of the non-resonant EMEH based on frequency-up conversion proposed by [102]

A non-resonant EMEH has been designed to harvest energy from human motion [103]. It consists of a spherical neodymium magnet encased inside a spherical cavity as shown in Figure 1.40.

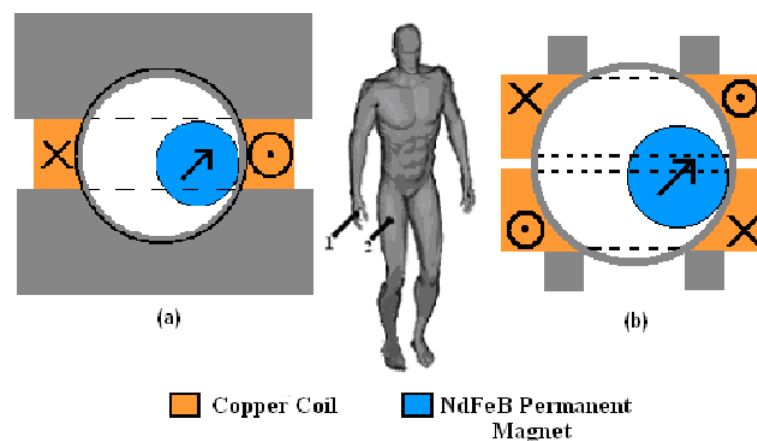


Figure 1.40: Structure of the non-resonant EMEH based on human motion proposed by [103]

## 1.9.2 Non-Resonant Piezoelectric Energy Harvesters

A NR-PEEH is proposed by Aktakka et al. [104]. The principle of the harvester is based on the motion of a green beetle wings. Two prototypes are proposed and are composed of two piezoelectric bimorph beams (PZT-5H/brass/PZT-5H) having volumes of  $11 \text{ mm}^3$  and  $5.6 \text{ mm}^3$  and a thickness of  $380 \mu\text{W}$ . These beams are attached to the beetle. During flying, the harvester can provide  $11.5 \mu\text{W}$  at a frequency of  $85 \text{ Hz}$  and  $7.5 \mu\text{W}$  at  $100 \text{ Hz}$ .

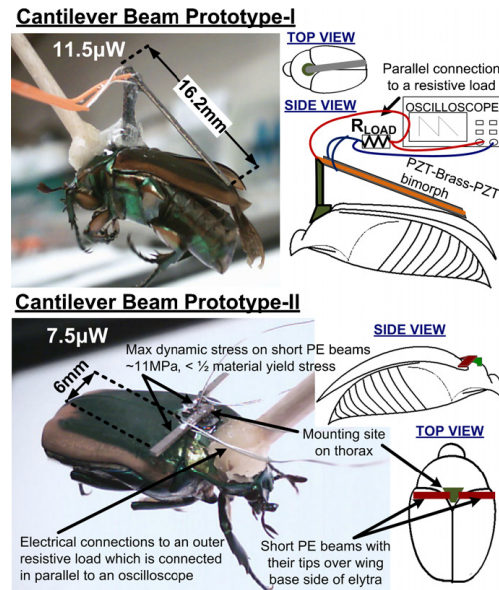


Figure 1.41: A NR-PEEH based on the wings motion of a beetle consisting of two piezoelectric bimorph beams attached to the wings [104]

An other example of a piezoelectric energy harvesting module based on non-resonant excitation is proposed by Frey et al. [105]. The design consists of a tire pressure monitoring system (TPMS). The proposed energy harvester consists of thin coating of piezoelectric material deposited on a base cantilever beam. The harvester's non-resonant behavior is achieved by utilizing the device's damping mechanism which is investigated by finite element modeling and experimentation. To obtain a maximum power, a triangular shaped cantilever beam is considered. When the road is in contact with the tire treads, force pulses are produced. These forces are the origins of the device excitation.

Moreover, Liu et al. [106] proposed a harvester composed of two PE cantilevers as displayed in Figure 1.42. The first piezoelectric cantilever is a low-resonant-frequency one having a frequency of  $36 \text{ Hz}$ . As to the second, it is a high-resonant-frequency cantilever with a frequency of  $618 \text{ Hz}$ . The two cantilevers are connected in parallel. For an excitation acceleration of  $0.1 g$ , the structure provides a response similar to a linear system. When the excitation is higher, the two systems interact better and respond to low frequencies resulting in a larger bandwidth.

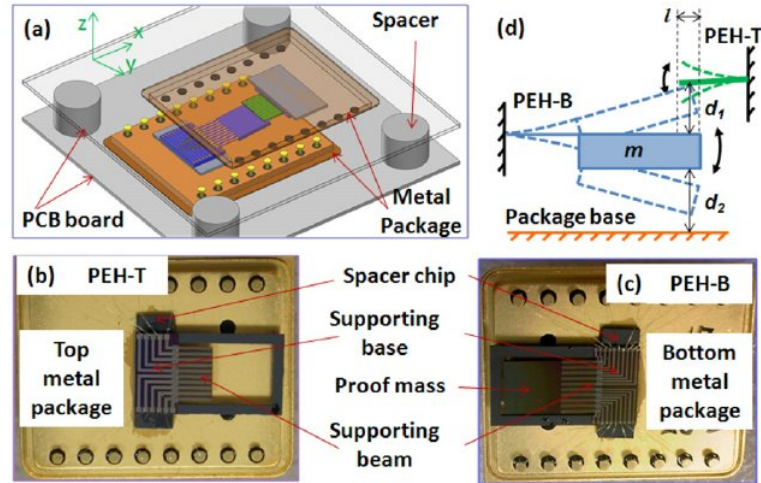


Figure 1.42: (a) Design of the proposed NR-PEEH system. (b) Working mechanism of the NR-PEEH system. (c) The bottom NR-PEEH structure top view. (d) The top NR-PEEH structure top view. [106]

## 1.10 Improvement techniques for multi-directional systems

The last mentioned examples of harvesters work in only one dimension. In this paragraph, some harvesters subjected to two and three-dimensional excitation direction and the corresponding improvement techniques are discussed.

### 1.10.1 Bi-dimensional harvesting

In this section, we will detail some examples of 2D harvesting systems based on perpendicular springs, 2D in-plane and rotational movement.

- Perpendicular springs:** The use of two perpendicular springs, which can be cantilevers [107] or magnetic springs [108], is the simplest method for building a bi-directional harvester. Because it may be considered as two separate 1D harvesting systems with distinct orientations, such system is easy to design and install. Wang et al. [109] proposed to harvest energy from Friction Induced Vibrations (FIV). In this context, they suggest a mechanism, shown in Figure 1.43a, made up of two piezoelectric cantilevers placed on the pad of a braking system able to collect energy from both normal and tangential vibrations. In Figure 1.43b, the FFT of the resultant vibration and voltage signals created by braking along the tangential and normal vectors is illustrated. At frequencies  $158\text{ Hz}$  and  $316\text{ Hz}$ , we can see two peaks, indicating that the device was able to collect energy from both directions.
- 2D in-plane:** 2D in-plane (2D-IP) motions are more difficult to design, but they are more suited for MEMS integration. In this context, such systems are built around a seismic mass that is linked to highly flexible mechanical springs that allow obtaining two-degrees-of-freedom in-plane. Bartsch et al. [110] proposed a such design which consists of a disk-shaped seismic mass

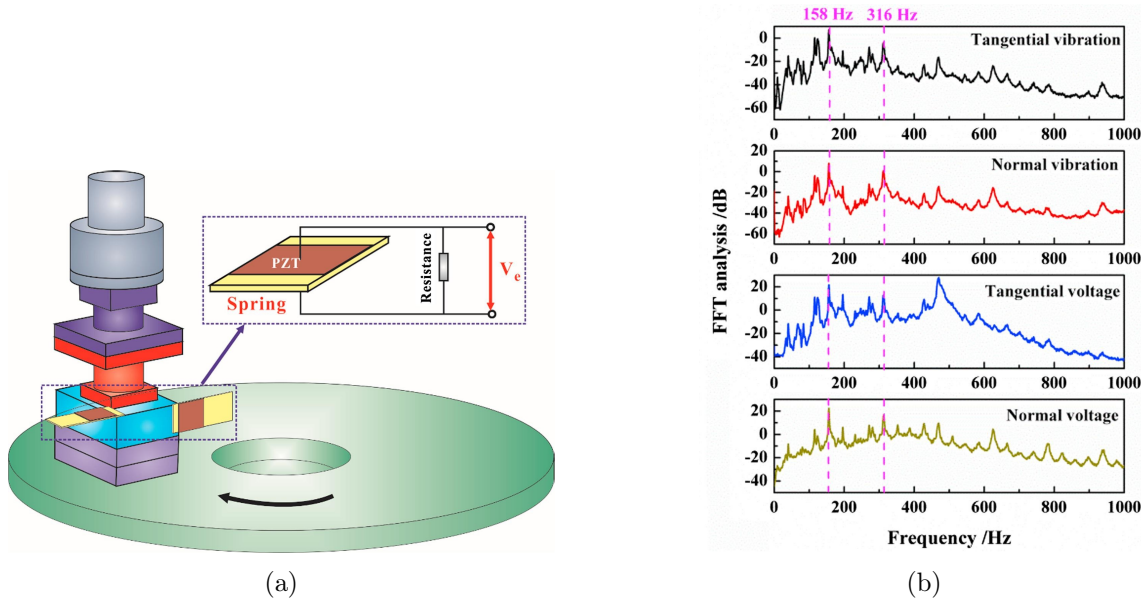


Figure 1.43: Design of the 2D harvester proposed by [109] : (a) The device design, (b) The FFT analysis results.

suspended by two concentric rings, as depicted in Figure 1.44. Nine bridges linked these springs together to produce a narrow circular-shaped spring. The 2D in-plane motions are possible due to the dispersion of the bridges between the rings and the seismic mass. The efficiency of their construction in extracting energy from an external driving oscillator has been examined. Also, it has been proven that the normalized average harvested energy for isotropic spring materials (i.e. x- and y-axis resonance frequencies are equal) is double that of a 1D system. Because resonance frequencies along both axes are not equal in the real life due to material anisotropic characteristics, the average harvested energy is decreased, but it is still more effective than 1D harvesting.

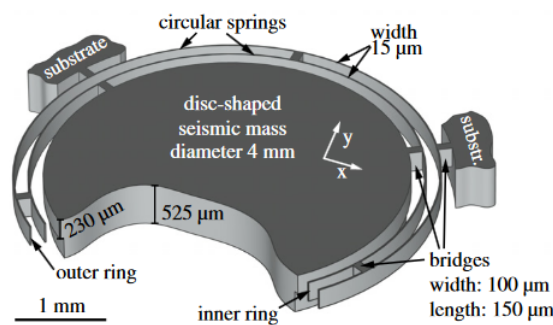


Figure 1.44: Schematic design of the 2D In-plane harvester proposed by [110]

- **Rotational movement:** A pendulum and rotational motions have been both explored as 2D harvesting systems, especially for rotating machinery and automobile tires. Febbo et al. [111] suggested a harvester that consists of two beams facing each other, each with two masses on the tip connected by a spring, as well as a piezoelectric layer placed on one of the beams. As



illustrated in Figure 1.45a, the system is installed on a rotating platform. The latter oscillates by utilizing the gravitational force. As a result, when rotating, the mass at the bottom position pulls the second. Consequently, during a cycle, the movement of the masses continue by alternating the roles. We note that low-frequency rotations were the major focus of the harvester. For a rotational frequency of  $2.54\text{ Hz}$ , a maximum harvested power of  $104.74\text{ W}$  was obtained (Figure 1.45b).

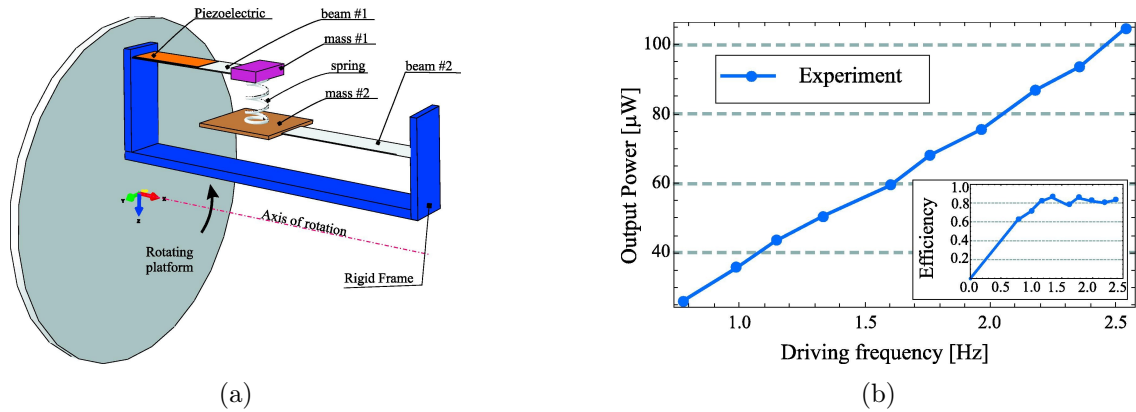


Figure 1.45: 2D rotating harvester proposed by [111]: (a) Design of the proposed device, (b) Output power.

### 1.10.2 Tri-dimensional harvesting

In the literature, the least amount of works in the field of harvesters concern the 3-D harvesting systems can be found . In fact, the ability of a single device to scavenge energy from all directions with a significant amount of harvested power is still a scientific challenge that few researchers have explored. Liu et al. [112] were the first to propose a harvester able to harvest energy from three directions. The suggested design is displayed in Figure 1.46 and consisting of a vibrating MEMS structure placed below a beam supporting a permanent magnet.

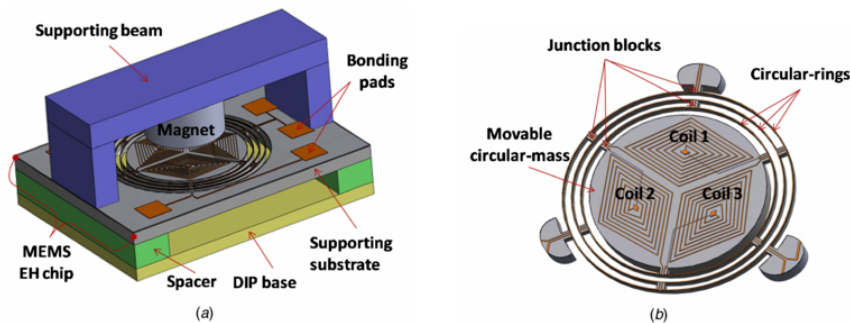


Figure 1.46: Design of a 3-D harvester proposed by [112]

The MEMS structure consists of a movable circular seismic mass. Three coils are printed on the surface and are held in place by three concentric rings. A series of bridges link the mass and the rings

together. As a result, the seismic mass oscillates in three modes. The first mode consists of an out of plane oscillation along the  $z$ -axis where the resonant frequency is of  $1216\text{ Hz}$ . In-plane oscillations with resonance frequencies of  $1479$  and  $1522\text{ Hz}$  along the  $y$ -axis and  $x$ -axis, respectively, correspond to Mode II and III. The same authors [113] have proposed later an improved structure displayed in Figure 1.47. The system has 6 degrees of freedom (DoF), which allows 3D translation and rotation. In a similar way, a permanent magnet is suspended from a supporting beam above a vibrating MEMS assembly. The seismic mass of the MEMS structure, as shown in Figure 1.47 is made up of a disk with a radius on the inside that permits the magnet to fit within. The metal coil designed on the seismic mass is made up of seven wire winding cycles. Five vibration modes exist in the circular mass. The resonance frequency of Mode I is of  $988\text{ Hz}$ , which corresponds to an out-of-plane oscillation along the  $z$ -axis. Torsion vibrations along the  $x$ - and  $y$ -axes, with resonance frequencies of  $1333$  and  $1355\text{ Hz}$ , respectively, represent modes II and III. In-plane oscillations along the  $x$ - and  $y$ -axes, with resonance frequencies of  $1494$  and  $1513\text{ Hz}$ , respectively, are represented by Modes IV and V. When the device is subjected to an excitation of  $1g$ , it provides voltages of  $3.7$ ,  $1.1$  and  $3.2\text{ mV}$  at  $840$  (mode I),  $1070$  (modes II and III) and  $1490\text{ Hz}$  (modes IV and V) respectively.

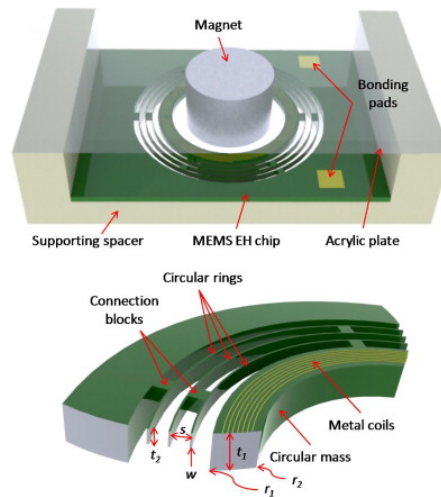


Figure 1.47: Design of a multifrequency 3-D harvester proposed by [113]

## 1.11 Summary

This chapter constitutes the state of art of the vibration energy harvesting field. We have reviewed the importance of the energy harvesting and its different sources. We focused then on the ambient sources as an unlimited one. A review on the full starting from energy harvesting till loading a sensor is discussed. A summary of the transduction techniques has been conducted and a qualitative comparison has been done. It has been shown that electromagnetic and piezoelectric techniques allow the highest output energy and are more compatible with different applications. Finally, techniques used for the enhancement of the energy harvester output in terms of the harvested power and frequency bandwidth

are discussed. In the next chapter, the proposed vibration energy harvester will be presented and its model and techniques used to enhance its performance will be, as well, developed.





## Chapter 2

# Theoretical analysis and experimental study for electromagnetic energy harvester by functionalization of energy localization and nonlinear dynamics

### Contents

---

<b>2.1</b>	<b>Introduction</b> . . . . .	<b>45</b>
<b>2.2</b>	<b>Modeling of the dynamic system</b> . . . . .	<b>45</b>
2.2.1	Device of the proposed vibration energy harvester . . . . .	45
2.2.2	Mechanical model . . . . .	46
<b>2.3</b>	<b>Experimental protocol and model confrontation</b> . . . . .	<b>52</b>
2.3.1	Device manufacture . . . . .	52
2.3.2	Experimental test bench . . . . .	52
2.3.3	Energy harvester characterization . . . . .	54
<b>2.4</b>	<b>Illustration of mode localization phenomenon</b> . . . . .	<b>55</b>
<b>2.5</b>	<b>Preliminary study of the linear harvester</b> . . . . .	<b>58</b>
2.5.1	Linear one-beam harvester . . . . .	58
2.5.2	Linear harvester in the case of two beams . . . . .	61
<b>2.6</b>	<b>Preliminary study of the nonlinear harvester</b> . . . . .	<b>65</b>
2.6.1	Nonlinear one beam harvester . . . . .	66
2.6.2	Nonlinear harvester in the case of two beams: Resolution procedure . . . . .	68
<b>2.7</b>	<b>Robustness of energy localization phenomenon and combination of non-linear dynamics with mode localized phenomenon</b> . . . . .	<b>70</b>
2.7.1	Robustness of energy localization . . . . .	70

2.7.2	Performance comparison of different configurations . . . . .	71
2.7.3	Experimental validation of the retained configuration . . . . .	73
<b>2.8</b>	<b>Experimental investigation of energy localization and nonlinear dynamics combination . . . . .</b>	<b>74</b>
2.8.1	Energy localization and harvested power in linear and nonlinear cases . . . . .	74
2.8.2	Experimental optimization of the harvester performance by combining energy localization and nonlinear dynamics . . . . .	75
<b>2.9</b>	<b>Summary . . . . .</b>	<b>77</b>

---

## 2.1 Introduction

IN this chapter, the electromagnetic transduction for vibration energy harvesting is investigated. The presentation of the proposed electromagnetic energy device and its manufacture are presented. Then, the corresponding mechanical model is developed and the experimental test bench is depicted. After that, the resolution procedure of the nonlinear system is presented. Next, the mode localization phenomenon is explained and illustrated. In the next stage, we study the linear and nonlinear systems and present the experimental prototype. Through the experimental study, the energy harvester is characterized and the model is validated. Lastly, the simultaneous combination of nonlinearity and mode localization is proposed to improve the output performance of the harvester. Hence, the benefits of the functionalization of energy localization and nonlinear dynamics are investigated and are validated experimentally.

## 2.2 Modeling of the dynamic system

### 2.2.1 Device of the proposed vibration energy harvester

The device of the proposed vibration energy harvester is shown in Figure 2.1. It is based on magnetic transduction. This harvester is made up of  $N_b$  identical bi-clamped beams magnetically coupled by  $N$  moving magnets, fixed at the middle of each magnet.

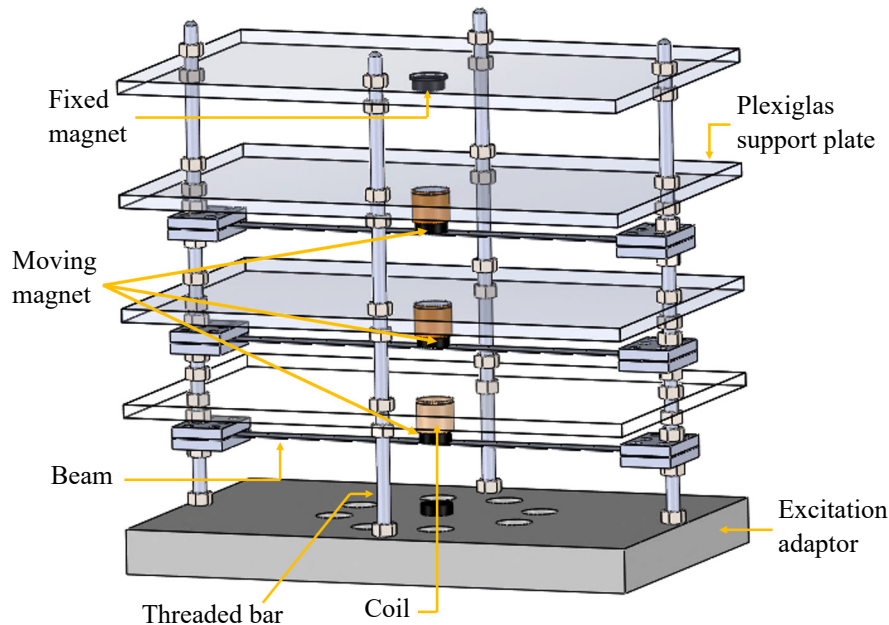


Figure 2.1: 3D schematic of the proposed vibration energy harvester

Two fixed magnet are placed at the top and the bottom of the system. The magnetic poles are arranged so that between each two adjacent magnets a repulsive force is created. A wire-wound copper

coil is wrapped horizontally around each moving magnet as depicted in Figure 2.2. The whole structure is subjected to a harmonic excitation as shown in Figure 2.2.

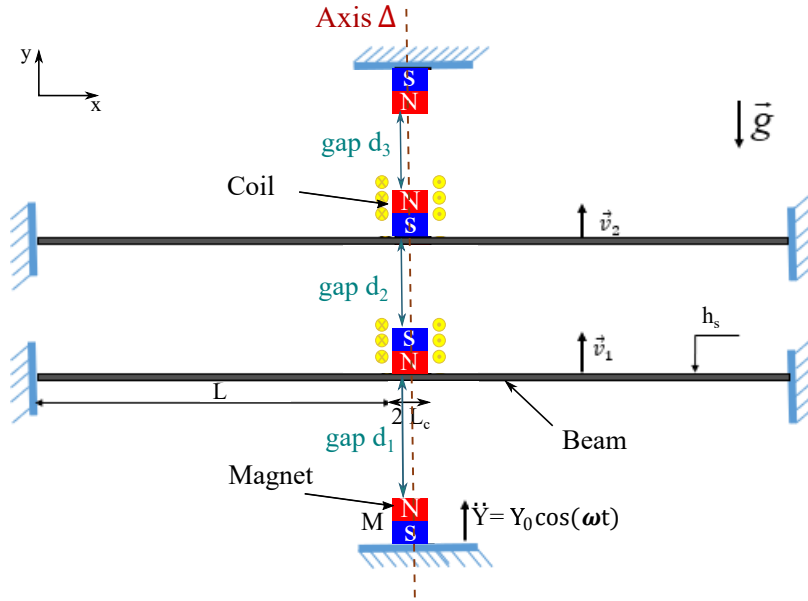


Figure 2.2: 2D representation of the vibration energy harvester

## 2.2.2 Mechanical model

In this section, we will determine the equation of motion for the  $N$  coupled beam. The geometry of the proposed system is symmetric with respect to the  $\Delta$ -axis (Figure 2.2). Therefore, in order to simplify the modeling of the harvester, the dynamic study will be limited to a single symmetric part. We assume that the beams and the magnets are identical.

For large displacement, the axial deformation  $\varepsilon_{11}$  in the  $\vec{x}$  direction of the  $n$  beam ( $n = 1, 2, \dots, N$ ) is given by the following expression while neglecting terms of order higher than 2 in the strain tensor:

$$\varepsilon_{11} = \frac{1}{2}v_n'^2 + yv_n'' \quad (2.1)$$

where  $v_n$  is the transverse displacement of the magnet  $n$  and  $'$  denotes the derivative with respect to the spatial variable  $x$ .

According to Euler-Bernoulli theory [114], it is assumed that  $\theta_n = \frac{\partial v_n}{\partial x}$ . Thereafter, the curvature radius  $\kappa$  is defined as follows:

$$\kappa = \frac{\partial \theta_n}{\partial x} = \frac{\partial^2 v_n}{\partial x^2} = v_n'' \quad (2.2)$$

The kinetic energy of the  $n^{th}$  beam is the sum of the elastic and rigid parts' kinetic energies. Then, it can be written as follows:

$$E_{c,n} = \frac{1}{2} \rho_s S_s \int_0^L \dot{v}_n^2 dx + \frac{1}{2} \frac{M}{L_c} \int_L^{L+L_c} (\dot{v}_n + L_c \dot{v}_n')^2 dx \quad (2.3)$$

where  $\rho_s$  is the steel beam density,  $S_s$  is the beam section,  $L$  is the beam length,  $M$  is the magnet mass,  $L_c$  is the magnet radius and "." denotes the derivative with respect to time.

The elastic energy is written as follows:

$$E_{p,n} = \frac{1}{2} \int_0^L (N_f \varepsilon_{11} + M_m \kappa) dx \quad (2.4)$$

where  $N_f$  is the axial resultant force and  $M_m$  is the bending moment.

We proceed, in what follows, for the determination of  $N_f$  and  $M_m$ . For an unspecified cross section, the stress tensor  $\underline{\sigma}$  at a point has the following form

$$\underline{\sigma} = \begin{pmatrix} \sigma_{11} & \sigma_{12} & \sigma_{13} \\ \sigma_{21} & 0 & 0 \\ \sigma_{31} & 0 & 0 \end{pmatrix} \quad (2.5)$$

The axial resultant force is defined by the following expression:

$$N_f = \frac{1}{L} \int_0^L \int_{-\frac{h_s}{2}}^{\frac{h_s}{2}} (b \sigma_{11} dy) dx = \frac{E_s S_s}{2L} \int_0^L v_n'^2 dx \quad (2.6)$$

where  $E_s$  stands for the steel beam young modulus,  $b$  is the beam width and  $h_s$  is the beam thickness.

The bending moment is defined as follows:

$$M_m = \int_{-\frac{h_s}{2}}^{\frac{h_s}{2}} \sigma_{11} y dy dz = \int_{-\frac{h}{2}}^{\frac{h}{2}} b E_s \varepsilon_{11} y dy = E_s I_s \kappa \quad (2.7)$$

where  $I_s$  is the quadratic moment which is equal to :  $I_s = \frac{b h_s^3}{12}$ .

Thus, the elastic energy is written as following:

$$E_{p,n} = \frac{E_s S_s}{8L} \left( \int_0^L v_n'^2 dx \right)^2 + \frac{E_s I_s}{2} \left( \int_0^L v_n'' dx \right)^2 \quad (2.8)$$

It is assumed that the magnets and the beams are identical and that we have the same distance between the beams (same gap  $d$ ). According to Foisal et al. [115], the exact magnetic force is written as follows

:

$$F_m^{exact} = \frac{\mu_0 Q}{4\pi} \left( \frac{1}{(d - (v_n - v_{n-1}))^2} - \frac{1}{(d + (v_n - v_{n+1}))^2} \right) \quad (2.9)$$

where  $n$  represents the index of the concerned beam.

An electrical circuit is implemented. It generates an electromagnetic force which is proportional to the electrical damping  $c_e$ , and a dissipative mechanical force which is proportional to the mechanical damping  $c_m$ . The total non-conservative force is, then, written as

$$F_{nc} = c_m \dot{v}_n + \frac{c_e}{L_c} \dot{v}_n|_{x=L} \quad (2.10)$$

To simplify the development of equations, the magnet mass has been considered to be a localized point mass for the mode of interest (1st). FEM simulations under ANSYS have been run to support this hypothesis. The illustrations of the distributed magnet mass and of the localized point mass are shown in Figures 2.3a and 2.3c respectively. As reported in Figures 2.3b and 2.3d, the frequency of the beam and its mode shape are the same for the two configurations (Errors of 0.005%, 0.003% and 0.09% respectively in terms of displacement in the center, slope and frequency).

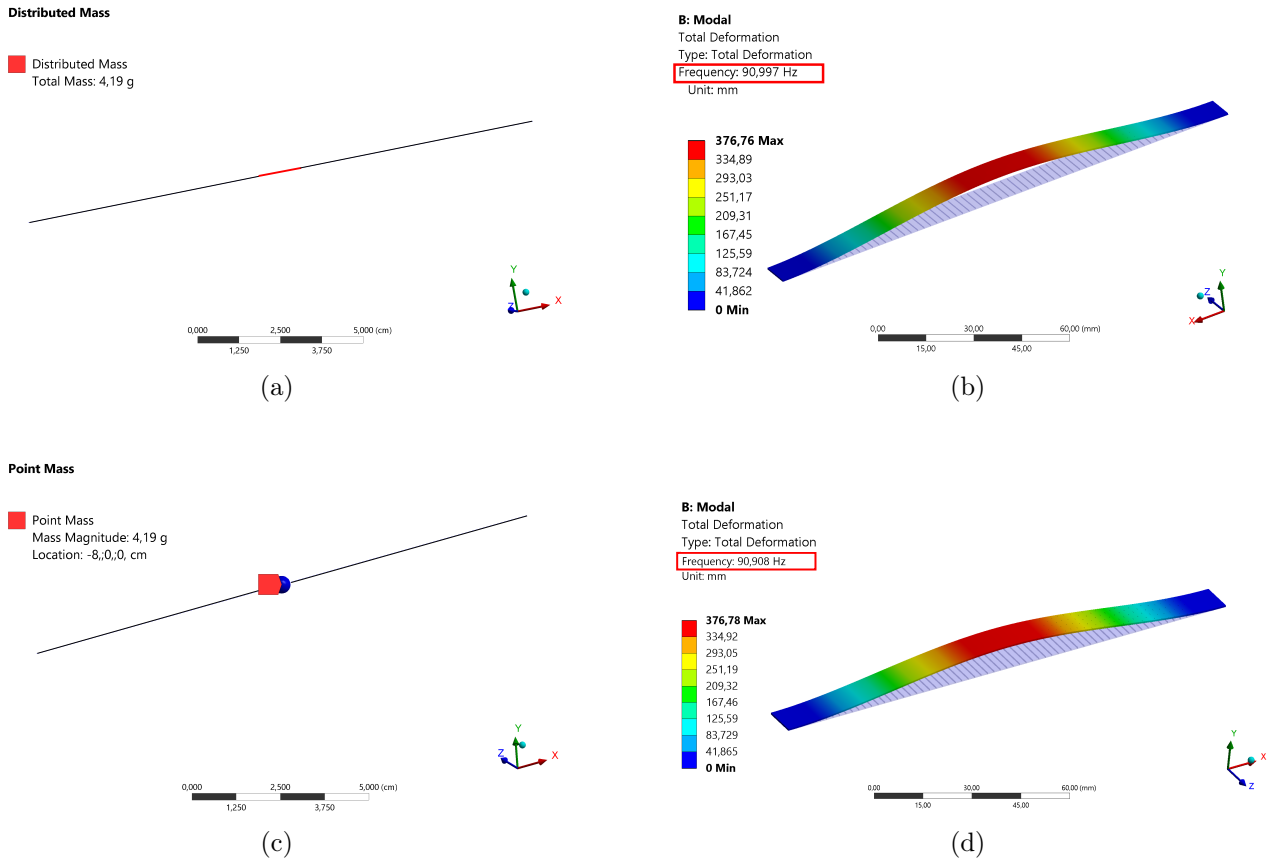


Figure 2.3: About the hypothesis of point mass magnet: Beam frequency response with point mass and with distributed mass

We define the Hamiltonian function  $J$  by

$$J = \sum_n J_n, \quad J_n = \int_{t_0}^{t_f} (W_c^n - W_p^n + W_{ext}^n) dt \quad (2.11)$$

where  $W_c^n$ ,  $W_p^n$  and  $W_{ext}^n$  are respectively the work of non-conservative, damping and external forces. We define the Hamiltonian functions as:

$$H_1(x) = \begin{cases} 1 & \text{if } x \in [0, L] \\ 0 & \text{if } x \in [L, L + L_c] \end{cases} \quad (2.12)$$

and

$$H_2(x) = \begin{cases} 0 & \text{if } x \in [0, L] \\ 1 & \text{if } x \in [L, L + L_c] \end{cases} \quad (2.13)$$

For reasons of symmetry, the beam is fixed at  $x = 0$  and guided at  $x = L$ , so the associated boundary conditions are:

$$\begin{cases} v_n(0, t) = v_n'(0, t) = 0 \\ E_s I_s v_n'''(L, t) - M \ddot{v}_n(L, t) = 0 \end{cases} \quad (2.14)$$

Therefore, after applying the boundary conditions, for  $\delta J = 0$ , we obtain the following equation:

$$\begin{aligned} & \left[ \rho_s S_s \ddot{v}_k + E_s I_s v_n^{IV} + c_m \dot{v}_n - \frac{E_s S_s}{2L} v_n'' \int_0^L v_n' dx \right] H_1(x) + \left[ \frac{c_e}{L_c} (\dot{v}_n - \dot{v}_{n-1}) + F_m \right] H_2(x) \\ & = - \left[ \rho_s S_s H_1(x) + \frac{M}{L_c} H_2(x) \right] \ddot{Y} \end{aligned} \quad (2.15)$$

The magnetic transduction is provided by a coil wound wrapped around the separation distance between two consecutive magnets. The oscillatory motion of the moving magnet causes a variation of the magnetic field in this area and gives rise to an induced electric current  $i(t)$  (Lenz's law). This induced current can be written as a function of the magnet velocity and the electromagnetic coefficient  $\delta$ .  $\delta$  is a function of the parameters of the coil and the magnet such that  $\delta = N \times B \times l$ , where  $N$  is the number of turns of the coil,  $B$  is the magnetic field and  $l$  is the length of the coil.

By applying Kirchhoff's law to the electrical circuit, we obtain the following mechanical-magnetic coupling equation for each DOF  $n$  ( $n = 1, 2, \dots, N$ ):

$$i_n(t) = \frac{\delta}{R_{load}^n + R_{int}} \dot{v}_n|_{x=L} \quad (2.16)$$

where  $R_{load}^n$  and  $R_{int}$  are respectively the load and the internal resistances.

It is assumed that the internal resistances of the coils  $R_{int}$  are identical.

According to Mann and Simms [86], electrical damping is defined as follows:

$$c_e = \frac{\delta^2}{R_{load} + R_{int}} \quad (2.17)$$

We introduce the following non-dimensional variables in order to simplify the equations:

$$v_d = \frac{v}{d}; Y_0 = \frac{Y}{d}; T = \frac{t}{\tau}; X = \frac{x}{\tau}; \tau = L^2 \sqrt{\frac{\rho S}{EI}} \quad (2.18)$$



Therefore, the coupled continuum multi-physics problem is equivalent to the following system of equations:

$$\left\{ \begin{array}{l} \left[ \rho_s S_s \frac{d}{\tau^2} \ddot{v}_{d,n} + E_s I_s \frac{d}{L^4} v_{d,n}^{IV} + c_m \frac{d}{\tau} \dot{v}_{d,n} - \frac{E_s S_s}{2L} \frac{d}{L^2} L v_{d,n}'' \int_0^1 (v'_{d,n}) dX \right] H_1(X) + \\ \left[ \frac{c_e}{\tau L_c} d(2\dot{v}_{d,n} - \dot{v}_{d,n-1} - \dot{v}_{d,n+1}) + F_m \right] H_2(X) \\ = - \left[ \rho_s S_s H_1(X) + \frac{M}{L_c} H_2(X) \right] \frac{d}{\tau^2} \ddot{Y} \\ i_k(t) = \frac{\delta d}{(R_{load} + R_{int})\tau} \dot{v}_{d,n} \end{array} \right. \quad (2.19)$$

where

$$F_m = \frac{\mu_0 Q}{4\pi L_c d^2} \left( \frac{1}{(1 - (v_{d,n} - v_{d,n-1}))} - \frac{1}{(1 + (v_{d,n} - v_{d,n+1}))} \right) \quad (2.20)$$

The boundary conditions become equivalent to:

$$\left\{ \begin{array}{l} v_{d,n}(0, T) = v'_{d,n}(0, T) = 0 \\ v'_{d,n}(1, T) = \frac{E_s I_s}{L^3} v_{d,n}'''(1, T) - \frac{M}{\tau^2} \ddot{v}_{d,n}(1, T) = 0 \end{array} \right. \quad (2.21)$$

In order to transform the continuous multiphysics problem into a system of discrete ordinary differential equations in the time domain, Galerkin modal decomposition is used in order to generate a reduced model using only the 1<sup>st</sup> mode of the beam. The displacements are projected on a single mode basis to solve the previous system. Each  $n$  DOF oscillator displacement is written as follows:

$$v_{d,n}(X, T) = \phi(X) a_n(T) \quad (2.22)$$

where  $n = 1, 2$ ,  $\phi(X)$  is the projection base and  $a_n(T)$  are the generalized coordinates.

In order to simplify the modal projection, the electromagnetic force is developed in Taylor series up to order 3 expressed as  $F_m^{Taylor}$ . By eliminating all even terms in the expression of  $F_m^{Taylor}$ , we obtain the expression  $F_m$ . In Figure 2.4,  $F_m^{exact}$ ,  $F_m^{Taylor}$  and  $F_m$  are plotted. Based on this figure, we can conclude that the approximation of the exact force by Taylor expansion is valid when the relative displacement doesn't exceed 18 mm. Below this value, the curves of the exact force and its approximations are superposed.

Consequently, the exact force  $F_m^{exact}$  can be approximated by the expression of  $F_m$ . As it is presented in [85], this approximation can be written in the form of a combination of linear  $k_{mg}^L$  and nonlinear stiffness  $k_{mg}^{NL}$

$$F_m^n = k_{mg}^L v_{d,n} + k_{mg}^{NL} v_{d,n}^3 \quad (2.23)$$

where

$$k_{mg}^L = \frac{\mu_o Q^2}{\pi L_c d^3}, k_{mg}^{NL} = \frac{\mu_o Q^2}{\pi L_c d^5} \quad (2.24)$$

It is assumed that the magnetic nonlinearity is neglected compared to the mechanical nonlinearity in the case of a weak coupling between the two beams.

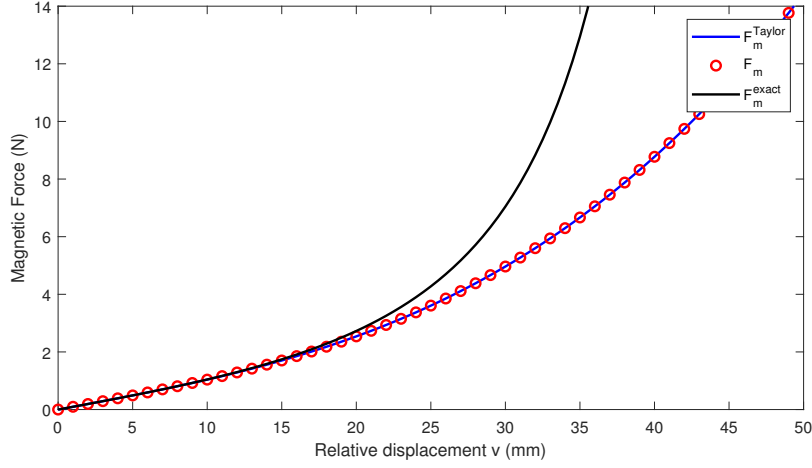


Figure 2.4: Variation of the exact magnetic force  $F_m^{exact}$  and its approximations  $F_m^{Taylor}$  (Taylor series of  $F_m^{exact}$  up to order 3) and  $F_m$  ( $F_m^{Taylor}$  with the elimination of even terms) with the relative displacement.

By replacing equations 2.23 and 2.24 in Equation (2.19), multiplying by  $\phi$ , integrating between 0 and  $L$  and taking into consideration the boundary conditions, the equations of the motion of the  $n^{th}$  DOF are expressed as follows:

$$\begin{aligned} & \left[ \int_0^1 \phi^2 dX \right] \ddot{a}_n + \left[ \int_0^1 \phi \phi^{IV} dX \right] a_n + \left[ \frac{c_m L^4}{E_s I_s \tau} \int_0^1 \phi^2 dX \right] \dot{a}_n - \left[ \frac{S_s d^2}{2 I_s} \int_0^1 \phi^3 \phi'' dX \right] a_n^3 \\ & + \frac{L^4}{E_s I_s} \int_1^{1+\frac{L_c}{L}} \left[ \frac{c_e}{\tau L_c} \phi^2(1) (\dot{a}_n - \dot{a}_{n-1}) + F_m \right] dX = - \left[ \int_0^1 \phi^2(X) dX + \frac{M \phi(1)}{\rho_s S_s L} \right] \ddot{Y} \end{aligned} \quad (2.25)$$

Therefore, the equations of the multi-physics problem are equivalent to:

$$\begin{cases} \ddot{a}_n + \left[ \int_0^1 \phi^2(X) dX + \frac{M}{\rho_s S_s L} \right]^{-1} \times \left\{ \left[ \frac{c_m L^4}{E_s I_s \tau} \int_0^1 \phi^2 dX + \frac{L^3 c_e}{\tau E I} \right] \dot{a}_n + \left[ \left( \frac{2L^3}{E_s I_s} \frac{\mu_0 Q^2}{\pi d^3} \phi^2(1) + \int_0^1 \phi''^2 dX \right) a_n \right. \right. \\ \left. \left. - \frac{L^3}{E_s I_s} \frac{\mu_0 Q^2}{\pi d^3} (a_{n-1} + a_{n+1}) + \left[ \frac{S d^2}{2 I} \int_0^1 \phi'^2(X) dX + \frac{d^2 L^3}{E_s I_s} \frac{2Q^2}{\pi d^5} \right] a_n^3 \right\} \\ = - \left[ \int_0^1 \phi(X) dX + \frac{M}{\rho_s S_s L} \right] \times \left[ \int_0^1 \phi^2(X) dX + \frac{M}{\rho_s S_s L} \right]^{-1} \ddot{Y} \\ i_n(T) = \frac{\delta d}{(R_{load}^n + R_{int})\tau} \dot{a}_n, n = 1, 2, \dots, N \end{cases} \quad (2.26)$$

To simplify calculations, we choose an admissible function that represents the first mode shape in a polynomial form as follows:  $\phi(X) = 3\left(\frac{X}{L}\right)^2 - 2\left(\frac{X}{L}\right)^3$ . It satisfies  $\phi(0) = \phi'(0) = 0$ ,  $\phi(1) = 1$  and  $\phi'(1) = 0$ . Therefore, the equations of the multiphysics problem can be written, with generalized coordinates and with only mechanical nonlinearity, as follows:

$$\begin{cases} M_{eq} \ddot{a}_n + c_{eq} \dot{a}_n + [k_{mec}^L + 2k_{mg}^L] a_n - k_{mg}^L (a_{n-1} + a_{n+1}) + k_{mec}^{NL} a_n^3 = -f \ddot{Y} \\ i_n(T) = \frac{\delta d}{R_{load}^n + R_{int}} \dot{a}_n, n = 1, 2 \end{cases} \quad (2.27)$$

where:

$$\left\{ \begin{array}{l} M_{eq} = \int_0^1 \phi^2(X) dX + \frac{M}{\rho_s S_s L} \\ c_{eq} = \frac{c_m L^4}{E_s I_s \tau} \int_0^1 \phi^2(x) dx + \frac{L^3 c_e}{E_s I_s \tau} \\ k_{mec}^L = \int_0^L \phi''^2(X) dX \\ k_{mg}^L = \frac{L^3 \mu_0 Q^2}{E_s I_s \pi d^3} \\ k_{mec}^{NL} = \frac{S_s d^2}{2I} \int_0^1 \phi'(X) dX + \frac{d^2 L^3}{E_s I_s} \frac{2Q^2}{\pi d^5} \\ f = \int_0^L \phi(X)^2 dX + \frac{M}{\rho_s S_s L} \\ f = F \times M_{eq} \end{array} \right. \quad (2.28)$$

## 2.3 Experimental protocol and model confrontation

### 2.3.1 Device manufacture

The electromagnetic harvester presented in Figure 2.6 is composed of steel beams, neodymium cylindrical magnets, copper coils, an excitation adapter and plexiglass coil fixing plates. For its manufacture, we needed to design the beams, the excitation adapter, the parts to ensure the embedding of the beams and the plexiglas coil carrying plates. The dimensions of the beam are shown in the schematic drawing in Figure 2.5 below.

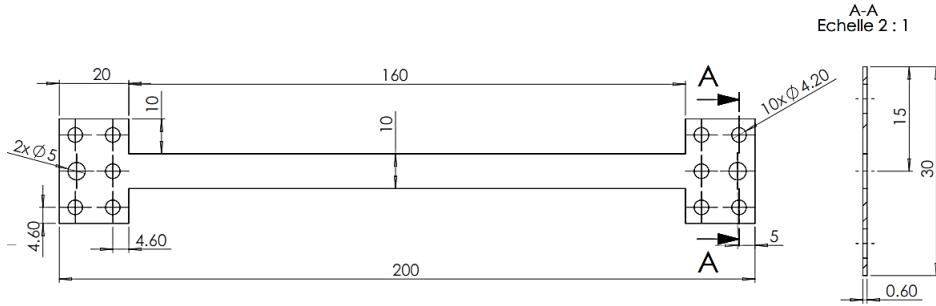


Figure 2.5: Representation of the beam dimensions

### 2.3.2 Experimental test bench

The test bench, illustrated in Figure 2.7, on which the experimental tests were carried out, is made up of several elements which are a shaker in order to vibrate the structure, a laser vibrometer for non-contact vibration measurement of the magnet displacement and an accelerometer attached to the excitation adapter measuring the acceleration of the shaker. The electrical signal coming from the accelerometer is amplified and displayed on the oscilloscope. In order to measure the generated power of the VEH, the output current of the coils is discharged in load resistances tuned by a potentiometer

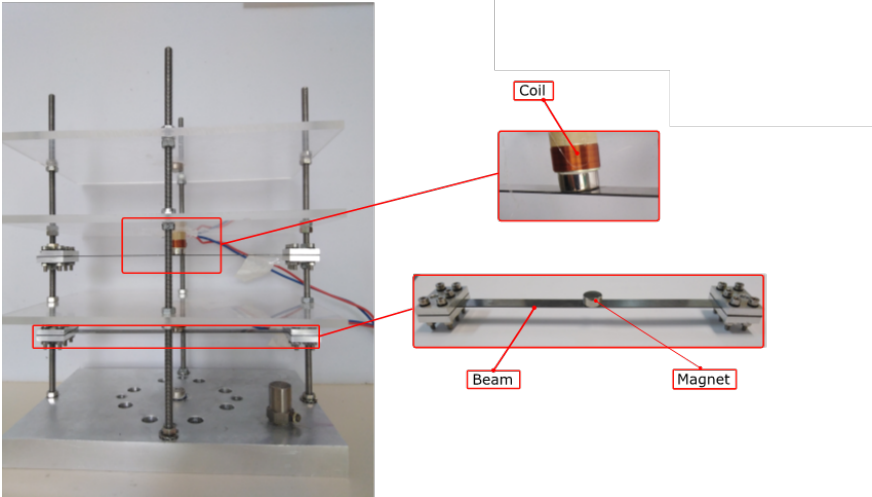


Figure 2.6: The proposed vibration energy harvester

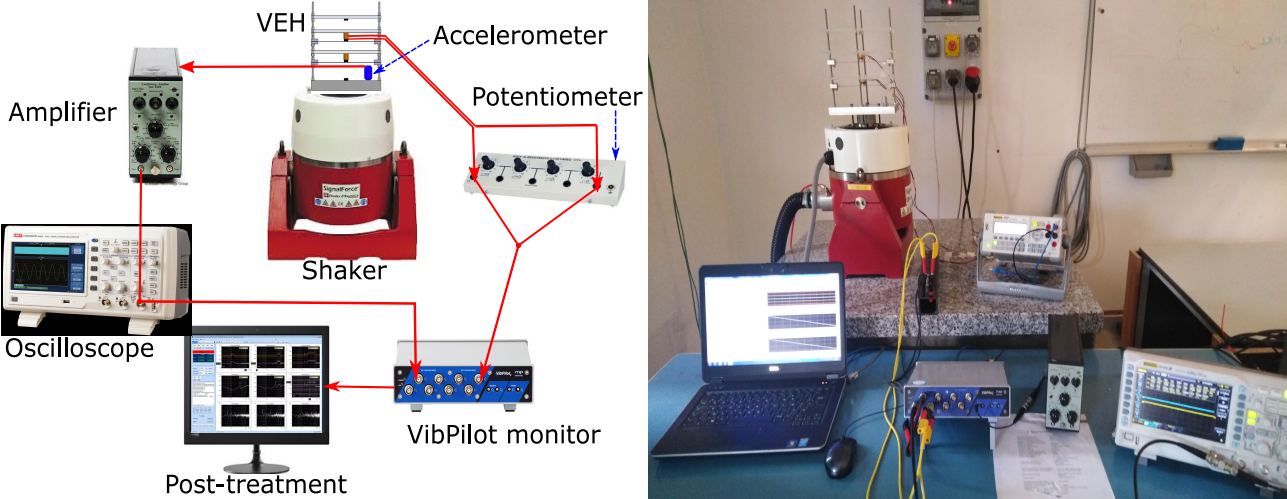


Figure 2.7: Experimental test bench

and treated by "m + p VibRunner" pilot software. During the experimental tests, the fabricated device is mounted on the shaker which supplies vibrations to the VEH as a response to the input accelerations. The frequency is swept from  $73\text{ Hz}$  to  $100\text{ Hz}$  and the applied acceleration was controlled by an accelerometer mounted on the excitation adapter. In the case of open-loop circuit, the DOFs velocities are measured by the laser Doppler vibrometer while for the case of closed-loop circuit, the coils' voltages are measured through load resistances varied by potentiometers.

### 2.3.3 Energy harvester characterization

#### Characterization of $E$ and $\rho$

To determine the effective density  $\rho$  and Young's modulus  $E$  of the beam, we measure its various dimensions (width, length, thickness, etc.) and its mass. To determine the density of the beam, we use the following formula:  $\rho = \frac{M_{eq}}{V}$ . Then, we measure its equivalent mass and knowing its volume, we determine its density.

As for the Young's modulus, we start by experimentally determining the resonant frequency of the beam. From an experimental point of view, obtaining a perfect clamping conditions is challenging. Therefore, in this section we will determine an effective Young modulus in order to match the resonance frequencies defined as:

$$\omega_0 = \sqrt{\frac{k_{mec}^L}{M_{eq}}}; k_{mec}^L = \frac{12EI}{L^3} \quad (2.29)$$

Therefore, we obtain

$$\rho_s = 7694 \text{ Kg.m}^{-3} \text{ and } E_s = 289 \text{ GPa} \quad (2.30)$$

#### Determination of mechanical and electrical damping coefficients

To estimate the mechanical damping, we excite our structure with a low acceleration to ensure linear behavior of the resonator while making sure that the electrical circuit is open (= no electrical damping). The mechanical damping is calculated based on 3 dB method also called half-power method at the first resonance frequency. By looking at 3 dB down from the peak amplitude level corresponding to:  $A = \frac{A_{max}}{\sqrt{2}}$ , the difference between these two frequencies, noted  $\Delta f$ , makes it possible to estimate the damping rate as follows  $\xi_m = \frac{\Delta f}{2\omega_0}$ . Therefore, the mechanical damping coefficient is estimated as:  $\xi_{mec} = 0.6\%$ .

For the electrical damping coefficient, we follow the same procedure but this time, the electrical circuit is closed to determine the total damping coefficient of the structure. The electrical damping coefficient is the difference between the total damping coefficient and the mechanical one:

$$\xi_{tot} = \xi_{mec} + \xi_c \quad (2.31)$$

The electrical damping coefficient changes when varying the load resistance  $R_{load}$  according to Equation 2.3.3. The variation of the electric damping is illustrated in Figure 2.8. This figure shows that the electric damping and the load resistance are related according to a hyperbolic law which explains the form of Equation .

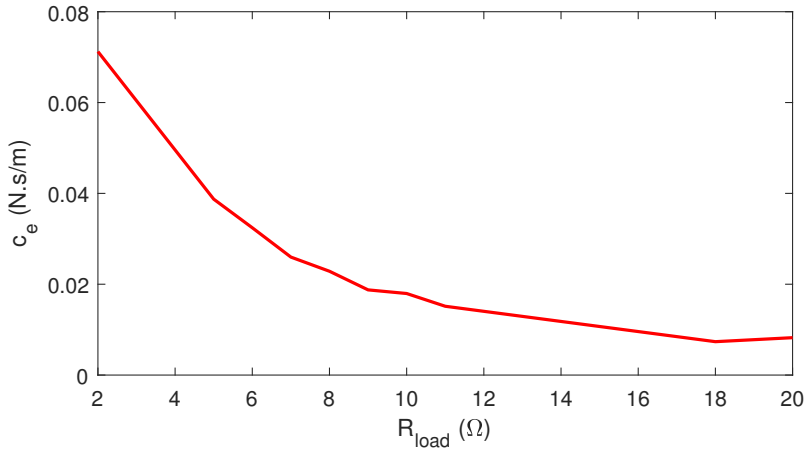


Figure 2.8: Variation of electrical damping as a function of load resistance

## 2.4 Illustration of mode localization phenomenon

In the next section, we will perform numerical simulations in order to illustrate the mode localization phenomenon. Based on what was presented in section 1.8.2, it is assumed that the energy localization phenomenon occurs in the case of internal weak coupling for quasiperiodic structures. When a small irregularity or disorder is introduced in the periodic system, its symmetry is broken. This results in energy trapping in the perturbed regions. Therefore, finite element method under ANSYS is used in order to illustrate the bending modes of 10 bi-clamped beams supposed to be perfectly periodic as illustrated in Figure 2.9. The coupling between them is ensured by spring connections. The stiffness of the beams are fixed in a way that the coupling between them is weak ( $\simeq 1\%$ ). The weak coupling assumption leads to the creation of closed modes. The normal frequencies of the modes,  $\omega_n$ , can be expressed via the following formula with respect to the reference frequency  $\omega_0$ :

$$\omega_n = \omega_0(1 + \Lambda)^{1/2} \quad (2.32)$$

where:  $n = 1, 2, \dots, N$ ,  $\Lambda = 2\beta(1 - \cos(\frac{n\pi}{N+1})) \ll 1$  and  $\beta \simeq 1\%$  represents the coupling factor.

The approximate solution of all normal frequencies is given by the Taylor expansion of  $\cos(\frac{n\pi}{N+1})$ :

$$\omega_n \approx \omega_0 \left(1 + \frac{1}{2}\Lambda\right) \quad (2.33)$$

This assumption allows creating closed modes in order to investigate the phenomena of energy localization. Table 2.1 illustrates the natural eigenfrequencies of the 10-beams system. To observe the

Table 2.1: The 10-beams system's natural eigenfrequencies in Hz

$\omega_1$	$\omega_2$	$\omega_3$	$\omega_4$	$\omega_5$	$\omega_6$	$\omega_7$	$\omega_8$	$\omega_9$	$\omega_{10}$
120.8924	120.8996	120.9109	120.9253	120.9418	120.9590	120.9756	120.9900	121.0013	121.0084

confinement of the energy in perturbed zone, we will follow the following strategy. First, a periodic

system is simulated. Second, mass mistuning is introduced for 3 beams of the structure. Third, the same amount of mistuning is kept but the position of the beams is changed. Finally, the position of beams is the same but this time the amount of the mistuning changes. Figure 2.9 depicts the first mode forms and their sensitivity to the imposed mistuning. The periodic system's vibrations are distributed in a uniform way, as shown in Figure 2.9a. In fact, all the beams vibrate in the same manner and so have the same amount of kinetic energy. Then, we have chosen to vary the density of 3 arbitrary beams among 10 by 6%. The mistuning was introduced to the 10-beam structure (the 3<sup>rd</sup>, 6<sup>th</sup> and 9<sup>th</sup> beams and the 2<sup>nd</sup>, 5<sup>th</sup> and 8<sup>th</sup> beams counting from the bottom in Figures 2.9b and 2.9c respectively). The perturbed beams have significantly more displacements than the others, which is modeled in terms of kinetic energy confined in the mistuned regions of Figure 2.9b.

When comparing the results of the configurations shown in Figures 2.9c and 2.9d, where the irregularities are applied in the same positions but with different amounts, the energy localization is more pronounced, and the kinetic energies of the perturbed beams are more important than the others in the case of a 10% density mistuning.

Therefore, a criterion is proposed in order to quantify mode localization and predict its occurrence. For each mode, the following ratio between the modal kinetic energy of the concerned local DOFs and the global structure will be calculated:

$$E_n = \frac{x_n^T M_n x_n}{X^T M X} \quad (2.34)$$

where  $M_n$  represents the mass matrix of the  $n$ -element area,  $x_n$  stands for the eigenvector area restriction, and  $X$  and  $M$  are the considered mode's eigenvector and the full model's mass matrix, respectively.

It is noted that  $E_1$  and  $E_2$  applied to the first and second DOFs in periodic (Figure 2.9a) and quasiperiodic (Figure 2.9b) arrangements is 20% and 50%, respectively. Based on this phenomenon illustration, we can conclude that the localized energy in 2-DOFs of the quasiperiodic system is equivalent to the energy of 5-DOFs in the periodic system.

This criteria may be expressed as follows for the DOF  $n$  in the case of a discrete system with  $N$  DOFs:

$$E_n = \frac{m_n x_n^2}{\sum_{i=1}^N m_i x_i^2} \quad (2.35)$$

where  $m_n$  and  $x_n$  are the mass and displacement of the corresponding DOF  $n$ , respectively.

Since the main objective of this chapter is the fonctionnalization of energy localization and nonlinear dynamics, the benefits of these phenomena will be introduced separately in the next section. For that, a preliminary study of linear and nonlinear single and two DOFs harvester is presented. The objective of this study is to introduce important characteristics that will be exploited in the coming sections.

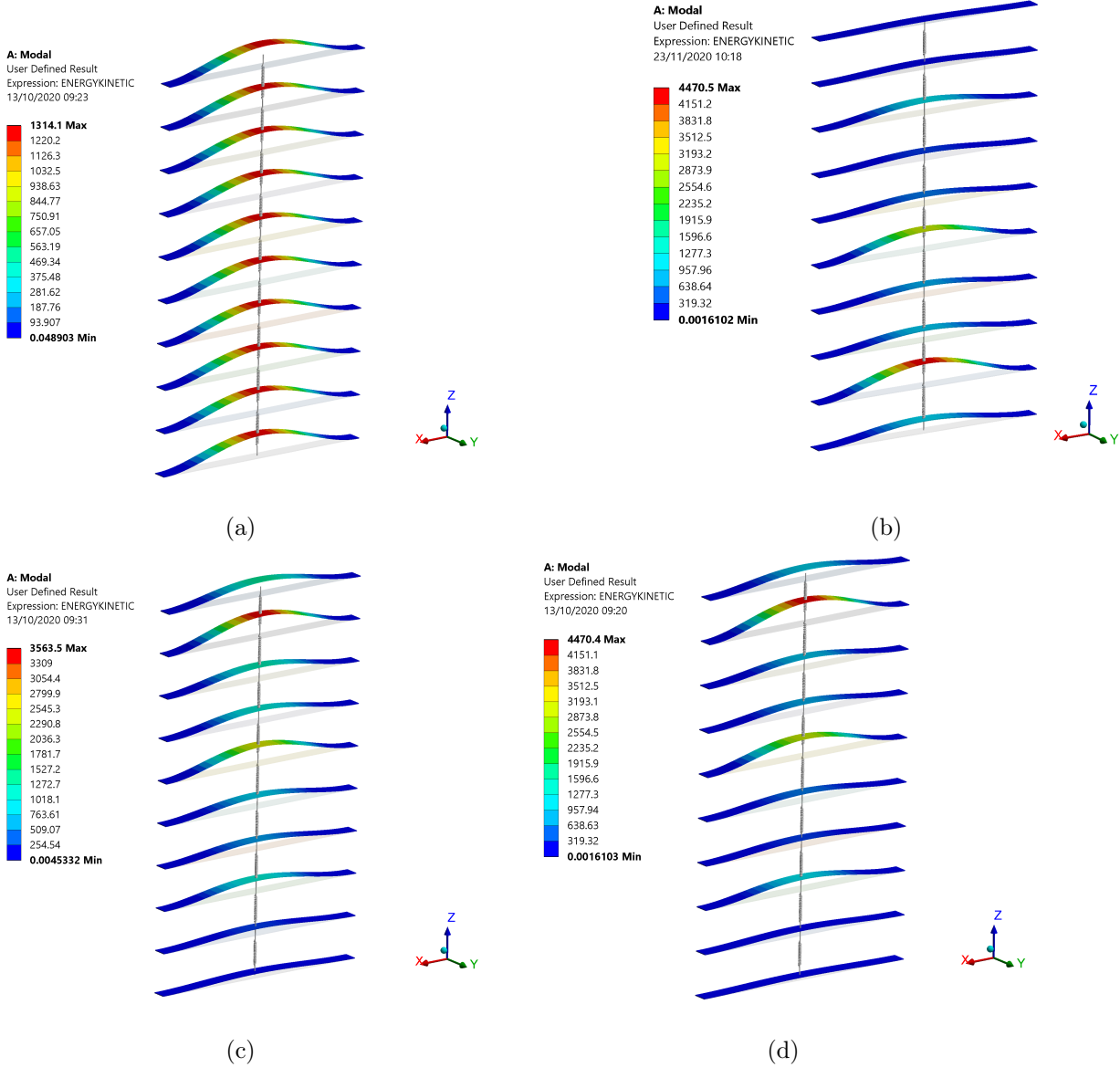


Figure 2.9: Bending vibration modes of the 10-coupled beams with variation in mass density by : (a) 0 % (periodic system), (b) 10 % of the 2<sup>nd</sup>, 5<sup>th</sup> and 8<sup>th</sup> beams counting from the bottom, (c) 6 % and (d) 10 % of the 3<sup>rd</sup>, 6<sup>th</sup> and 9<sup>th</sup> beams counting from the bottom.



## 2.5 Preliminary study of the linear harvester

### 2.5.1 Linear one-beam harvester

#### System of equations

We treat in this section a linear 1-DOF harvester. The electrical energy generated by the transducer is not directly usable to power a storage device. To ensure that, an energy extraction circuit must be implemented and will be attached to the coils of the device. For the case of 1-DOF, the multiphysics problem is modeled by the following system of coupled equations (Equation 2.27 for  $n = 1$ ):

$$\begin{cases} \ddot{a}_1 + c_1 \dot{a}_1 + \omega_0^2 a_1 = -F\dot{Y} \\ i_1(t) = \frac{\delta}{(R_{load}^1 + R_{int}^1)} \dot{a}_1 \end{cases} \quad (2.36)$$

where:  $c_1 = \frac{c_m + c_e}{M_{eq}}$ ,  $c_m = 2\xi_m \omega_0 M_{eq}$ ,  $\omega_0 = \sqrt{\frac{k_{mec}^L}{M_{eq}}}$ ,  $c_e = \frac{\delta^2}{R_{load} + R_{int}}$ ,  $k_L = k_{mec}^L + k_{mg}^L = \int_0^1 \phi_1^2(x) dx + \frac{k_L^{mg} L^3}{EI} = 12 + \frac{k_L^{mg} L^3}{EI}$ ,  $M_{eq} = \int_0^1 \phi(x) dx + \frac{M}{\rho SL} = \frac{13}{35} + \frac{M}{\rho SL}$  and  $F = \frac{f}{M_{eq}} = \frac{\int_0^1 \phi_1(x) dx + \frac{M}{\rho SL}}{M_{eq}} = \frac{\frac{1}{2} + \frac{M}{\rho SL}}{M_{eq}}$ .

Let  $a_n = A_n e^{i\omega t}$  be the expression of the amplitude of vibration of the  $n^{th}$  beam.

The induced current flowing through the load resistor provides an electrical power expressed as follows:

$$P_n(t) = R_{load} \cdot i_n(t)^2 \quad (2.37)$$

Therefore, the average power of the  $n^{th}$  beam is expressed by:

$$P_n = \sum_n R_{load}^n \left[ \frac{\delta \omega A_n^{max}}{(R_{load}^n + R_{int}^n)} \right]^2 \quad (2.38)$$

where  $R_{load}^n$  and  $R_{int}^n$  are respectively the load and internal resistances of the  $n^{th}$  load circuit.  $A_n^{max}$  stands for the maximum vibration amplitude value deduced from  $a_n$  of the corresponding DOF  $n$ .

#### Determination of the electromagnetic coefficient $\delta$

In practice, the relative movement between a conductive material (copper coil) placed near a magnet induces an electromotive force at the terminals of the conductor. A magnetic flux then characterizes the magnet/coil couple. When a current flows in the conductor, a magnetic field is created which opposes the variation of this initial flux. The latter results in a force proportional to the current which is applied between the magnet and the coil. The variation of the flux  $\phi_m$  is considered constant and equal to the intrinsic electromechanical coupling coefficient  $\delta$  defined as [116]:

$$\delta = \frac{\partial \phi_m(y)}{\partial y} = H_y \frac{d}{dz} \int_{\frac{H_y}{2} + y}^{-\frac{H_y}{2} + y} B(y) dy \quad (2.39)$$

where  $H_y$  is the height of the coil,  $y$  is the coil axis and  $B$  is the magnetic field vector.

In order to determine the distribution of the magnetic field, Finite Element Method Magnetics (FEMM) software is used. This open software allows solving problems of magnetostatic and electromagnetism. The magnetic field in the center of the coil depends on the characteristics of the coils, the magnets, the gaps and the beams. In the following Table 2.2, we mention the characteristics of the used coils and magnets which are considered as identical. The problem is considered as an axisymmetric one and is illustrated in Figure 2.10a. The characteristics of the used coil, beam and magnet and the structure meshing are illustrated in Figure 2.10b.

Table 2.2: Characteristics of the used coils and magnets

Parameter	Designation / value
Magnet Type	Neodymium magnet
Magnetization	N45
Magnet diameter	12 mm
Magnet height	4 mm
Residual magnetic field	1.37 T
Type of coil	Copper coil
Diameter of coil	14 mm
Number of coil turns $N$	73
Internal resistance $R_{int}$	3.4 $\Omega$

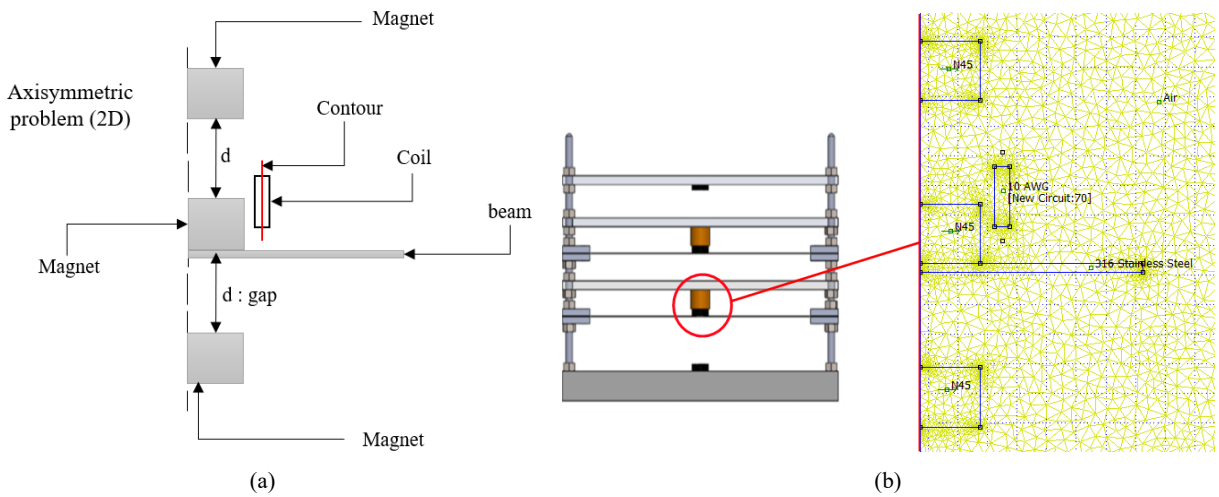


Figure 2.10: (a) Axisymmetric (2D) modeling of the structure under FEMM, (b) Characteristics and meshing of the structure under FEMM

The distribution of the magnetic field along the designed coil contour is shown in Figure 2.11. The contour is represented in red in these two figures. The exportation of the magnetic field vector  $B(y)$  and the calculation through the formula of Equation 2.39 leads to an electromagnetic coefficient  $\delta$  equal to  $1.04 V.s.m^{-1}$ . The expression of  $\delta = N \times B \times l$ , mentioned before, leads to the same result.

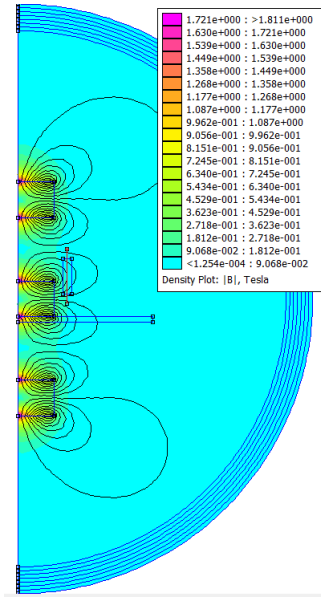


Figure 2.11: Results of the magnetic field  $B$  distribution

### Harvested power with load resistance

For the case of a single DOF, the harvested power is expressed as follows:

$$P_1 = R_{load}^1 \left[ \frac{\delta \omega A_1^{max}}{(R_{load}^1 + R_{int})} \right]^2 \quad (2.40)$$

This harvested power depends on the load resistance. For the design parameters summarized in Table 4.1, Figure 2.12 illustrates the power as a function of the load resistance. As shown, while varying the resistances, there is an optimum load resistance value  $R_{load}^{opt}$  for which the power reaches its maximum.

Table 2.3: Design parameters for a single ddl system

Parameter	Designation	Value	Unity
$L$	Beam half-length	74	$mm$
$b$	Beam width	10	$mm$
$L_c$	Moving magnet mid-length	6	$mm$
$h_s$	Steel beam thickness	0.6	$mm$
$d$	Gap between magnets	70	$mm$
$M$	Magnet mass	4.5	$g$
$H_s$	Coercive force	860	$kA.m^{-3}$
$S$	Beam section	6	$mm^2$
$\xi_m$	Mechanical damping coefficient	0.6 %	**

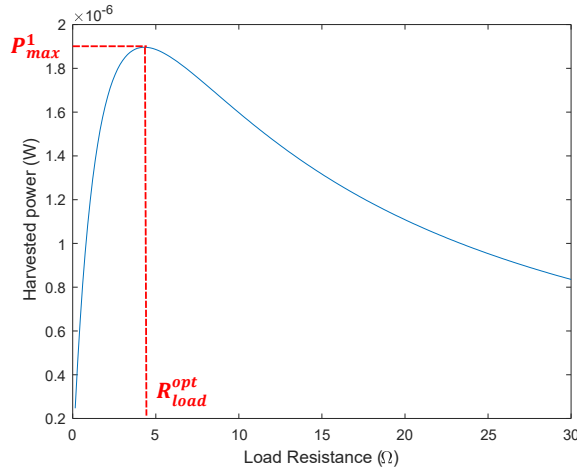


Figure 2.12: Harvested power with load resistance

### 2.5.2 Linear harvester in the case of two beams

The electromagnetic harvester of 2-DOFs oscillators and its equivalent model are presented in Figures 2.13a and 2.13b, respectively.

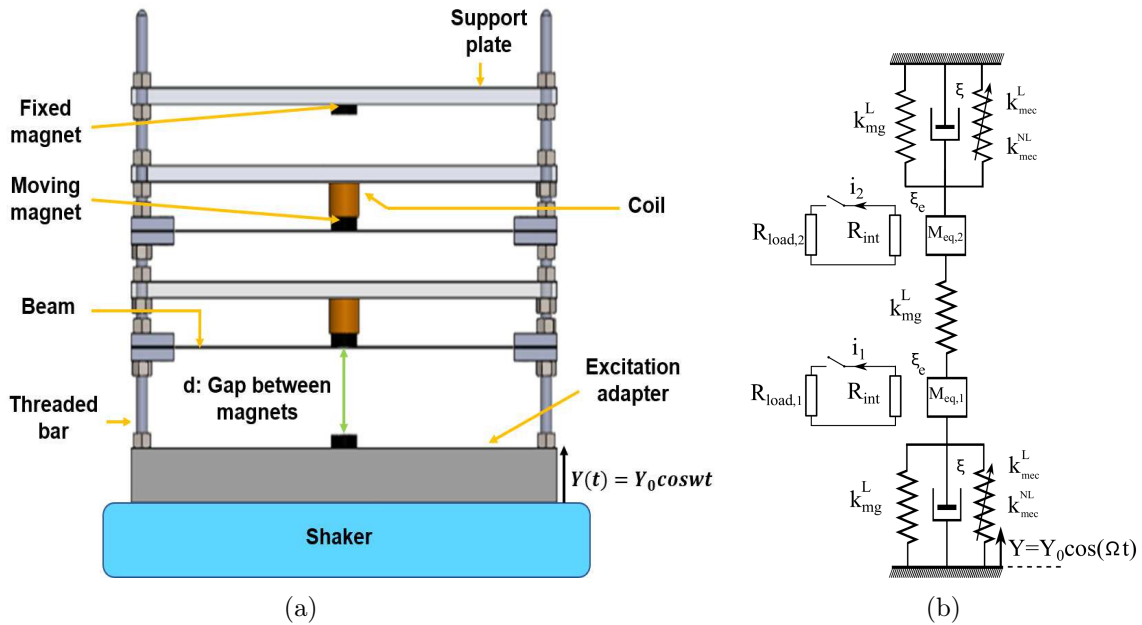


Figure 2.13: (a) The designed electromagnetic vibration energy harvester (b) The mechanical model of the harvester

In this section, we note that the 2 beams, the 4 magnets, the magnets' gaps  $d$  and the coils are identical (same  $R_{int}$ ). For the case of a periodic two-beams structure, the linear coupled multiphysics

problem is expressed as follows (Equation 2.27 with  $n = 2$ ):

$$\begin{cases} M_{eq,1}\ddot{a}_1 + c_{eq}\dot{a}_1 + (k_{mec}^L + 2k_{mg}^L)a_1 - k_{mg}^La_2 = -f\ddot{Y} \\ M_{eq,2}\ddot{a}_2 + c_{eq}\dot{a}_2 + (k_{mec}^L + 2k_{mg}^L)a_2 - k_{mg}^La_1 = -f\ddot{Y} \\ i_n(t) = \frac{\delta}{(R_{load}^n + R_{int})} \dot{a}_n, n = 1, 2 \end{cases} \quad (2.41)$$

Although the manufacturing processes and tools are advanced, obtaining two perfectly identical parts remains a near-impossible affair. This is why these irregularities are usually taken into account in such calculations. These irregularities will be the source of the appearance of the localization phenomenon which will be exploited to trap the maximum energy limited in the source zone [91]. As presented in section 1.8.2, the presence of small irregularities in weakly coupled periodic systems affects the behavior of the system in terms of the location of the vibration mode. Indeed, the modes of vibration are localized to a limited region of the system. This phenomenon was first predicted by Anderson [91] studying random networks. In the context of the vibration of structures, two first studies, in which the localization of the mode was discussed, were given by Hodges [92] and Hodges and Woodhouse [93]. In order to activate the functionnalization of this phenomenon, mass mistuning will be introduced. Based on the observed benefits of the illustrated phenomenon in section 2.4, small mass mistuning will be introduced to only the second magnet mass. Thus, the energy will be harvested from the DOF which has been perturbed. One implements, therefore, for the whole structure only one electrical circuit related to the perturbed magnet.

Our structure is assumed to be weakly coupled. Two parameters are introduced: the coupling factor  $\beta$  and the mistuning  $\alpha$ . In the case of a mass mistuning, Equation 2.41 becomes equivalent to:

$$\begin{cases} M_{eq,1}\ddot{a}_1 + c_m\dot{a}_1 + (k_{mec}^L + 2k_{mg}^L)a_1 - k_{mg}^La_2 = -f\ddot{Y} \\ \alpha M_{eq,1}\ddot{a}_2 + c_{eq}\dot{a}_2 + (k_{mec}^L + 2k_{mg}^L)a_2 - k_{mg}^La_1 = -f\ddot{Y} \end{cases} \quad (2.42)$$

We define the defect or the mistuning introduced by  $\alpha = \frac{M_{eq2}}{M_{eq1}}$  and the coupling coefficient  $\beta = \frac{k_{mg}^L}{k_{mec}^L}$ . We define  $Y = Y_0e^{i\omega t}$  and  $a_n = A_n e^{i\omega t}$  ( $n = 1, 2$ ).

By integrating the expressions of the displacements and the excitation, we obtain the following system:

$$\begin{pmatrix} -\Omega^2 + i\Gamma_1\Omega + (1 + 2\beta) & -\beta \\ -\beta & -\alpha\Omega^2 + i\Gamma_2\Omega + (1 + 2\beta) \end{pmatrix} \begin{pmatrix} A_1 \\ A_2 \end{pmatrix} = \begin{pmatrix} (1 + p)Y_0\Omega \\ (\alpha + p)Y_0\Omega \end{pmatrix} \quad (2.43)$$

where

$$\Omega = \frac{\omega}{\omega_0} \quad \omega_0 = \sqrt{\frac{k_{mec}}{M_{eq,1}}} \quad \Gamma_1 = \frac{c_m}{\omega_0 M_{eq,1}} \quad \Gamma_2 = \frac{c_e + c_m}{\omega_0 M_{eq,1}} = \frac{c_{eq}}{\omega_0 M_{eq,1}} \quad p = \frac{9L\rho S}{70M_{eq,1}}$$

Referring to Cramer's formulas for a linear system, we find the expressions for the two amplitudes

$A_1$  and  $A_2$  , if we scavenge the energy only from the vibrations of the disturbed mass, as follows:

$$\begin{cases} A_1 = \frac{(1+p)(-\alpha\Omega^2+i\Gamma_2\Omega+2\beta+1)+\beta(\alpha+p)}{(-\Omega^2+i\Gamma_1\Omega+2\beta+1)\times(-\alpha\Omega^2+i\Gamma_2\Omega+2\beta+1)-\beta^2} \times Y_0\Omega \\ A_2 = \frac{(\alpha+p)(-\Omega^2+i\Gamma_1\Omega+2\beta+1)+\beta(1+p)}{(-\Omega^2+i\Gamma_1\Omega+2\beta+1)(-\alpha\Omega^2+i\Gamma_2\Omega+2\beta+1)-\beta^2} \times Y_0\Omega \end{cases} \quad (2.44)$$

For a homogeneous problem, the system of equations becomes equivalent to:

$$\begin{cases} M_{eq,1}\ddot{a}_1 + (k_{mec}^L + 2k_{mg}^L)a_1 - k_{mg}^La_2 = 0 \\ \alpha M_{eq,1}\ddot{a}_2 + (k_{mec}^L + 2k_{mg}^L)a_2 - k_{mg}^La_1 = 0 \end{cases} \quad (2.45)$$

The normalized natural frequencies  $\Omega_1$  and  $\Omega_2$  are expressed as follows:

$$\Omega_{1,2}^2 = \frac{(\alpha + 1)(1 + 2\beta) \pm \sqrt{(\alpha - 1)^2(1 + 4\beta) + 4(\alpha - \alpha + 1)\beta}}{2\alpha} \omega_0^2 \quad (2.46)$$

In Figure 2.14, we represent the veering phenomenon [92, 93]. This phenomenon of mode shift occurs in systems with a variable parameter. As the mistuning varies, so do the natural frequencies. When two natural frequencies get closer to each other while varying the mistuning, they often present a veering instead of intersecting. The relation between this veering and the localization of the modes in a perturbed periodic structures was studied by Pierre et al. in [117, 118]. They assert that this phenomenon only occurs in coupled oscillator networks when the coupling is weak.

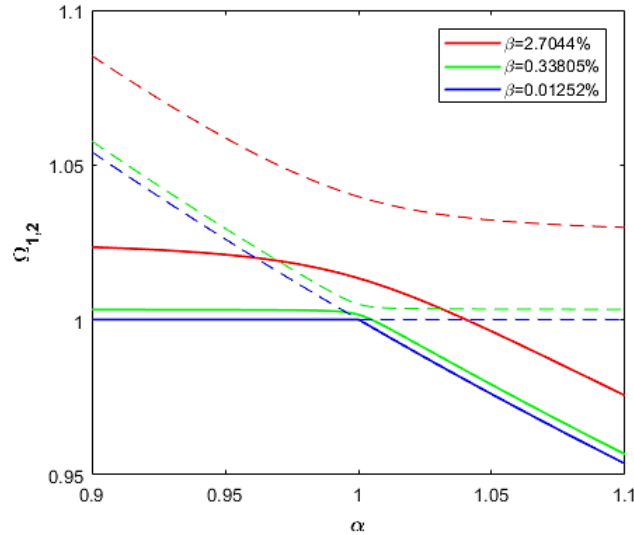


Figure 2.14: Veering phenomenon: Normal frequencies with mass mistuning coefficient while variation of the coupling coefficient

In Figure 2.14, it is shown that the variation of the coupling affects the veering phenomenon. Indeed, if the coupling tends more and more towards 0 and  $\alpha = 1$ , then the frequencies  $\Omega_1$  and  $\Omega_2$

become equal to each others. We set the load resistance to  $R_{load} = 12 \Omega$ ,  $Y_0 = 0.02 \text{ mm}$  and  $d = 70 \text{ mm}$  and one plots the variation of the amplitudes according to the introduced mistuning as illustrated in Figure 2.15. We find that for  $\alpha = 1$ , the amplitudes are equal and move away from 1. For  $\alpha = 1.054$ , we find that we have the highest difference between the amplitudes. In the coming sections, we will fix the mistuning to be equal to the value that ensures the largest difference. Then, we will be interested on harvesting energy from the DOF which presents the highest amplitude and so the highest localized kinetic energy.

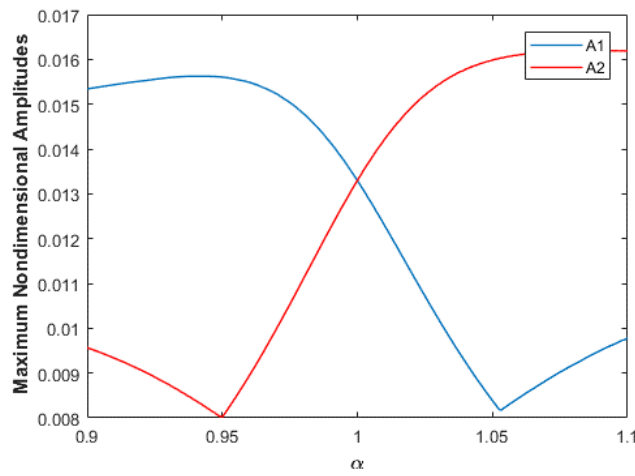


Figure 2.15: Maximum amplitudes with mistuning  $\alpha$  ( $\beta = 2.2\%$  and  $c_m = 0.03 \text{ N.s/m}$ )

Figure 2.16 shows the two vibrating beams maximum amplitudes while varying the load resistance and the introduced mistuning. The difference between the maximum amplitudes of the two beams is maximum when the ratio of the mechanical stiffnesses and the load resistance are equal to  $\alpha = 1.054$  and  $R_{load} = 45 \Omega$ .

The expression of power is as follows:

$$P(\alpha, \beta, R_{load}^2) = R_{load} \left[ \frac{\delta \omega_0 A_2^{max}}{(R_{load}^2 + R_{int})} \right]^2 \quad (2.47)$$

where  $\omega_0$  is the frequency at which the amplitude  $A_2$  is maximum.

Figure 2.17 shows the power harvested by varying the load resistance and the mistuning introduced. From this figure, we can determine the optimal parameters  $\alpha$  and  $R_{load}^2$  that can provide the maximum power. According to calculation leading to this illustration, these optimal parameters are  $\alpha = 1.03$  and  $R_{load}^2 = 25 \Omega$ .

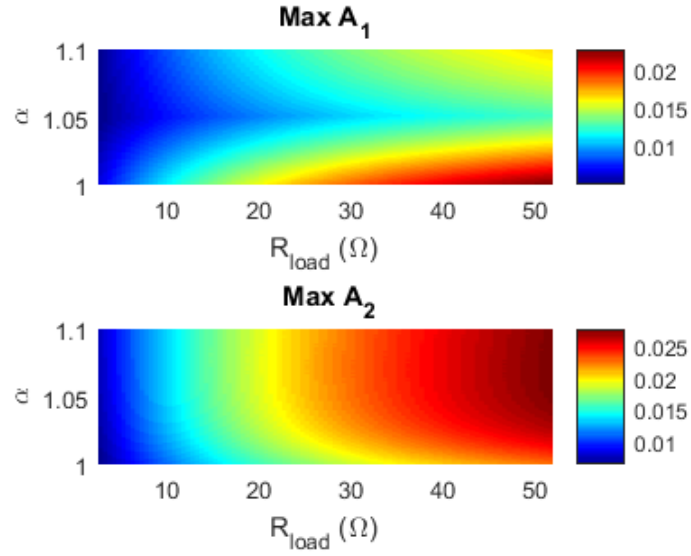


Figure 2.16: Maximum amplitudes with mistuning  $\alpha$  and load resistance  $R_{load}$  ( $\beta = 2.2\%$  and  $c_m = 0.03N.s/m$ )

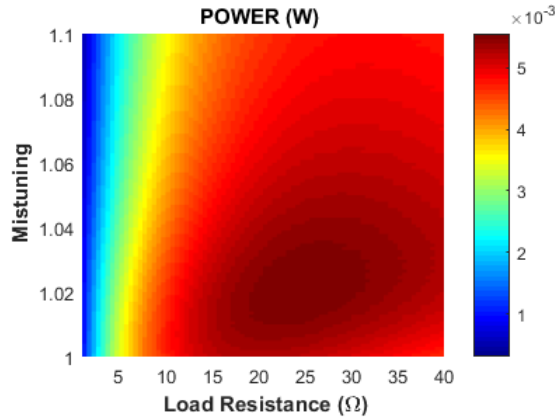


Figure 2.17: Harvested power with mistuning  $\alpha$  and load resistance  $R_{load}$

Referring to Equation 2.47, the optimal value  $R_{load}^*$  for which the power is maximum ( $\frac{\partial P}{\partial R_{load}} = 0$ ) can be determined through this expression:

$$R_{load}^* = R_{int} + \frac{h^2 f (f^2 + 5\beta^2)}{q(f^4 + \beta^2(2 - 2\alpha + 3\beta)^2 + f^2((\alpha - 1)^2 - 4\beta(\alpha - 1) + 10\beta^2))} \quad (2.48)$$

where  $q = \omega_0 M_{eq,1}$ ,  $f = \frac{c_m}{q}$  and  $c_m = 2\xi_m \omega_0 M_{eq,1}$ .

## 2.6 Preliminary study of the nonlinear harvester

In this section, we will just consider the mechanical nonlinearity. It is assumed, for the moment, that the magnetic nonlinearity is neglected. To solve the nonlinear equation, the method of multiple scales (MMS) (called also the multiple-scale analysis) [114] will be used. This method consists of



solving ordinary differential perturbative equations by introducing different time scales that replace the single time variable. Through this method, valid approximations to the solutions of the perturbation problems are constructed. The solutions depend simultaneously on widely different scales. In the following section, this method will be applied for 1-DOFs and 2-DOFs systems.

### 2.6.1 Nonlinear one beam harvester

#### Determination of amplitude and phase

For 1-DOF system, the equation of motion is written in the following form:

$$\ddot{a}_1 + c_1 \dot{a}_1 + \omega_0^2 a_1 + f_{NL} a_1^3 = F \ddot{Y} \quad (2.49)$$

Referring to the multiple scales perturbation method [114], we pose:

$$a(t) = \sum_{i=0}^n \varepsilon^i a_i[T_0, T_1, \dots, T_n] \quad (2.50)$$

where  $T_n = \varepsilon^n t$ ,  $T_0 = t$  and  $T_1 = \varepsilon t$ .

For  $n = 0, 1$

$$a^{(0,2)} + 2a^{(1,1)} + \Gamma_1 a^{(0,1)} + \omega_0 a + f_{nl} a^3 = F Y_0 \Omega^2 \cos(\Omega t) \quad (2.51)$$

We neglect terms of order higher than 1, then:

$$a_0 = A(T_1) e^{i\omega_0 T_0} + cc \quad (2.52)$$

$$\ddot{a}(t) = 2\varepsilon a_0^{(1,1)} + \varepsilon a_1^{(0,2)} + a_0^{(0,2)} \quad (2.53)$$

We define  $\Omega = \omega_0 + \sigma\varepsilon$ .  $\varepsilon$  is a dimensionless small parameter and  $\sigma$  is a detuning parameter.

One integrates the equations in this system, we obtain:

$$\begin{aligned} \left( 2\varepsilon a_0^{(1,1)} + \varepsilon a_1^{(0,2)} + a_0^{(0,2)} \right) + \varepsilon \Gamma_1 \left( a_0^{(0,1)} + \varepsilon a_0^{(1,0)} + \varepsilon a_1^{(0,1)} \right) + \omega_0 (a_0 + \varepsilon a_1) + \varepsilon f_{nl} (a_0 + \varepsilon a_1)^3 \\ = -\varepsilon F Y_0 \Omega^2 \cos(\Omega t) \end{aligned} \quad (2.54)$$

Thus, we obtain the following system:

$$\begin{cases} \omega_0 a^{(1,0)} + \frac{\Gamma_1}{2} a = \frac{-F Y_0 \Omega^2}{2} \sin(\sigma T_1 - \beta) \\ \frac{3}{8} f_{nl} a^3 - \omega_r \beta^{(1,0)} a = \frac{-F Y_0 \Omega^2}{2} \cos(\sigma T_1 - \beta) \end{cases} \quad (2.55)$$

We define  $\gamma = \sigma T_1 - \beta \Rightarrow \gamma^{(1,0)} = \sigma - \beta^{(1,0)}$ .

The system becomes equivalent to:

$$\begin{cases} a^{(1,0)} = \frac{FY_0\Omega^2}{2\omega_0} \sin \gamma - \xi \omega_0 a \\ \gamma^{(1,0)} = \frac{FY_0\Omega^2}{2a\omega_0} \cos \gamma - \frac{3}{8a\omega_0} f_{nl} a^3 + \sigma \end{cases} \quad (2.56)$$

For a fixed point  $a^{(1,0)} = \gamma^{(1,0)} = 0$ , the amplitude and phase equations are found in the following form:

$$\begin{cases} a = \frac{F}{2\xi\omega_0} \sin \gamma \\ \sigma = \xi \omega_0 \cot \gamma + \frac{3F}{16\xi\omega_0^3} f_{nl} \sin \gamma \end{cases} \quad (2.57)$$

### Critical force, amplitude and resistance

The critical amplitude is the amplitude of transition from linear to nonlinear behaviour of the harvester. Its determination is important because it gives information of the the linear dynamic range of the proposed device.

We proceed to determine the critical amplitude  $A_c$  [119]. It can be captured when  $\frac{d\sigma}{d\gamma} = 0$ . We define  $X = \frac{1}{2\omega_0^2} f_{nl}$ , so that:

$$\frac{d\sigma}{d\gamma} = \frac{3FX \sin 2\gamma (1 - \cos 2\gamma) - 32\xi^3 \omega_0^4}{16\xi\omega_0^3 \sin \gamma} = 0 \quad (2.58)$$

We define  $\chi = \sin 2\gamma$ . So,

$$\sin 4\gamma = 2 \sin 2\gamma \cos 2\gamma = 2 \sin 2\gamma \sqrt{1 - \sin^2 2\gamma} \quad (2.59)$$

We have so,

$$\frac{3F^2 X}{32\xi^3 \omega_0^4} \chi - \chi \sqrt{1 - \chi^2} - 1 = 0 \quad (2.60)$$

Solving this equation provides four solutions of which 3 are to be rejected. In the expression of the accepted solution, it appears  $\sqrt{-16(\frac{3FX}{32\xi^3\omega_0^4})^6 + 27(\frac{3FX}{32\xi^3\omega_0^4})^8}$ .

So, after solving, the coefficient  $\frac{3FX}{32\xi^3\omega_0^4}$  should be equal to  $\frac{4}{3\sqrt{3}}$ , hence  $\gamma = \frac{\pi}{3}$ . For these values, the critical force  $F_c$  is expressed as:

$$F_c = \frac{8 \times \sqrt{2} \xi^{\frac{3}{2}} \omega_0^2}{3\sqrt[4]{3}\sqrt{X}} \quad (2.61)$$

The critical amplitude is expressed as follows for  $\gamma = \frac{\pi}{3}$ :

$$A_c = \frac{4\sqrt{2}\sqrt{\xi}}{3\sqrt[4]{3}\sqrt{X}} \quad (2.62)$$

The critical resistance  $R_c$  characterizes the linear dynamic range upper bound limit of the device.

We can determine it when  $A = A_c$  and  $F = F_c$ . So, the critical resistance is expressed as:

$$R_c = \frac{2.677 \delta^2 L^3}{M_{eq,1} \tau E I} \times \frac{1}{\frac{F X^{\frac{1}{3}}}{1.71 \omega_0} - \frac{\omega_0}{Q}} \quad (2.63)$$

where  $Q$  is the quality factor and  $Q = \frac{\omega_0}{c_m}$ .

Nonlinearity is usually used to enhance the bandwidth of any structure. In order to illustrate the importance of the nonlinear dynamics in improving the frequency bandwidth, we illustrate in Figure 2.18 the linear, critical and nonlinear behaviors of the device while varying the excitation amplitude ( $Y_0 = 0.01 \text{ mm}$ ,  $Y_0 = 0.03 \text{ mm}$ ,  $Y_0 = 0.06 \text{ mm}$ , respectively). The bandwidth increases considerably when the harvester is driven in nonlinear mode ( $BW_{NL} > BW_L$ ).

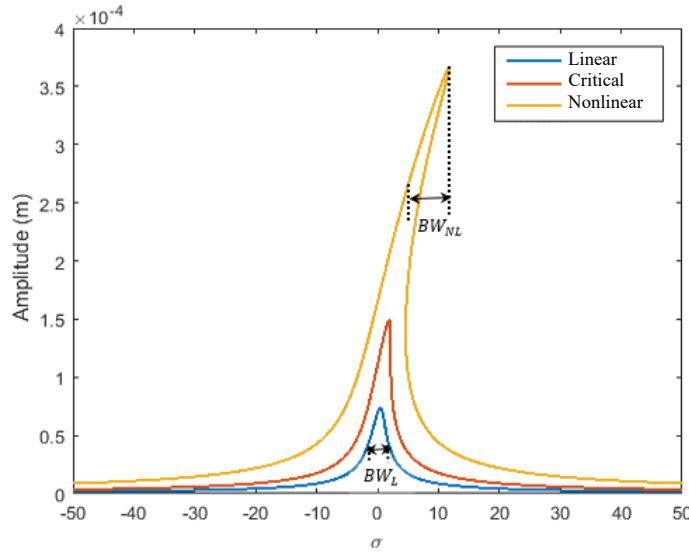


Figure 2.18: Linear, critical and nonlinear configurations.

### 2.6.2 Nonlinear harvester in the case of two beams: Resolution procedure

We will consider in this section, a 2-DOFs system with mass mistuning introduced in the second mass magnet. The equations of motion of the two beams is solved using the solution procedure for the nonlinear system which is the method of multiple scales [120]. The independent variables are introduced according to:

$$T_p = \varepsilon^p t \quad \text{for } p = 0, 1, 2, \dots \quad (2.64)$$

The equations of motion are expressed as follows:

$$\begin{cases} \ddot{a}_1 + \varepsilon c a_1 + \omega_0^2 [(1 + 2\varepsilon\beta)a_1 - \varepsilon\beta a_2] + \varepsilon f_{nl} a_1^3 = \varepsilon(1 + p)\ddot{Y} \\ \ddot{a}_2 + \frac{1}{\alpha}(\varepsilon c a_2 + \omega_0^2 [(1 + 2\varepsilon\beta)a_2 - \varepsilon\beta a_1] + \varepsilon f_{nl} a_2^3) = \varepsilon(1 + \frac{p}{\alpha})\ddot{Y} \end{cases} \quad (2.65)$$

We define  $a_k$  ( $k = 1, 2$ ) as a function of the new scales, it can be represented by:

$$a_k(t, \varepsilon) = \sum_p^{\infty} \varepsilon^n a_{k,n}(T_0, T_1, T_2, \dots) \quad (2.66)$$

We substitute Equation (2.67) and into Equation (2.65). Then, we differentiate the equations according to  $\varepsilon$  order. The order 0 gives the following equations:

$$\begin{cases} \frac{\partial^2 a_{10}}{\partial t^2} + \omega_1^2 a_{10} = 0 \\ \frac{\partial^2 a_{20}}{\partial t^2} + \frac{\omega_1^2}{\alpha} a_{20} = 0 \end{cases} \quad (2.67)$$

Let  $\omega_2 = \frac{\omega_1}{\alpha}$ . These equations are solved and they have the following expression

$$\begin{cases} a_{10} = A_1 e^{i\omega_1 t} + c.c \\ a_{20} = A_2 e^{i\omega_2 t} + c.c \end{cases} \quad (2.68)$$

where c.c represents the conjugate of the complex entities. Thereafter,

$$\omega_2 = \omega_1 + \sigma_1 \varepsilon \quad \text{and} \quad \Omega = \omega_1 + \sigma_2 \varepsilon \quad (2.69)$$

where  $\sigma_1$  is the detuning parameter.

Applying the similar steps for order  $O(\varepsilon^1)$ , we obtain:

$$\begin{cases} \frac{\partial^2 a_{11}}{\partial t^2} + 2 \frac{\partial^2 a_{10}}{\partial t \partial T} + c \frac{\partial a_{10}}{\partial t} + \omega^2 \beta (2 a_{10} - a_{20}) + \omega_1^2 a_{11} + f_{nl} a_{10}^3 = \frac{(1+p)F_n}{2} e^{i(\omega_1 + \sigma_2 \varepsilon)t} \\ \frac{\partial^2 a_{21}}{\partial t^2} + 2 \frac{\partial^2 a_{20}}{\partial t \partial T} + \frac{c_1}{\alpha} \frac{\partial a_{20}}{\partial t} + \frac{\omega^2 \beta}{\alpha} (2 a_{20} - a_{10}) + \omega_2^2 a_{21} + \frac{f_{nl}}{\alpha} a_{20}^3 = \frac{(1+\frac{p}{\alpha})F_n}{2} e^{i(\omega_1 + \sigma_2 \varepsilon)t} \end{cases} \quad (2.70)$$

where

$$Y = Y_0 e^{(\Omega t)} \quad \text{and} \quad F_n = Y_0 \Omega^2 \quad (2.71)$$

We eliminate the secular terms and substitute Equation (2.68) into Equation (2.70). Therefore, the following system of equations is obtained:

$$\begin{cases} 2i\omega_1 \frac{\partial A_1}{\partial T} + ic\omega_1 A_1 + \omega^2 \beta (2 A_1 - A_2 e^{i\sigma_1 T}) + 3f_{nl} A_1^3 = \frac{(1+p)F_n}{2} e^{i\sigma_2 T} \\ 2i\omega_2 \frac{\partial A_2}{\partial T} + i\frac{c_1}{\alpha} \omega_2 A_2 + \frac{\omega^2 \beta}{\alpha} (2 A_2 - A_1 e^{-i\sigma_1 T}) + 3\frac{f_{nl}}{\alpha} A_2^3 = \frac{(1+\frac{p}{\alpha})F_n}{2} e^{i(\sigma_2 T - \sigma_1 T)} \end{cases} \quad (2.72)$$

The following polar transformation is expressed as following:

$$A_n = \frac{a_n}{2} e^{i\beta_n} \quad (2.73)$$

We substitute (2.73) in (2.72), the following system is obtained:

$$\begin{cases} 2i\omega_1 \left( \frac{\dot{a}_1}{2} + i\dot{\beta}_1 \frac{a_1}{2} \right) + ic\omega_1 \frac{a_1}{2} + \omega^2\beta \left( a_1 - \frac{a_2}{2} e^{i(\sigma_1 T + \beta_2 - \beta_1)} \right) + 3f_{nl} \frac{a_1^3}{8} = \frac{(1+p)F_n}{2} e^{i(\sigma_2 T - \beta_1)} \\ 2i\omega_2 \left( \frac{\dot{a}_2}{2} + i\dot{\beta}_2 \frac{a_2}{2} \right) + i\frac{c_1}{\alpha}\omega_2 \frac{a_2}{2} + \frac{\omega^2\beta}{\alpha} \left( a_2 - \frac{a_1}{2} e^{i(-\sigma_1 T) + \beta_1 - \beta_2} \right) + 3f_{nl} \frac{a_2^3}{8\alpha} = \frac{(1+\frac{p}{\alpha})F_n}{2} e^{i(\sigma_2 T - \sigma_1 T - \beta_2)} \end{cases} \quad (2.74)$$

We introduce the variable change as follows:

$$\gamma_1 = \sigma_1 T + \beta_2 - \beta_1 \quad \text{and} \quad \gamma_2 = \sigma_2 T - \beta_1 \quad (2.75)$$

Their derivation gives:

$$\begin{cases} \dot{\beta}_1 = \sigma_2 - \dot{\gamma}_2 \\ \dot{\beta}_2 = (\dot{\gamma}_1 - \dot{\gamma}_2) + (\sigma_2 - \sigma_1) \end{cases} \quad (2.76)$$

For a steady state solution, the parameters  $\dot{a}_n$  and  $\dot{\gamma}_n$  are set to zero. We differentiate the complex and imaginary equation, hence the following equations are obtained:

$$\begin{cases} \sigma_2 - \frac{\omega^2\beta}{\omega_1} \left( 1 - \frac{a_2}{2a_1} \cos\gamma_1 \right) - 3f_{nl} \frac{a_1^2}{8\omega_1} + \frac{(1+p)F_n}{2\omega_1 a_1} \cos\gamma_2 = 0 \\ -c\frac{a_1}{2} + \omega^2\beta \frac{a_2}{2\omega_1} \sin\gamma_1 + \frac{(1+p)F_n}{2\omega_1} \sin\gamma_2 = 0 \\ \sigma_2 - \sigma_1 - \frac{\omega^2\beta}{\alpha\omega_2} \left( 1 - \frac{a_1}{2a_2} \cos\gamma_1 \right) - 3f_{nl} \frac{a_2^2}{8\alpha\omega_2} = \frac{(1+\frac{p}{\alpha})F_n}{2\omega_2 a_2} \cos(\gamma_2 - \gamma_1) = 0 \\ -c_1 \frac{a_2}{2\alpha} - \omega^2\beta \frac{a_1}{2\alpha\omega_2} \sin\gamma_1 + \frac{(1+\frac{p}{\alpha})F_n}{2\omega_2} \sin(\gamma_2 - \gamma_1) = 0 \end{cases} \quad (2.77)$$

The system of equations 2.77 will be solved in order to calculate the vibration amplitudes, the harvested powers and the energy localization rates in the following sections.

## 2.7 Robustness of energy localization phenomenon and combination of nonlinear dynamics with mode localized phenomenon

### 2.7.1 Robustness of energy localization

Based on Equation 2.34 quantifying the energy localization defined in section 2.4, the optimum energy localization rate is plotted with respect to the variation of the mistuning coefficients in Figure 2.19. It is proved that the energy localization rate in the nonlinear case is more robust towards the input parameters comparing to the linear case. This characteristic is important especially for the experimental results. If the optimum mistuning coefficient is fixed and error measurements occur, the results won't be affected significantly because of the robustness of the optimum. In the case of linear dynamics, a small variation of the maximum energy localization rate changes significantly the magnitude rate.

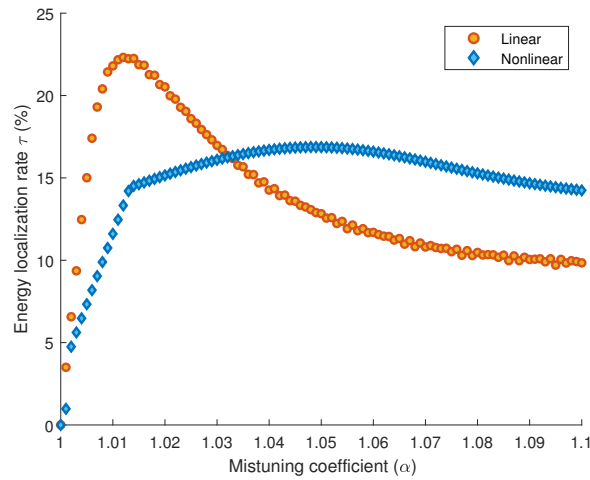


Figure 2.19: Robustness of energy localization rate in the nonlinear configuration: Energy localization rate with variation of the mistuning coefficient in an open-loop circuit

## 2.7.2 Performance comparison of different configurations

In this section, we will discuss 3 different configurations of a 2-DOFs system in order to highlight the importance of energy localization phenomenon. The first configuration consists of a periodic 2-DOFs system (Figure 2.20a). A coil is placed in front of each vibrating magnet. Therefore, the total harvested power  $P$  will be equal to:  $P = P_1 + P_2$  with  $P_1$  and  $P_2$  are the harvested powers from the 1<sup>st</sup> and 2<sup>nd</sup> DOFs oscillators, respectively. The second configuration involves the implementation of a coil for each moving magnet but with mistuning of the 2<sup>nd</sup> magnet mass (Figure 2.20b). In this case, the total power is expressed as follows:  $P = P_1 + P_2$ . As to the third configuration, only one coil is implemented below the perturbed magnet (Figure 2.20c). Therefore, the total power is equivalent to:  $P = P_2$ .

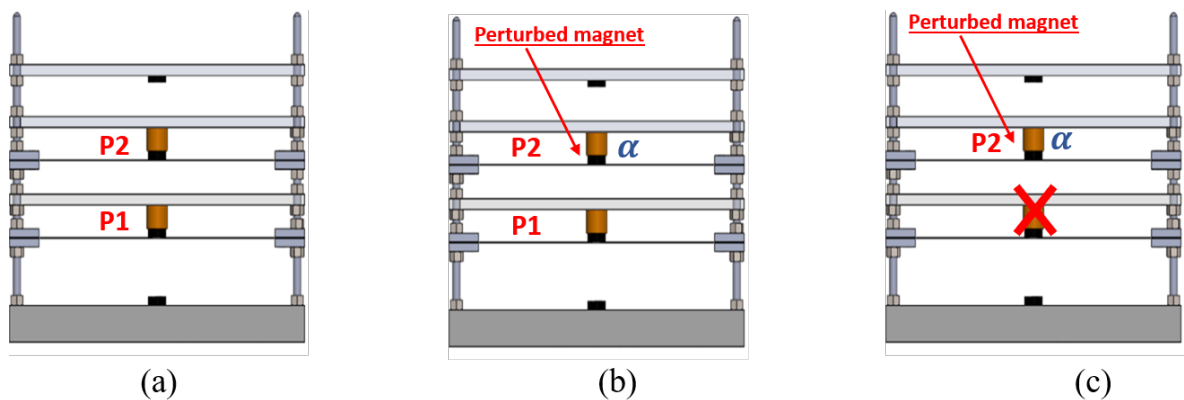


Figure 2.20: Illustration of the 3 studied configurations: (a) Periodic structure, (b) Quasiperiodic structure and harvesting energy from both DOFs oscillators and (c) Quasiperiodic structure and harvesting energy from only perturbed DOF oscillator.

The coupling is fixed to  $\beta = 0.85\%$  and the basis acceleration  $Y_0$  is equal to  $1g$ . In the case the periodic structure, the power with frequency and with varying load resistances are depicted in Figures

2.21a and 2.21b, respectively. From Figure 2.21b, we can capture the optimal load resistance that maximizes the power which is equal to  $R_{load}^* = 6 \Omega$ . We proceed now to determine the optimal mass mistuning coefficient to be injected in the model of configurations 2 and 3. For that, we fix  $R_{load} = 6 \Omega$ , and we plot the maximum obtained amplitudes with varying the mass mistuning coefficient. The results are illustrated in Figure 2.22.

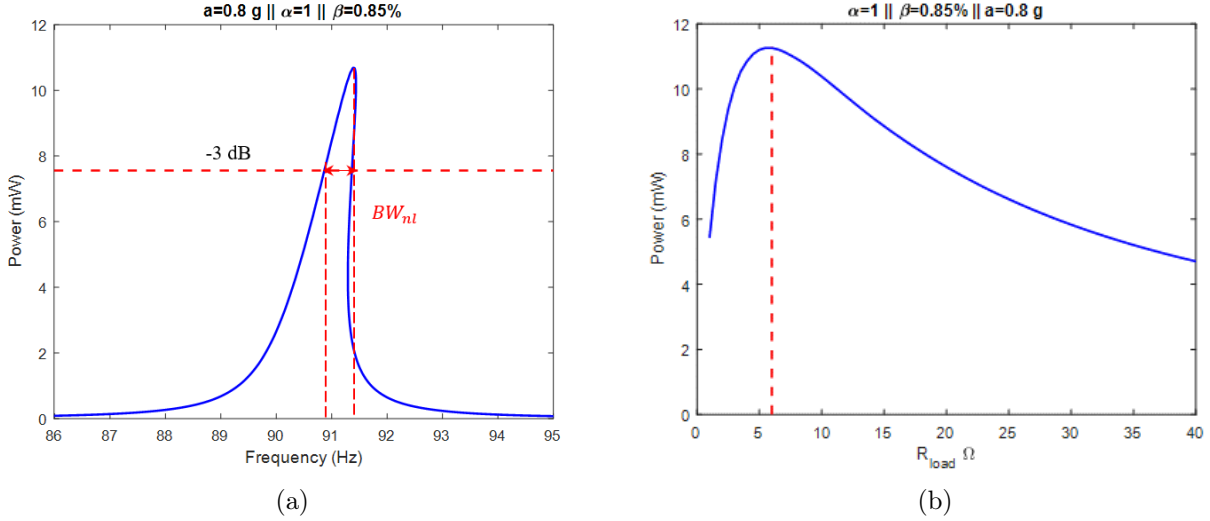


Figure 2.21: (a) Harvested power vs frequency of the periodic 2-DOFs system (b) Total power of the periodic system with load resistances

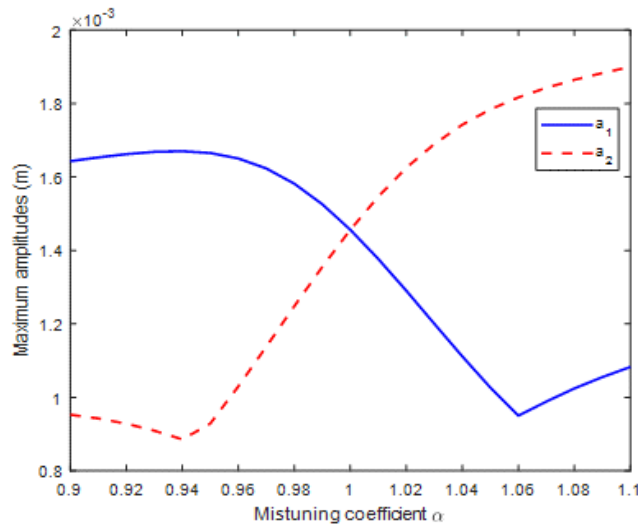


Figure 2.22: Maximum amplitudes in nonlinear case with mass mistuning coefficient: search for the optimal mass mistuning

Based on this figure, the optimal mass mistuning coefficient is equal to  $\alpha^* = 1.06$ . We inject this value in the quasiperiodic model equations and we determine the power and the bandwidth of each configuration. The best configuration in terms of highest bandwidth and power is the configuration 2. Concerning the configuration 3, it provides nearly identical harvested power compared to

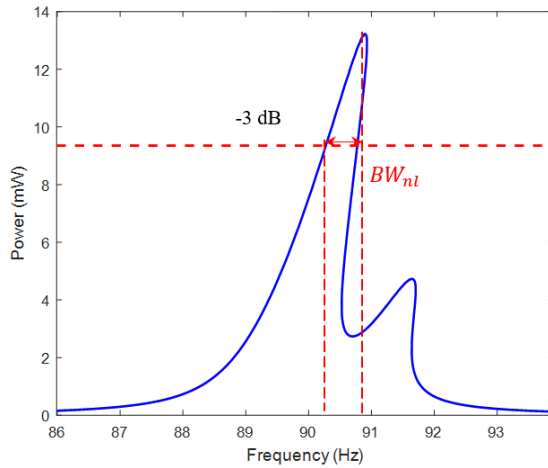


Figure 2.23: Harvested power with frequency of the retained configuration 3.

the configuration 1 (difference of 0.98%). As to the frequency bandwidth, it is enhanced by 13.23% in configuration 3 compared to configuration 1. From this result, we can conclude that it is possible to harvest energy from only one perturbed magnet. Thus, we implement only one electric harvesting circuit instead of two while keeping nearly the same harvested power and the frequency bandwidth is enhanced. Therefore, when considering the cost of electric circuits and technological limits, configuration 3 is the retained one because it reduces the number of electrical circuits which are expensive occupy space and while maintaining the same harvested power and improving the frequency bandwidth compared to the periodic structure illustrated by configuration 1. The results of configuration 3 are illustrated in Figure 2.23. Hence, the fonctionnalization of the localization phenomenon in combination with the nonlinear dynamics proves its benefits in increasing the performance of the suggested device. In fact, it solves the problem of improving the system's harvested power and bandwidth.

### 2.7.3 Experimental validation of the retained configuration

An experimental validation has been done for the maximum amplitudes in order to obtain the mistuning that gives the largest difference between the two amplitudes. The load resistance is fixed to  $R_{load} = 6 \Omega$  based on the numerical obtained optimal load resistance. Since this load resistance is fixed, we drive the system to its nonlinear behavior by imposing the acceleration to  $\ddot{Y}$ . Only one coil is positioned below the chosen magnet to be perturbed. Small masses have been added to the second magnet mass. Up and down sweeps have been performed for each measurement in order to capture the maximum amplitude of the nonlinear response.

The obtained results in terms of voltages are illustrated in Figure 2.24a. We can observe that the maximum of difference between the two voltages amplitudes is obtained when  $\alpha = 1.06$  which is in good agreement with the obtained numerical value. Knowing, now, the optimal mistuning coefficient, we vary the load resistances in order to capture the maximum harvested power. To obtain the power,



the voltages are measured and the power is calculated for each load resistance as follows:

$$P = \frac{\max(V_n)^2}{R_{load}^n} \quad (2.78)$$

where  $V_n$  is the generated voltage of the coil  $n$  when the corresponding load resistance is fixed to  $R_{load}^n$ . The harvested power with load resistances is illustrated in Figure 2.24b. We can see that we have a good agreement between the experimental and the numerical results. We can explain the slight difference between numerical and experimental results by the beams manufacturing defects that affect the measured and calculated mass mistuning coefficients and that the periodicity of the structure. It can be also caused by the potentiometer accuracy while tuning the load resistances the fact that affects both the harvested power and the bandwidth and by non-perfect clamping conditions.

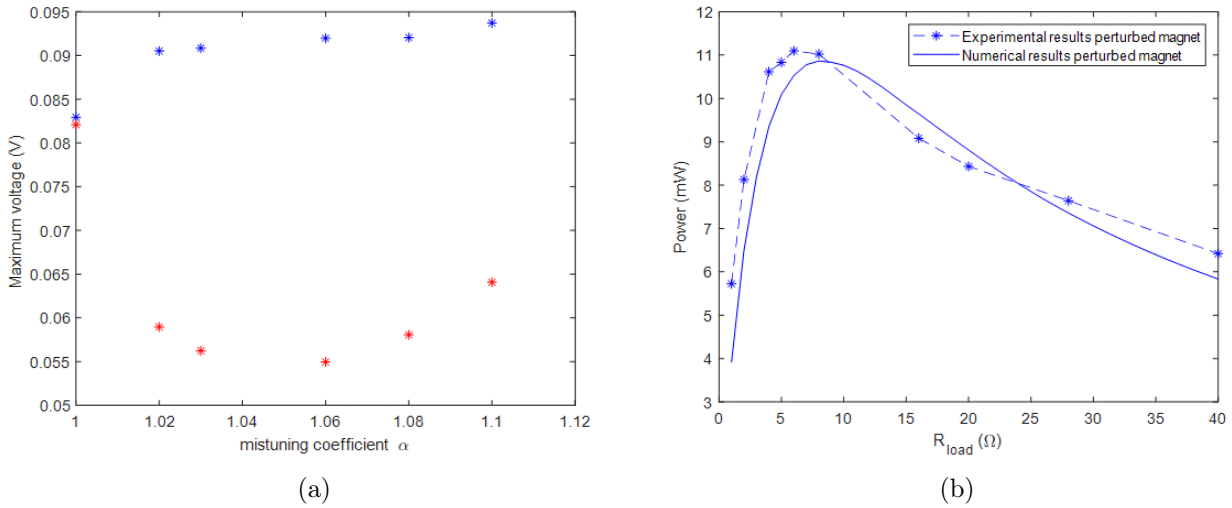


Figure 2.24: (a) Maximum voltage with mass mistuning coefficient (b) Experimental-numerical confrontation of the harvested power with load resistances

## 2.8 Experimental investigation of energy localization and nonlinear dynamics combination

### 2.8.1 Energy localization and harvested power in linear and nonlinear cases

For this study, we fix the acceleration at  $0.6g$  and the coupling at  $\beta = 0.1\%$ . We assume that the magnetic nonlinearity is neglected compared to the mechanical nonlinearity. By solving the system of Equation 2.77 derived from the multiple scales method, energy localization rate and harvested power while varying the mistuning coefficient and the load resistance for the linear and nonlinear cases are illustrated in Figure 2.25. It has been shown that the maximum of energy localization rate in the nonlinear case is slightly minimized compared to the one of the linear case. On the other hand, the maximum harvested powers in the linear and nonlinear cases are nearly the same. The parameters leading to the maximum harvested powers in the two cases lead to nearly identical

mode localization rates. We can conclude that when we introduce nonlinear dynamics, the frequency

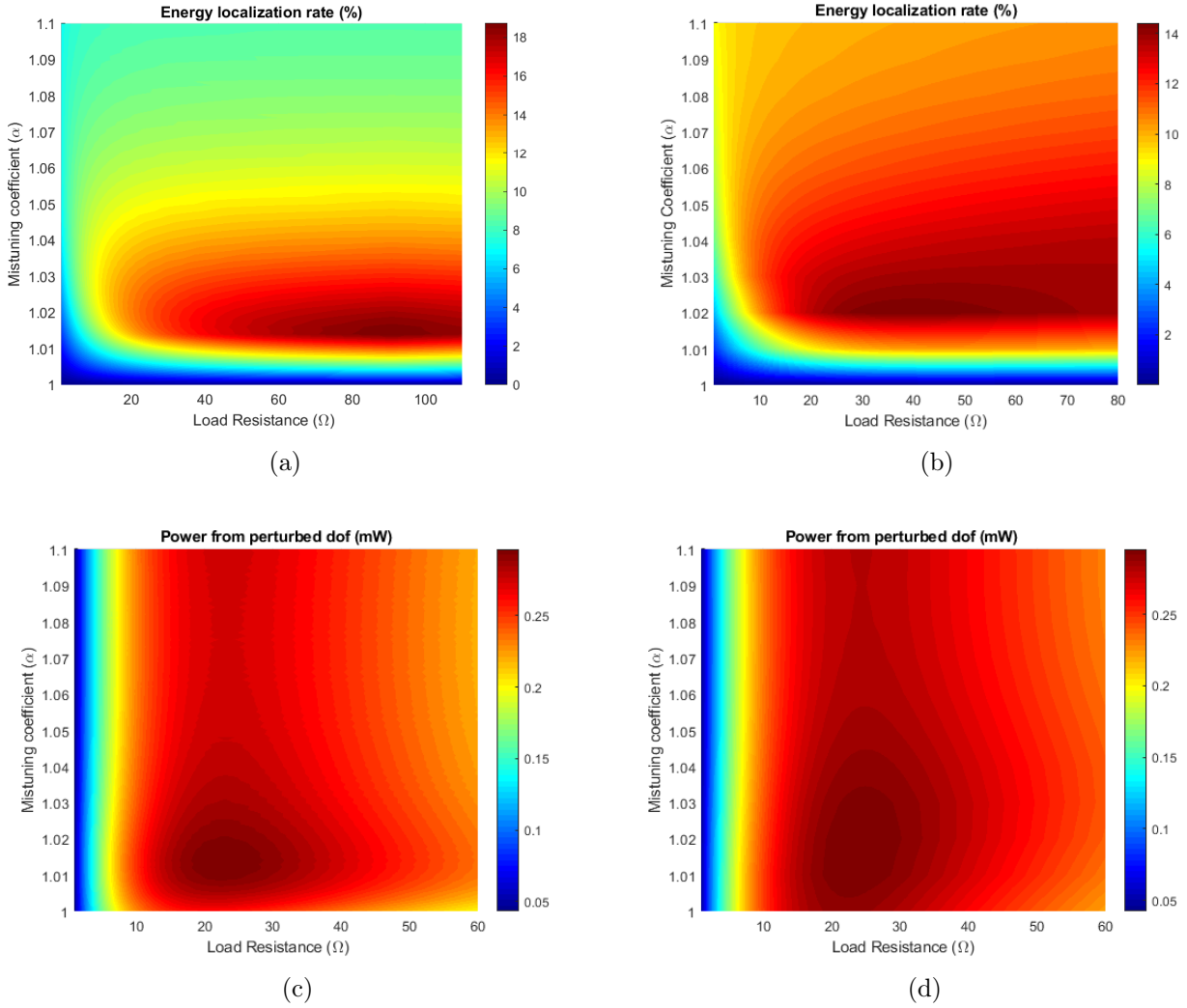


Figure 2.25: Energy localization rate with mass mistuning and load resistance in a) linear and b) nonlinear cases. Harvested power with mass mistuning and load resistance in a) linear and b) nonlinear cases.

bandwidth is improved while keeping nearly the same amount of the harvested energy and the same energy localization rate comparing to the linear configuration. Add to that, nonlinear dynamics offer a robustness of the optimum localization rate in comparison with the one in linear case. These benefits will be validated experimentally in the following section.

## 2.8.2 Experimental optimization of the harvester performance by combining energy localization and nonlinear dynamics

In order to optimize the harvester performance, we will proceed to determine the mistuning coefficient and the load resistance that can enhance simultaneously the harvested power and the frequency bandwidth.

For this study, the coupling is fixed to be weak ( $\beta = 0.1\%$ ). Therefore, we can assume that the closed-form expressions determined in section 2.6.1 remain valid for the case of 2-DOFs. The classical

form of the critical amplitude for a Duffing oscillator with mechanical nonlinearity is given by [119]:  $A_c = 1.687 h_s / \sqrt{Q}$ . Applying this formula, we find that  $A_c = 0.11 \text{ mm}$  which is in good agreement with the obtained experimental results. Based on Equation 2.62 from section 2.6.1, we can identify  $f_{nl} = 1.28 \cdot 10^6 \text{ (m.s)}^{-2}$ .

To make sure that the resonator has a nonlinear behavior, it should be driven beyond its corresponding critical amplitude. Then, in order to tune the nonlinearity level, the system is driven beyond its critical resistance which characterizes the lower bound limit of the harvester critical behavior. The critical resistance will be determined for each mistuning coefficient. In fact, for each mass mistuning value, we variate the resonance till we obtain the critical behavior. The load resistance that changes the behavior from critical to nonlinear is captured and fixed as the critical resistance. This is done for different values of the mass mistuning coefficient as illustrated in Figure 2.26. To guarantee a nonlinear behavior for the harvester, the load resistances should be higher than the maximum obtained critical load resistance  $R_{load}^{min}$  ( $R_{load} > 15 \Omega$ ).

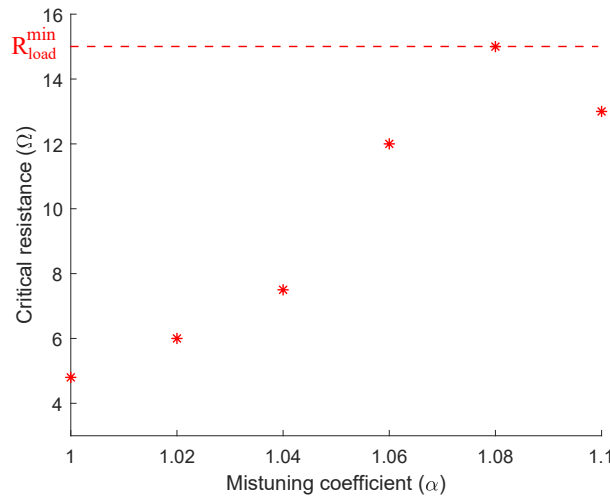


Figure 2.26: Variation of the measured critical resistances with the mistuning coefficients

Fixing the limit of the load resistances, we plot the harvested power and the frequency bandwidth while varying the load resistance and the mass mistuning coefficient. The results are illustrated in Figures 2.27a and 2.27b. Based on Figure 2.27a, we can conclude that the maximum of power is obtained when  $\alpha = 1.06$  and  $R_{load} = 35 \Omega$ . Concerning the frequency bandwidth, its maximum is obtained for  $\alpha = 1.06$  and  $R_{load} = 30 \Omega$  as shown in Figure 2.27b. Although the harvested power and the frequency bandwidth of the proposed harvester are enhanced, their maxima are not obtained at the same parameters values. Then, in order to obtain the optimal configuration that allows enhancing the resonator performance, a simultaneous tune of the mass mistuning and the load resistances should be ensured. Moreover, since it is difficult and delicate to obtain exactly the same parameters, it is more accurate to define an interval of optimal solutions. Therefore, among diverse admissible solutions, the optimal ones that guarantee simultaneous maximization of energy localization and frequency bandwidth are included in the design spaces  $\alpha^* \in [1.04, 1.06]$  and  $R_{load}^* \in [28, 35 \Omega]$ . From the defined

optimal intervals, we chose a couple of optimal parameters ,  $\alpha^* = 1.06$  and  $R_{load}^* = 35 \Omega$ . For these values, the frequency bandwidth and the harvested power are enhanced respectively by 19.4% and 116% comparing to the nonlinear periodic system performance.

A quantitative comparison between experimental and theoretical results is accomplished. The eigenfrequencies calculated theoretically is in good agreement with the one obtained experimentally with an error less than 1%. After injecting  $\alpha^*$  and  $R_{load}^*$  in the model, this latter predicts the harvested power and the frequency bandwidth with errors of 16% and 8%, respectively. This discrepancy is due to the potentiometer precision while tuning the load resistances and to the manufacturing defects of the coils and the beams, the fact that affects both the frequency bandwidth and the harvested power.

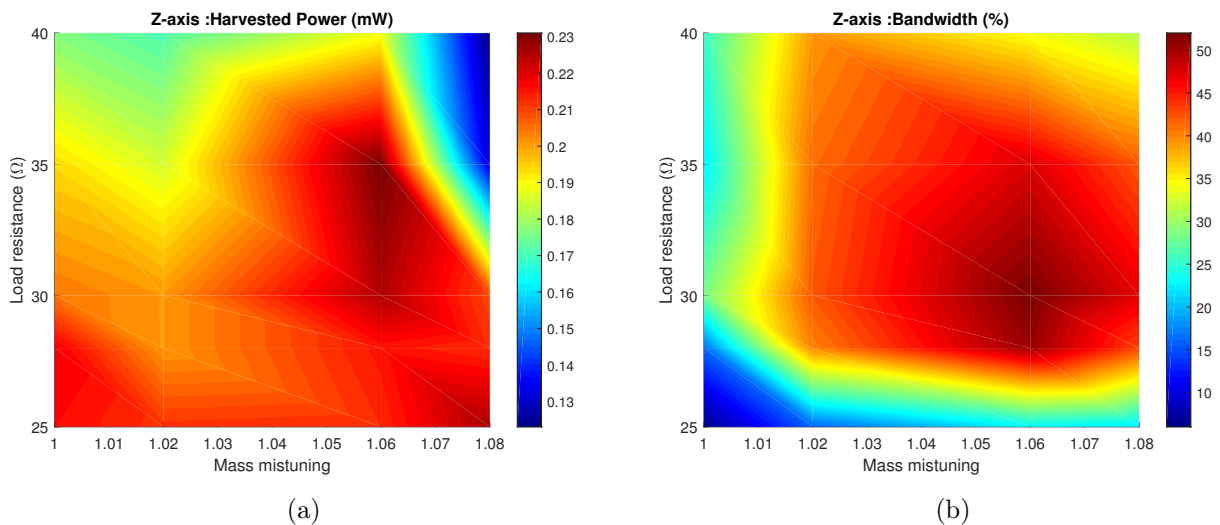


Figure 2.27: (c) Harvested power from the perturbed dof and (d) Frequency bandwidth with load resistances and mass mistuning ( $a_{rms} = 0.09g$ ).

## 2.9 Summary

In this chapter, a theoretical analysis and experimental study for the proposed VEH has been discussed. The mechanical model of the structure has been developed and the experimental setup has been presented. Through the experimental study, the harvester was characterized and the model was validated. To enhance the output performance of the harvested, the combination of nonlinear dynamics and energy localization has been proposed. For that, the energy localization phenomenon has been illustrated and comparison between linear and nonlinear cases has been accomplished. It has been shown that the introduction of nonlinear dynamics allows the robustness of energy localization phenomenon compared to the linear configuration in addition to the enhancement of the frequency bandwidth. It has been also proven that the simultaneous fonctionnalization of nonlinearity and mode localization permits the improvement of the frequency bandwidth and the output harvested power. Indeed, the frequency bandwidth has been improved by 19.4% and the harvested power increased by

116% compared to the nonlinear periodic system. In the next chapter, the actual oscillator will be generalized to 5-DOFs one. A multiobjective optimization procedure will be performed in order to further improve the harvester's output performance.

# Chapter 3

## Multiobjective optimization of a multimodal electromagnetic VEH by functionalization of mode localization and nonlinear dynamics

### Contents

---

<b>3.1</b>	<b>Introduction</b>	<b>80</b>
<b>3.2</b>	<b>Multiobjective optimization</b>	<b>80</b>
3.2.1	General formulation of a multiobjective optimization problem	80
3.2.2	Pareto dominance and optimality concepts	81
3.2.3	NSGA-II algorithm	82
<b>3.3</b>	<b>Mechanical Model</b>	<b>85</b>
3.3.1	Proposed Design	85
3.3.2	Equation of Motion	85
<b>3.4</b>	<b>Multiobjective optimization of the validated two-coupled-beams harvester</b>	<b>86</b>
3.4.1	Numerical-Experimental confrontation of the 2-DOFs harvester	86
3.4.2	Optimization of the validated 2-DOFs model	88
<b>3.5</b>	<b>Multiobjective optimization of the five-coupled-beams model</b>	<b>90</b>
3.5.1	Determination of the introduced mistuning optimal positions	91
3.5.2	Multiobjective optimization of the five-coupled-beams harvester	92
3.5.3	Figure of merit for comparison to the state of art	96
<b>3.6</b>	<b>Summary</b>	<b>97</b>

---

## 3.1 Introduction

IN this chapter, the concept of the 2-DOFs harvester studied in chapter 2 is generalized to a 5-DOFs one. This generic model based on electromagnetic transduction investigates nonlinear dynamics and energy localization tuning. In order to enhance the output performance of the proposed harvester, a multiobjective optimization procedure is adopted. A general introduction of this method will be discussed in the first section mentioning the principle of NSGA-II algorithm that we will be used. The 2-DOFs harvester is optimized using this procedure to improve its output performance. Concerning the 5-DOFs harvester, two DOFs oscillators are perturbed among 5. A multiobjective optimization is, also, conducted to determine the optimal position of the introduced mistuning and then to derive the optimal output performance in terms of harvested power and frequency bandwidth. To prove the importance of multimodal configuration, the quasiperiodic 2-DOFs harvester is compared to the 5-DOFs one.

## 3.2 Multiobjective optimization

The optimization procedure is another tool that we can use to enhance the performance of the energy harvesters. In this section, a general introduction of the multiobjective problems formulation and the most used algorithms will be discussed.

### 3.2.1 General formulation of a multiobjective optimization problem

The multiobjective optimization consists of searching for the values of the variables that maximize or minimize one or more objective functions [121]. It may be used, for example, to minimize a cost of production, streamline the use of resources, improve the energy performance of an industrial process, etc. Thus, it proceeds with the prior definition of the quality criteria of the problem solution, then the optimization algorithm will solve the problem by seeking the best solutions according to these criteria. Therefore, the formulation of the optimization problem includes the following steps:

- Express criteria or functions 'objective' of optimality
- Choose optimization parameters (or variables)
- Define an eligible space for optimization variables
- Define associated constraints (imperative or indicative)

A multiobjective optimization problem can be formulated, in general, according to the following equations:

$$\left\{ \begin{array}{ll} \text{Minimize (or maximize) } f_i(X_i) & i = 1, 2, \dots, m \\ \text{Constraints} & \\ g_j(X) \geq 0 & j = 1, 2, \dots, q \\ h_k(X) = 0 & k = 1, 2, \dots, p \end{array} \right.$$

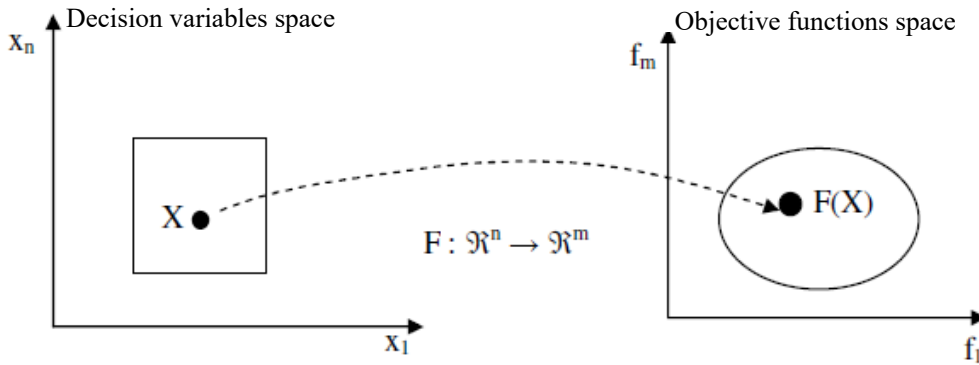


Figure 3.1: Multiobjective problem representation [122]

where  $m$  is the objective functions number and  $X = [x_1, x_2, \dots, x_n]$  is a vector of  $n$  decision variables.  $g_j(X)$  and  $h_k(X)$  are respectively constraints of inequalities and equalities.

The objective functions of the optimization problem form a multidimensional space called the objective functions space, in addition to the decision variables space. The diagram of Figure 3.1 illustrates the two spaces where, for each solution  $X = [x_1, x_2, \dots, x_n]$  in the space of the variables of decision, there is a point in the objective functions space such that  $F(X) = (f_1(X), f_2(X), \dots, f_m(X))$ .

The search for the optimal solution for a multiobjective optimization problem raises some thoughts about the notion of optimality. Indeed, it is impossible to find a single optimal solution for a multiobjective problem, because there is no combination of the decision variables that minimizes (or maximizes) all the components of the vector  $F$  simultaneously. Multiobjective problems usually have a set of optimal solutions whose values of functions are in fact the best possible compromises in the space of objective functions. It is therefore necessary to use another definition of the "best solution", in order to determine exactly which solution can be considered better compared to another. The concept of "Pareto optimality" is thus used to establish a hierarchy between the solutions of a multiobjective problem in order to determine whether a solution really belongs to the set of best compromises [123–125].

### 3.2.2 Pareto dominance and optimality concepts

To better understand the concept of 'Pareto optimality', let's first introduce the notion of 'Pareto dominance'. Let be two vectors  $U$  and  $V$  in the space of objective functions where a minimization problem is considered. We say that the vector  $U = (u_1, u_2, \dots, u_m)$  dominates the vector  $V = (v_1, v_2, \dots, v_m)$ , if and only if all the components of  $U$  are less than or equal to the corresponding ones in  $V$ , and at least one component of  $U$  is strictly less than the corresponding one in  $V$ . The principle of dominance is illustrated in Figure 3.2. A solution  $X$  to a multiobjective problem is said to be 'Pareto optimal' with respect to the entire space of decision variables if and only if there is no other solution  $X'$  such as the function  $F(X')$  dominates  $F(X)$ . The set of optimal solutions is called the 'optimal Pareto set', and the set of values of the corresponding objective functions in the space of the objective functions is called the 'Pareto front'. Depending on the problems to be treated, the Pareto front can have a very



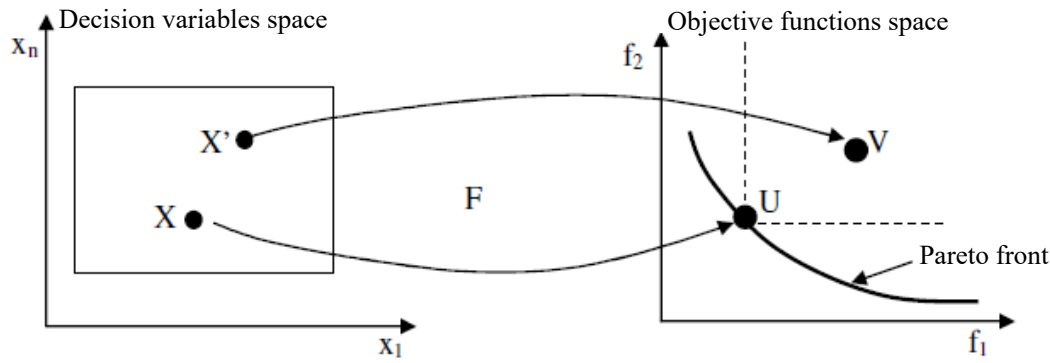


Figure 3.2: Pareto dominance and optimality [122]

complex configuration (e.g., continuity, discontinuity, convexity, disjunction etc.).

In most multiobjective optimization algorithms, the notion of dominance is used to compare two solutions. A solution is dominant if both of the following conditions are satisfied [126]:

- The solution is not good compared to other solutions in all objectives
- The solution is the best compared to the other solutions in at least one of the objectives

Solving a multiobjective optimization problem can therefore prove to be long and tedious if the appropriate methods are not implemented. In an industrial environment where optimization problems are very complex (e.g., multiple objectives, several variables and constraints, non-linearities), the search time for optimal solutions also becomes an important factor to take into account. This is how several methods are generally used to solve these types of problems, by seeking, failing to find the global optimum, to get as close as possible to the latter, by making a compromise with the computation time.

### 3.2.3 NSGA-II algorithm

#### Generalities

Inspired by the biological mechanism of natural selection and the survival of individuals best suited to the environment [127], Holland [128] laid the foundations for the optimization technique called Genetic Algorithms (GA) . But, it was Goldberg [129] who subsequently got involved in the study of GA and developed the current one. GA is the most used algorithm in optimization problems. Over the years, this technique has been developed. Among the first evolutionary algorithms of multi-objective optimization, we find the genetic algorithm with vector evaluation (VEGA) presented in 1985 by [130]. This method is easy to implement, but its major drawback is that it tends to generate the best solutions for one goal, without considering the other goals. Since the appearance of the VEGA algorithm, a considerable number of genetic algorithms for multi-objective optimization have been developed such as NSGA-II algorithms. Among various optimization algorithms, the Non-dominated Sorting Genetic Algorithm (NSGA) is mostly used because it can be adapted to generate the optimal solution for multiobjective optimization problems [131, 132]. It is an evolutionary multiobjective algorithm that

uses a type of measure of crowding around each individual in order to ensure the diversity of the population. It is based on the selective principle and on the explicit diversity of conservation tools. This algorithm is able to solve a problem of multiple objective functions simultaneously. The NSGA has had relatively good success in several work and application areas. NSGA-II, developed by Deb et al. [131], is an improved version of the NSGA and NSGA-I. It is developed to overcome the limitations of the typical NSGA algorithm which has some disadvantages namely the calculation complexity, the selection absence and the need to specify the distribution parameter. This algorithm reduces the complexity of the ancient one. The NSGA-II is considered to be the best and most efficient of its predecessors, as it does not require any parameter adjustment. It also uses a sorting method based on the principle of non-dominance which is faster.

To explain briefly its algorithm, we consider that we have a population  $R_t$  constituted by the union between  $P_t$  and  $Q_t$  as follows  $R_t = P_t \cup Q_t$  where  $P_t$  is the parents population of size  $N$  and  $Q_t$  is the ascendants population generated from parents through crossbreeding and mutation operators. The size of  $R_t$  is  $2N$ . This population is, then, classified into different non-dominance fronts ( $F_1, F_2, \dots, F_n$ ), using the concept of Pareto dominance as illustrated in Figure 3.3.

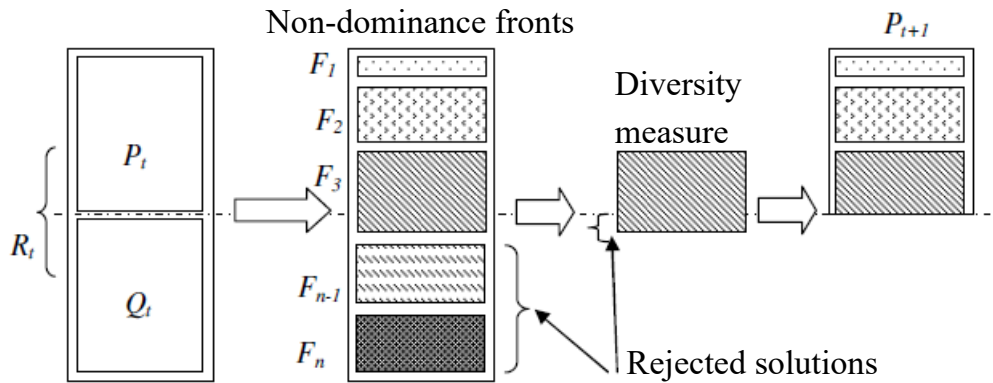


Figure 3.3: Principle of NSGA-II algorithm [122].

Individuals on the first front are obviously better than individuals on the second front. The latter in turn are better than the individuals of the third front and so on. The focus is then on the best individuals and therefore in this case on the individuals on the first front, who are then kept in an archive. If the number of individuals of this front is less than the fixed size  $N$ , then all the individuals of this front will be part of the next population  $P_{i+1}$ . To complete the size of the population  $P_{i+1}$  to  $N$ , the new members must be chosen from the remaining fronts, according to their rank. So the members of the second front  $F_2$  are chosen, then the members of  $F_3$  and so on until you get a new population of size  $N$ . If all the members of a front cannot enter the population without exceeding the size  $N$ , then the members of this front are classified according to a measure of diversity which determines the population around each individual taken separately. According to this classification, the most isolated individuals are admitted to the list of  $P_{i+1}$  until the size of the latter is completed. Individuals who cannot join the population are simply rejected.

### NSGA-II Algorithm Pseudo-code

After detailing the theoretical principle of the NSGA algorithm, we present the outline of the NSGA-II algorithm. We note  $<_n$ , called crowded-comparaison , an operator which makes it possible to identify the best between two solutions. In the NSGA-II approach, each solution has a rank and the one with the smallest will be preferred. For two solutions that are part of the same Pareto frontier, we choose the one that is located in the region of low density.

Table 3.1: Algorithm NSGA-II

---

<b>Algorithm NSGA-II</b>
thickline 1. For each iteration $t$ do
2. $R_t = P_t \cup Q_t$ (Combine the two populations)
3. F= Fast-non-dominated-sort ( $R_t$ ) (Calculation of the non dominated of $R_t$ )
4. $P_t = \emptyset, i = 1$
5. <b>While</b> $ P_t  +  F_i  \leq N$ (As long as the population is not full ) <b>do</b>
6. $t = t + 1$
7. $P_{t+1} = P_{t+1} \cup F_i$ (Include the $i$ non dominated front in $P_{t+1}$ )
8. Crowding-distance-assignment ( $F_i$ )
9. Sort out ( $F_i <_n$ ) (Sort out in ascendant using the comparison operator $<_n$ )
10. $P_{t+1} = P_{t+1} \cup F_i [1 : (N -  P_{t+1} )]$ (Choose of the $N -  P_{t+1} $ )
11. Best-distributed front individuals
12. Generate a new ascendant population ( $Q_{t+1}$ ) by selection, crossing and mutation
13. $t = t + 1$ (Increment the generation counter)
14. <b>Fin NSGA-II</b>

---

This algorithm is designed using an elitist approach allowing only the best individuals (solutions) to be retained over the generations. Several comparative studies have shown the superiority of the NSGA-II algorithm over other used algorithms such us the Multi-Objective Genetic Algorithm (MOGA) [133] and Niche-Pareto Genetic Algorithm NPGA algorithms [134].

### NSGA-II to optimize energy harvesters

In the field of energy harvesting, different researches have used the multiobjective optimization to enhance the output performance of the harvester. Foong et al. [135], as an example, performed an optimization procedure to optimize the structural aspect of the proposed electromagnetic energy harvester under a set of constraints and with the objective of maximizing the output harvested power. Also, Abed et al. [87] developed nonlinear oscillator arrays under magnetic levitation and performed an optimization procedure to enhance the frequency bandwidth and the harvested power using the NSGA-II algorithm. In the following, we will use the NSGA-II algorithm to optimize the output performance of the proposed VEH.

### 3.3 Mechanical Model

#### 3.3.1 Proposed Design

The suggested vibration energy harvester is depicted in Figure 3.4. It is based on the same principle of the 2-DOFs device studied in chapter 2 but generalized in this chapter to a 5-DOFs one. It is made up of  $N$  neodymium moving magnets that are guided by steel beams. These magnets are weakly coupled by repulsive magnetic forces. The moved ones are positioned between two fixed magnets in the top and bottom of the structure. The coupling between them can be tuned by changing the distance between each two adjacent magnets. This can be ensured thanks to the position variation done by changing the beams placement which are inserted into threaded rods. The moving magnets are enveloped in wire-wound copper coils. Each moving magnet oscillates around its equilibrium position when the device is subjected to a harmonic base excitation  $\ddot{Y} = Y_0 \cos(\omega t)$ , where  $Y_0$  is the imposed acceleration amplitude and  $\omega$  is the excitation frequency. As a result of Lorentz' law, a current is induced in each coil. The displacement of the magnets is quantified by  $v_n$  ( $n = 0, \dots, N + 1$ ). Since, the two magnets at the array's ends are assumed to be fixed,  $v_0 = v_{N+1} = 0$ . By mistuning a few magnet masses, the structure's periodicity is broken. Thus, the structure is considered as a multimodal quasiperiodic one.

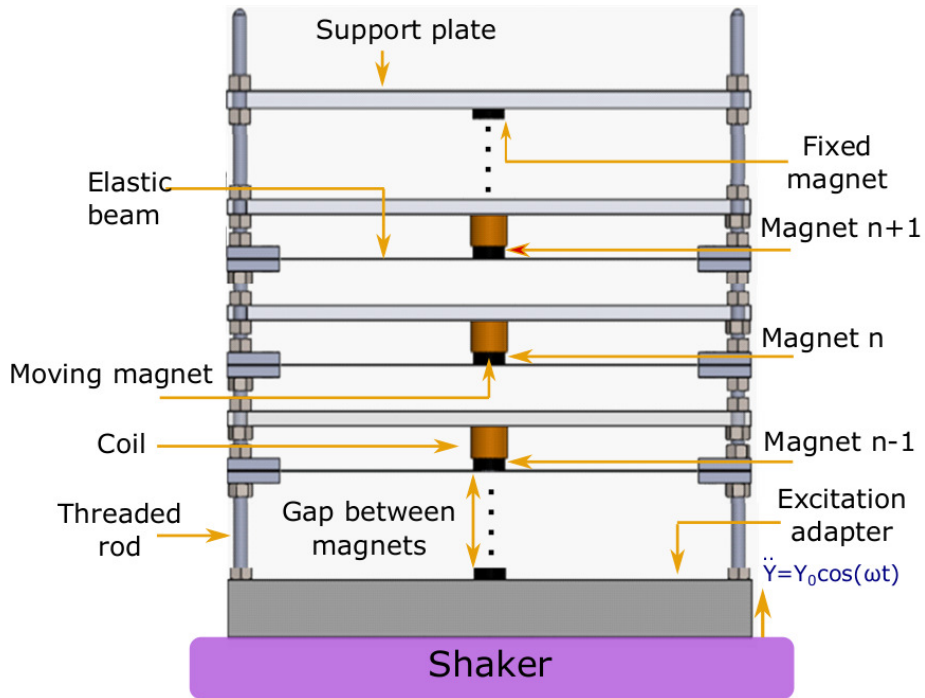


Figure 3.4: Device of the  $N$  coupled magnets electromagnetic vibration energy harvester

#### 3.3.2 Equation of Motion

The continuous multiphysics problem is transformed into a system of discrete ordinary differential equations in the time domain using the Galerkin modal decomposition as detailed in chapter 2. Based on the obtained equations in section 2.2.2, the  $n^{th}$  DOF multiphysics equations of motion is expressed

as follows in terms of generalized coordinates:

$$\begin{cases} \ddot{a}_n + c\dot{a}_n + \omega_0^2 [(1 + 2\beta)a_n - \beta(a_{n-1} + a_{n+1})] + f_{nl}a_n^3 = -(1 + p)\dot{Y} \\ i_n(t_1) = \frac{\delta d}{(R_{load} + R_{int})T} \dot{a}_n, \quad n = 1..N \end{cases} \quad (3.1)$$

Comparing the mechanical nonlinear term to the magnetic nonlinear one, we find that  $k_{mg}^{NL}/k_{mec}^{NL} = 0.28\%$ . We assume that the magnetic nonlinear term is neglected in the case of a weak coupling between the two beams.  $p$  is a mass ratio, and  $\omega_0$  stands for the eigenfrequency of the decoupled 1-DOF oscillator.

We note that  $Y_1$ ,  $t_1$ ,  $M_{eq}$ ,  $c_{eq}$ ,  $k_{mg}^L$ ,  $k_{mec}^L$  and  $k_{mec}^{NL}$  are detailed in Equation 2.28. We introduce the mass mistuning coefficient  $\alpha_n$  into the equations. As a result, the  $n^{th}$  magnet's equation of motion may be expressed as follows:

$$\ddot{a}_n + c\dot{a}_n + \frac{\omega_0^2}{\alpha_n} [(1 + 2\beta)a_n - \beta(a_{n+1} + a_{n-1})] + \frac{f_n}{\alpha_n} a_n^3 = (1 + \frac{p}{\alpha_n})\ddot{Y}_1 \quad (3.2)$$

where

$$\begin{cases} \alpha_n \neq 1 & \text{for the mistuned DOF } n \\ \alpha_n = 1 & \text{for the non-mistuned DOF } n \end{cases} \quad \text{with } n = 1, \dots, N.$$

Since we considered that we have two extra fixed magnets added to the array's top and bottom ends, we have:  $a_0 = a_{N+1} = 0$ .

## 3.4 Multiobjective optimization of the validated two-coupled-beams harvester

### 3.4.1 Numerical-Experimental confrontation of the 2-DOFs harvester

To improve the performance of a periodic weakly coupled electromagnetic VEH device, a concept combining the benefits of geometric nonlinearities and energy localization is presented. We have studied, in a previous work [136], the impacts on the frequency bandwidth as well as the harvested power. As was presented in the last chapter, we have proven that energy may be harvested from one perturbed magnet instead of two, and only one electric circuit can be used. The maximum harvested energies are equivalent and the bandwidth is increased when compared to the results of the periodic structure. As shown in chapter 2, the manufacture and experimental characterization of the proposed device under harmonic excitation were studied. The critical resistances were varied to adjust the nonlinearity level, and mass mistuning was used to regulate the energy localization. The experimental tuning of these phenomena has been validated, allowing the improve of the VEH performance in terms of frequency bandwidth and harvested energy, and the compromise solution that optimizes the

major objectives concurrently has been experimentally found. Furthermore, it has been demonstrated that nonlinear dynamics provide a more robust energy localization than linear dynamics. Despite the significant improvement in the 2-DOFs device's performance, a total multiobjective optimization is required to further optimize the generic harvester. First, a 2-DOF system is investigated. Only the oscillations of the second perturbed magnet are used to generate power. As a result, the harvested power is represented as follows:

$$P_2 = R_{load}^2 \left( \frac{\omega_0 \delta}{R_{load} + R_{int}} \right)^2 A_{2max}^2 \quad (3.3)$$

The maximum amplitude of the frequency response of the second perturbed DOF oscillator, the transduction circuit load resistance, the coil internal resistance, and the electromagnetic coefficient are represented, respectively, by  $A_{2max}$ ,  $R_{load}$ ,  $R_{int}$  and  $\delta$ .

The 2-DOFs model system of equations where the mass of the 2<sup>nd</sup> DOF oscillator is mistuned is generated based on Equation 3.2. The ode45 method is used to solve it. The harvested power and amplitudes are determined. All numerical simulations are run with an  $Y_{rms} = 1g$  basis acceleration, a gap  $d = 50mm$  and a coupling coefficient  $\beta = 0.11\%$ . Figure 3.5 shows the kinetic energy based on the criteria specified in Equation 2.35 as a function of the mass mistuning value.

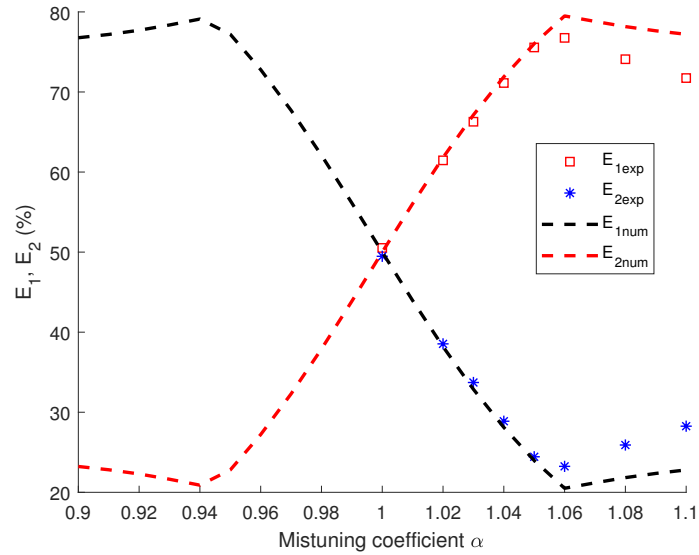


Figure 3.5: The first and second DOFs' numerical and experimental energies vs mass mistuning coefficient ( $a_{rms} = 1g$ ,  $R_{load} = 6\Omega$ ).

When  $\alpha = 1.06$ , the largest difference in the kinetic energies is obtained, as seen in Figure 3.5. Several tests were carried out to validate the numerical results using the test bench described in chapter 2. To do that, the magnets masses are perturbed by adding small masses to them. Up and down frequency sweeps for all the experimental tests were performed in order to properly measure the voltage peak. This allows the identification of the bifurcation points of the nonlinear frequency response. In addition, while varying the mass mistuning coefficients, the amplitudes and masses of the 2-DOFs oscillator are

obtained. Therefore, the associated kinetic energies are calculated using Equation 2.35 and displayed in Figure 3.5. The optimal mass mistuning, as indicated, is  $\alpha = 1.06$ , which is in good agreement with the numerical calculations.

Based on Equation 3.3, the harvested power with load resistances is numerically calculated at the optimal mistuning value of  $\alpha = 1.06$  (Equation 3.3). The current flowing through each load resistance  $R_{load}$  throughout the experimental testing produces an electric power calculated as  $P = max(V)^2/R_{load}$ , where  $V$  is the voltage created by the coil. For both experimental and analytical studies, the optimal load resistance  $R_{load}^*$  that delivers the highest power  $P_{max}$  is  $6 \Omega$ , as shown in Figure 3.6.

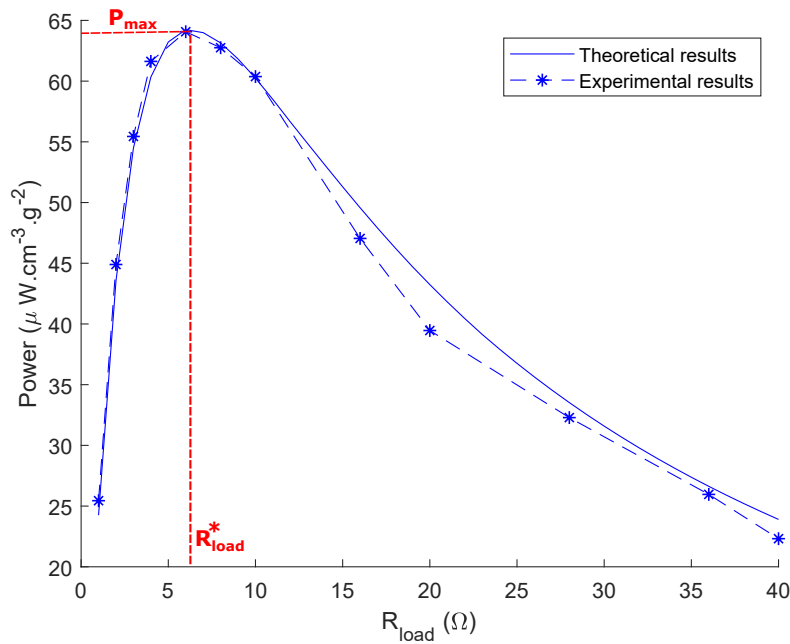


Figure 3.6: (a) The first and second DOFs' numerical and experimental energies vs mass mistuning coefficient ( $a_{rms} = 1g$ ,  $R_{load} = 6 \Omega$ ). (b) The harvested power from the perturbed magnet with variation of load resistance ( $a_{rms} = 1g$ ,  $\alpha = 1.06$ )

It is possible to do a quantitative comparison between theoretical and numerical results. The ideal mass mistuning and optimal load resistance are, in fact, very close to the experimental values ( $Error < 1\%$ ). With an error less than 1%, the model predicts the values of the maximum harvested powers.

### 3.4.2 Optimization of the validated 2-DOFs model

During simulations, it was possible to obtain a maximum power but a minimum bandwidth. While tuning nonlinearity and mode localization enhanced the harvester's performance in terms of harvested power and frequency bandwidth, a multiobjective optimization is required to further optimize the harvester and find its optimum parameters. This method has been used in different fields where optimum decisions must be made in presence of trade-offs between several objectives.

To do that, the Non-dominated Sorting Genetic Algorithm II (NSGA-II) [137] is used. This algorithm

is an extension of the Genetic Algorithm (GA) [138] for multiple objectives. NSGA-II is related to evolutionary multiobjective algorithms which seeks to improve a population's adaptive fit to a Pareto front made up of a set of compromise solutions between the objective functions. The problem's formulation is defined in Table 3.2.

Table 3.2: The optimization model for the 2-DOFs harvester: objective function and constraints

Maximize: $(P, BW)=f(\alpha, \beta, R_{load})$
Constraints
$1 \leq \alpha \leq 1.1$
$0 < \beta \leq 3\%$
$R_c < R_{load}$

where  $R_c$  is the critical load resistance used to tune the nonlinearity level. Obtained from experiments, it is equivalent to  $15\Omega$ . To guarantee the nonlinear behavior of the harvester, the load resistances used in the following optimization procedure should be higher than  $R_c$ .

MATLAB's ode45 tool was used to generate the frequency responses of all the candidate solutions. The bandwidth and average harvested power are determined assuming that the bifurcation point of the nonlinear response curves corresponds with the maximum value of the frequency response.

The following Pareto front, shown in Figure 3.7, is generated after running the multiobjective algorithm appropriate for this configuration.

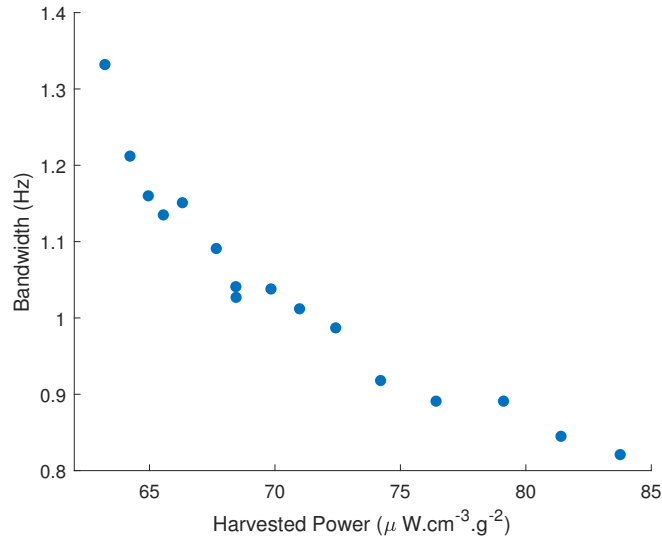


Figure 3.7: The 2-DOFs system Pareto front: illustration of Frequency bandwidth with harvested power

The compromise solution for the current situation is the one that optimizes the two objective functions at the same time. As a result, Table 3.4 lists the chosen Pareto solution and its corresponding parameters.

The corresponding optimal parameters,  $\alpha^*, \beta^*$  and  $R_{load}^*$  are reproduced in the experimental tests in order to compare between the numerical and experimental results. Figure 3.8 shows the result of



Table 3.3: The multiobjective optimization results of the 2-DOFs harvester

<p><b>Compromise solution</b>  <math>(P^*, BW^*) = (69.84 \mu W.cm^{-3}.g^{-2}, 1.038Hz)</math>                  With  <math>\alpha^* = 1.03</math>  <math>\beta^* = 1.5\%</math>  <math>R_{load}^* = 20 \Omega</math></p>
--

the measurements. The frequency response is obtained by doing up and down frequency sweeps in order to capture the bifurcation point where the solution goes from stable to non-stable branches. The bandwidth is calculated based on the half-power method where the maximum amplitude is considered to be the one that corresponds to the bifurcation point.

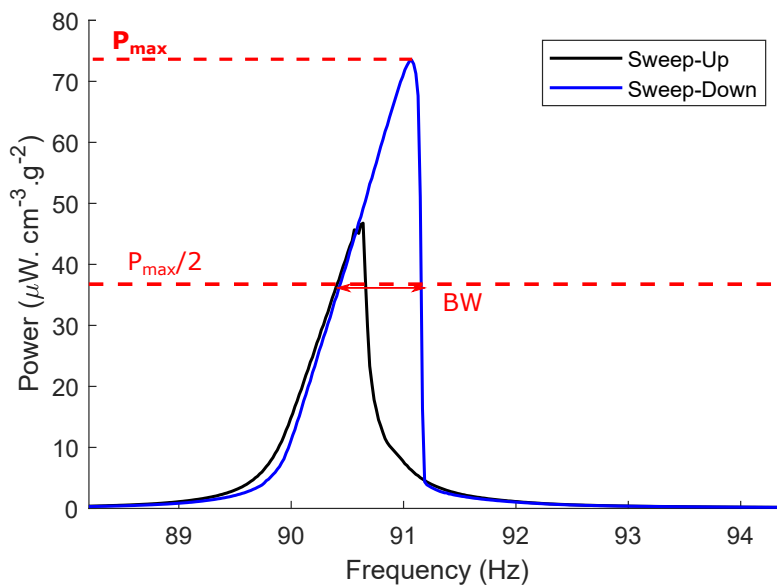


Figure 3.8: Experimental validation of the 2-DOFs model optimal configuration in terms of average harvested power and the corresponding frequency bandwidth BW

We compare the maximum obtained power from experiments with the one resulting from the optimization procedure. We obtain an error between experimental and numerical results of 5% and 0.5% in terms of the obtained maximum harvested power and frequency bandwidth, respectively. As a consequence, we may conclude that the optimized model agrees well with the experimental results.

### 3.5 Multiobjective optimization of the five-coupled-beams model

Since a proof-of-concept of the 2-DOFs structure was developed, modeled, manufactured, and characterized, exhibiting better power and bandwidth performance, the 2-DOFs model is expanded to a quasi-periodic 5-DOFs one.

### 3.5.1 Determination of the introduced mistuning optimal positions

The generalized periodic 5-DOFs system's governing equations are as follows:

$$\left\{ \begin{array}{l} \ddot{a}_1 + c\dot{a}_1 + \omega_0^2[(1 + 2\beta)a_1 - \beta a_2] + f_{nl}a_1^3 = (1 + p)\ddot{Y} \quad (1) \\ \ddot{a}_2 + c\dot{a}_2 + \omega_0^2[(1 + 2\beta)a_2 - \beta(a_3 + a_1)] + f_{nl}a_2^3 = (1 + p)\ddot{Y} \quad (2) \\ \ddot{a}_3 + c\dot{a}_3 + \omega_0^2[(1 + 2\beta)a_3 - \beta(a_2 + a_4)] + f_{nl}a_3^3 = (1 + p)\ddot{Y} \quad (3) \\ \ddot{a}_4 + c\dot{a}_4 + \omega_0^2[(1 + 2\beta)a_4 - \beta(a_3 + a_5)] + f_{nl}a_4^3 = (1 + p)\ddot{Y} \quad (4) \\ \ddot{a}_5 + c\dot{a}_5 + \omega_0^2[(1 + 2\beta)a_5 - \beta a_4] + f_{nl}a_5^3 = (1 + p)\ddot{Y} \quad (5) \end{array} \right. \quad (3.4)$$

Based on the benefits of the combination of nonlinearity and energy localization and the characterization of the previous configuration, for the 5-DOFs system, the masses of two moving among 5 are mistuned. To each perturbed magnet mass, a mass mistuning coefficient and a corresponding load resistance will be assigned. We choose to keep the same gap between the magnets. The positions of the two mistuned DOF oscillators can be combined in the following possibilities: (1,2), (1,3), (1,4), (1,5), (2,3), (2,4) and (2,5), where (1) stands for the DOF (1) as shown in Equation 3.4. The position of the two DOFs that will be perturbed will be decided in accordance with the configuration that offers the highest harvested power, as described in Table 3.4.

Table 3.4: Objective function and constraints to obtain the optimal position of the introduced two mistunings

<b>Objective function</b>
Maximize: $P = f(\alpha_1, \alpha_2, \beta, R_{load}^1, R_{load}^2)$
Constraints
$1 \leq \alpha_1, \alpha_2 \leq 1.1$
$0 < \beta \leq 3\%$
$R_c < R_{load}^1, R_{load}^2 \leq 40$

A continuous optimization procedure incorporating discrete variables is used in order to accomplish this objective [139]. The mistuning coefficients of the two perturbed oscillators  $\alpha_1$  and  $\alpha_2$  represent the set of discrete variables. The possible combinations that we can have from the positions of the perturbed DOFs are treated. Each combination of discrete variables triggers a continuous optimization process, which is implemented in MATLAB according to steps illustrated in the diagram of Figure 3.9.

Those discrete variables represent the position and value of the mistuning at the same time throughout the continuous optimization. For this reason, they are treated as discrete in the beginning and then as continuous. During the simulations, the possibility of having a combination of two successive perturbed magnets is eliminated and not treated. This choice is made in order to have dispersed perturbations over the network, allowing more efficient energy localisation.

Several numerical simulations have been performed based on the explained strategy. The optimal configuration's mass mistuning position and maximum harvested power are returned by the optimization output. It has been proven that the system with perturbation of the 2<sup>nd</sup> and the 4<sup>th</sup> DOFs, illustrated

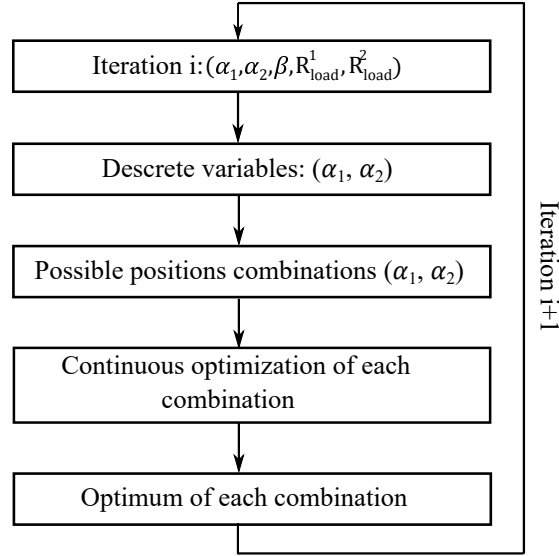


Figure 3.9: Diagram of continuous optimization with discrete variables steps

by its equivalent model in Figure 3.10, provides the highest harvested power. Consequently, the harvested power will be calculated using this expression:  $P = P_2 + P_4$ , where  $P_2$  and  $P_4$  stands for the harvested power from the DOFs 2 and 4, respectively.

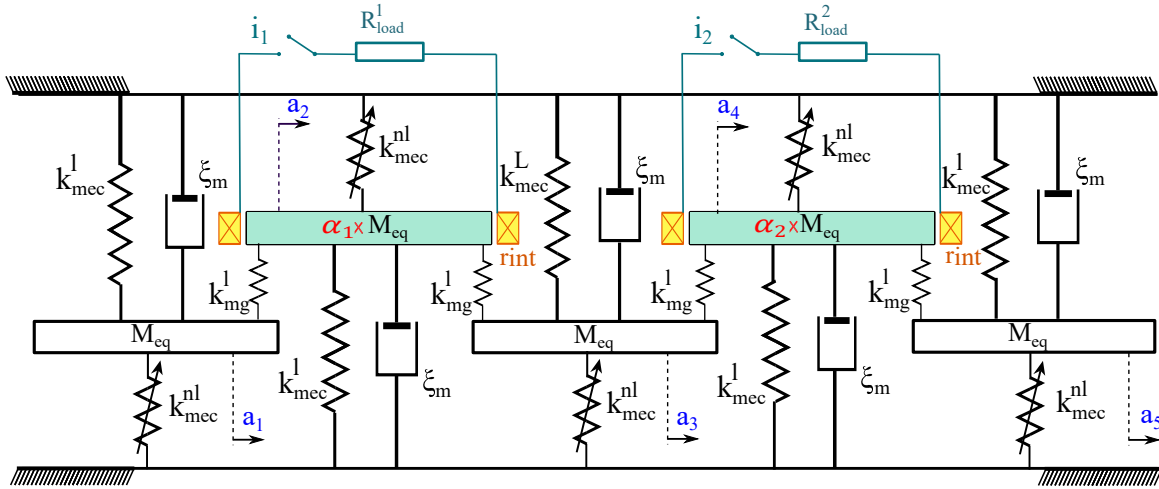


Figure 3.10: The equivalent model of the 5-DOFs vibration energy harvester with mistuning of the 2<sup>nd</sup> and 4<sup>th</sup> DOFs masses

### 3.5.2 Multiobjective optimization of the five-coupled-beams harvester

A multiobjective optimization based on the genetic algorithm is carried out to improve simultaneously the harvested power and the frequency bandwidth of the 5-DOFs harvester with two introduced mistuning. The Pareto front of the mistuned magnets' kinetic energies is displayed, as shown in Figure 3.11, in order to observe their trending variations. It is shown that the kinetic energy of the two perturbed DOFs differ from one solution to the next. To increase harvester performance, the perturbed DOFs' kinetic energies should be maximized so that their total is maximized in the following. Conse-

quently, to take advantages from the vibrations of both mistuned DOFs, they must vibrate in similar proportions and so have close energies. To do that, during the optimization procedure, the energy rates of the mistuned DOFs are adjusted and controlled. This restriction is considered as an extra subjective preference information that may be used to select the optimal solution for the harvester and will be added as a constraint in the multiobjective procedure formulation.

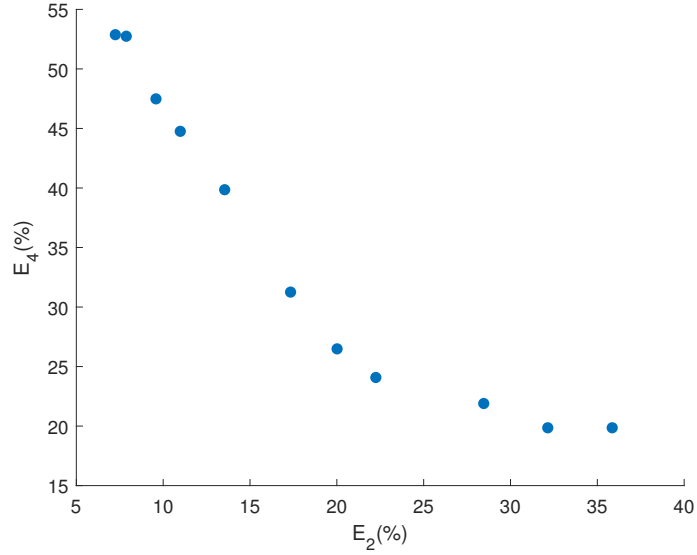


Figure 3.11:  $E_2$  versus  $E_4$ : Pareto front of the 5-DOFs model.

To accomplish this, the energy localization rate between the 2<sup>nd</sup> and the 4<sup>th</sup> DOFs is defined as follows:

$$\tau_{24}(\%) = E_2 + E_4 \quad (3.5)$$

Therefore, the multiobjective optimization problem is defined as follows in Table 3.5.

Table 3.5: The optimization problem formulation for the 5-DOFs harvester: objective function and constraints

<p><b>Objective function</b>  Maximize: <math>(P, BW, \tau_{24}) = f(\alpha_1, \alpha_2, \beta, R_{load}^1, R_{load}^2)</math>  Constraints  <math>1 \leq \alpha_1, \alpha_2 \leq 1.1</math>  <math>0 &lt; \beta \leq 3\%</math>  <math>R_c &lt; R_{load}^1, R_{load}^2 \leq 40</math></p>
--

Figure 3.12 depicts the Pareto optimum multiobjective optimization solutions, whereas Figure 3.13 shows its two-dimensional projection with precision of the sum and the difference of the 2<sup>nd</sup> and 4<sup>th</sup> DOFs kinetic energies for each point result. In this concept, the solution that minimizes the difference between  $E_2$  and  $E_4$  is used as the selection criterion.

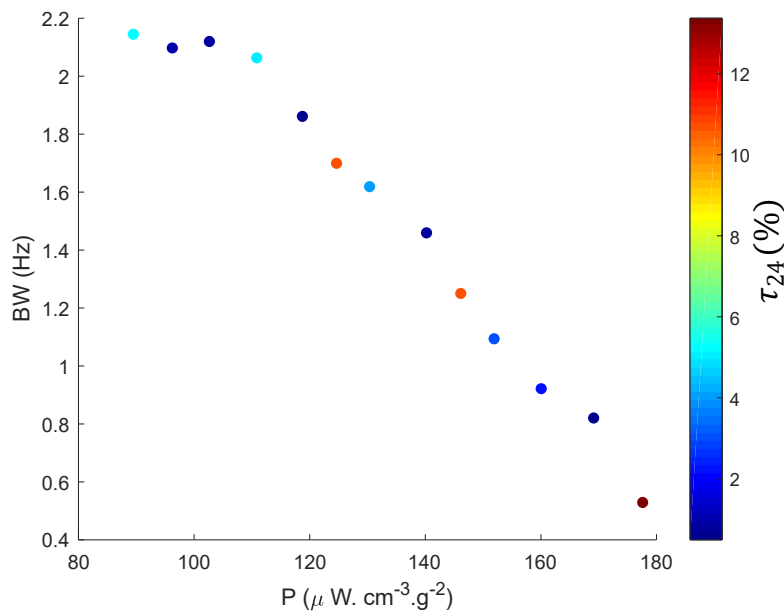


Figure 3.12: The 5-DOFs system’s Pareto front: illustration of the frequency bandwidth with harvested power and the % of corresponding energy localization rates.

To accomplish so, the difference between  $E_2$  and  $E_4$  for each solution of the compromise interval is calculated and shown in 'red' in Figure 3.13. As a result, taking into account this extra subjective preference constraint to the formulation of our optimization, the compromised solution that simultaneously maximizes the harvested power and the frequency bandwidth and ensures vibration of the considered beams in close proportions is reported in Table 3.6.

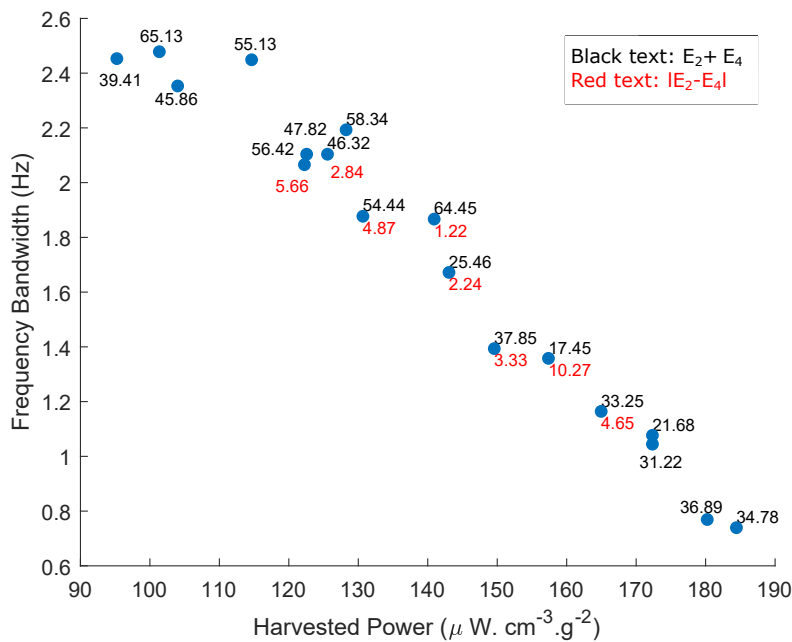


Figure 3.13: The Pareto front 2-D projection of Figure 3.12 with precision of the sum and the difference of the optimal solutions corresponding energy rates of the 2<sup>nd</sup> and 4<sup>th</sup> DOFs oscillators

Table 3.6: The harvester's 5-DOFs optimization results

<b>Compromise solution</b>
$(P^*, BW^*, \tau_{24}^*) = (140.923 \mu W.cm^{-3}.g^{-2}, 1.87Hz, 64.45)$
With
$\alpha_1^* = 1.03$
$\alpha_2^* = 1.045$
$\beta^* = 2.4 \%$
$R_{load}^{1,*} = 28.5 \Omega$
$R_{load}^{2,*} = 26 \Omega$

After including these obtained optimal values into the model, the corresponding frequency response in terms of harvested power is calculated and plotted as depicted in Figure 3.14.

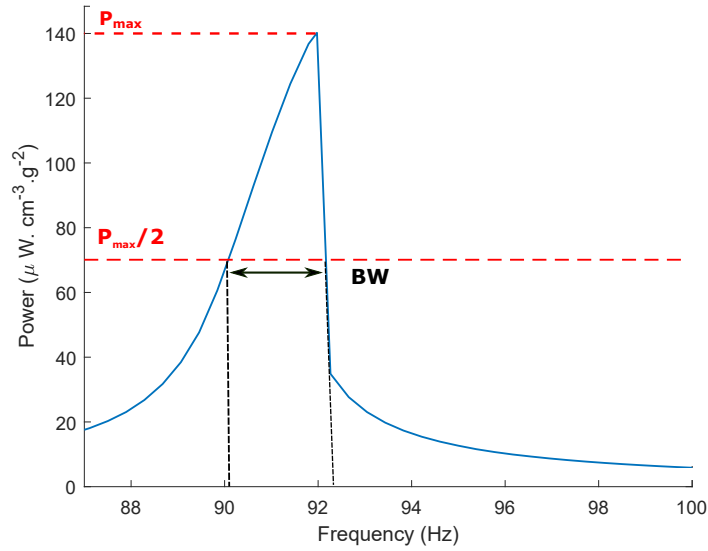


Figure 3.14: Harvested power amount and frequency bandwidth of the optimal configuration with reproducing the obtained optimal values in experimental tests.

In comparison to the performances of the 2-DOFs nonlinear system with only one perturbed DOF, the simultaneous functionalization of the nonlinear dynamics, the energy localization phenomenon, and the multimodal configuration for an optimized 5-DOFs system shows an improvement of 101 % of the harvested power and 79 % of the frequency bandwidth. Also, the performance of the optimized quasiperiodic 5-DOFs system is compared to that of the 5-DOFs periodic system. In this latter case, all of the vibrating 5-DOF oscillators are used to generate electricity. Consequently, the power is harvested from the 5 vibrating oscillators ( $P = \sum_{n=1}^5 P_n$ ). Following the same strategy applied for the optimization of the 5-DOFs quasiperiodic system, Pareto front of the 5-DOFs periodic system determined on the aim to maximize the harvested power and the frequency bandwidth is displayed in Figure 3.15. The optimal parameters for the periodic 5-DOFs system that maximize simultaneously both harvested power and frequency bandwidth are  $\beta = 1.1 \%$ ,  $R_{load} = 22 \Omega$ . In comparison to the periodic 5-DOFs system, the presented results demonstrate that the proposed quasiperiodic model

provides a larger bandwidth while keeping comparable harvested power. In actual fact, the difference in terms of harvested powers between the two configurations is 6.15 %, while the frequency bandwidth of the optimized quasiperiodic system is higher by 18 %.

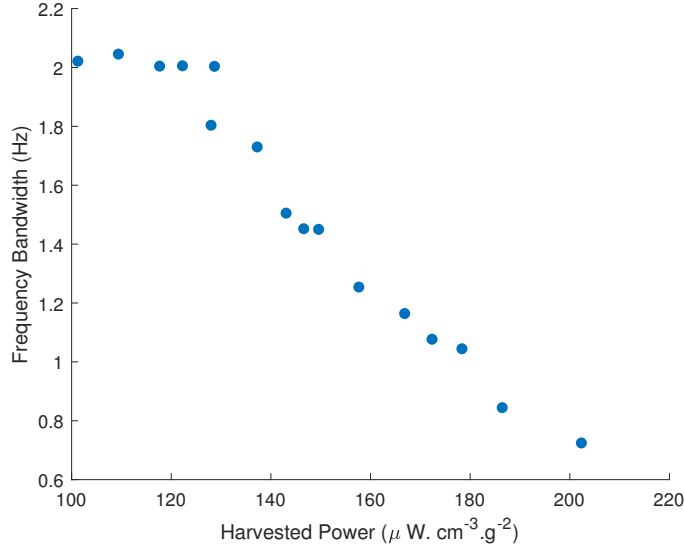


Figure 3.15: The periodic 5-DOFs system’s Pareto front resulting from the multiobjective optimization

Based on these results, we can conclude that the functionalization of nonlinearity and mode localization in a multimodal device overcomes the problem of increasing harvested energy and frequency bandwidth. Furthermore, by combining these phenomena, energy may be harvested from only two DOF oscillators instead of five, while maintaining equivalent performance. This characteristic has the advantage of lowering the cost and number of the electrical circuits to be implemented (2 instead of 5) as well as the structure’s technological restrictions.

### 3.5.3 Figure of merit for comparison to the state of art

In order to compare the optimized suggested harvester performance to the present state of the art, the volume figure of merit ( $FoM_v$ ) proposed by Mitcheson et al. [140] was chosen as the most generic criteria among many performance metrics in the literature. It is noted that this volume figure of merit is defined by the ratio of the harvester’s useful output power that is transferred to the load to the maximum theoretical one flowing into an equivalent structure represents. This equivalent device should have the same cubic geometry as the original device of the harvester, but having a proof mass with the density of gold  $\rho_{Au}$  filling half of the volume, while the other half is devoted to oscillation [140]. Accordingly, the following expression is used to calculate this figure of merit:

$$FoM_v(\%) = \frac{\text{useful power}}{\frac{1}{16} Y_0 \rho_{Au} Vol^{\frac{4}{3}} \omega_0^3} \quad (3.6)$$

where  $Y_0$  denotes the imposed acceleration amplitude,  $\omega_0$  is the resonant frequency,  $\rho_{Au}$  stands for the gold density, and Vol is the harvester volume.

According to this figure of merit, Figure 3.16 depicts the present work harvester's performance, as well as that of other harvesters. As can be shown, the optimized proposed 5-DOFs harvester present competitive output performance compared to other harvesters based on electromagnetic transduction as well as harvesters based on hybrid piezoelectric-electromagnetic transduction.

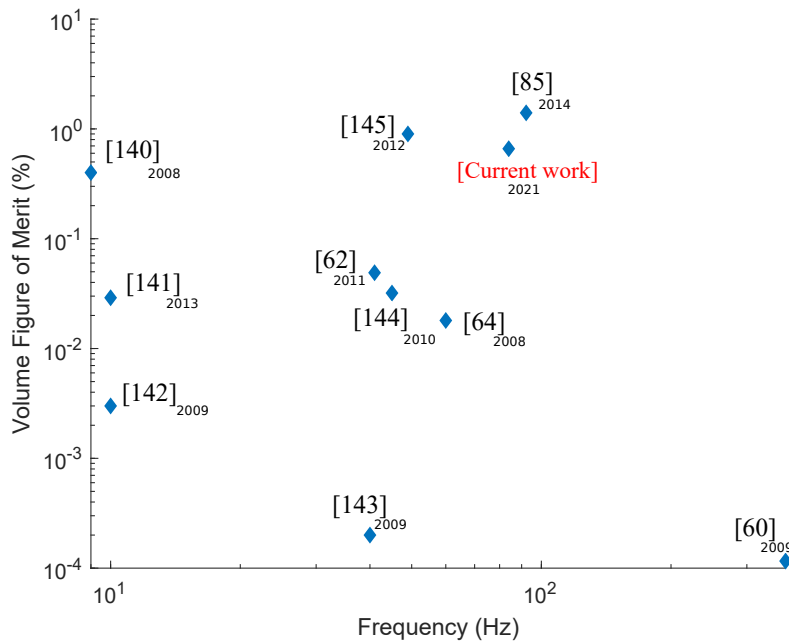


Figure 3.16: Comparison of the optimized current harvester with to some standards from state-of-art using the  $FoM_v$  criteria [60, 62, 64, 85, 141–146]

### 3.6 Summary

This chapter investigates the optimization of a general model of a nonlinear quasiperiodic VEH based on electromagnetic transduction. Firstly, the VEH with 2-DOFs with functionalization of nonlinear dynamics and mode localization is experimentally validated Afterwards, the validated 2-DOFs device is optimized applying a multiobjective optimization procedure with the aim of the simultaneous maximization of the harvested power and the frequency bandwidth. Subsequently, the concept is expanded to a 5-DOF structure, and the optimal results are obtained by applying a multiobjective optimization technique. It has been demonstrated that the obtained optimal parameters derived from the multiobjective procedure allow improving the quasiperiodic 5-DOFs device performance. In fact, this procedure allows increasement in harvested power and frequency bandwidth up to 101 % and 79 %, respectively in comparison to the 2-DOFs harvester. Furthermore, it has been proved that by comparing the performance of a quasiperiodic 5-DOFs system with well-chosen mistuning positions to a 5-DOFs periodic one, the functionalization of nonlinearity and energy localization provides more efficient frequency bandwidth while maintaining comparable harvested powers. As a result, this improvement in performance



results also in the harvester improvement by reducing the number (2 instead of 5) and the manufacture cost of the transduction circuits to be implemented and also by reducing the technological constraints of the device. Additionally, when compared to the existing state-of-the-art of harvesters with different transduction techniques, the improved harvester provides competitive performance. Finally, despite the fact that the generic VEH performances are optimized, additional transduction technique will be added and an other method will be applied in order to further enhance the output performance of our proposed VEH. Future work will include piezoelectric transduction in addition to the electromagnetic one with functionalization of the nonlinear internal resonance phenomenon.

# Chapter 4

## 2:1 Internal resonance for a hybrid electromagnetic-piezoelectric vibration energy harvester

### Contents

---

- 4.1 Introduction . . . . . 100**
- 4.2 Hybrid electromagnetic-piezoelectric vibration energy harvester . . . . . 100**
  - 4.2.1 Design of the proposed device . . . . . 100
  - 4.2.2 Modeling of the piezoelectric harvester . . . . . 101
  - 4.2.3 Amplitude and power expressions . . . . . 106
  - 4.2.4 Theoretical results and experimental validation . . . . . 106
- 4.3 2:1 Internal resonance . . . . . 108**
  - 4.3.1 Proposed device . . . . . 108
  - 4.3.2 Mechanical model to obtain commensurate natural frequencies . . . . . 109
  - 4.3.3 Results . . . . . 110
- 4.4 Energy storage . . . . . 113**
  - 4.4.1 Literature review on storage circuits and devices . . . . . 113
  - 4.4.2 Energy storage test . . . . . 116
- 4.5 Summary . . . . . 119**

---

## 4.1 Introduction

IN this chapter, we will adopt other techniques in order to further enhance the harvester output performance. In fact, a new transduction technique is added to the previous electromagnetic one. We propose to explore the piezoelectric transduction. Therefore, the system is being based on hybrid electromagnetic-piezoelectric transduction techniques. This is achieved by bonding two piezoelectric layers to each elastic beam. The hybrid configuration is proposed in order to enhance the output harvested power. Furthermore, the phenomenon of internal resonance will be investigated in order to further enhance the output power and to improve the frequency bandwidth. In this context, the corresponding numerical model of the 2-DOFs hybrid structure will be developed and the experimental tests will be performed. Storage test using a capacitor will be achieved with the establishment of charging and discharging cycles.

## 4.2 Hybrid electromagnetic-piezoelectric vibration energy harvester

Piezoelectric technology is widely used thanks to its simplicity in design and its ability to provide higher power densities. In this part, we maintain the same configuration of the proposed electromagnetic harvester described in 2.2.1 and we add two piezoelectric patches to the elastic beams. Each piezoelectric layer will be linked to the beam near to its clamped end. To study the dynamic response of the system, one determines the equation of the vibrations using the principle of Euler-Lagrange and calculates the natural frequencies of the structure and its associated modes.

### 4.2.1 Design of the proposed device

Based on the same structure, two piezoelectric layers are attached to each beam near to their clamped ends. The representation of the hybrid configuration is illustrated in Figure 4.1 including a schematic and a real beam illustrations. A two-dimensional (2D) representation of the hybrid 2-DOFs structure based on the 2D illustration of the electromagnetic harvester is depicted in Figure 4.2.

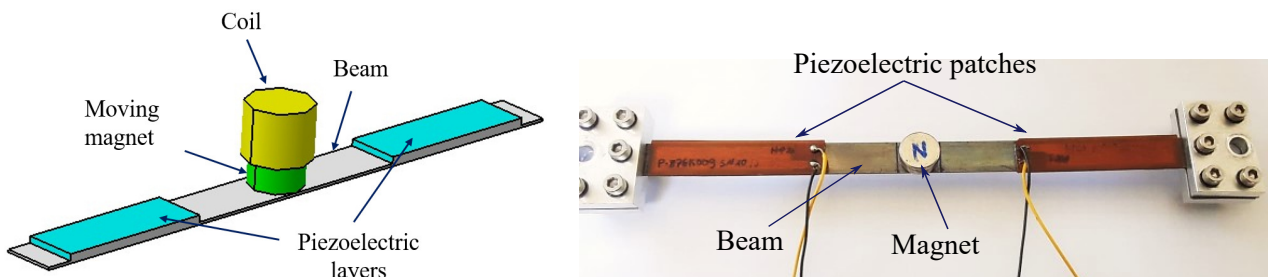


Figure 4.1: Schematic and real representations of the electromagnetic-piezoelectric energy harvester

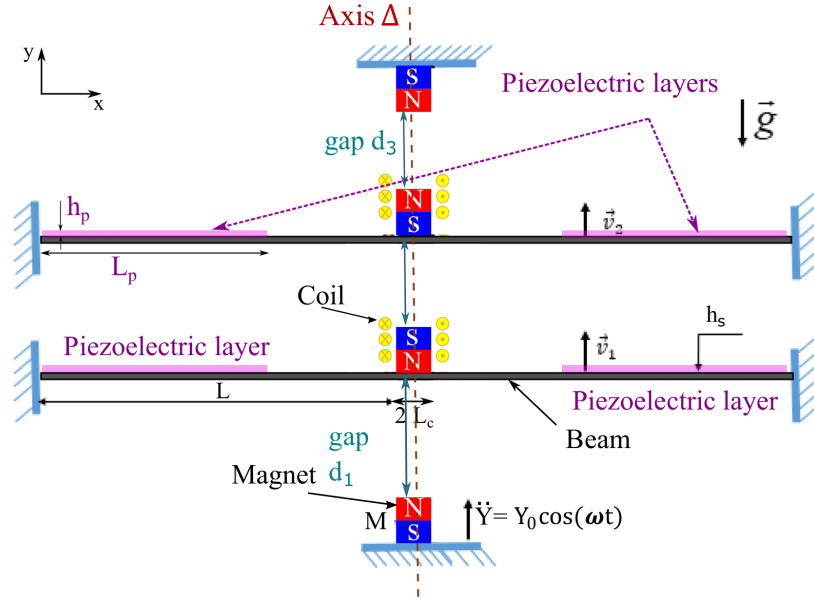


Figure 4.2: 2D illustration of the 2-DOFs hybrid structure

In order to avoid confusion with the steel beam geometric parameters used in the last sections when establishing piezoelectric equations in the following paragraph, we define  $L_p$  is the length of the piezoelectric layer,  $b_p$  is the piezoelectric layer,  $h_p$  is the thickness of piezoelectric.

As mentioned in [chapter 1](#), piezoelectric transducers are based on the property of the electrical polarization of piezoelectric material under the action of a mechanical stress. For this case, the direct effect of piezoelectric materials will be investigated. The exploration of this technique aids in the enhancement of the system's total harvested electrical power. The design characteristics of the piezoelectric layers are depicted in [Table 4.1](#).

Table 4.1: Design parameters of the piezoelectric patches

Parameter	Designation	Value	Unity
$e_{31}$	Piezoelectric coupling coefficient	-13.87	$C.m^{-2}$
$\epsilon$	Piezoelectric permittivity	$1500 \epsilon_0$	$F.m^{-1}$
$\epsilon_0$	Vacuum permittivity	$8.854.10^{-12}$	$F.m^{-1}$
$\rho_p$	Piezoelectric density	7500	$Kg.m^{-3}$
$\nu_p$	Piezoelectric poisson ratio	0.31	
$L_p$	Piezoelectric layer length	49	$mm$
$b_p$	Piezoelectric layer width	11	$mm$
$E_p$	Piezoelectric layer Young Modulus	69.7	$GPa$
$h_p$	Thickness of the piezoelectric layer	0.16	$mm$

## 4.2.2 Modeling of the piezoelectric harvester

The beam is composed of two parts. A part with steel and piezoelectric layer and a part af only steel. Therefore, we will develop the equations for the beam sections  $[0, L_p]$  and  $[L_p, L]$ . The kinetic and

potential energies of the  $n^{th}$  bimorph beam of length  $L_p$  is defined as:

$$T_n^1 = \frac{1}{2} (\rho_s S_s + \rho_p S_p) \int_0^{L_p} \dot{v}_p^2 dx \quad (4.1)$$

Where  $S_p$  is the section of the piezoelectric layer and  $v_p$  is the displacement at the piezoelectric-steel part .

The potential energy is expressed as:

$$Ep_n^1 = \frac{E_s S_s + E_p S_p}{8 L_p} \left[ \int_0^{L_p} v'_{p,n}{}^2 dx \right]^2 + \frac{E_s I_s + E_p I_p}{2} \int_0^{L_p} v''_{p,n}{}^2 dx - b e_{31} (h_p + h_s) V_n(t) \int_0^{L_p} v''_{p,n} dx \quad (4.2)$$

For the steel beam of length  $[L - L_p]$ , we have the following expressions. The kinetic energy is defined as:

$$T_n^2 = \frac{1}{2} \rho_s S_s \int_{L_p}^L \dot{v}_{s,n}^2 dx \quad (4.3)$$

Where  $v_s$  is the displacement at the steel part of the beam.

The kinetic energy of the mass  $M_n$  for  $x = L$  is defined as:

$$T_n^3 = \frac{1}{2} M_n \dot{v}_{s,n}^2 \quad (4.4)$$

The kinetic energy is defined as:

$$Ep_n^2 = \frac{E_s S_s}{8 (L - L_p)} \left[ \int_{L_p}^L v'_{s,n}{}^2 dx \right]^2 + \frac{E_s I_s}{2} \int_{L_p}^L v''_{s,n}{}^2 dx \quad (4.5)$$

And, the potential energy of the magnetic stiffness is defined as following for  $x = L$ :

$$Ep_n^3 = \frac{1}{2} k_{mg}^L v_{s,n}^2 + \frac{1}{4} k_{mg}^{NL} v_{s,n}^3 \quad (4.6)$$

The total kinetic energy  $T_n$  of the substructure  $n$  is then equivalent to:

$$T_n = T_n^1 + T_n^2 + T_n^3 \quad (4.7)$$

And, the total potential energy  $Ep_n$  of a substructure  $n$  is expressed as follows:

$$Ep_n = Ep_n^1 + Ep_n^2 + Ep_n^3 \quad (4.8)$$

The Lagrangian of the system is defined as follows:

$$\mathcal{L} = \sum_{i=1}^3 T_n^i - Ep_n^i \quad (4.9)$$

The transverse displacements can be written as a function of the imposed displacement  $Y$  and of the relative displacements  $v_{pr,n}$  and  $v_{sr,n}$  of the piezoelectric and steel layers respectively as follows:

$$v_{p,n} = v_{pr,n} + Y \qquad v_{s,n} = v_{sr,n} + Y$$

We obtain then:

$$\begin{aligned} \mathcal{L} = & \frac{1}{2} (\rho_s S_s + 2\rho_p S_p) \int_0^{L_p} (v_{pr,n} + Y)^2 dx + \frac{1}{2} \rho_s S_s \int_{L_p}^L (v_{sr,n} + Y)^2 dx + \frac{1}{2} M (\dot{v}_{sr,n} + \dot{Y})^2 \Big|_{x=L} \\ & - \frac{E_s S_s + 2E_p S_p}{8L_p} \left[ \int_0^{L_p} v_{pr,n}^2 dx \right]^2 + \frac{E_s I_s + E_p I_p}{2} \int_0^{L_p} v_{pr,n}''^2 dx - be_{31} (h_p + h_s) V(t) \int_0^{L_p} \bar{v}'_{pr,n} dx \\ & - \frac{E_s S_s}{8(L - L_p)} \left[ \int_{L_p}^L \bar{v}_{sr,n}^2 dx \right]^2 + \frac{E_s I_s}{2} \int_{L_p}^L \bar{v}_{sr,n}''^2 dx - \left[ \frac{1}{2} k_{mg}^L v_{s,n}^2 + \frac{1}{4} k_{mg}^{NL} v_{s,n}^3 \right]_{x=L} \end{aligned} \quad (4.10)$$

We introduce the non-dimensionless variables defined in 2.18 in order to simplify the equations. To develop a reduced model, we express the displacement  $v_p$  and  $v_s$  at the piezoelectric and steel part using the Galerkin method limited to the first mode. We have, then:

$$v_n = \begin{cases} v_{p,n}(x, t) = \phi_p(x) a_{p,n}(t), & x \in [0, L_p] \\ v_{s,n}(x, t) = \phi_s(x) a_{s,n}(t), & x \in [L_p, L] \end{cases} \quad (4.11)$$

where:

$$\begin{cases} \phi_p(x) = \Delta_1 \cos(\sqrt{\omega}x) + \Delta_2 \sin(\sqrt{\omega}x) + \Delta_3 \cosh(\sqrt{\omega}x) + \Delta_4 \sinh(\sqrt{\omega}x) \\ \phi_s(x) = \Delta_5 \cos(\sqrt{\omega}x) + \Delta_6 \sin(\sqrt{\omega}x) + \Delta_7 \cosh(\sqrt{\omega}x) + \Delta_8 \sinh(\sqrt{\omega}x) \end{cases} \quad (4.12)$$

An admissible function is chosen to represents the first mode shape in a polynomial form.

We define the Heaviside functions  $H_p(x)$  and  $H_s(x)$  as follows:

$$\begin{cases} H_p(x) = \begin{cases} 1 & ; x \in \left[0; \frac{L_p}{L}\right] \\ 0 & ; x \in \left[\frac{L_p}{L}; 1\right] \end{cases} \\ H_s(x) = \begin{cases} 0 & ; x \in \left[0; \frac{L_p}{L}\right] \\ 1 & ; x \in \left[\frac{L_p}{L}; 1\right] \end{cases} \end{cases} \quad (4.13)$$

The total deformation of the beam can be defined as follows:

$$\phi(x) = \phi_p(x) H_p(x) + \phi_s(x) H_s(x) \quad (4.14)$$

The boundary conditions can be defined as follows:

- Embedding in  $x = 0$ :

$$\begin{cases} \phi_p(0) = 0 \\ \phi_p'(0) = 0 \end{cases} \quad (4.15)$$

- Guiding in  $x = 1$ :

$$\begin{cases} \frac{\omega^2 M}{\tau^2} \phi_s(1) + \frac{E_p I_p}{L^3} \phi_s'''(1) = 0 \\ \phi_s'(1) = 0 \end{cases} \quad (4.16)$$

- Continuity in  $x = \frac{L_p}{L}$ :

$$\begin{cases} \phi_p\left(\frac{L_p}{L}\right) = \phi_s\left(\frac{L_p}{L}\right) \\ \phi_p'\left(\frac{L_p}{L}\right) = \phi_s'\left(\frac{L_p}{L}\right) \\ (E_s I_s + E_p I_p) \phi_p''\left(\frac{L_p}{L}\right) = E_s I_s \phi_s''\left(\frac{L_p}{L}\right) \\ (E_s I_s + E_p I_p) \phi_p'''\left(\frac{L_p}{L}\right) = E_s I_s \phi_s'''\left(\frac{L_p}{L}\right) \end{cases} \quad (4.17)$$

The equations 4.15, 4.16 and 4.17 permit expressing the equation of the problem. We substitute Equation 4.11 into Equation 4.10 and applying Euler-Lagrange principle, Equation 4.18, we obtain the Duffing equation describing the behavior of the piezoelectric harvester as follows:

$$\frac{d}{dt} \frac{\partial \mathcal{L}}{\partial \dot{a}_n} - \frac{\partial \mathcal{L}}{\partial a_n} = 0 \quad (4.18)$$

$$\ddot{a}_n + c \dot{a}_n + \omega_0^2 a_n + D_3 a_n^3 - \Theta V_n = F \ddot{Y} \quad (4.19)$$

Where:  $c = \frac{\omega_0}{Q_2}$  and  $\omega_0 = \sqrt{\frac{D_2}{\lambda_2}}$ ,  $Q$  is the quality factor.

$$\begin{aligned} \lambda_2 &= \int_0^{\frac{L_p}{L}} \phi_p^2(x) dx + \frac{\rho_s S_s}{\rho_s S_s + 2\rho_s S_s} \int_{\frac{L_p}{L}}^1 \phi_s^2(x) dx + \frac{M}{L(\rho_s S_s + 2\rho_s S_s)} \phi_s^2(1) \\ D_2 &= \int_0^{\frac{L_p}{L}} \phi_p(x)''^2 dx + \frac{E_s I_s}{E_s I_s + E_p I_p} \int_{\frac{L_p}{L}}^1 \phi_s(x)''^2 dx + \frac{K_1 L^3}{E_s I_s + E_p I_p} \phi_s^2(1) \\ D_3 &= \frac{1}{\lambda_2 (E_s I_s + E_p I_p)} \left[ \frac{(E_s S_s + 2E_p S_p) L r^2}{2L_p} \left( \int_0^{\frac{L_p}{L}} \phi_p(x)'^2 dx \right)^2 \right] \\ &+ \frac{1}{\lambda_2 (E_s I_s + E_p I_p)} \left[ \frac{E_s S_s L r^2}{2(L - L_p)} \left( \int_{\frac{L_p}{L}}^1 \phi_s(x)'^2 dx \right)^2 \right] + \frac{K_3 r^2 L^3}{\lambda_2 (E_s I_s + E_p I_p)} \phi_s^4(1) \\ \Theta &= \frac{be_{31}(h_p + h_s) L^2}{\lambda_2 (E_s I_s + E_p I_p) r} \phi_p'\left(\frac{L_p}{L}\right) \\ F_2 &= \frac{\Omega^2 Y}{\lambda_2} \left[ \int_0^{\frac{L_p}{L}} \phi_p(x) dx + \frac{\rho_s S_s}{\rho_s S_s + 2\rho_s S_s} \int_{\frac{L_p}{L}}^1 \phi_s(x) dx + \frac{M}{L(\rho_s S_s + 2\rho_s S_s)} \phi_s(1) \right] \end{aligned} \quad (4.20)$$

We assume that only the electric field  $E_2$  in the direction  $y$  is considered non-zero for the case of transverse vibrations of the piezoelectric layers. So, the axial component of the electric field is negligible.

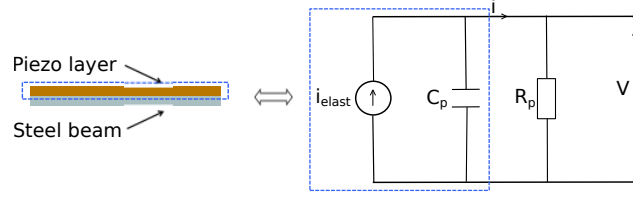


Figure 4.3: Equivalent circuit of the energy harvester with a steel and a piezoelectric layers

Consequently, in the following the transduction will depend only on the electric field  $E_2$ .

In this context, the electrical displacement field  $D$  is defined by the following equation:

$$D(x, t) = e_{31} \varepsilon_{11} + \epsilon_{33} \frac{V}{h_p} \quad (4.21)$$

Where  $e_{31}$ ,  $\epsilon_{33}$ ,  $V$  and  $\varepsilon_{11}$  stand for the piezoelectric coupling coefficient ( $C.m^{-2}$ ), the relative permittivity of the piezoelectric layer ( $F.m^{-1}$ ), the electrical potential generated by the piezoelectric layer and the axial deformation, respectively.

We recall the expression of the axial deformation  $\varepsilon_{11}$ :

$$\varepsilon_{11} = \frac{1}{2} \left( \frac{\partial v}{\partial x} \right)^2 + y \frac{\partial^2 v}{\partial x^2} \quad (4.22)$$

The Gauss law of electrostatic in a piezoelectric layer is written:

$$\frac{\partial D(x, y, t)}{\partial y} = 0 \Rightarrow D(x, y, t) = Cste \quad (4.23)$$

We integrate Equation 4.23 between  $y_1$  and  $y_2$  considering that  $|y_2 - y_1| = h_p$  and we replace  $D(x, t)$  by Equation 4.21, we obtain:

$$D(x, t) = \frac{e_{31}}{h_p} \int_{y_1}^{y_2} \varepsilon_{11}(x, y, t) dy - \frac{\epsilon_{33}}{h_p} V(x, t) dx \quad (4.24)$$

The piezoelectric transduction can be modeled by an equivalent circuit where the electrical charge generated by the piezoelectric layers is discharged through a resistance  $R_p$  as shown in Figure 4.3. The current generated by the piezoelectric layer is calculated by first differentiating the electric displacement  $D(x, t)$  with respect to time  $t$ , and then integrating across the whole length  $L_p$  of the piezoelectric layer, as shown below.

$$i(x, t) = \frac{V}{R_p} = \underbrace{\frac{b_p e_{31}}{h_p} \int_0^{L_p} \int_{y_1}^{y_2} \dot{\varepsilon}_{11}(x, y, t) dy dx}_{i_{elast}} - \underbrace{\frac{b_p L_p \epsilon_{33}}{h_p} \dot{V}(x, t)}_{i_c} \quad (4.25)$$

Where:

- $i_{elast}$  represents the elastic current generated by the mechanical deformation of the structure



- $i_c$  is the current generated by the capacitive behavior of the piezoelectric layer considering that:

$$C_p = \frac{L_p b_p \epsilon_{33}}{h_p} \quad (4.26)$$

- $R_p$  represents the resistance in which the electric power generated by the piezoelectric layer is discharged.

We substitute Equation 4.22 into Equation 4.25, we obtain for each piezoelectric patch  $n$ :

$$\frac{V_n}{R_p} = b_p e_{31} \int_0^{L_p} \frac{\partial v_n}{\partial x} \frac{\partial \dot{v}_n}{\partial x} dx - \frac{b_p e_{31} (h_s + h_p)}{2} \int_0^{L_p} \frac{\partial^2 \dot{v}_n}{\partial x^2} dx - \frac{L_p b_p \epsilon_{33}}{h_p} \dot{V}_n \quad (4.27)$$

Consequently,

$$\frac{V_n}{R_p} = I_{elas} - C'_p \dot{V}_n \quad (4.28)$$

Where

$$I_{elas} = \frac{b_p e_{31} d^2}{L \tau} \int_0^{L_p/L} \frac{\partial v_n}{\partial x} \frac{\partial \dot{v}_n}{\partial x} dx \quad (4.29)$$

and

$$C'_p = \frac{b_p L_p \epsilon_{33}}{h_p \tau} \quad (4.30)$$

### 4.2.3 Amplitude and power expressions

To determine the voltage  $V_n$  for each piezoelectric layer  $n$  for a harmonic case, a complex notation is used such as  $V_n(t) = V_n e^{2j\omega t}$ . Thus, the modulus of the generated voltage of each patch  $n$  attached to the beam  $n$  is expressed as follows:

$$\|V_n\| = \frac{\frac{j\omega_n b_p e_{31} d^2 a_n^2}{L^2} \int_0^1 \phi'^2(x) dx - \frac{b_p e_{31} (h_s + h_p) \omega_n a_n d}{2\tau} \int_0^1 \phi''(x) dx}{\sqrt{\frac{1}{R_p^2} + (\omega_n C'_p)^2}} \quad (4.31)$$

Where  $\omega_n$  stands for the frequency that corresponds to the maximum amplitude of the magnet  $n$  and

$$C'_p = \frac{L_p b_p \epsilon_{33}}{2 h_p \tau}.$$

For the piezoelectric transduction, the harvested power is defined as the square of the voltage generated by the piezoelectric layers divided by the corresponding load resistance  $R_p$  for each beam. Consequently, the harvested power from the layer  $n$  attached to the beam  $n$  is expressed as follows:

$$P_{p,n} = \frac{V_n^2}{R_p} \quad (4.32)$$

### 4.2.4 Theoretical results and experimental validation

In order to highlight the importance of the proposed hybrid system performance, we have performed a numerical simulations where we consider a 2-DOFs system based on standalone electromagnetic transduction and a 2-DOFs system based on hybrid electromagnetic-piezoelectric transduction. In the

following, we note that  $P_{tot}^{EM}$  is the total power harvested from the system based on electromagnetic transduction and  $P_{tot}^H$  is the total harvested power from the system based on hybrid transduction.  $P_{PE}$  stands for the power harvested from one piezoelectric patch and  $P_{EM}$  is the power harvested from one coil. For a system including 4 piezoelectric patches and 2 coils, we find out that the  $P_{EM}$  is equivalent to  $9 \times P_{PE}$ .

We neglect the magnetic nonlinearity and suppose that only the mechanical nonlinearity resulting from high displacements is considered. The system of equations of the hybrid system is solved using the multiple scales method. It has been proven that  $P_{tot}^H$  is improved by 25 % compared to  $P_{tot}^{EM}$ . So, the total power is divided into approximately 77 % transduced by electromagnetically and 23 % harvested piezoelectrically. Later, this enhancement in total energy of the hybrid system will be validated experimentally.

Next, we performed experimental tests in order to validate the proposed model. To do that we fix the basis acceleration to  $0.7g$  and the gap to  $50mm$ . Then, we construct the nonlinear frequency response of the system by performing sweep up and sweep down to cover all the stable branches. While varying the load resistances, we measure the output voltage. Therefore, the output harvested power from the bottom-left piezoelectric patch is calculated using Equation 4.32. In Figure 4.4, we illustrate the theoretical-experimental confrontation of the piezoelectric harvested power with load resistances  $R_p$ . According to this Figure, we can observe that we have good agreement between theoretical and experimental results. The small discrepancy between the results can be due to the positions of the piezoelectric patches and their bonding way. Also, it can be due to potentiometer errors occurring while changing the load resistances especially for the higher ones. We note that the maximum output power is captured for  $150k\Omega$  for both experimental and theoretical results. This resistance is the optimal one for the piezoelectric transduction and is noted  $R_p^*$ . At this optimal load resistance value, we have an error of 2.5 % in the maximum harvested power between theoretical and experimental results.

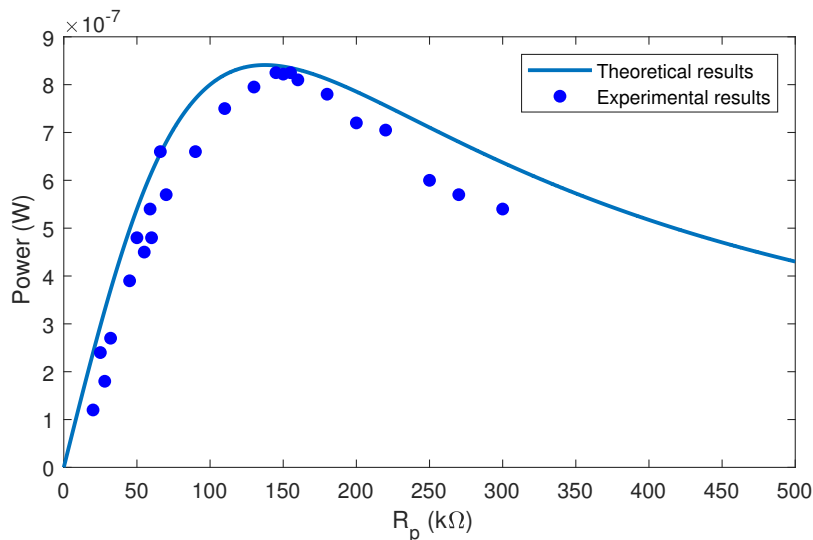


Figure 4.4: Experimental-theoretical confrontation of the harvested power from a piezoelectric patch

In the next section, we will investigate the phenomenon of nonlinear internal resonance in order to further enhance the output harvested power. In this section, the magnetic nonlinearity is considered as a tuning parameter in order to maximise the EH power. To do so, the magnetic nonlinearity is obtained by bringing the magnets closer to each others. As explained in section 1.8.1, the nonlinear resonance phenomenon can be activated when we have commensurate natural frequencies. We will be interested in two-in-one (2 : 1) internal resonance. In order to obtain commensurate frequencies, we will tune the gaps till we obtain the specific ones ensuring commensurable natural frequencies. The up magnet will be removed in order to perturb the symmetry of the magnetic field. The corresponding mechanical model will be developed and the expression of the natural frequencies will be determined.

### 4.3 2:1 Internal resonance

#### 4.3.1 Proposed device

The proposed hybrid energy harvester integrating simultaneously piezoelectric and electromagnetic conversion mechanisms is designed, its illustration is depicted in Figure 4.5 and its characterization was made on the experimental test bench is shown in Figure 2.7. The design includes two piezoelectric layers attached on the top surface of each beam near its clamped ends. It consists of two center movable coupled magnets supported by the compound elastic beams. The coupling between the magnets is tuned by varying the gap using the threaded rigid bars. The magnetic poles are oriented in such a way that magnetic repulsive forces are created between each two adjacent magnets. Unlike the lower moving magnet, the upper magnet is not subjected to a magnetic field from a fixed magnet at the top. A wire-wound copper coil is placed around each moving magnet. In this section, we will be working on 2-DOFs oscillators structure.

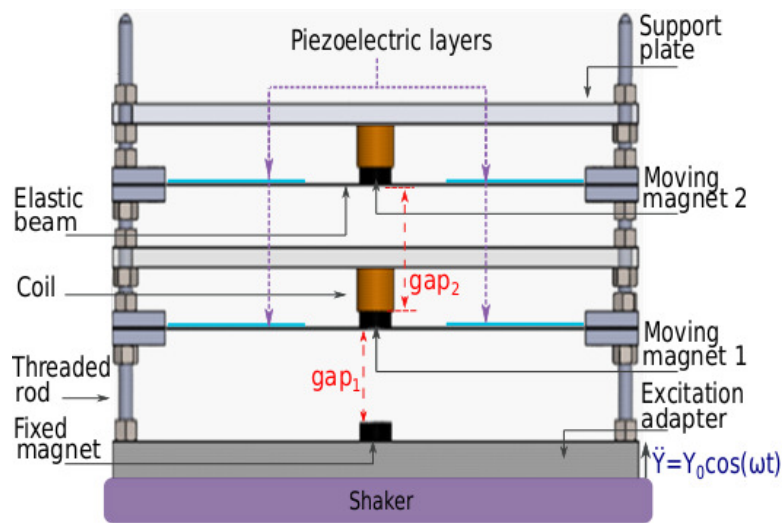


Figure 4.5: The proposed hybrid energy harvester destined to activate the internal resonance phenomenon



such that

$$\omega_{1,2} = \omega_0 \frac{\sqrt{2(1 + \beta_1) + \beta_2 \mp \sqrt{4\beta_1^2 + \beta_2^2}}}{\sqrt{2}} \quad (4.36)$$

Based on Equation 4.36, it is shown that the natural frequencies of the system can be easily tuned while tuning the linear magnetic force which is a function of the separation distance between the magnets defined by the gaps  $d_1$  and  $d_2$ . By tuning the distance between the two magnets, the relationship between the first and second global natural frequencies becomes commensurable with different ratios. This can be seen in Figure 4.6. The separation distances  $d_1$  and  $d_2$  can be adjusted so that a modal interaction of 2:1 ratio is achieved and thus 2:1 internal resonance occurs. Fixing  $d_2 = 35 \text{ mm}$ , the required distance  $d_1$ , where the second resonance frequency equal to twice the first resonance, is equal to  $12.74 \text{ mm}$ .

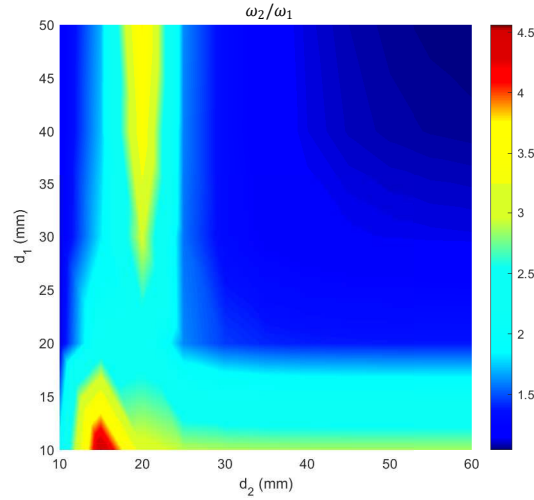


Figure 4.6: Ratio of the natural frequency  $\omega_2$  to  $\omega_1$  while varying the separation distances  $d_1$  and  $d_2$

### 4.3.3 Results

Experimental tests are performed and the corresponding harvester including 4 piezoelectric layers, two for each vibrating beam, is illustrated in Figure 4.7.

The harvested power is evaluated according to  $P = V^2/R_{load}$  for different load resistance at the base excitation level of  $0.7 \text{ g}$  where  $R_{load}$  is either  $R_p$  or  $R_{em}$  according to the conversion mechanism. Throughout the experiments, the voltage frequency responses are recorded in terms of the root-mean-square (RMS) value.

A basis acceleration of  $0.7 \text{ g}$  is applied. Up and down sweeps are done during the experiments to capture the bifurcation points of the nonlinear frequency responses. The EM and PE voltages are measured. As depicted in Figure 4.8a, it is shown that the PE load resistance doesn't affect the EM voltage. Similarly, the PE voltage is illustrated in Figure 4.8b. Fixing different values of EM load resistance when varying the PE voltage with PE load resistances doesn't affect the PE voltage.

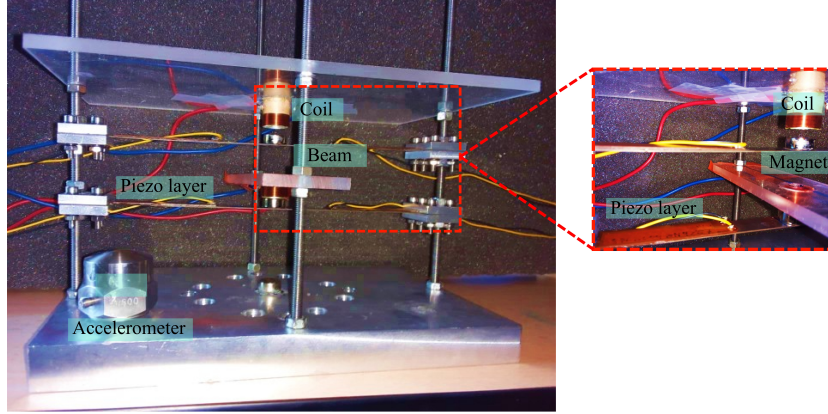


Figure 4.7: The experimental device for the case of internal resonance

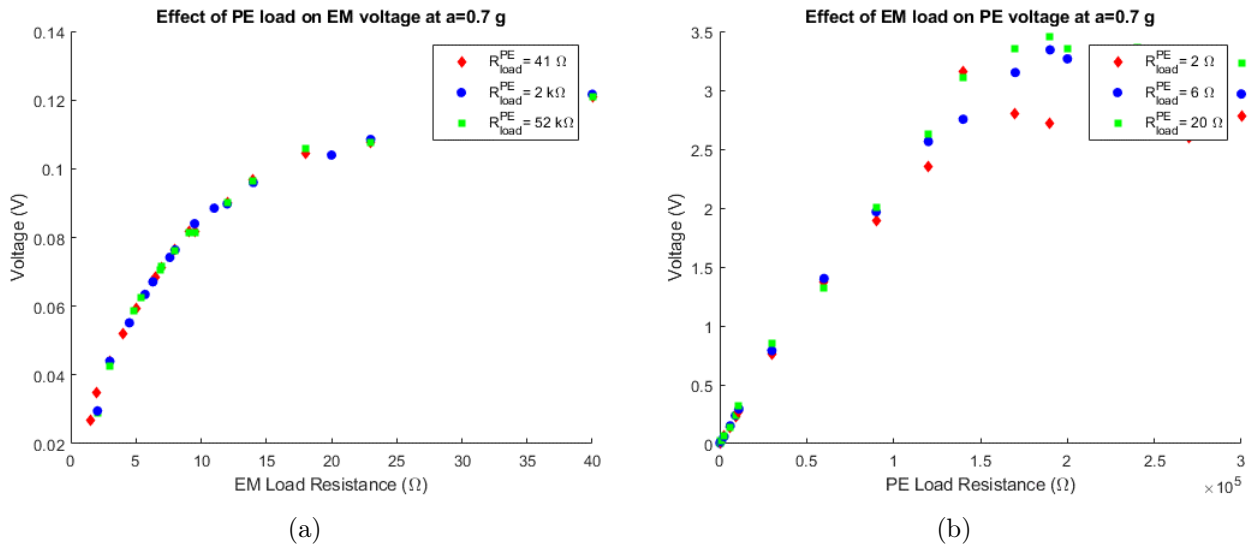


Figure 4.8: Voltage with load resistances a) EP b) PE

The corresponding EM and PE optimal resistances maximizing the total PE and EM powers are obtained at  $R_{em}^* = 7\Omega$  and  $R_p^* = 1.5 \cdot 10^5\Omega$  respectively as depicted in Figure 4.9.

For the optimal load resistances and fixed gaps, the results of the activated internal resonance phenomenon are shown in Figure 4.10.

The response curves show the existence of an additional peak that appears around the frequency of the first mode of the bottom DOF where hardening and softening responses are simultaneously observed. These results clearly demonstrate the modal interaction and energy transfer between the first and second modes that occurred because of the designed proportional relationship of natural frequencies. To prove the importance of the internal resonance phenomenon toward the output performance of the harvester, a configuration away from internal resonance is studied. Based on Equation (4.36) and Figure 4.36, the distances  $d_1$  and  $d_2$  are fixed both to  $50\text{ mm}$  such that  $\omega_1 = \omega_2$ . Figure 4.11 shows the output power of the hybrid energy harvester away from the 2:1 internal resonance condition. Only hardening nonlinearity is demonstrated.

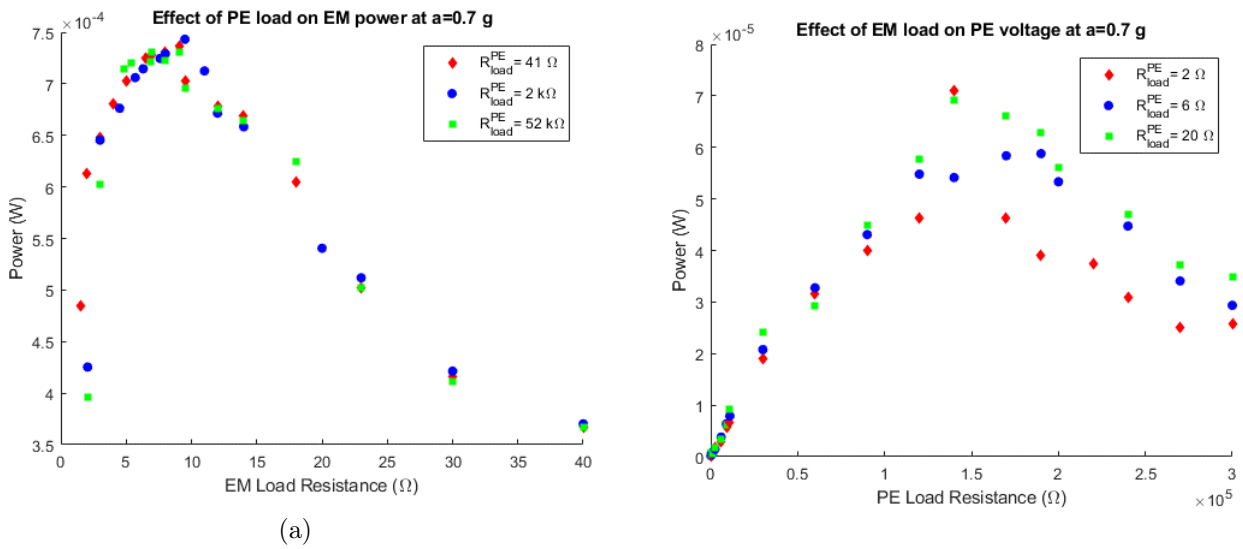


Figure 4.9: Power with load resistances a) EM b) PE

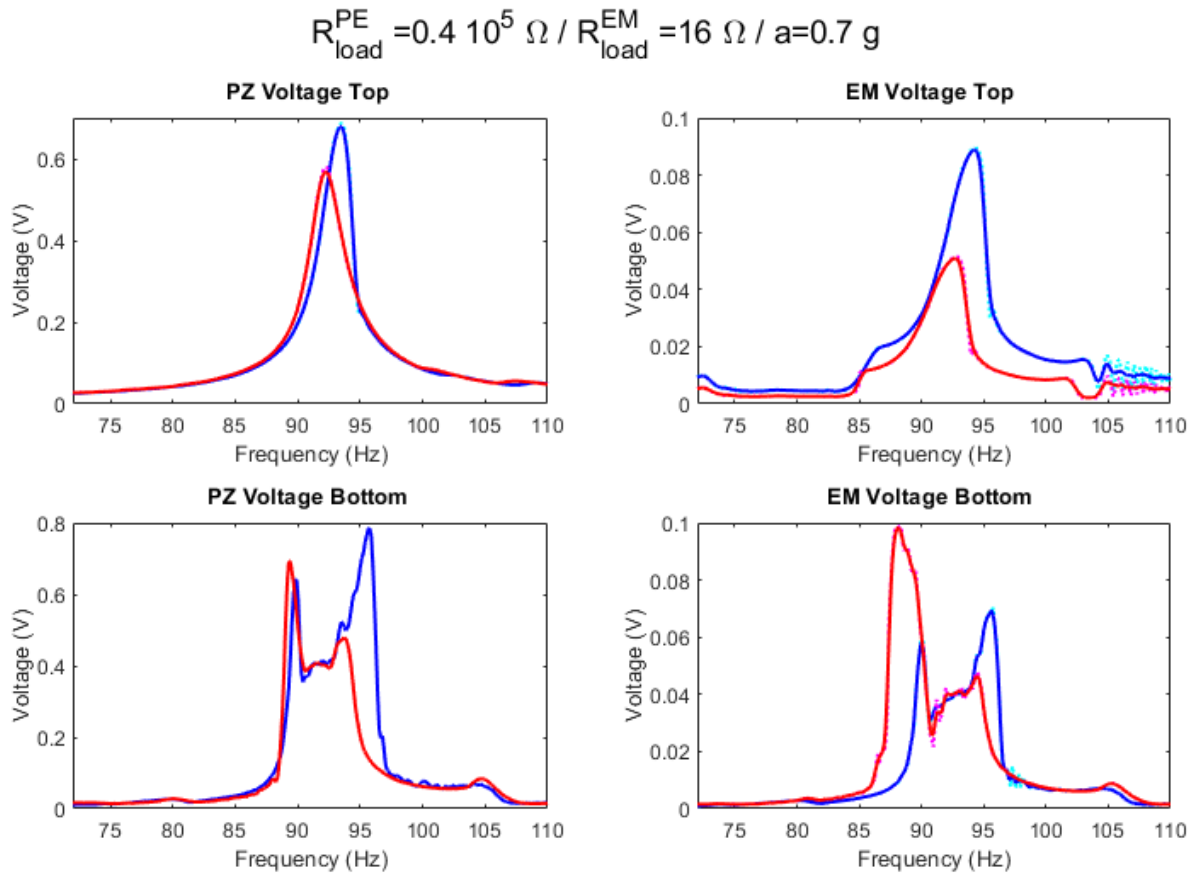


Figure 4.10: PE and EM DOFs frequency responses for the internal resonance phenomenon

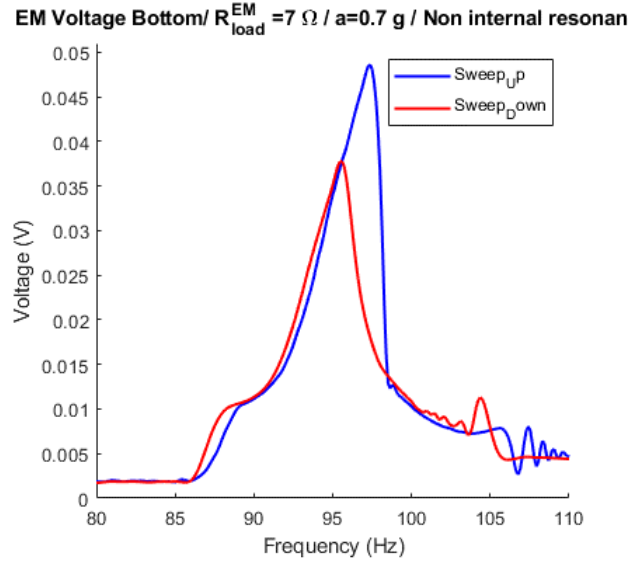


Figure 4.11: Frequency response with optimal parameters away from internal resonance condition

For the same optimal parameters, the EM corresponding frequency response is measured and illustrated in Figure 4.12. It is observed that the activation of the internal resonance results in increasing both the power density and the frequency bandwidth. An enhancement of 100% of power density is achieved compared to the generator results away from the 2:1 internal resonance. Considering this result, it has been shown that for well-chosen gaps resulting in 2:1 internal resonance, it is possible to reduce the volume of the harvester by almost two times and achieve 100% increase in the harvested power. By defining the internal resonance frequency bandwidth as the two upward peaks on both sides of the downward peak, it is also shown that the internal resonance widens the frequency bandwidth by 300% comparing to the case of hardening response away from 2:1 internal resonance illustrated in Figure 4.12.

## 4.4 Energy storage

In this section, we present a brief literature review on storage circuits and devices. Then, we carry out manipulations in order to experimentally ensure harvesting energy storage while vibrations of our structure.

### 4.4.1 Literature review on storage circuits and devices

The electrical energy generated by the transducer is not directly usable to power a storage device. An energy extraction circuit must be used, and its performance optimized to optimally convert the recovered energy. Its main role is to convert the alternating voltages generated into direct voltages, to adapt their levels to those required by the storage system used, and to regulate them in such a way as to generate source-independent voltages or load variations. Generally, electronic circuits for energy



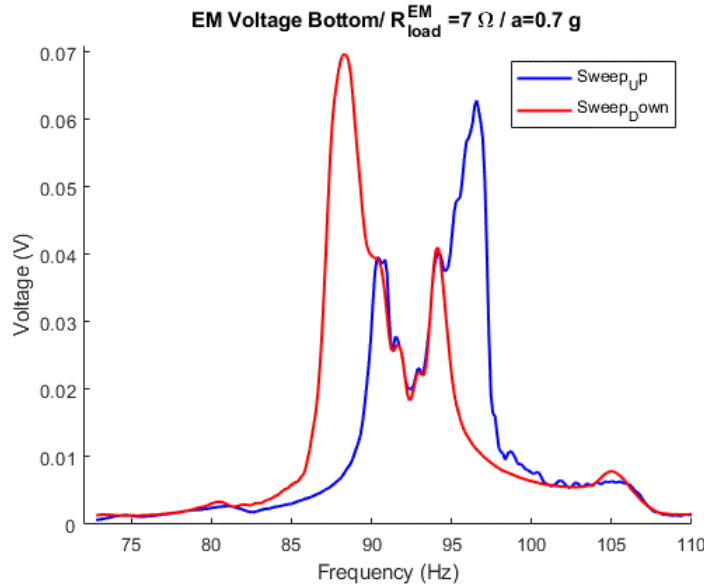


Figure 4.12: Frequency response with optimal parameters ensuring the activation of the internal resonance phenomenon

harvesting consist of a rectifier and a DC-DC converter as illustrated in Figure 4.13.

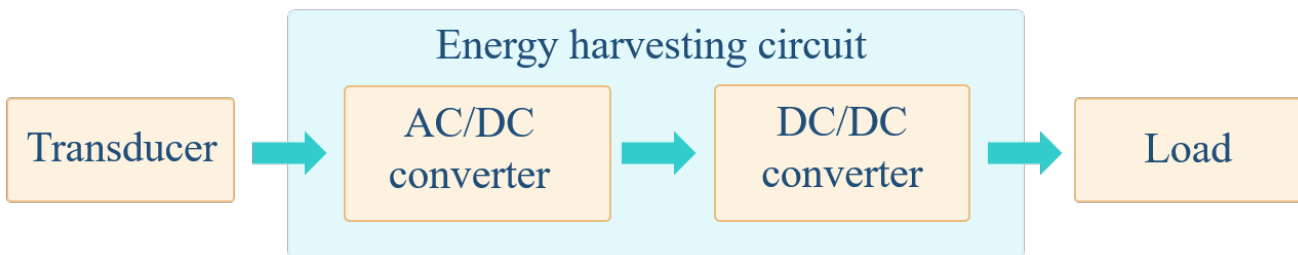


Figure 4.13: Structure of a typical energy harvesting circuit

- The rectifier (AC-DC converter): its role is the conversion of the alternating voltages generated at the terminals of a piezoelectric element or in the coil of an electromagnetic generator into direct voltages . To cope with the low voltages generated by non-optimized electromagnetic generators, by MEMS type generators, or under low amplitude of solicitation, dedicated solutions have been developed allowing the conversion of very low voltages. Marzencki et al. [147] propose a voltage multiplier rectifier based on very low threshold voltage diodes formed by DTMOS transistors. This harvester and its circuit permit to charge a supercapacitor even when we are in the case of very small accelerations. Minimizing losses induced in the current is required because in some applications like piezoelectric harvesting, the provided current is low. In this context, Guo and Lee [148] developed a rectifier with a, efficiency of 95 %.
- The regulator (DC-DC converter): it consists of adapting the voltages generated to the level of the load, or maximizing the power transferred from the source to the load by adapting the impedance

of the circuit to that of the transducer. Ottman et al. [149] proposed a step-down voltage chopper able to adapt and maximize the power scavenged by a piezoelectric element and charged in a battery. They show that the power is improved by 400% compared to a circuit without a DC / DC converter. The same principle is applied by Cao et al. [150] for electromagnetic harvesters where its energy scavenging circuit of the boost converter is shown in Figure 4.14.

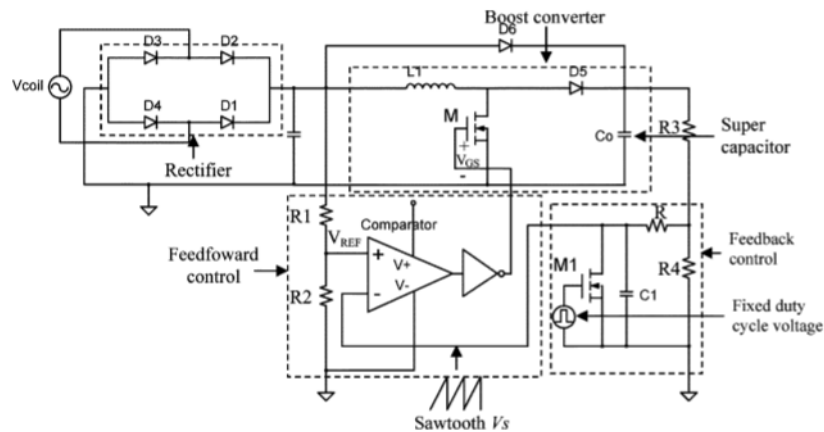


Figure 4.14: Energy harvesting circuit with a DC-DC amplifier converter [150]

The energy scavenged by these different systems is not sufficient to power the electronic systems. Therefore, it is compulsory to store energy and accumulate it until it reaches a sufficient level. We can distinguish two types of storage devices namely electrochemical and electrostatic storage.

- Electrochemical storage device: An electrochemical generator is a device for generating an electric current from a chemical reaction. If the reaction is reversible, we speak of an accumulator, rechargeable battery or secondary battery; otherwise, it will be a cell or a primary battery. In the field of energy harvesting, accumulators and rechargeable batteries are used to store energy. A comparison between batteries and rechargeable batteries is illustrated in Table 4.2. Based on this table, we can conclude that rechargeable batteries are more suitable for energy harvesting than regular ones.

Table 4.2: Comparison between accumulators and rechargeable batteries

Comparison criterion	Battery	Rechargeable battery
Number of times used	Can be charged only one time	Can be recharged for more than 500 times
Environment	Less friendly	More friendly
Price	Cheap	More expensive

- Electrostatic storage device: Capacitors and super-capacitors are electrostatic storage devices where no chemical reaction takes place, which eliminates or reduces certain problems associated with electrochemical storage, in particular temperature limits and damage during charge/discharge

cycles. A comparison between capacitors and super-capacitors is illustrated in Table 4.3. Based on this table and having the property of storing more energy in the same volume, we can conclude that super-capacitors are more suitable for energy harvesting than regular ones.

Table 4.3: Comparison between capacitors and super-capacitors

Comparison criterion	Capacitors	Super-capacitors
Energy density	Low comparing to the super-capacitors	have the highest energy density
Energy capacity	Less than super-capacitors	Higher than capacitors by more than 100 times
Price	Cheap	More expensive

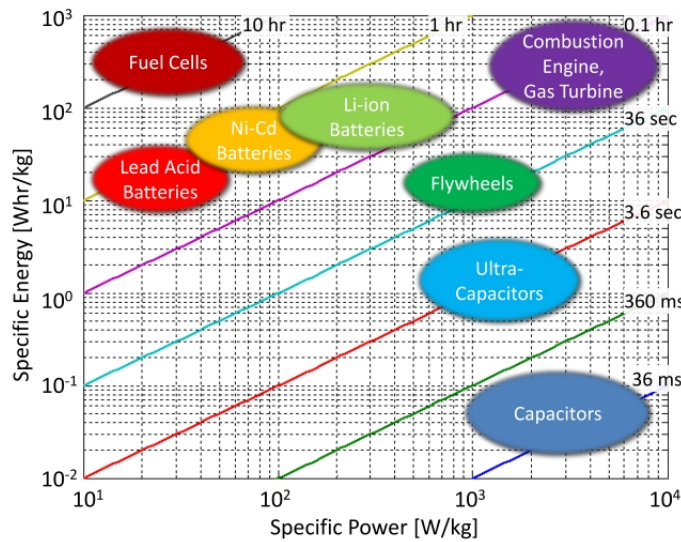


Figure 4.15: Ragone Diagram [151]

A Ragone plot [151] is illustrated in Figure 4.15 to compare performance of different energy storage devices in terms of energy densities. Comparing the devices dedicated to energy harvesting field, it is shown that super-capacitors have a high power density. This enables these devices to provide a very important peak power in milliseconds. Moreover, Lithium-based batteries have good energy and power densities. This compromise makes this type of batteries an attractive choice for multiple applications. As for Li-Ion battery, they have high energy density and specific power.

#### 4.4.2 Energy storage test

The harvested energy from the hybrid structure needs to be stored in a storage device to power low-power systems. As the harvester output signals are alternative (AC), they need to be transformed to direct ones (DC) before being stored. Accordingly, an energy storage circuit including the rectifier, the filter and the signal regulator is designed as depicted in Figure 4.16.

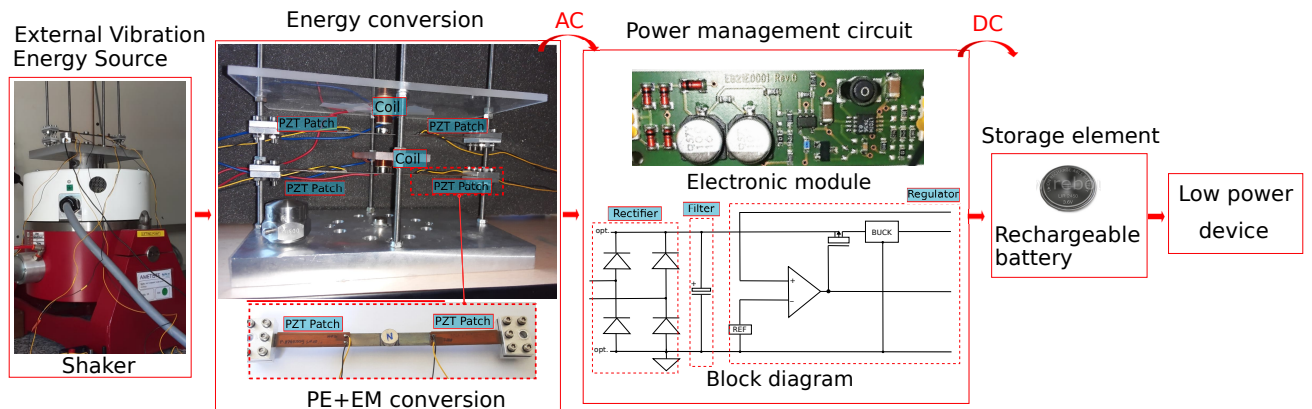


Figure 4.16: Energy storage

The first tests consist of using the electronic model shown in Figure 4.16 in order to regulate the output signals. We started by a storage test of the voltage generated from a piezoelectric patch. After being rectified, a storage test has been done in a Lithium-ion rechargeable battery. We have found that the output stored voltages is very low. Based on the work of Sodano et al. [152], it is turned out that this type of batteries require supplementary charge controller and voltage regulator that should be incorporated into the circuitry. We have chosen to perform the storage test using a  $100 \mu F$  capacitor. To do that, the corresponding circuit has been established as shown in Figure 4.17.

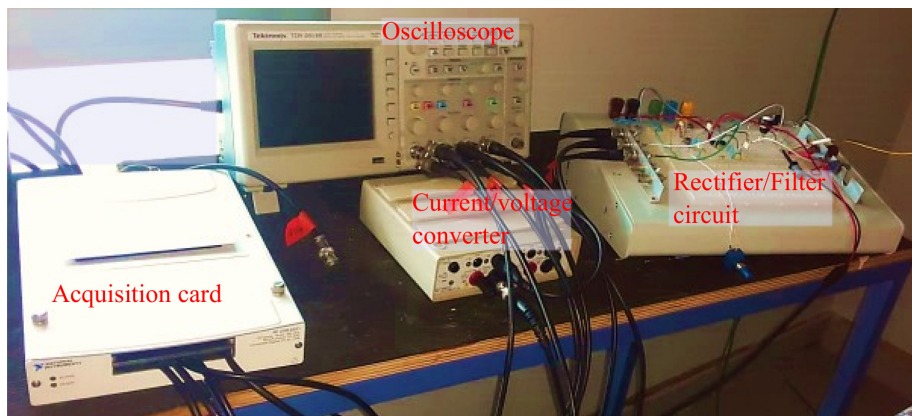


Figure 4.17: Experimental test bench for energy storage using capacitors

We used this circuit to charge a  $100 \mu F$  capacitor. We note that we kept the frequency resonance at  $94 Hz$  which gives the maximum amplitude for the nonlinear behavior. The load resistance of the discharging circuit is fixed to the obtained optimal load resistance that maximizes the piezoelectric patches harvested power which is  $R_p^* = 150 k\Omega$ . The test takes 3 minutes: 2 minutes for charging and 1 minute for discharging. The data acquisition is done using an acquisition card (National Instruments brand) and a computer.

We illustrate in Figure 4.18 the voltage with time of the piezoelectric patch. The maximum voltage

obtained is  $0.44\text{ V}$ . In Figure 4.19, we illustrate the evolution with time on this load capacitor in the charging and discharging phases. The maximum voltage obtained across the capacitor is equal to  $0.384\text{ V}$ . This value is less than the voltage across the piezoelectric patch. This is due to the losses in the rectification circuit.

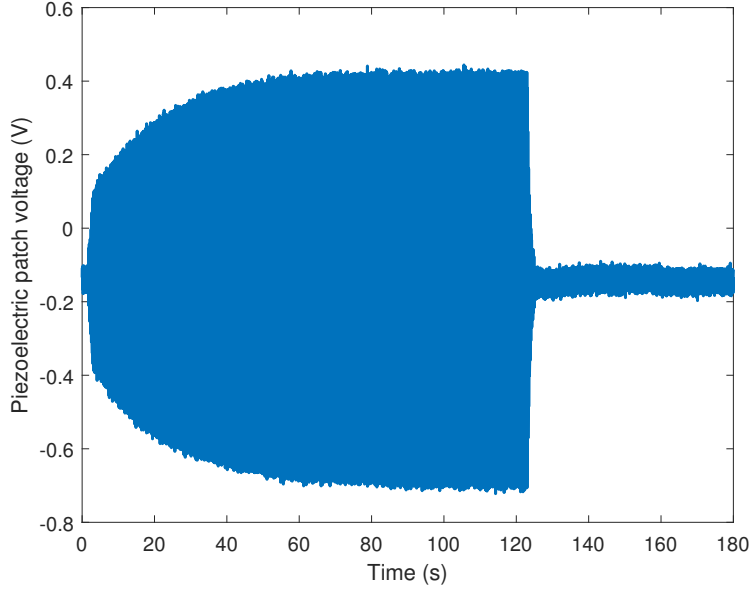


Figure 4.18: Voltage of the piezoelectric patch

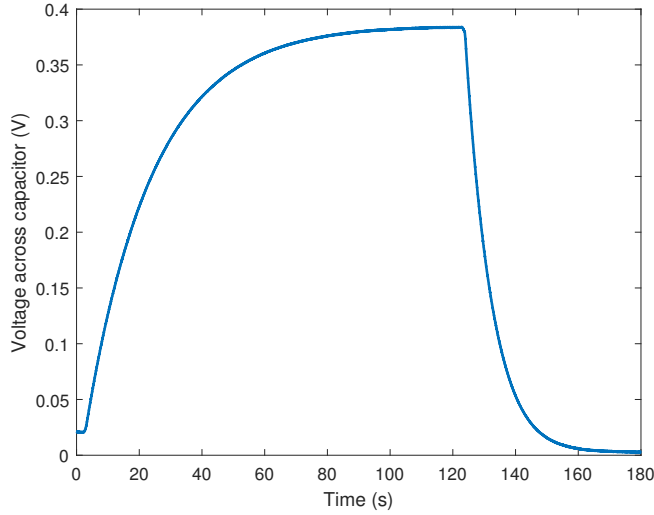


Figure 4.19: Voltage across a  $100\ \mu\text{F}$  capacitor

Based on the voltage variation on the capacitor, we can calculate the instantaneous power that is transferred to the load [147]:

$$P_{inst} = \frac{\Delta E}{\Delta t} = \frac{1}{2} C_L \frac{V_{out}^2(t_2) - V_{out}^2(t_1)}{t_2 - t_1} \quad (4.37)$$

Where  $\Delta E$  is the difference in the energy stored in the capacitor between the instants  $t_1$  and  $t_2$ ,  $C_L$  is the capacitance of the used capacitor and  $V_{out}$  is the load capacitor voltage.

Between  $t_1 = 1\text{ s}$  and  $t_2 = 120\text{ s}$ , the voltage raises from  $0.02\text{ V}$  to  $0.38\text{ V}$ . Between  $t_1$  and  $t_2$ , the instantaneous power delivered to the load capacitor is of  $62\text{ nW}$ .

In order to obtain the discharge current, we divide the voltage across resistor of discharge circuit by the fixed discharging resistance. According to Figure 4.20, the obtained discharge current is low and is of  $0.58\text{ }\mu\text{A}$ .

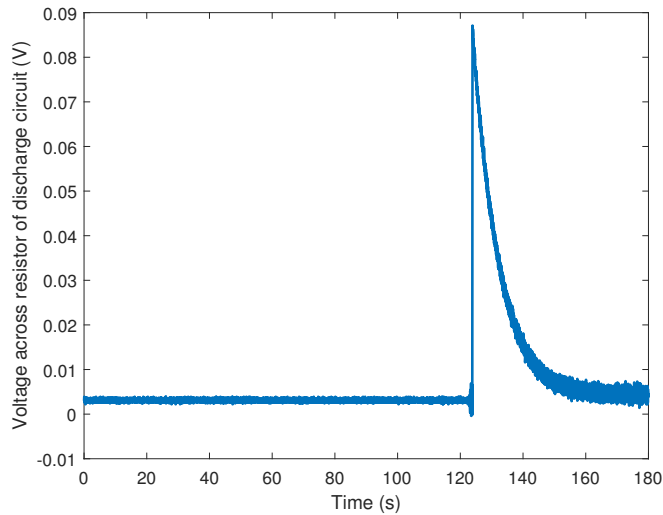


Figure 4.20: Voltage across resistance of discharge circuit

## 4.5 Summary

In this chapter, a hybrid piezoelectric-electromagnetic energy harvester has been developed. The hybrid configuration has proved its benefits in enhancing the output performance in terms of harvested power comparing to harvesters with only one transduction technique. Furthermore, the phenomenon of internal resonance is investigated. The tune of distance between magnets permitted to ensure commensurable natural frequencies. Hence, the internal resonance is activated and the frequency response shows two peaks that appear around the frequency of the first mode instead of only one peak. The bending of the frequency response curve to the left and to the right simultaneously results immediately in a significant increase in the frequency bandwidth. Add to that, the magnitude of amplitude and then the amount of the maximum harvested power is enhanced. This phenomenon increases simultaneously the bandwidth and the power by just tuning the gaps between magnets. Comparing to the case of nonlinear harvester away from internal resonance, this phenomenon combined with the hybrid transduction provides promising results. In fact, we have found that the harvested energy has been increased by 100 % and the frequency bandwidth has been enlarged by 300 %. The storage test has been done using

a  $100\ \mu F$  capacitor. Charging and discharging cycles have been performed for a piezoelectric patch during 3 minutes where 2 minutes are taken for charging phase where the structure is subjected to basis excitation. This storage test is only proof of charging. However, storing the harvested energy from the two sources of energy in a permanent reservoir as a rechargeable battery or a super-capacitor should be carried out.

# Conclusion

In this thesis, novel concepts have been investigated in order to improve the output performance of the proposed vibration energy harvester. It includes, firstly, the combination of nonlinear dynamics and energy localization phenomenon for a 2-DOFs and 5-DOFs harvester. Secondly, a multiobjective optimization has been carried out to improve the performance of the 5-DOFs generalized harvester. The concepts are theoretically demonstrated and experimentally verified. Finally, the phenomenon of internal resonance has been investigated for a 2-DOFs hybrid piezoelectric-electromagnetic harvester. These proposed concepts proved their efficiency in providing a way to further enhance vibration energy harvesters' performance.

## Main achievements

### **Performance enhancement based on tuning localization and nonlinear dynamics**

The first studied system is a 2-DOFs one based on electromagnetic transduction. Nonlinear dynamics has been introduced by imposing large displacements to the structure. The novelty was to combine nonlinear dynamics with mode localization phenomenon. The introduced nonlinearity enhances the frequency bandwidth and also it has been proven that it offers a robustness of the maximum energy localization rates compared to the linear configuration. Add to that, the simultaneous functionalization of these phenomena allows enhancing the output performances in terms of harvested energy and frequency bandwidth by 116 % and 19.4 %, respectively compared to the nonlinear periodic system. This concept has been theoretically demonstrated and the model has been experimentally validated.

### **Performance enhancement based on multiobjective optimization procedure**

As a second improvement area, we investigated a multiobjective optimization procedure in order to increase the frequency bandwidth and the harvested power of a nonlinear generalized harvester. The 2-DOFs harvester has been extended to a 5-DOFs one. The generic model has been established. Then, the introduction of nonlinear dynamics and mode localization phenomenon has been investigated. We have chosen to introduce two mass mistuning in the 5-DOFs harvester. For that, a multiobjective optimization has been performed in order to obtain the optimal positions of the introduced perturbations. For the well-chosen mistuning, a multiobjective optimization is also carried out to enhance the output



performance. It has been shown that this procedure allows increasing the frequency bandwidth and the harvested power by 79 % and 101 % respectively compared to the case of 2-DOFs harvester. Furthermore, it has been proven that a quasiperiodic 5-DOFs system with well-chosen introduced mistuning provides comparable energy with a 5-DOFs system but with enhancement in frequency bandwidth. This property allows using 2 coils instead of 5 the fact that reduces the cost of electrical circuits and thus alleviate the technological constraints of the structure.

### **2:1 Internal resonance**

Finally, two piezoelectric patches were added to each steel beams in order to improve the total harvested power. The hybrid electromagnetic-piezoelectric harvester provides an important increase in the output harvested power in comparison with the electromagnetic harvester. To further increase, the output performance, the phenomenon of internal resonance has been investigated for the hybrid system. The activation of the internal resonance phenomenon has been done through gap tuning based on magnetic nonlinearity. It has been shown that both the power density and the frequency bandwidth has been improved. In fact, when compared to the configuration of nonlinear harvester away from the 2:1 internal resonance, we obtain that the harvested energy has been increased by 100 % and the frequency bandwidth has been extended by 300 %. As a result, it has been demonstrated that for well-chosen gaps resulting in 2:1 internal resonance, it is possible to reduce the harvester's volume by nearly two times while achieving a 100 % increase in harvested power.

## **Perspectives**

The proposed vibration energy harvester has certainly demonstrated its competitive performance, but other improvement areas can be investigated.

### **Internal resonance analytical model**

For lack of time, we haven't achieved the analytical model of the internal resonance phenomenon. It is the first axis to be investigated in the continuation of his research.

### **Clamping system**

Throughout the experimental manipulations, we used a Nut-based tightening system and the position adjustment has been done through threaded rods. These two solutions weren't the optimal ones. We have seen that a slight difference in tightening torque leads to a significant changing of the mechanical stiffness and therefore to the resonance frequency. Also, fixing both sides of the beams at the same positions was difficult to have and needs a lot of manipulations and consequently more time. We suggest the use of worm drive system for the fixing of beams positions and tap and die system where the beams are linked definitively to the threaded part in a way we avoid clamping problems. The

system will have the form of two interlocking rings where the beams are linked to the interior one which has threads.

### **Changing coils/ beams/ magnets**

Throughout this study, we assumed that we have identical beams, magnets and coils. We can, in future work, investigate this point by working on beam array having different sections. Optimization of coils and magnets can also be investigated in order to ensure better electromagnetic output power.

### **Miniaturization**

We worked on this thesis on a large harvester as a proof of concept. Future work will include the miniaturization of this device and experimental validation will be performed to study the scale factor effect on the previously validated performance.

### **Storage**

For the moment, the storage has been done through temporarily storage device which is a capacitor. For an effective storage, super-capacitors or rechargeable batteries should be used in future works. Add to that, the storage has been done for only one type of transduction, methods of collecting outputs of different transduction techniques in the same storage device should be investigated.

### **Type of excitation**

In these thesis works, we assumed that the acceleration at the base is mono-harmonic. To get closer to the reality of the ambient vibratory energy sources, we can consider extending the study by applying multi-harmonic or random basis acceleration.

### **Electrostatic nonlinearity**

Our study was based on mechanical and magnetic nonlinearity. We can investigate the area of electrostatic nonlinearity. In fact, we haven't taken into consideration the nonlinearity coming from piezoelectric patches when the structures is subjected to large displacements.

### **Metastructures**

The last perspective of the non-exhaustive perspectives list for this thesis is the use of a large array of oscillators. We were limited to a 5-DOFs harvester in the numerical study and a 2-DOFs one in the experimental investigations. In future work, we propose to get closer to real applications by working on meta-structures.



# Conferences and publications

## Publications in international peer-reviewed journals

- Aouali, Kaouthar, et al. "On the Optimization of a Multimodal Electromagnetic Vibration Energy Harvester Using Mode Localization and Nonlinear Dynamics." *Actuators*. Vol. 10. No. 2. Multidisciplinary Digital Publishing Institute, 2021.  
<https://doi.org/10.3390/act10020025>
- Aouali, Kaouthar, et al. "Efficient broadband vibration energy harvesting based on tuned non-linearity and energy localization." *Smart Materials and Structures* 29.10 (2020): 10LT01.  
<https://doi.org/10.1088/1361-665X/abaa95>

## Publications in international conferences with proceedings

- Aouali, Kaouthar, et al. "Exploiting Nonlinear Dynamics and Energy Localization to Enhance the Performances of an Electromagnetic Vibration Energy Harvester." *ASME 2019 International Design Engineering Technical Conferences and Computers and Information in Engineering Conference*. American Society of Mechanical Engineers Digital Collection, Anaheim, California, USA, August 18-21, 2019.  
<https://doi.org/10.1115/DETC2019-97862>
- Aouali, Kaouthar, et al. "Effect of the localization on the response of a quasi-periodic electromagnetic oscillator array for vibration energy harvesting." *International Conference on Structural Nonlinear Dynamics and Diagnosis*, Tangier, Morocco, June 25-27, 2018.  
<https://doi.org/10.1051/mateconf/201824101003>
- Aouali, K., et al. "Nonlinear multimodal electromagnetic device for vibration energy harvesting". *14th Congress of Mechanics*, Rabat, Morocco, April 16-19, 2019.  
<https://doi.org/10.1051/mateconf/201928601003>

## Publications in national conferences without proceedings

- Dowlati, S., Aouali, K., Kacem, N. and Bouhaddi N., "On the energy trapping in a periodic system for vibration energy harvesting", *10th National Days on Energy Harvesting and Storage (JNRSE)*, Grenoble, France, June 14-15, 2021

- Aouali, K., Kacem, N. and Bouhaddi N., “Performance enhancement of an electromagnetic vibration energy harvester by nonlinear dynamics and energy localization”, Journées Jeunes Chercheuses et Chercheurs Acoustique, vibration et Bruit (JJCAB), Lyon, France, November 19-20, 2020.
- Aouali, K., Kacem, N. and Bouhaddi N., “Enhancement of the performances of an electromagnetic device for vibration energy harvesting by nonlinear dynamics and energy localization.” 9th National Days on Energy Harvesting and Storage (JNRSE), Blois, France, May 23-24, 2019.
- Aouali, K., Kacem, N. and Bouhaddi N., “Nonlinear dynamics of a mode-localized electromagnetic device: a way to enhance the performances of vibration energy harvesting”, Séminaire franco-polonais, Besançon, France, June 6-7, 2019.
- Aouali, K., Kacem, N. and Bouhaddi N., “Enhancement of the performances of a quasi-periodic electromagnetic vibration energy harvester by energy localization”, 8th National Days on Energy Harvesting and Storage (JNRSE), Besançon, France, May 14-15, 2018.

# Bibliography

- [1] *Web of Science* <https://apps.webofknowledge.com>.
- [2] Elaheh Bozorgzadeh Dang, Nga and Nalini Venkatasubramanian. Energy harvesting for sustainable smart spaces. In *Advances in Computers*, volume 87, pages 203–251. Elsevier, 2012.
- [3] Matthias Geisler. *Récupération d'énergie mécanique pour vêtements connectés autonomes*. PhD thesis, the Doctoral School of Engineering - Materials, Mechanics, Environment, Energy, Processes, Production (IMEP2), 2018.
- [4] <https://www.fujitsu.com/global/about/resources/news/press-releases/2010/1209-01.html>.
- [5] Emmanuelle Arroyo. *Récupération d'énergie à partir des vibrations ambiantes: dispositif électromagnétique et circuit électronique d'extraction synchrone*. PhD thesis, The doctoral school of Science and Engineering of Environmental Systems Membership and Organizations (SISEO), 2012.
- [6] S. Beeby and N.White. *Energy harvesting for autonomous systems*. Artech House, 2010.
- [7] Bilel Maamer, Ayda Boughamoura, Ahmed MR Fath El-Bab, Laurent A Francis, and Farès Tounsi. A review on design improvements and techniques for mechanical energy harvesting using piezoelectric and electromagnetic schemes. *Energy Conversion and Management*, 199:111973, 2019.
- [8] Clemens Cepnik, Roland Lausecker, and Ulrike Wallrabe. Review on electrodynamic energy harvesters—a classification approach. *Micromachines*, 4(2):168–196, 2013.
- [9] Roundy , Shad. Improving power output for vibration-based energy scavengers. *IEEE Pervasive computing*, 4(1):28–36, 2005.
- [10] Neil G Stephen. On energy harvesting from ambient vibration. *Journal of sound and vibration*, 293(1-2):409–425, 2006.
- [11] Xingyu Xiong. *Development of vibration-based multi-resonance energy harvesters using piezoelectric materials*. PhD thesis, School of Mechanical, Aerospace and Civil Engineering, University of Manchester., 2014.

- 
- [12] Ali E. Kubba and Kyle Jiang. A comprehensive study on technologies of tyre monitoring systems and possible energy solutions. *A comprehensive study on technologies of tyre monitoring systems and possible energy solutions*, 14(6):10306–10345, 2014.
- [13] Luay Y. Taha Aljadiri, Rita T. and Paul Ivey. Electrostatic energy harvesting systems: A better understanding of their sustainability. *Journal of Clean Energy Technologies*, 5(5):409–416, 2017.
- [14] F. E. H. Tay Dhakar, Lokesh and Chengkuo Lee. Investigation of contact electrification based broadband energy harvesting mechanism using elastic pdms microstructures. *Journal of Micromechanics and Microengineering*, 24(10):104002, 2014.
- [15] F. E. H. Tay Dhakar, Lokesh and Chengkuo Lee. Analysis of a micro-electric generator for microsystems. *Sensors and Actuator A: Physical*, 52(1-3):8–11, 1996.
- [16] et al. Beeby, Steve P. A micro electromagnetic generator for vibration energy harvesting. *Journal of Micromechanics and microengineering*, 17(7):1257, 2007.
- [17] Dirk Spreemann and Yiannos Manoli. *Electromagnetic vibration energy harvesting devices: Architectures, design, modeling and optimization*, volume 35. Springer Science Business Media, 2012.
- [18] M Demartin Maeder, D Damjanovic, and NJJoE Setter. Lead free piezoelectric materials. *Journal of electroceramics*, 13(1):385–392, 2004.
- [19] Jacques Curie and Pierre Curie. Contractions et dilatations produites par des tensions électriques dans les cristaux hémihédres à faces inclinées. *Compt. Rend.*, 93:1137–1140, 1881.
- [20] <http://piezolighter.weebly.com/description.html>.
- [21] Gabriel Lippmann. Principe de la conservation de l’électricité, ou second principe de la théorie des phénomènes électriques. *Journal de Physique Théorique et Appliquée*, 10(1):381–394, 1881.
- [22] <https://www.explainthatstuff.com/quartzclockwatch.html>.
- [23] Hailing Fu, Guangzhu Chen, and Nan Bai. Electrode coverage optimization for piezoelectric energy harvesting from tip excitation. *Sensors*, 18(3):804, 2018.
- [24] Thorsten Hehn and Yiannos Manoli. Piezoelectricity and energy harvester modelling. In *Cmos circuits for piezoelectric energy harvesters*, pages 21–40. Springer, 2015.
- [25] Morgan Matoroc. Piezoelectric ceramics databook for designers. *Morgan Matoroc Ltd*, 1996.
- [26] Jose Luis Gonzalez, A Rubio, and F Moll. A prospect on the use of piezoelectric effect to supply power to wearable electronic devices. In *Fourth Int. Conf. Mater. Eng. Resources, ICMR*, pages 202–206, 2001.

- [27] SP Beeby, MJ Tudor, and NM White. Energy harvesting vibration sources for microsystems applications. *Measurement science and technology*, 17(12):R175, 2006.
- [28] Scott Meninger, Jose Oscar Mur-Miranda, Rajeevan Amirtharajah, Anantha Chandrakasan, and Jeffrey H Lang. Vibration-to-electric energy conversion. *IEEE Transactions on Very Large Scale Integration (VLSI) Systems*, 9(1):64–76, 2001.
- [29] Shad Roundy, Paul K Wright, and Kristofer SJ Pister. Micro-electrostatic vibration-to-electricity converters. In *ASME international mechanical engineering congress and exposition*, volume 36428, pages 487–496, 2002.
- [30] Zhong Lin Wang. Triboelectric nanogenerators as new energy technology and self-powered sensors—principles, problems and perspectives. *Faraday discussions*, 176:447–458, 2015.
- [31] Feng-Ru Fan, Zhong-Qun Tian, and Zhong Lin Wang. Flexible triboelectric generator. *Nano energy*, 1(2):328–334, 2012.
- [32] Lei Wang and FG Yuan. Vibration energy harvesting by magnetostrictive material. *Smart Materials and Structures*, 17(4):045009, 2008.
- [33] Lin Dong, Andrew B Closson, Congran Jin, Ian Trase, Zi Chen, and John XJ Zhang. Vibration-energy-harvesting system: Transduction mechanisms, frequency tuning techniques, and biomechanical applications. *Advanced materials technologies*, 4(10):1900177, 2019.
- [34] SJ Roundy. Energy scavenging for wireless sensor nodes with a focus on vibration to electricity conversion [ph. d. thesis]. *University of California, Berkeley, Berkeley, CA, USA*, 2003.
- [35] Henry A Sodano, Gyuhae Park, and DJ Inman. Estimation of electric charge output for piezoelectric energy harvesting. *Strain*, 40(2):49–58, 2004.
- [36] Jyoti Ajitsaria, Song-Yul Choe, D Shen, and DJ Kim. Modeling and analysis of a bimorph piezoelectric cantilever beam for voltage generation. *Smart Materials and Structures*, 16(2):447, 2007.
- [37] R Ly, M Rguiti, S D’astorg, A Hajjaji, C Courtois, and A Leriche. Modeling and characterization of piezoelectric cantilever bending sensor for energy harvesting. *Sensors and Actuators A: Physical*, 168(1):95–100, 2011.
- [38] L Zhou, J Sun, XJ Zheng, SF Deng, JH Zhao, ST Peng, Y Zhang, XY Wang, and HB Cheng. A model for the energy harvesting performance of shear mode piezoelectric cantilever. *Sensors and Actuators A: Physical*, 179:185–192, 2012.
- [39] Kuok H Mak, Atanas A Popov, and Stewart McWilliam. Experimental model validation for a nonlinear energy harvester incorporating a bump stop. *Journal of Sound and Vibration*, 331(11):2602–2623, 2012.



- 
- [40] Anurag Kasyap, J Lim, David Johnson, Stephen Horowitz, Toshikazu Nishida, Khai Ngo, Mark Sheplak, and Louis Cattafesta. Energy reclamation from a vibrating piezoceramic composite beam. In *Proceedings of 9th International Congress on Sound and Vibration*, volume 9, pages 36–43. Orlando, FL, USA, 2002.
- [41] R Elfrink, TM Kamel, M Goedbloed, S Matova, D Hohlfeld, Y Van Andel, and R Van Schaijk. Vibration energy harvesting with aluminum nitride-based piezoelectric devices. *Journal of Micromechanics and Microengineering*, 19(9):094005, 2009.
- [42] Shad Roundy and Paul K Wright. A piezoelectric vibration based generator for wireless electronics. *Smart Materials and structures*, 13(5):1131, 2004.
- [43] J Xu and J Tang. Multi-directional energy harvesting by piezoelectric cantilever-pendulum with internal resonance. *Applied Physics Letters*, 107(21):213902, 2015.
- [44] Shanshan Li, Andrea Crovetto, Zhuoteng Peng, Ai Zhang, Ole Hansen, Mingjiang Wang, Xinxin Li, and Fei Wang. Bi-resonant structure with piezoelectric pvdf films for energy harvesting from random vibration sources at low frequency. *Sensors and Actuators A: Physical*, 247:547–554, 2016.
- [45] Kangqi Fan, Jianwei Chang, Witold Pedrycz, Zhaohui Liu, and Yingmin Zhu. A nonlinear piezoelectric energy harvester for various mechanical motions. *Applied Physics Letters*, 106(22):223902, 2015.
- [46] Yang Bai, Pavel Tofel, Zdenek Hadas, Jan Smilek, Petr Losak, Pavel Skarvada, and Robert Macku. Investigation of a cantilever structured piezoelectric energy harvester used for wearable devices with random vibration input. *Mechanical Systems and Signal Processing*, 106:303–318, 2018.
- [47] Tian-Bing Xu, Emilie J Siochi, Jin Ho Kang, Lei Zuo, Wanlu Zhou, Xiudong Tang, and Xiaoning Jiang. Energy harvesting using a pzt ceramic multilayer stack. *Smart Materials and Structures*, 22(6):065015, 2013.
- [48] Jiangxin Zhao, Jin Yang, Zhiwei Lin, Nian Zhao, Jun Liu, Yumei Wen, and Ping Li. An arc-shaped piezoelectric generator for multi-directional wind energy harvesting. *Sensors and Actuators A: Physical*, 236:173–179, 2015.
- [49] Ziping Cao, Jinya Zhang, and Hiroki Kuwano. Design and characterization of miniature piezoelectric generators with low resonant frequency. *Sensors and Actuators A: Physical*, 179:178–184, 2012.
- [50] Boram Yang and Kwang-Seok Yun. Piezoelectric shell structures as wearable energy harvesters for effective power generation at low-frequency movement. *Sensors and Actuators A: Physical*, 188:427–433, 2012.

- [51] Dibin Zhu, Stephen P Beeby, Michael J Tudor, and Nick R Harris. A credit card sized self powered smart sensor node. *Sensors and Actuators A: Physical*, 169(2):317–325, 2011.
- [52] Elie Lefeuvre, Adrien Badel, Claude Richard, Lionel Petit, and Daniel Guyomar. A comparison between several vibration-powered piezoelectric generators for standalone systems. *Sensors and Actuators A: Physical*, 126(2):405–416, 2006.
- [53] CB Williams, C Shearwood, MA Harradine, PH Mellor, TS Birch, and RB Yates. Development of an electromagnetic micro-generator. *IEE Proceedings-Circuits, Devices and Systems*, 148(6):337–342, 2001.
- [54] Dibin Zhu, Steve Beeby, John Tudor, and Nick Harris. A planar electromagnetic vibration energy harvester with a halbach array. 2011.
- [55] M El-Hami, P Glynne-Jones, NM White, M Hill, Stephen Beeby, E James, AD Brown, and JN Ross. Design and fabrication of a new vibration-based electromechanical power generator. *Sensors and Actuators A: Physical*, 92(1-3):335–342, 2001.
- [56] Peter Glynne-Jones, Michael John Tudor, Stephen Paul Beeby, and Neil M White. An electromagnetic, vibration-powered generator for intelligent sensor systems. *Sensors and Actuators A: Physical*, 110(1-3):344–349, 2004.
- [57] Wen J Li, Zhiyu Wen, PK Wong, Gordon MH Chan, and PHW Leong. A micromachined vibration-induced power generator for low power sensors of robotic systems. In *Proc. Of the World Automation Congress, Hawaii, USA*, 2000.
- [58] Peihong Wang, Huiting Liu, Xuhan Dai, Zhuoqing Yang, Zhongzhu Wang, and Xiaolin Zhao. Design, simulation, fabrication and characterization of a micro electromagnetic vibration energy harvester with sandwiched structure and air channel. *Microelectronics Journal*, 43(2):154–159, 2012.
- [59] CR Saha, T O’donnell, N Wang, and P McCloskey. Electromagnetic generator for harvesting energy from human motion. *Sensors and Actuators A: Physical*, 147(1):248–253, 2008.
- [60] Bin Yang, Chengkuo Lee, Wenfeng Xiang, Jin Xie, Johnny Han He, Rama Krishna Kotlanka, Siew Ping Low, and Hanhua Feng. Electromagnetic energy harvesting from vibrations of multiple frequencies. *Journal of micromechanics and microengineering*, 19(3):035001, 2009.
- [61] Niell G Elvin and Alex A Elvin. An experimentally validated electromagnetic energy harvester. *Journal of Sound and Vibration*, 330(10):2314–2324, 2011.
- [62] Emilio Sardini and Mauro Serpelloni. An efficient electromagnetic power harvesting device for low-frequency applications. *Sensors and Actuators A: Physical*, 172(2):475–482, 2011.

- 
- [63] E Bouendeu, A Greiner, PJ Smith, and JG Korvink. An efficient low cost electromagnetic vibration harvester. In *The 9th international workshop on micro and nanotechnology for power generation and energy conversion applications*, pages 320–323, 2009.
- [64] Santosh Kulkarni, Elena Koukharenko, Russell Torah, John Tudor, Steve Beeby, Terence O'Donnell, and Saibal Roy. Design, fabrication and test of integrated micro-scale vibration-based electromagnetic generator. *Sensors and Actuators A: Physical*, 145:336–342, 2008.
- [65] Dibin Zhu, Stephen Roberts, Michael J Tudor, and Stephen P Beeby. Design and experimental characterization of a tunable vibration-based electromagnetic micro-generator. *Sensors and Actuators A: Physical*, 158(2):284–293, 2010.
- [66] Anthony Marin, John Turner, Dong Sam Ha, and Shashank Priya. Broadband electromagnetic vibration energy harvesting system for powering wireless sensor nodes. *Smart Materials and Structures*, 22(7):075008, 2013.
- [67] K Kucab, G Górski, and J Mizia. Energy harvesting in the nonlinear electromagnetic system. *The European Physical Journal Special Topics*, 224(14):2909–2918, 2015.
- [68] Perpetuum, url = <http://www.perpetuum.com>.
- [69] FerroSolutions, url = <http://www.ferrosi.com>.
- [70] Mide Technology, url = <http://www.mide.com>.
- [71] Adaptive Energy, url = <http://www.adaptivenergy.com>.
- [72] Cedrat Technologies, url = <https://www.cedrat-technologies.com>.
- [73] Microstrain, url = <http://www.microstrain.com>.
- [74] AdvancedCeramics, url = <http://www.advancedceramics.com>.
- [75] Yuantai Hu, Huan Xue, and Hongping Hu. A piezoelectric power harvester with adjustable frequency through axial preloads. *Smart materials and structures*, 16(5):1961, 2007.
- [76] Christoph Eichhorn, Frank Goldschmidtboeing, and Peter Woias. A frequency tunable piezoelectric energy converter based on a cantilever beam. *Proceedings of PowerMEMS*, 9(12):309–312, 2008.
- [77] Eli S Leland and Paul K Wright. Resonance tuning of piezoelectric vibration energy scavenging generators using compressive axial preload. *Smart Materials and Structures*, 15(5):1413, 2006.
- [78] Dylan J Morris, John M Youngsman, Michael J Anderson, and David F Bahr. A resonant frequency tunable, extensional mode piezoelectric vibration harvesting mechanism. *Smart Materials and Structures*, 17(6):065021, 2008.

- [79] J Loverich, R Geiger, and J Frank. Stiffness nonlinearity as a means for resonance frequency tuning and enhancing mechanical robustness of vibration power harvesters. In *Active and passive smart structures and integrated systems 2008*, volume 6928, page 692805. International Society for Optics and Photonics, 2008.
- [80] Cevat Volkan Karadag and Nezh Topaloglu. A self-sufficient and frequency tunable piezoelectric vibration energy harvester. *Journal of Vibration and Acoustics*, 139(1), 2017.
- [81] SM Shahruz. Design of mechanical band-pass filters for energy scavenging. *Journal of sound and vibration*, 292(3-5):987–998, 2006.
- [82] Ibrahim Sari, Tuna Balkan, and Haluk Kulah. An electromagnetic micro power generator for wideband environmental vibrations. *Sensors and Actuators A: Physical*, 145:405–413, 2008.
- [83] RM Toyabur, M Salauddin, Hyunok Cho, and Jae Y Park. A multimodal hybrid energy harvester based on piezoelectric-electromagnetic mechanisms for low-frequency ambient vibrations. *Energy conversion and management*, 168:454–466, 2018.
- [84] M Amri, P Basset, F Cottone, D Galayko, F Najjar, and T Bourouina. Novel nonlinear spring design for wideband vibration energy harvesters. *Proc. PowerMEMS*, pages 189–193, 2011.
- [85] Saber Mahmoudi, Najib Kacem, and Nouredine Bouhaddi. Enhancement of the performance of a hybrid nonlinear vibration energy harvester based on piezoelectric and electromagnetic transductions. *Smart materials and structures*, 23(7):075024, 2014.
- [86] BP Mann and ND Sims. Energy harvesting from the nonlinear oscillations of magnetic levitation. *Journal of sound and vibration*, 319(1-2):515–530, 2009.
- [87] Issam Abed, Najib Kacem, Nouredine Bouhaddi, and Mohamed Lamjed Bouazizi. Multi-modal vibration energy harvesting approach based on nonlinear oscillator arrays under magnetic levitation. *Smart Materials and Structures*, 25(2):025018, 2016.
- [88] Cyril Drezet, Najib Kacem, and Nouredine Bouhaddi. Design of a nonlinear energy harvester based on high static low dynamic stiffness for low frequency random vibrations. *Sensors and Actuators A: Physical*, 283:54–64, 2018.
- [89] Liuyang Xiong, Lihua Tang, and Brian R Mace. Internal resonance with commensurability induced by an auxiliary oscillator for broadband energy harvesting. *Applied Physics Letters*, 108(20):203901, 2016.
- [90] Li-Qun Chen, Wen-An Jiang, Meghashyam Panyam, and Mohammed F Daqaq. A broadband internally resonant vibratory energy harvester. *Journal of Vibration and Acoustics*, 138(6), 2016.
- [91] Philip W Anderson. Absence of diffusion in certain random lattices. *Physical review*, 109(5):1492, 1958.

- 
- [92] CH Hodges. Confinement of vibration by structural irregularity. *Journal of sound and vibration*, 82(3):411–424, 1982.
- [93] CH Hodges and James Woodhouse. Vibration isolation from irregularity in a nearly periodic structure: Theory and measurements. *The Journal of the Acoustical Society of America*, 74(3):894–905, 1983.
- [94] Zakaria Zergoune, Najib Kacem, and Nouredine Bouhaddi. On the energy localization in weakly coupled oscillators for electromagnetic vibration energy harvesting. *Smart Materials and Structures*, 28(7):07LT02, 2019.
- [95] PV Malaji and SF Ali. Energy harvesting from near periodic structures. In *Vibration Engineering and Technology of Machinery*, pages 411–420. Springer, 2015.
- [96] Diala Bitar. *Collective dynamics of weakly coupled nonlinear periodic structures*. PhD thesis, Université Bourgogne Franche-Comté, 2017.
- [97] Aymen Jallouli, Najib Kacem, and Nouredine Bouhaddi. Nonlinear dynamics of a 2d array of coupled pendulums under parametric excitation. In *5th ECCOMAS Thematic Conference on Computational Methods in Structural Dynamics and Earthquake Engineering (COMPdyn 2015)*, volume 8, 2015.
- [98] Vinod R Challa, MG Prasad, and Frank T Fisher. A coupled piezoelectric–electromagnetic energy harvesting technique for achieving increased power output through damping matching. *Smart materials and Structures*, 18(9):095029, 2009.
- [99] Wang Chen, Yanlong Cao, and Jin Xie. Piezoelectric and electromagnetic hybrid energy harvester for powering wireless sensor nodes in smart grid. *Journal of Mechanical Science and Technology*, 29(10):4313–4318, 2015.
- [100] Ping Li, Shiqiao Gao, Shaohua Niu, Haipeng Liu, and Huatong Cai. An analysis of the coupling effect for a hybrid piezoelectric and electromagnetic energy harvester. *Smart materials and structures*, 23(6):065016, 2014.
- [101] Ping Li, Shiqiao Gao, Huatong Cai, and Lisen Wu. Theoretical analysis and experimental study for nonlinear hybrid piezoelectric and electromagnetic energy harvester. *Microsystem Technologies*, 22(4):727–739, 2016.
- [102] Miah A Halim and Jae Y Park. A non-resonant, frequency up-converted electromagnetic energy harvester from human-body-induced vibration for hand-held smart system applications. *Journal of Applied Physics*, 115(9):094901, 2014.
- [103] Benjamin J Bowers and David P Arnold. Spherical magnetic generators for bio-motional energy harvesting. *Proceedings of PowerMEMS*, pages 281–284, 2008.

- [104] Ethem Erkan Aktakka, Hanseup Kim, and Khalil Najafi. Energy scavenging from insect flight. *Journal of Micromechanics and Microengineering*, 21(9):095016, 2011.
- [105] Alexander Frey, Julian Seidel, Matthias Schreiter, and Ingo Kuehne. Piezoelectric mems energy harvesting module based on non-resonant excitation. In *2011 16th International Solid-State Sensors, Actuators and Microsystems Conference*, pages 683–686. IEEE, 2011.
- [106] Huicong Liu, Chengkuo Lee, Takeshi Kobayashi, Cho Jui Tay, and Chenggen Quan. Investigation of a mems piezoelectric energy harvester system with a frequency-widened-bandwidth mechanism introduced by mechanical stoppers. *Smart Materials and Structures*, 21(3):035005, 2012.
- [107] Kang-Qi Fan, Feng-Bo Chao, Jian-Guo Zhang, Wei-Dong Wang, and Xiao-Huan Che. Design and experimental verification of a bi-directional nonlinear piezoelectric energy harvester. *Energy conversion and management*, 86:561–567, 2014.
- [108] Kangqi Fan, Shaohua Liu, Haiyan Liu, Yingmin Zhu, Weidong Wang, and Daxing Zhang. Scavenging energy from ultra-low frequency mechanical excitations through a bi-directional hybrid energy harvester. *Applied Energy*, 216:8–20, 2018.
- [109] DW Wang, JL Mo, XF Wang, H Ouyang, and ZR Zhou. Experimental and numerical investigations of the piezoelectric energy harvesting via friction-induced vibration. *Energy Conversion and Management*, 171:1134–1149, 2018.
- [110] U Bartsch, J Gaspar, and O Paul. Low-frequency two-dimensional resonators for vibrational micro energy harvesting. *Journal of Micromechanics and Microengineering*, 20(3):035016, 2010.
- [111] Mariano Febbo, Sebastián Pablo Machado, Claudio David Gatti, and Jose Miguel Ramirez. An out-of-plane rotational energy harvesting system for low frequency environments. *Energy conversion and management*, 152:166–175, 2017.
- [112] Huicong Liu, Bo Woon Soon, Nan Wang, CJ Tay, Chenggen Quan, and Chengkuo Lee. Feasibility study of a 3d vibration-driven electromagnetic mems energy harvester with multiple vibration modes. *Journal of Micromechanics and Microengineering*, 22(12):125020, 2012.
- [113] Huicong Liu, You Qian, and Chengkuo Lee. A multi-frequency vibration-based mems electromagnetic energy harvesting device. *Sensors and Actuators A: Physical*, 204:37–43, 2013.
- [114] Ali Hasan Nayfeh, Dean T Mook, and P Holmes. *Nonlinear oscillations*. 1980.
- [115] Abu Riduan Md Foisal, Chinsuk Hong, and Gwi-y-Sang Chung. Multi-frequency electromagnetic energy harvester using a magnetic spring cantilever. *Sensors and Actuators A: Physical*, 182:106–113, 2012.

- 
- [116] Dirk Spreemann and Yiannos Manoli. *Electromagnetic vibration energy harvesting devices: Architectures, design, modeling and optimization*, volume 35. Springer Science & Business Media, 2012.
- [117] Christophe Pierre. Mode localization and eigenvalue loci veering phenomena in disordered structures. *Journal of Sound and Vibration*, 126(3):485–502, 1988.
- [118] Christophe Pierre. Weak and strong vibration localization in disordered structures: a statistical investigation. *Journal of Sound and Vibration*, 139(1):111–132, 1990.
- [119] Najib Kacem, Sebastien Hentz, David Pinto, Bruno Reig, and V Nguyen. Nonlinear dynamics of nanomechanical beam resonators: improving the performance of nems-based sensors. *Nanotechnology*, 20(27):275501, 2009.
- [120] Ali H Nayfeh. *Perturbation methods*. John Wiley & Sons, 2008.
- [121] Kalyanmoy Deb. Multi-objective optimization. In *Search methodologies*, pages 403–449. Springer, 2014.
- [122] Jean Dipama. *Optimisation multi-objectif des systèmes énergétiques*. PhD thesis, École Polytechnique de Montréal, 2010.
- [123] Vilfredo Pareto. Cours d’économie politique, vol. 2. *Pichou, Paris*, 1897.
- [124] Panos Seferlis and Michael C Georgiadis. *The integration of process design and control*. Elsevier, 2004.
- [125] Kalyanmoy Deb and Himanshu Gupta. Searching for robust pareto-optimal solutions in multi-objective optimization. In *International conference on evolutionary multi-criterion optimization*, pages 150–164. Springer, 2005.
- [126] Nidamarthi Srinivas and Kalyanmoy Deb. Multiobjective optimization using nondominated sorting in genetic algorithms. *Evolutionary computation*, 2(3):221–248, 1994.
- [127] Charles Darwin. *L’origine des espèces au moyen de la sélection naturelle ou la lutte pour l’existence dans la nature*. C. Reinwald, 1887.
- [128] John Henry Holland et al. *Adaptation in natural and artificial systems: an introductory analysis with applications to biology, control, and artificial intelligence*. MIT press, 1992.
- [129] David E Goldberg, Jon Richardson, et al. Genetic algorithms with sharing for multimodal function optimization. In *Genetic algorithms and their applications: Proceedings of the Second International Conference on Genetic Algorithms*, pages 41–49. Hillsdale, NJ: Lawrence Erlbaum, 1987.

- [130] Carlos A Coello Coello Coello. A short tutorial on evolutionary multiobjective optimization. In *International Conference on evolutionary multi-criterion optimization*, pages 21–40. Springer, 2001.
- [131] Kalyanmoy Deb, Samir Agrawal, Amrit Pratap, and Tanaka Meyarivan. A fast elitist non-dominated sorting genetic algorithm for multi-objective optimization: Nsga-ii. In *International conference on parallel problem solving from nature*, pages 849–858. Springer, 2000.
- [132] Long Wang, Tong-guang Wang, and Yuan Luo. Improved non-dominated sorting genetic algorithm (nsga)-ii in multi-objective optimization studies of wind turbine blades. *Applied Mathematics and Mechanics*, 32(6):739–748, 2011.
- [133] Carlos M Fonseca, Peter J Fleming, et al. Genetic algorithms for multiobjective optimization: Formulation discussion and generalization. In *Icga*, volume 93, pages 416–423. Citeseer, 1993.
- [134] Jeffrey Horn, Nicholas Nafpliotis, and David E Goldberg. Multiobjective optimization using the niched pareto genetic algorithm. *IlliGAL report*, 93005, 1993.
- [135] Faruq Muhammad Foong, Chung Ket Thein, and Daniil Yurchenko. Important considerations in optimising the structural aspect of a sdof electromagnetic vibration energy harvester. *Journal of Sound and Vibration*, 482:115470, 2020.
- [136] Kaouthar Aouali, Najib Kacem, Noureddine Bouhaddi, Elyes Mrabet, and Mohamed Haddar. Exploiting nonlinear dynamics and energy localization to enhance the performances of an electromagnetic vibration energy harvester. In *International Design Engineering Technical Conferences and Computers and Information in Engineering Conference*, volume 59285, page V008T10A017. American Society of Mechanical Engineers, 2019.
- [137] Kalyanmoy Deb, Amrit Pratap, Sameer Agarwal, and TAMT Meyarivan. A fast and elitist multiobjective genetic algorithm: Nsga-ii. *IEEE transactions on evolutionary computation*, 6(2):182–197, 2002.
- [138] Abdullah Konak, David W Coit, and Alice E Smith. Multi-objective optimization using genetic algorithms: A tutorial. *Reliability engineering & system safety*, 91(9):992–1007, 2006.
- [139] Muriel Beckers. Dual methods for discrete structural optimization problems. *International Journal for Numerical Methods in Engineering*, 48(12):1761–1784, 2000.
- [140] Paul D Mitcheson, Eric M Yeatman, G Kondala Rao, Andrew S Holmes, and Tim C Green. Energy harvesting from human and machine motion for wireless electronic devices. *Proceedings of the IEEE*, 96(9):1457–1486, 2008.
- [141] K Ashraf, MH Md Khir, JO Dennis, and Z Baharudin. A wideband, frequency up-converting bounded vibration energy harvester for a low-frequency environment. *Smart materials and structures*, 22(2):025018, 2013.



- 
- [142] Tzeno Galchev, Hanseup Kim, and Khalil Najafi. A parametric frequency increased power generator for scavenging low frequency ambient vibrations. *Procedia Chemistry*, 1(1):1439–1442, 2009.
- [143] Michael Renaud, Paolo Fiorini, Rob van Schaijk, and Chris Van Hoof. Harvesting energy from the motion of human limbs: the design and analysis of an impact-based piezoelectric generator. *Smart Materials and Structures*, 18(3):035001, 2009.
- [144] Bin Yang and Chengkuo Lee. Non-resonant electromagnetic wideband energy harvesting mechanism for low frequency vibrations. *Microsystem Technologies*, 16(6):961–966, 2010.
- [145] Dibin Zhu, Steve Beeby, John Tudor, and Nick Harris. Vibration energy harvesting using the halbach array. *Smart Materials and Structures*, 21(7):075020, 2012.
- [146] David F Berdy, Pornsak Srisungsitthisunti, Byunghoo Jung, Xianfan Xu, Jeffrey F Rhoads, and Dimitrios Peroulis. Low-frequency meandering piezoelectric vibration energy harvester. *IEEE transactions on ultrasonics, ferroelectrics, and frequency control*, 59(5):846–858, 2012.
- [147] Marcin Marzencki, Yasser Ammar, and Skandar Basrour. Integrated power harvesting system including a mems generator and a power management circuit. *Sensors and Actuators A: Physical*, 145:363–370, 2008.
- [148] Song Guo and Hoi Lee. An efficiency-enhanced integrated cmos rectifier with comparator-controlled switches for transcutaneous powered implants. In *2007 IEEE Custom Integrated Circuits Conference*, pages 385–388. IEEE, 2007.
- [149] Geffrey K Ottman, Heath F Hofmann, Archin C Bhatt, and George A Lesieutre. Adaptive piezoelectric energy harvesting circuit for wireless remote power supply. *IEEE Transactions on power electronics*, 17(5):669–676, 2002.
- [150] Xinping Cao, Wen-Jen Chiang, Ya-Chin King, and Yi-Kuen Lee. Electromagnetic energy harvesting circuit with feedforward and feedback dc–dc pwm boost converter for vibration power generator system. *IEEE Transactions on Power Electronics*, 22(2):679–685, 2007.
- [151] Mohammed Farag. *Lithium-ion batteries: Modelling and state of charge estimation*. PhD thesis, 2013.
- [152] Henry A Sodano, Daniel J Inman, and Gyuhae Park. Generation and storage of electricity from power harvesting devices. *Journal of intelligent material systems and structures*, 16(1):67–75, 2005.

# List of Figures

1.1	Publications number in Scopus in the field of energy harvesting [1] . . . . .	4
1.2	Different energy sources [4] . . . . .	5
1.3	Classification approach of MEH systems. . . . .	6
1.4	Structure of a typical vibration energy harvester: from vibration sources to applications	6
1.5	1-DOF energy harvester with base excitation . . . . .	7
1.6	Dimensionless power with normalized frequency based on Equation 1.9 for $\xi = 0.1$ . . .	9
1.7	Mechanisms for vibration energy harvesters including: a) piezoelectric energy harvesters including a configurations of cantilever with tip mass and top and bottom piezoelectric layers [11], b) electromagnetic energy harvester based on mass-spring resonance [12], c) electrostatic transduction [13], which is represented by parallel top and bottom cap electrodes and internal springs and d) triboelectric transduction represented by a cantilever with two triboelectric layers [14]. . . . .	9
1.8	Mechanisms for vibration energy harvesters including [16] . . . . .	10
1.9	Simplistic model of an electromagnetic transducer [17] . . . . .	11
1.10	Illustration of the direct piezoelectric effect in a lighter [20] . . . . .	12
1.11	Illustration of the inverse piezoelectric effect in a quartz watch (steps from 1 to 6) [22]	12
1.12	Piezoelectric transducer example [23] . . . . .	13
1.13	Electrostatic generators types: a) In-plane overlap varying, b) In-plane gap closing and c) Out-of-plane gap closing configurations . . . . .	14
1.14	Illustration of the structure and working principle of the triboelectric generator [31] a) The first designed triboelectric transducer with its working principle b) Proposed mechanism of the triboelectric generator (charges generation, triboelectric potential creation, flow of current in the external load). . . . .	15
1.15	Piezoelectric energy harvester developed by Roundy et al. [42] . . . . .	17
1.16	Design of the piezoelectric energy harvester based cantilever-pendulum [43] . . . . .	17
1.17	Configuration and vertical view of the piezoelectric harvester based on multiple mechanical motions [45] . . . . .	18
1.18	Electromagnetic energy harvester developed by [53] . . . . .	18
1.19	Design of the planar electromagnetic transducer developed by [54] . . . . .	20

1.20	a) Design of the electromagnetic harvester based cantilever-beam with two magnet masses fixed at its end [55] b) Prototype of electromagnetic harvester with a fixed coil and moving magnets [56] c) MEMS electromagnetic generator based on a planar spring and a center magnet [58] . . . . .	21
1.21	Illustration of the harvester consisting of a piezoelectric beam including two additional arms [76] . . . . .	24
1.22	Illustration of a resonance frequency tuning for a vibration energy harvester consisting of a simply supported piezoelectric bimorph [77] . . . . .	25
1.23	Illustration of an extensional mode resonator [78] . . . . .	25
1.24	Illustration of two coupled piezoelectric cantilevers to tune the natural frequency [80] .	26
1.25	a) Illustration of mechanical band-pass filter, b) The plots of the Bode magnitude and the filter frequency band [81] . . . . .	26
1.26	a) Illustration of the proposed multimodal electromagnetic harvester , b) The wide frequency bandwidth of the proposed harvester [82] . . . . .	27
1.27	Illustration of the harvester composed of a primary beam, four piezoelectric patches attached to the four secondary beams and magnet masses below coils [83] . . . . .	27
1.28	a) Linear behavior , b) Nonlinear hardening behavior . . . . .	28
1.29	a) Illustration of the proposed nonlinear harvester , b) Illustration of the frequency bandwidth in linear, critical and nonlinear configurations [85] . . . . .	28
1.30	a) Illustration of the proposed nonlinear harvester, b) Illustration of the frequency bandwidth in linear, critical and nonlinear configurations [87] . . . . .	29
1.31	Illustration of the nonlinear internal resonance . . . . .	30
1.32	a) Illustration of the proposed nonlinear harvester, b) Illustration of the frequency bandwidth in linear, critical and nonlinear configurations [89] . . . . .	30
1.33	a) Illustration of the proposed T-shaped piezoelectric beam, b) Comparison of the nonlinear behavior away from internal resonance and the case of internal resonance [90] . .	31
1.34	Coupled pendula arranged on a chain [92] . . . . .	32
1.35	Illustration of energy localization phenomenon in a cyclic structure consisting of a fan with 16 blades: a) periodic structure b) quasiperiodic structure . . . . .	32
1.36	Structure of the hybrid piezoelectric-electromagnetic vibration energy harvester proposed by [98] . . . . .	33
1.37	Structure of the hybrid piezoelectric-electromagnetic vibration energy harvester based on the vibration of two magnets guided by elastic bi-clamped beam proposed by [100].	33
1.38	(a) Design of the hybrid VEH proposed by [101] (b) Output power with different acceleration levels . . . . .	34
1.39	Structure of the non-resonant EMEH based on frequency-up conversion proposed by [102]	35
1.40	Structure of the non-resonant EMEH based on human motion proposed by [103] . . . .	35

1.41	A NR-PEEH based on the wings motion of a beetle consisting of two piezoelectric bimorph beams attached to the wings [104] . . . . .	36
1.42	(a) Design of the proposed NR-PEEH system. (b) Working mechanism of the NR-PEEH system. (c) The bottom NR-PEEH structure top view. (d) The top NR-PEEH structure top view. [106] . . . . .	37
1.43	Design of the 2D harvester proposed by [109] : (a) The device design, (b) The FFT analysis results. . . . .	38
1.44	Schematic design of the 2D In-plane harvester proposed by [110] . . . . .	38
1.45	2D rotating harvester proposed by [111]: (a) Design of the proposed device, (b) Output power. . . . .	39
1.46	Design of a 3-D harvester proposed by [112] . . . . .	39
1.47	Design of a multifrequency 3-D harvester proposed by [113] . . . . .	40
2.1	3D schematic of the proposed vibration energy harvester . . . . .	45
2.2	2D representation of the vibration energy harvester . . . . .	46
2.3	. . . . .	48
2.4	Variation of the exact magnetic force $F_m^{exact}$ and its approximations $F_m^{Taylor}$ (Taylor series of $F_m^{exact}$ up to order 3) and $F_m$ ( $F_m^{Taylor}$ with the elimination of even terms) with the relative displacement. . . . .	51
2.5	Representation of the beam dimensions . . . . .	52
2.6	The proposed vibration energy harvester . . . . .	53
2.7	Experimental test bench . . . . .	53
2.8	Variation of electrical damping as a function of load resistance . . . . .	55
2.9	Bending vibration modes of the 10-coupled beams with variation in mass density by : (a) 0% (periodic system), (b) 10% of the 2 <sup>nd</sup> , 5 <sup>th</sup> and 8 <sup>th</sup> beams counting from the bottom, (c) 6% and (d) 10% of the 3 <sup>rd</sup> , 6 <sup>th</sup> and 9 <sup>th</sup> beams counting from the bottom. . . . .	57
2.10	(a) Axisymmetric (2D) modeling of the structure under FEMM, (b) Characteristics and meshing of the structure under FEMM . . . . .	59
2.11	Results of the magnetic filed $B$ distribution . . . . .	60
2.12	Harvested power with load resistance . . . . .	61
2.13	(a) The designed electromagnetic vibration energy harvester (b) The mechanical model of the harvester . . . . .	61
2.14	Veering phenomenon: Normal frequencies with mass mistuning coefficient while variation of the coupling coefficient . . . . .	63
2.15	Maximum amplitudes with mistuning $\alpha$ ( $\beta = 2.2\%$ and $c_m = 0.03N.s/m$ ) . . . . .	64
2.16	Maximum amplitudes with mistuning $\alpha$ and load resistance $R_{load}$ ( $\beta = 2.2\%$ and $c_m = 0.03N.s/m$ ) . . . . .	65
2.17	Harvested power with mistuning $\alpha$ and load resistance $R_{load}$ . . . . .	65

2.18	Linear, critical and nonlinear configurations. . . . .	68
2.19	Robustness of energy localization rate in the nonlinear configuration: Energy localization rate with variation of the mistuning coefficient in an open-loop circuit . . . . .	71
2.20	Illustration of the 3 studied configurations: (a) Periodic structure, (b) Quasiperiodic structure and harvesting energy from both DOFs oscillators and (c) Quasiperiodic structure and harvesting energy from only perturbed DOF oscillator. . . . .	71
2.21	(a) Harvested power vs frequency of the periodic 2-DOFs system (b) Total power of the periodic system with load resistances . . . . .	72
2.22	Maximum amplitudes in nonlinear case with mass mistuning coefficient: search for the optimal mass mistuning . . . . .	72
2.23	Harvested power with frequency of the retained configuration 3. . . . .	73
2.24	(a)Maximum voltage with mass mistuning coefficient (b) Experimental-numerical confrontation of the harvested power with load resistances . . . . .	74
2.25	Harvested power from the perturbed dof oscillator in the linear case . . . . .	75
2.26	Variation of the measured critical resistances with the mistuning coefficients . . . . .	76
2.27	(c) Harvested power from the perturbed dof and (d) Frequency bandwidth with load resistances and mass mistuning ( $a_{rms} = 0.09g$ ). . . . .	77
3.1	Multiobjective problem representation [122] . . . . .	81
3.2	Pareto dominance and optimality [122] . . . . .	82
3.3	Principle of NSGA-II algorithm [122]. . . . .	83
3.4	Device of the N coupled magnets electromagnetic vibration energy harvester . . . . .	85
3.5	The first and second DOFs' numerical and experimental energies vs mass mistuning coefficient ( $a_{rms} = 1g, R_{load} = 6\Omega$ ). . . . .	87
3.6	(a) The first and second DOFs' numerical and experimental energies vs mass mistuning coefficient ( $a_{rms} = 1g, R_{load} = 6\Omega$ ). (b) The harvested power from the perturbed magnet with variation of load resistance ( $a_{rms} = 1g, \alpha = 1.06$ ) . . . . .	88
3.7	The 2-DOFs system Pareto front: illustration of Frequency bandwidth with harvested power . . . . .	89
3.8	Experimental validation of the 2-DOFs model optimal configuration in terms of average harvested power and the corresponding frequency bandwidth BW . . . . .	90
3.9	Diagram of continuous optimization with discrete variables steps . . . . .	92
3.10	The equivalent model of the 5-DOFs vibration energy harvester with mistuning of the 2 <sup>nd</sup> and 4 <sup>th</sup> DOFs masses . . . . .	92
3.11	$E_2$ versus $E_4$ : Pareto front of the 5-DOFs model. . . . .	93
3.12	The 5-DOFs system's Pareto front: illustration of the frequency bandwidth with harvested power and the % of corresponding energy localization rates. . . . .	94

3.13	The Pareto front 2-D projection of Figure 3.12 with precision of the sum and the difference of the optimal solutions corresponding energy rates of the 2 <sup>nd</sup> and 4 <sup>th</sup> DOFs oscillators . . . . .	94
3.14	Harvested power amount and frequency bandwidth of the optimal configuration with reproducing the obtained optimal values in experimental tests. . . . .	95
3.15	The periodic 5-DOFs system’s Pareto front resulting from the multiobjective optimization	96
3.16	Comparison of the optimized current harvester with to some standards from state-of-art using the $FoM_v$ criteria [60, 62, 64, 85, 141–146] . . . . .	97
4.1	Schematic and real representations of the electromagnetic-piezoelectric energy harvester	100
4.2	2D illustration of the 2-DOFs hybrid structure . . . . .	101
4.3	Equivalent circuit of the energy harvester with a steel and a piezoelectric layers . . . .	105
4.4	Experimental-theoretical confrontation of the harvested power from a piezoelectric patch	107
4.5	The proposed hybrid energy harvester destined to activate the internal resonance phenomenon . . . . .	108
4.6	Ratio of the natural frequency $\omega_2$ to $\omega_1$ while varying the separation distances $d_1$ and $d_2$	110
4.7	The experimental device for the case of internal resonance . . . . .	111
4.8	Voltage with load resistances a) EP b) PE . . . . .	111
4.9	Power with load resistances a) EM b) PE . . . . .	112
4.10	PE and EM DOFs frequency responses for the internal resonance phenomenon . . . . .	112
4.11	Frequency response with optimal parameters away from internal resonance condition .	113
4.12	Frequency response with optimal parameters ensuring the activation of the internal resonance phenomenon . . . . .	114
4.13	Structure of a typical energy harvesting circuit . . . . .	114
4.14	Energy harvesting circuit with a DC-DC amplifier converter [150] . . . . .	115
4.15	Ragone Diagram [151] . . . . .	116
4.16	Energy storage . . . . .	117
4.17	Experimental test bench for energy storage using capacitors . . . . .	117
4.18	Voltage of the piezoelectric patch . . . . .	118
4.19	Voltage across a 100 $\mu F$ capacitor . . . . .	118
4.20	Voltage across resistance of discharge circuit . . . . .	119



# List of Tables

1.1	Power density of different energy scavenging technologies [6] . . . . .	5
1.2	Piezoelectric constants for common materials for 31 and 33 modes [25,26] . . . . .	14
1.3	Comparison of the transduction mechanisms in the field of energy harvesting [32,33] .	16
1.4	Characteristics and performance of different piezoelectric energy harvesters: design, frequency (Freq), acceleration (Acc) or force (F), volume (Vol) and power density (PD)	19
1.5	Characteristics and performance of different electromagnetic energy harvesters: design, frequency (Freq), acceleration (Acc) or force (F), volume (Vol) and power density (PD)	22
1.6	Characteristics and performance of some commercialized electromagnetic and piezoelectric energy harvesters: design, frequency (Freq), acceleration (Acc) or force (F), volume (Vol) and power density (PD) . . . . .	23
2.1	The 10-beams system’s natural eigenfrequencies in Hz . . . . .	55
2.2	Characteristics of the used coils and magnets . . . . .	59
2.3	Design parameters for a single ddl system . . . . .	60
3.1	Algorithm NSGA-II . . . . .	84
3.2	The optimization model for the 2-DOFs harvester: objective function and constraints .	89
3.3	The multiobjective optimization results of the 2-DOFs harvester . . . . .	90
3.4	Objective function and constraints to obtain the optimal position of the introduced two mistunings . . . . .	91
3.5	The optimization problem formulation for the 5-DOFs harvester: objective function and constraints . . . . .	93
3.6	The harvester’s 5-DOFs optimization reults . . . . .	95
4.1	Design parameters of the piezoelectric patches . . . . .	101
4.2	Comparison between accumulators and rechargeable batteries . . . . .	115
4.3	Comparison between capacitors and super-capacitors . . . . .	116



**Titre:** Réseaux quasi-périodiques d'oscillateurs non-linéaires faiblement couplés pour la récupération d'énergie vibratoire par voies électromagnétique ou bien électromagnétique-piézoélectrique

**Mots-clés:** Récupération d'énergie vibratoire, quasi-périodicité, localisation d'énergie, non-linéarité, transductions électromagnétique et piézoélectrique, optimisation multi-objectifs, résonance interne.

Une étude sur les réseaux d'oscillateurs électromagnétiques et hybrides non-linéaires pour la récupération d'énergie vibratoire est menée dans cette thèse. Les limitations courantes des récupérateurs d'énergie, à savoir la bande passante étroite et la faible quantité d'énergie récupérée, sont surmontées en étudiant différentes approches d'amélioration. Dans un premier temps, le phénomène de localisation d'énergie a été fonctionnalisé pour un système à 2-ddls à transduction électromagnétique. Il a été montré qu'il permet de minimiser le coût, le nombre des circuits électriques et l'encombrement de la structure. De plus, la combinaison de la non-linéarité et de la localisation de mode a été étudiée. Il a été montré que la nonlinéarité assure une robustesse de la localisation de mode. Aussi, cette combinaison permet d'améliorer la puissance récupérée jusqu'à 19 % et la bande passante jusqu'à 116 %. En effectuant une optimisation multiobjectifs, il a été montré que

cette combinaison assure une amélioration jusqu'à 101 % et 79 % en termes de puissance récupérée et de bande passante dans le cas d'un dispositif quasi-périodique à 5-ddls. Par ailleurs, afin d'améliorer davantage la puissance totale récupérée, le système électromagnétique a été transformé en système hybride en ajoutant des couches piézoélectriques aux poutres. Le phénomène de résonance interne est également étudié pour la structure hybride. Des distances entre aimants bien choisies entraînent l'activation de la résonance interne 2:1 et une amélioration significative des performances de sortie du récupérateur hybride a été démontrée. Il a été démontré qu'il est possible de réduire le volume du récupérateur de près de deux fois tout en augmentant la bande passante de fréquence et la puissance récupérée de 300 % et 100 % respectivement par rapport à un récupérateur non-linéaire ne présentant pas la résonance interne .

**Title:** Quasiperiodic arrays of weakly coupled nonlinear oscillators for vibration energy harvesting by electromagnetic or electromagnetic-piezoelectric transductions

**Keywords:** Vibration energy harvesting, quasiperiodicity, energy localization, nonlinearity, electromagnetic and piezoelectric transduction, multiobjective optimization, internal resonance.

A study on nonlinear electromagnetic and hybrid oscillator arrays for vibration energy harvesting is conducted in this thesis. The common harvesters' limitations namely the narrow bandwidth and the low amount of the harvested energy are overcome by investigating different enhancement approaches. First, the energy localization phenomenon was functionalized in a 2-DOFs with electromagnetic transduction system. It has been shown that it permits minimizing the number and the cost of electrical circuits and therefore the technological constraints of the structure. After that, the combination of nonlinear dynamics with the mode localization phenomenon has been studied. It has been proven that nonlinear dynamics allow a robustness of the mode localization phenomenon. Add to that, this combination permits improving the harvested power up to 19. % and the frequency of the bandwidth up to 116 %. By performing a multiobjective optimization procedure,

it was shown that this combination ensures an enhancement up to 101 % and 79 % in terms of harvested power and frequency bandwidth in the case of quasiperiodic 5-DOFs device. Moreover, in order to further improve the total harvested power, the electromagnetic system was transformed into hybrid one by adding piezoelectric layers. The internal resonance phenomenon is, also, investigated for the hybrid electromagnetic-piezoelectric structure. Well-chosen gaps between the magnets result in activating the 2:1 internal resonance and a significant improvement of the hybrid harvester output performance has been demonstrated. It has been shown that it is possible to reduce the harvester's volume by nearly two times while increasing the frequency bandwidth and the harvested power by 300 % and 100 % respectively comparing to a nonlinear harvester away from internal resonance.